

LUCIO SALLES DE SALLES

SHORT CONTINUOUSLY REINFORCED CONCRETE PAVEMENT  
DESIGN RECOMMENDATIONS BASED ON NON-DESTRUCTIVE  
ULTRASONIC DATA AND STRESS SIMULATION

São Paulo

2017

LUCIO SALLES DE SALLES  
Civil Engineering, UFSM, 2011  
Master of Science in Engineering, EPUSP, 2014

SHORT CONTINUOUSLY REINFORCED CONCRETE PAVEMENT  
DESIGN RECOMMENDATIONS BASED ON NON-DESTRUCTIVE  
ULTRASONIC DATA AND STRESS SIMULATION

Thesis submitted to the Polytechnic School of  
the University of São Paulo in partial  
fulfillment of the requirements for the degree  
of Doctor of Science in Engineering

Concentration field: Transportation  
Engineering

Advisor: Prof. Dr. José Tadeu Balbo  
(University of São Paulo)

Co-Advisor: Prof. Dr. Lev Khazanovich  
(University of Pittsburgh)

São Paulo

2017

### Catálogo-na-publicação

Salles de Salles, Lucio  
SHORT CONTINUOUSLY REINFORCED CONCRETE PAVEMENT  
DESIGN RECOMMENDATIONS BASED ON NON-DESTRUCTIVE  
ULTRASONIC DATA AND STRESS SIMULATION / L. Salles de Salles – São  
Paulo, 2017.  
249 p.

Tese (Doutorado) - Escola Politécnica da Universidade de São Paulo.  
Departamento de Engenharia de Transportes.

1. Concrete Pavements 2. Stress simulation 3. Non-destructive testing  
4. Pavement design 5. Ultrasonic data I. Universidade de São Paulo. Escola  
Politécnica. Departamento de Engenharia de Transportes II.t.

## ACKNOWLEDGEMENTS

John Heywood once wrote that “many hands make light work” and that’s especially true for the research work described in this thesis. Without the help and support of so many friends and colleagues, to whom this thesis is dedicated for, my work would not only be harder, it would be impossible. Therefore, I would like to express my deepest gratitude to the individuals than one way or another aided me in this great task:

To my family: father, sisters, brothers-in-law and nephews for the support and understanding expressed in some many loving ways and especially to my mom who has always been my greater supporter never failing to encourage me through good and bad times – your love made what I am today. Also to my Uncles Claudio and Ligia and Cousins Claudia and Higino for the close and caring support since I arrived in São Paulo.

To my adviser José Tadeu Balbo for the technical knowledge so easily and willingly transmitted but also for the fatherly guidance that was decisive for developing my research skills in a healthy environment. It was a great pleasure and honor being your research partner for over five years.

To my co-adviser Lev Khazanovich for the most amazing opportunity of doing a part of my research at the University of Minnesota and also for being a researcher role model making me feel included since day one. Also, for the incredible kindness directed at me during a whole year from him and his wife Veronica.

To my great friend and first adviser Prof. Deividi Pereira for the assistance during the dynamic load testing and for the guidance in pretty much everything else.

To my qualification committee (Prof. Laura Motta and Prof. Sergio Furuie) for the valuable contributions to this research.

To the companies and institutions which supported the technical testing and information described in this thesis. To Dynatest and Copavel for the FWD testing. To engineer Massao Watanabe and EPT Engenharia for the short CRCP coring. To the SAISP, specially to

Cristiane Andrioli, for the meteorological data. To the University of São Paulo campus city hall, precisely Engineer Douglas Costa and his team for the assistance while performing load testing, crack and ultrasonic surveys.

To the professors and colleagues at LTC for the valuable classes and discussions.

To my colleagues and dear friends in São Paulo and in Minneapolis for the discussions and suggestions which definitely improved this research. Particularly, from São Paulo, many thanks to Andreia for the help during the ultrasonic surveys, Rafael for the welcome when I first arrived in São Paulo, Rodrigo and Bruno for the slab coring and extra ultrasonic testing, Sergio for the teaching opportunities, Henrique for the design chart discussion and Eric for the help with the FWD testing. From Minneapolis, thank you Kyle and Derek for the initial contact and training with MIRA processing, Katelyn for the HTI discussions, Aziz for the assistance while applying the MIRA simulation software, Ryan for the partnership during the MnDOT project and Abbas for showing me around the University in the first days.

To CAPES for the doctorate fellowship in Brazil and in the US.

To the staff of the Department of transportation at USP and of the Department of civil, environmental and geo-engineering at UofM, expressly to Patricia, Edson and Heather.

To my friends Karl, Katelyn, Andrew, Marcel and Royce for the English revisions.

To my roommates Francisco and Ariana (Brazil) and Royce and Marcel (US) for the great friendship needed during this exciting and stressful period.

To Andy for the amazing support during the last stages of this research.

To friends in Brazil, Minneapolis and around the world that although did not participate in any way technical in this work, made my life lighter while I was doing it.

To God for all those mentioned above.

## ABSTRACT

Four sections of continuously reinforced concrete pavement (CRCP) were constructed at the University of São Paulo campus in order to introduce this kind of pavement structure to Brazil's technical transportation community. Sections were designed as 50 m long concrete slab, short in comparison to traditional CRCP, in order to simulate bus stops and terminals – locations of critical interest for public infrastructure. The thesis presented herein concludes this research project initiated in 2010. As the initial goal of this study was the development of coherent, reliable and intuitive design recommendations for the use of CRCP technology in Brazil, a profound understating of its structural and performance peculiarities was needed. For that, the cracking process of the experimental CRCP sections was recorded over a span of seven years. Due to the sections' short length and lack of anchorage, the experimental "short" CRCP presented a cracking behavior quite different than traditional CRCP. There were much less visible cracks than expected. To address this issue, a novel technology in ultrasonic non-destructive testing of concrete structures was applied. Through ultrasonic signal interpretation it was possible to discover several incipient non-visible cracks within the slabs – many of these became apparent on the slab surface in later crack surveys – and to characterize visible and non-visible cracks regarding crack depth. The updated crack map with non-visible cracks showed similarities with traditional CRCP. Additionally, the ultrasonic data analysis provided important information on thickness variation, reinforcement location and concrete condition that were applied in theoretical simulations (finite element software) of the short CRCP. Simulations were attempted considering different slab geometries, firstly with transverse cracks as joints with high load transfer efficiency (LTE) and secondly with a continuous slab without cracks or joints. The latter simulation was more accurate reaching a shift factor between field and simulated stresses in the order of 0.7 to 1.0. Deflection data and LTE analysis from cracks and panels in between cracks further attested the slab continuous behavior, which contradicts current CRCP design models and performance predictors. Furthermore, critical traffic and environmental loading conditions concerning Brazil's climate and bus traffic characteristics were investigated and related using a selected fatigue model resulting in design recommendations in a chart format for the short CRCP aimed at long-term projects for over 20 years of operation. The design chart was successfully applied to

investigate three failures presented by the experimental short CRCP due to thickness deficiencies pointed out by the ultrasonic testing.

**Keywords:** Continuously reinforced concrete pavement; short length; bus stops; cracks; ultrasonic non-destructive testing; stress simulation; design.

## RESUMO

Quatro seções de pavimento de concreto continuamente armado (PCCA) foram construídas no campus da Universidade de São Paulo, com o objetivo de introduzir esta estrutura, de reconhecido sucesso internacional, à comunidade técnica de engenharia de transportes brasileira. As seções foram projetadas com uma placa de concreto de 50 m de extensão, curta em comparação ao PCCA tradicional, com a finalidade de simular paradas e terminais de ônibus - locais de grande interesse para a infraestrutura pública. A tese aqui apresentada conclui este projeto de pesquisa iniciado em 2010. Como o objetivo inicial deste estudo foi o desenvolvimento de recomendações de projeto coerentes, confiáveis e intuitivas para a utilização do PCCA no Brasil, foi necessário um profundo entendimento de suas peculiaridades estruturais e de desempenho. Para isso, o processo de fissuração das seções experimentais foi acompanhado durante sete anos. Devido à curta extensão e falta de ancoragem das seções, o PCCA "curto" apresentou um padrão de fissuração diferente do PCCA tradicional com muito menos fissuras visíveis na superfície do que o esperado. Para abordar esta questão, uma nova tecnologia ultrassônica para ensaios não destrutivos de estruturas de concreto foi aplicada. Pela interpretação do sinal de ultrassom, foi possível descobrir várias fissuras incipientes (não visíveis) dentro das placas - muitas dessas foram observadas na superfície da placa em levantamentos de fissuras posteriores - e caracterizar fissuras visíveis e não-visíveis quanto à profundidade da fissura. O mapa de fissuração atualizado com fissuras não visíveis mostrou semelhanças com PCCA tradicional. Além disso, a análise dos dados de ultrassom forneceu informações importantes sobre a variação da espessura, localização da armadura longitudinal e condição do concreto, que foram aplicados em simulações teóricas (software de elementos finitos) do PCCA curto. Simulações foram propostas considerando diferentes geometrias, primeiramente com fissuras transversais como juntas com alta eficiência de transferência de carga (LTE) e posteriormente com uma placa contínua, sem fissuras ou juntas. Esta última simulação foi mais precisa alcançando um fator de conversão entre tensões de campo e simuladas na ordem de 0,7 a 1,0. Dados de deflexão e análise de LTE em fissuras e placas entre fissuras atestaram novamente o comportamento contínuo das placas, o que vai em contradição com os modelos atuais de dimensionamento e de previsão de desempenho para o PCCA. Ademais, o tráfego crítico e condições de carga ambiental correspondentes ao clima e tráfego de ônibus típicos brasileiros foram investigados

e relacionados usando um modelo de fadiga resultando em recomendações de projeto para o PCCA de curta extensão sendo direcionado para projetos de longo prazo para mais de 20 anos de operação. O gráfico de projeto foi aplicado com sucesso para investigar três falhas apresentadas pelo PCCA curto experimental devido a deficiências de espessura apontadas pelo teste ultrassônico.

Palavras chave: pavimento de concreto continuamente armado; curta extensão; paradas de ônibus; fissuração; ensaios não destrutivos ultrassônicos; simulação de tensões; projeto

## LIST OF FIGURES

Figure 1. 1– Basic design and structural differences between CRCP and JPCP (Adapted from SALLES and BALBO, 2015).....	29
Figure 2. 1 - Effect of differential thermal gradients in slab stresses (CHOI <i>et al.</i> , 2011) .....	35
Figure 2. 2 - Illustration of the major factors affecting CRCP performance (RASMUSSEN <i>et al.</i> , 2009).....	36
Figure 2. 3 - Sensitivity analysis of the MEPDG prediction model (VANDENBOUSSCHE <i>et al.</i> , 2012).....	37
Figure 2. 4 - Effect of stabilized bases in CRCP performance (ROESLER e HILLER, 2013)	38
Figure 2. 5 - Effect of base type and LTE in CRCP performance (VANDENBOSSCHE <i>et al.</i> , 2012).....	38
Figure 2. 6 - (a) Deep punchout and (b) partial punchout (JUNG <i>et al.</i> 2012) .....	39
Figure 2. 7 – Punchout predictions according to (a) MEPDG and (b) erosion based model (JUNG <i>et al.</i> , 2012) .....	41
Figure 2. 8 – Punchout number regarding: (a) slab thickness and (b) steel amount (ROESLER and MILLER, 2013) .....	42
Figure 2. 9 – Steel restraint on concrete subjected to a linear temperature gradient (CHOI <i>et al.</i> , 2011).....	43
Figure 2. 10 – Comparison of one-mat to two-mat placement of longitudinal steel regarding (a) vertical stress distribution and (b) effect of the bar diameter (CHOI <i>et al.</i> , 2011) .....	44
Figure 2. 11 – Temperature variations near the edge (SUN <i>et al.</i> 2011a).....	46
Figure 2. 12 – Steel coating analysis in a bridge (HUNGESCHMIDT, 2002) .....	51
Figure 2. 13 – Presence of free water beneath slab (SCULLION, 2006).....	52
Figure 2. 14 – Delamination areas identification with infrared tomography (CLARK <i>et al.</i> , 2003).....	53

Figure 2. 15 – MIT Scan 2 application results for dowel bars (HOSSAIN and ELFINO, 2006)	54
Figure 2. 16 – MIRA device and transducers (BISHKO, <i>et al.</i> 2008; RAPAPORT, 2011) ....	56
Figure 2. 17 – Transducer interaction in MIRA’s linear array .....	57
Figure 2. 18 – Impact echo <i>versus</i> MIRA (VANCURA <i>et al.</i> 2013).....	58
Figure 2. 19 – MIRA reading example (HOEGH <i>et al.</i> 2011).....	58
Figure 2. 20 – Forensic evidence of delamination presence in a concrete slab (HOEGH <i>et al.</i> , 2013).....	59
Figure 2. 21 – MIRA sensitivity analysis (VANCURA <i>et al.</i> , 2013) .....	60
Figure 2. 22 – Correlation index between the cores and MIRA of (a) concrete cover and (b) slab thickness (HOEGH <i>et al.</i> , 2011) .....	61
Figure 2. 23 – MIRA scan (a) at the joint right side, (b) at the joint middle and (c) trench proving (HOEGH <i>et al.</i> , 2011) .....	61
Figure 2. 24 – Example of SAFT-Pan utilization to visualize cracks (HOEGH and KHAZANOVICH, 2015) .....	62
Figure 2. 25 - Detachment between two asphalt layers (HOEGH <i>et al.</i> 2012b).....	63
Figure 2. 26 – LTE prediction from Crovetti and Zollinger models versus ISLAB2000 LTE (KHAZANOVICH and GOTLIF, 2003).....	67
Figure 2. 27 – LTE as function of joint stiffness by aggregate interlock (KHAZANOVICH and GOTLIF, 2003).....	69
Figure 2. 28 – Interlocking modulus versus (a) LTE and (b) aggregate size with different crack widths (MAITRA <i>et al.</i> , 2010) .....	71
Figure 2. 29 – Load transfer and joint stiffness relation to joint opening (JEONG and ZOLLINGER, 2001) .....	72
Figure 2. 30 – Suggested crack width for a given slab thickness to achieve an 91% LTE (Jeong and ZOLLINGER, 2001).....	72
Figure 2. 31 - Stiffness distribution of (a) cracks and (b) joints (KHAZANOVICH and GOITLIF, 2003) .....	73

Figure 2. 32 - Distribution of LTE mean values in (a) cracks and (b) joints (KHAZANOVICH and GOITLIF, 2003) .....	74
Figure 2. 33 - Doweled and nondoweled joints LTE asses (KHAZANOVICH and GOITLIF, 2003).....	75
Figure 2. 34 – LTE versus dowel diameter (KHAZANOVICH and GOITLIF, 2003).....	75
Figure 2. 35 – Distribution of joint LTE versus base type in (a) doweled joints and (b) non-doweled joints (KHAZANOVICH and GOITLIF, 2003) .....	76
Figure 2. 36 – (a) Crack width and (b) LTE variation over time for two temperature settings (HA <i>et al.</i> 2012).....	78
Figure 2. 37 – CRCP top surface stresses obtained from ISLAB2000 and by using equivalent structure concept (KHAZANOVICH <i>et al.</i> , 2001).....	82
Figure 2. 38 – Stress output example of mechanist model (SELEZNEVA <i>et al.</i> , 2004) .....	84
Figure 2. 39 – Construction details of the experimental short CRCP sections .....	93
Figure 3. 1 – Steel depth and location and slab thickness measuring stations .....	97
Figure 3. 2 – Short CRCP March, 2015 crack map .....	98
Figure 3. 3 – Illustration of MIRA linear array and signal time of flight equation (HOEGH and KHAZANOVICH, 2015).....	99
Figure 3. 4 – Direct arrival pulse in a Section 2 thickness measurement.....	101
Figure 3. 5 – Shear wave velocity determination for location 1.3-B (3 <sup>rd</sup> scan).....	102
Figure 3. 6 - MIRA signals examples for undamaged and damaged specimens (FREESEMAN <i>et al.</i> 2015).....	103
Figure 3. 7– Raw signal (Red) and Hilbert Transform envelope (Blue) (FREESEMAN <i>et al.</i> , 2015).....	104
Figure 3. 8 – Locations of backwall signals in a MIRA grid simulation .....	105
Figure 3. 9 – 3D geometry view of Section 1.....	110
Figure 3. 10 – 3D geometry view of Section 2.....	110
Figure 3. 11 – 3D geometry view of Section 3.....	111

Figure 3. 12 – 3D geometry view of Section 4.....	111
Figure 3. 13 – Crack F4.2 at thickness measurement location 3B-L in Section .....	112
Figure 3. 14 – HTI color map .....	113
Figure 3. 15 – Thickness <i>versus</i> shear wave velocity for MIRA thickness reading.....	114
Figure 3. 16 - HTI <i>versus</i> shear wave velocity for MIRA thickness readings .....	114
Figure 3. 17 – Steel depth on B scans for (a) Section 1, location 3A, position right and (b) Section 4, location 2A, position center.....	115
Figure 3. 18 – Steel spacing on SAFT-Pan scans for (a) Section 3, location 3B, position left and (b) Section 2, location 1A, position left.....	115
Figure 3. 19 – Thickness simulations for (a) section 4 (4.3A-R) and (b) section 2 (2.2A-C)	120
Figure 3. 20 – Reinforcement simulations for (a) section 2 (2.1B-C) and (b) section 1 (1.4B-R) .....	121
Figure 3. 21 – Signal simulation for reinforcement inclusions .....	122
Figure 3. 22 – Field and simulated signals for (a) section 4 (4.3A-R) and (b) section 2 (2.2A-C) .....	122
Figure 3. 23– Field and simulated signals for (a) loss signal due to inclusion (b) inclusion reflection.....	123
Figure 3. 24 – Core extracted from (a) section 4 (4.3A-C) and (b) section 1 (1.1B-R) .....	124
Figure 3. 25 – Signals for (a) thickness measurement (location 3.3B-R) and (b) crack F3.3 (Right).....	125
Figure 3. 26 – Examples of typical SAFT-Pan reconstructions at transversal cracks.....	125
Figure 3. 27 – Normalized HTI for every signal in crack F2.3-R (first scan).....	127
Figure 3. 28 – Simulation of crack F2.5-R scans based on HTI.....	127
Figure 3. 29 – Signal loss due to high HTI in two partial cracks .....	128
Figure 3. 30 – Illustration of crack types.....	129
Figure 3. 31 – Simulation of (a) Full crack, (b) Top-Down Crack and (c) Bottom-Up Crack .....	129

Figure 3. 32 – SAFT-Pan reconstruction of panel between cracks F4.8 and F4.7 in Section 4 .....	130
Figure 3. 33 – SAFT-Pan reconstruction of panel between Section 1 and F2.2 in Section 2	131
Figure 3. 34 – HTI trough Section 1.....	132
Figure 3. 35 – HTI trough Section 2.....	133
Figure 3. 36 – HTI trough Section 3.....	134
Figure 3. 37 – HTI trough Section 4.....	135
Figure 3. 38 - Distresses in the transaction between interlock pavement and the short CRCP section 1 .....	136
Figure 3. 39 – Crack F4.3 visualization .....	136
Figure 3. 40 – Signal loss simulation for full, partial top-down (TD) and partial bottom-up (BU) crack .....	137
Figure 3. 41 – Signal loss due to high HTI in non-visible cracks .....	138
Figure 4. 1 – Updated crack map (June 2015).....	139
Figure 4. 2– Crack pattern evolution.....	140
Figure 4. 3 – Cumulative crack spacing regarding visible cracks.....	142
Figure 4. 4 – Divided crack (a) in section 3 and “Y” crack (b) in section 1 .....	142
Figure 4.5– Crack map with visible and non-visible cracks.....	144
Figure 4. 6 – Cumulative crack spacing for non-visible crack map.....	145
Figure 4. 7 – Sun light condition at the short CRCP surface .....	147
Figure 4. 8 – Climate conditions during and prior to the crack width survey.....	148
Figure 4. 9 – HTI versus surface crack width.....	149
Figure 4. 10 – Illustration of FWD position to evaluate crack LTE.....	150
Figure 4. 11 – Winter 2013 crack map (FWD locations) .....	151
Figure 4. 12 - - Climate conditions for (a) air temperature and relative humidity and (b) precipitation during and prior to the FWD testing .....	153

Figure 4. 13 – Summer 2015 crack map (FWD locations).....	154
Figure 4. 14 – Maximum deflections trough the section length.....	156
Figure 4. 15 – FWD testing map with non-visible cracks (Section 4) .....	157
Figure 4. 16 – Deflection basins for panel (P) locations .....	158
Figure 4. 17 – Deflection basins for crack (F) locations .....	159
Figure 4. 18 – FWD testing maximum deflection versus ultrasonic testing slab thickness ...	159
Figure 4. 19 – LTE in two different seasons .....	160
Figure 4. 20 – Load transfer efficiency <i>versus</i> (a) crack width and (b) crack spacing.....	161
Figure 4. 21 – Cracking distresses visible at the short CRCP surface .....	164
Figure 4. 22 – Cracking distress in section 1 in (a) 2013 and (b) 2017.....	164
Figure 5. 1 – Strain gauge location in Section 3.....	166
Figure 5. 2 – Stress diagram for SGs 30 and 31 in DLTs 01 and 10 (DWA) .....	169
Figure 5. 3 – ISLAB simulation of section 3.....	171
Figure 5. 4 - DWA stresses on (a) and (b) SG16; and (c) and (d) SG30 with vehicle distance from the edge.....	172
Figure 5. 5 - Longitudinal top stresses (DWA) on three simulation models for DLT 05 .....	173
Figure 5. 6 – Stress increase factor for SG 29 .....	174
Figure 5. 7 – Wheel load effect on stress diagram at crack.....	175
Figure 5. 8 – Correlation between field and ISLAB stresses for (a) surface, (b) top and (c) bottom SGs .....	180
Figure 5. 9 – Braking position in the instrumented segment.....	181
Figure 5. 10 – Section 3 areas with different thickness according to the ultrasonic survey...	182
Figure 5. 11 – Simulation of constant thickness 212.98 mm slab (Case A); 215 mm slab (Case B); slab with thickness variation (Case C); and 215 mm slab with thermal gradient (case D) .....	183

Figure 6. 1 – Critical loading locations: 1 (center); 2 (mid-center); 3 (edge); 4 (center-edge); and 5 (corner).....	184
Figure 6. 2 – Principal stresses in a slab under a 10°F (5.55°C) thermal differential for (a) Top and (b) bottom positions .....	185
Figure 6. 3 – Illustration of the conceptual tire/pavement contact area and its ISLAB model .....	188
Figure 6. 4 – Mesh refinement in (a) custom medium mesh and (b) customized mesh.....	189
Figure 6. 5 – Short CRCP stresses due to thermal gradient variation for several slab thickness .....	191
Figure 6. 6 – Short CRCP stresses due to slab thickness and thermal gradient variation .....	191
Figure 6. 7 – Short CRCP stresses due to axle load and thermal differential variation .....	192
Figure 6. 8 – Stress in slabs with different lengths subjected to thermal gradient variation..	193
Figure 6. 9 – (a) Analyzed fatigue models and (b) fatigue models with field/lab shift factor applied to laboratory only models .....	199
Figure 6. 10 – Equivalent zero-thermal gradient load for 80 kN vehicle load in different slab thicknesses.....	201
Figure 6. 11 – Equivalent zero-thermal gradient load versus principal stresses for different slab thicknesses .....	201
Figure 6. 12 – Selected fatigue model for a range of concrete modulus of rupture .....	202
Figure 6. 13 – Short CRCP design chart for a 80 kN axle load.....	203
Figure 6. 14 – Equivalent 250 mm slab load <i>versus</i> (a) equivalent load for all thickness and (b) adapted critical value only lines.....	204
Figure 6. 15 – Complete design chart for the short CRCP .....	205
Figure 6. 16 – Short CRCP design example for a 300 mm slab.....	206
Figure 6. 17 – Proposed transition joint from short CRCP to JPCP (Adapted from Roesler <i>et al.</i> , 2016).....	218
Figure 6. 18 – Proposed transition joint from short CRCP to asphalt pavement (ROESLER <i>et al.</i> , 2016).....	219

Figure B. 1 – Short CRCP design chart for a 60 kN axle load.....	244
Figure B. 2 – Short CRCP design chart for a 100 kN axle load.....	245
Figure B. 3 – Short CRCP design chart for a 120 kN axle load.....	246
Figure B. 4 – Short CRCP design chart for a 140 kN axle load.....	247

## LIST OF TABLES

Table 2. 1 – Classic CRCP performance aspects regarding basic design parameters .....	33
Table 2. 2 – Recommended joint/crack stiffness (KHAZANOVICH and GOITLIF, 2003) ...	73
Table 2. 3 – Effective temperatures ranges (ARA, 2003) .....	87
Table 2. 4 – Backcalculated friction values (RAO <i>et al.</i> , 2004).....	91
Table 2. 5 –Short experimental CRCP design features .....	94
Table 3. 1 – Signal locations in MIRA grid simulation .....	106
Table 3. 2 – Thickness, shear wave velocity and HTI results for Sections 1 and 2 .....	108
Table 3. 3 - Thickness, shear wave velocity and HTI results for Sections 3 and 4.....	109
Table 3. 4 – Average thickness per position and location .....	112
Table 3. 5 – MIRA data for longitudinal steel in Sections 1 and 2 .....	116
Table 3. 6 – MIRA data for longitudinal steel in Sections 3 and 4 .....	118
Table 3. 7 – Design data <i>versus</i> Mira data .....	119
Table 3. 8 – Correlation between MIRA thickness measurements and cores .....	124
Table 3. 9 – Crack ultrasonic evaluation .....	126
Table 3. 10 – Non-visible cracks .....	137
Table 4. 1 – Surface crack width in three positions .....	146
Table 4. 2 – Surface crack width <i>versus</i> steel percentage .....	148
Table 4. 3 – Backcalculation and LTE results from 2013 winter FWD test .....	152
Table 4. 4 – Deflection data from February 2015 FWD test.....	154
Table 4. 5 – Deflection data from February 2015 FWD test: Part II.....	155
Table 4. 6 – LTE for cracks (F) and panels (P) on FWD summer survey.....	163

Table 5. 1 – Dynamic load test stresses (MPa).....	167
Table 5. 2 – Dynamic load test stresses (MPa): part II.....	168
Table 5. 3 – Shift factor for DLT simulations: model trials .....	171
Table 5. 4 – Shift factor between field and theoretical stresses: Part I.....	176
Table 5. 5 – Shift factor between field and theoretical stresses: Part II .....	177
Table 5. 6 – Shift factor between field and theoretical stresses: Part III.....	178
Table 5. 7 – Shift factor (SF) for field/ISLAB stresses .....	179
Table 6. 1 – Stresses due to thermal gradient of 10°F (5.55°C) in different slab locations ...	186
Table 6. 2 – Stresses due to thermal gradient of 20°F (10.11°C) in different slab locations .	186
Table 6. 3 – Stresses due to thermal gradients and vehicle loading in different slab locations .....	187
Table 6. 4 – Input parameters for short CRCP simulation .....	188
Table 6. 5 – Principal stresses due to axle loading and thermal differential for a 200 mm slab .....	190
Table 6. 6 – Slab bottom stresses direction versus slab length for different thermal gradients .....	194
Table 6. 7 – Design trials for a heavy traffic bus corridor applying the short CRCP design .	208
Table 6. 8 – Design trials for a heavy traffic bus corridor applying the short CRCP design chart with different axle loads .....	209
Table 6. 9 – Number of axle repetitions for the time when each distress became visible at the slab surface .....	210
Table 6. 10 – Fatigue consumption analysis for the experimental short CRCP.....	210
Table 6. 11 – Thermal gradient seasonal daily variation (Adapted from: PMSP, 2004b) .....	211
Table 6. 12 – Traffic distribution and respective thermal gradient for the experimental short CRCP.....	211

Table 6. 13 – Detailed fatigue consumption analysis for the experimental short CRCP during spring .....	213
Table 6. 14 – Detailed fatigue consumption analysis for the experimental short CRCP during summer .....	214
Table 6. 15 – Detailed fatigue consumption analysis for the experimental short CRCP during fall.....	215
Table 6. 16 – Detailed fatigue consumption analysis for the experimental short CRCP during winter.....	216
Table A. 1 – Equivalent zero-thermal gradient loads for different thermal gradients in a 200 mm concrete slab.....	241
Table A. 2 – Equivalent zero-thermal gradient loads for different thermal gradients in a 250 mm concrete slab.....	241
Table A. 3 – Equivalent zero-thermal gradient loads for different thermal gradients in a 300 mm concrete slab.....	242
Table A. 4 – Equivalent zero-thermal gradient loads for different thermal gradients in a 350 mm concrete slab.....	242
Table A. 5 – Equivalent zero-thermal gradient loads for different thermal gradients in a 400 mm concrete slab.....	243
Table C. 1 – Proposed fatigue consumption analysis for short CRCPs .....	248

## LIST OF ACRONYMS AND ABBREVIATIONS

AASTHO	American Association of State Highway and Transportation Officials
ATB	Asphalt Treated Base
ADT	Average Daily Traffic
Avg.	Average
BRT	Bus Rapid Transit
BU	Bottom-Up Crack
C	Center
SF	Shift Factor
CRCP	Continuously Reinforced Concrete Pavement
CTB	Cement Treated Base
CTE	Coefficient of Thermal Expansion
DLT	Dynamic Load Test
DWA	Dual Wheel Load
EASL	Equivalent Single Axle Load
EFIT	Elastodynamic Finite Integration Technique
F	Fully Developed Crack
FWD	Falling Weight Deflectometer
GPR	Ground Penetrating Radar
IC	Non-Visible Crack
IRI	International Roughness Index
JPCP	Jointed Plain Concrete Pavement
L	Left
Loc.	Location
LTE	Load Transfer Efficiency
LTPP	Long-Term Pavement Performance
MEPDG	Mechanistic-Empirical Pavement Design Guide
MIT	Magnetic Imaging Tools
MR	Modulus of Rupture
NA	Not Available

NC	Non-Conclusive
R	Right
ROI	Region of Interest
SAFT	Synthetic Aperture Focusing Technique
SEF	Stress extension factor
SF	Shift-factor
SG	Strain Gauges
SSR	Stress-Strength Ratio
Std.	Standard Deviation
SWA	Single Wheel Load
TD	Top-Down Crack
Vel.	Velocity

## LISTLE OF SYMBOLS

%	Percentage
$\hat{o}$	Image reflectivity
$\emptyset$	Diameter
$^{\circ}\text{C}$	Celsius degree
$^{\circ}\text{F}$	Fahrenheit degree
2D	Two dimensional
3D	Three dimensional
$\Delta\text{T}$	Thermal gradient
A	Apodization coefficient
a	Plate radio
AGG	Aggregate interlock shear stiffness by unit length;
agg	Nominal size of coarse aggregates
AGG <sup>*</sup>	Dimensionless joint stiffness of pavement without transfer bars
AGG <sub>0</sub>	Joint stiffness corresponding to aggregate interlock
ar	Load equivalent radius
C	Bradbury correction factor
c <sub>1</sub>	First bond stress coefficient
c <sub>2</sub>	Second bond stress coefficient
CC	Mixture cement content
cm	Centimeter
cw	Crack width
D	Shear stiffness of a single dowel bar
D <sup>*</sup>	Dimensionless joint stiffness of pavement with transfer bars
E	Modulus of elasticity
ESR	Equivalent shear ratio
ev	Electromagnetic speed
f	Base friction coefficient
f <sub>c28</sub>	Concrete compressive strength at 28 days
Fd	Fatigue damage
ft	Concrete tensile strength

GHz	Giga Hertz
h	Slab thickness
HT	Hilbert Transform
in	Inches
$J_c$	Dimensionless aggregate interlock factor
$j_s$	Lane-shoulder joint stiffness
k	Subgrade reaction modulus
kg	Kilogram
kHz	Kilo Hertz
km	Kilometers
kN	Kilo Newton
L	Crack spacing
l	Slab length
$\ell$	Slab's radius of relative stiffness
m	Meters
$m^3$	Cubic meter
MHz	Mega Hertz
mm	Millimeter
MPa	Mega Pascal
ms	Milliseconds
$N_{ESAL}$	Number of ESALs
N	Number of allowable load repetitions
P	Percent of longitudinal reinforcement
rh	Relative concrete humidity
s	Second
sd	Steel depth
sp	Dowel bars spacing
T	Temperature
$U_m$	Peak bond stress
V	Shear wave velocity
y	Concrete thermal diffusivity
Z	Concrete shrinkage
$\alpha$	Coefficient of thermal expansion

$\gamma$	Slab unit self-weight
$\delta$	Deflection
$\varepsilon$	Strain
$\mu$	Poisson's ratio
$\sigma$	Stress/tension
T	Shear stress

# CONTENTS

<b>1. INTRODUCTION</b> .....	<b>27</b>
<b>1.2 Research Objective</b> .....	<b>30</b>
<b>1.2 Thesis structure</b> .....	<b>31</b>
<b>2. LITERATURE REVIEW</b> .....	<b>33</b>
<b>2.1 Continuously reinforced concrete pavement (CRCP): state of the art</b> .....	<b>34</b>
2.1.1 Improvements and changes in CRCP design concepts .....	35
2.1.2 Joint-related issues in CRCP .....	45
2.1.3 CRCP overlay .....	47
<b>2.2 Modern non-destructive evaluation techniques for concrete pavements</b> .....	<b>48</b>
2.2.1 Ground Penetrating Radar (GPR) .....	49
2.2.2 Infrared tomography .....	52
2.2.3 Magnetic tomography (MIT Scan 2) .....	54
2.2.4 Modern ultrasonic techniques .....	55
<b>2.3 Load transfer efficiency (LTE) in joints and cracks</b> .....	<b>64</b>
<b>2.4 CRCP design models and equations</b> .....	<b>77</b>
2.4.1 1986 AASTHO design guide .....	79
2.4.2 Other studies .....	80
2.4.3 MEPDG .....	84
2.4.4 2008 AASTHO Guide .....	92
<b>2.5 Experimental short CRCP sections (current research)</b> .....	<b>92</b>
<b>3. ULTRASONIC TESTING</b> .....	<b>96</b>
<b>3.1 Ultrasonic data collection procedure</b> .....	<b>96</b>
3.1.1 Ultrasonic data processing .....	98
3.1.1.1 SAFT Panoramic .....	102
3.1.1.2 Hilbert Transform Indicator (HTI) .....	103
3.1.1.3 MIRA numerical simulations .....	106
<b>3.2 Experimental short CRCP ultrasonic survey results</b> .....	<b>107</b>
3.2.1 Longitudinal reinforcement depth and spacing .....	115
3.2.2 Mira Simulations for slab thickness and reinforcement position .....	119

3.2.3 Core proving.....	123
<b>3.3 Ultrasonic Crack characterization .....</b>	<b>124</b>
3.3.1 MIRA simulations of transverse cracks .....	128
3.3.2 Non-visible cracks.....	130
<b>4. CRACK PATTERN ANALYSIS.....</b>	<b>139</b>
<b>4.1 Non-visible crack pattern .....</b>	<b>143</b>
<b>4.2 Crack width .....</b>	<b>145</b>
<b>4.3 Falling Weight Deflectometer (FWD) testing and previous data .....</b>	<b>149</b>
4.3.1 Deflection data analysis .....	156
4.3.3 Load transfer efficiency (LTE) analysis.....	159
4.3.2.1 Panel LTE.....	162
<b>4.4 Short CRCP visual distresses.....</b>	<b>163</b>
<b>5 FIELD STRESSES SIMULATIONS .....</b>	<b>166</b>
<b>5.1 Field stress simulation procedure.....</b>	<b>169</b>
<b>5.2 Shift factor between field and theoretical stresses .....</b>	<b>174</b>
5.2.1 Field stress simulation regarding thickness variation .....	181
<b>6. DESIGN RECOMMENDATIONS FOR THE SHORT CRCP .....</b>	<b>184</b>
<b>6.1 Critical stress loading position.....</b>	<b>184</b>
<b>6.2 Short CRCP simulation procedure .....</b>	<b>187</b>
6.1.1 Tire/pavement contact area and finite element mesh .....	188
<b>6.3 Short CRCP simulation analysis .....</b>	<b>189</b>
<b>6.4 Fatigue model selection and analysis .....</b>	<b>195</b>
<b>6.5 Short CRCP design chart.....</b>	<b>200</b>
6.5.1 Fatigue life consumption.....	207
6.5.2 Analysis of the experimental short CRCP regarding the proposed design method.....	209
<b>6.6 Short CRCP design guidelines and final recommendations .....</b>	<b>217</b>
<b>7. CONCLUSIONS.....</b>	<b>220</b>
<b>REFERENCES .....</b>	<b>224</b>
<b>APPENDIX A .....</b>	<b>241</b>
<b>APPENDIX B.....</b>	<b>244</b>
<b>APPENDIX C .....</b>	<b>248</b>
<b>VITA .....</b>	<b>249</b>

## 1. INTRODUCTION

São Paulo City Hall along with the Brazilian federal government has made amplification of the city's bus corridor systems a leading public action for both terms. From 2012 to 2016 the length of exclusive bus lanes jumped from 90 km to over 500 km. As a result, the implementation of bus lanes for large urban areas is showing great traffic benefits. In São Paulo buses traveling in the exclusive bus corridor present an average velocity 68% higher than buses traveling in non-exclusive lanes (EL PAIS, 2014). Unfortunately, with the recent economic recession, the funds available for the construction and rehabilitation of the bus corridors has seen a considerable decline of over 50% in the first two months of 2016 (ESTADÃO, 2016). With less money, the search for more durable and less problematic pavement structures as well as reliable, inexpensive, and productive pavement evaluation methods becomes primordial.

From a structural point of view, since 2012 some bus corridors in São Paulo have had their asphalt pavement replaced by jointed plain concrete pavements (JPCP). The hot climate added to specific traffic characteristic of buses (channeled, slow and heavy), makes basic asphalt pavements not recommended for bus corridors, stops and terminals. This has been the case of the corridor Campo Limpo – Rebouças – Downtown with a length of 10.1 km, as seen in *Infrasestrutura Urbana* (2011). However, many of the new corridors are being implemented only by delimiting a single lane in an existing street or avenue. No additional study or evaluation has been made to assess the compatibility of the existing asphalt pavement, many of which already presents distresses from the new traffic configuration. Even when applying a concise design procedure as was the case of the Bus Rapid Transit (BRT) in Rio de Janeiro (asphalt pavement), the pavement still suffered from severe rutting due to elevated temperatures and channeled traffic (O DIA, 2014).

Moreover, poor construction practices for concrete pavements have been a constant issue in Brazil from great constructions enterprises to small avenues. The Mario Covas beltway (around the São Paulo metropolitan area) presented distresses only two weeks after being opened to traffic (FOLHA DE SÃO PAULO, 2010). In the same way, a JPCP designed for bus corridors showed construction problems relating to the joints in Santa Barbara D'Oeste (138 km from São Paulo). A more severe joint-related distress in a newly constructed JPCP was observed on the BRT pavement in Porto Alegre (southern Brazil). Three BRT corridors

needed rehabilitation before traffic opening due to premature cracking. Forensic investigation showed issues with curing and joint cutting time (ZERO HORA, 2014). Furthermore, for both asphalt and JPCP structures the main region of distresses are bus stops and terminals, which are areas that experience slower velocity, braking and accelerating operations, as well as completely stopped vehicles that potentiates the bus load effect.

In order to keep focus on concrete structures while mitigating the joint-related issues, this thesis proposes the use of continuously reinforced concrete pavements (CRCP) as a potential pavement solution for bus corridors stops and terminals. CRCP is a concrete pavement without contraction joints. The concrete slab has no length restriction as long as the concreting continues. Only when the concrete pouring has ended or stopped is a constructive joint performed. Common knowledge says that concrete being a very fragile material has a high cracking tendency, both in its fresh and hard states. Due to this unwanted property, contraction joints are needed in JPCP; by slab sawing cut, it is possible to induce/control cracks in a place where the dowel bars will provide load transfer between slabs. The CRCP's concrete shows no different behavior – it still cracks. The major difference between CRCP and JPCP is that the former has a high steel percentage placed above the slab's half-height. The major role of this reinforcement is to keep the inevitable cracks tight, thus making their presence imperceptible to the user and providing highly satisfactory load transfer between cracks by means of aggregate interlock. Therefore, there is not a crack control or inducement because of the whole steel structure designed to maintain the slab's structural and functional integrity (ROESLER *et al.*, 2016). Figure 1.1 illustrates the major differences between JPCP and CRCP.

Several studies point out that the CRCP major advantages are its durability and low maintenance needs, making it a very suitable solution for bus corridors in Brazil. Dossey and Hudson (1994) estimated that the first heavy maintenance intervention (resurfacing) in CRCP occurs at an average age of 17 years, but for many sections, the overlay was only necessary after 20 years of life service. Tayabji *et al.* (1995) determined the International Roughness Index (IRI) for several CRCP in Texas; the authors reached values between 0.84 m/km and 2.48 m/km, which indicate a smooth ride quality as the slabs' ages ranged from 0.3 years to 22 years. Gharaibeh *et al.* (1999) disclosed that despite differences in the design, all analyzed CRCP supported a greater amount of traffic than the designed traffic, and lasted longer than

their project design life. Won (2011) found that even pavements with 33-years of traffic exposure still had tightly closed cracks on its surface and that inherent to the pavement's age and distress presence, the load transfer efficiency (LTE) between cracks was always greater than 90%.

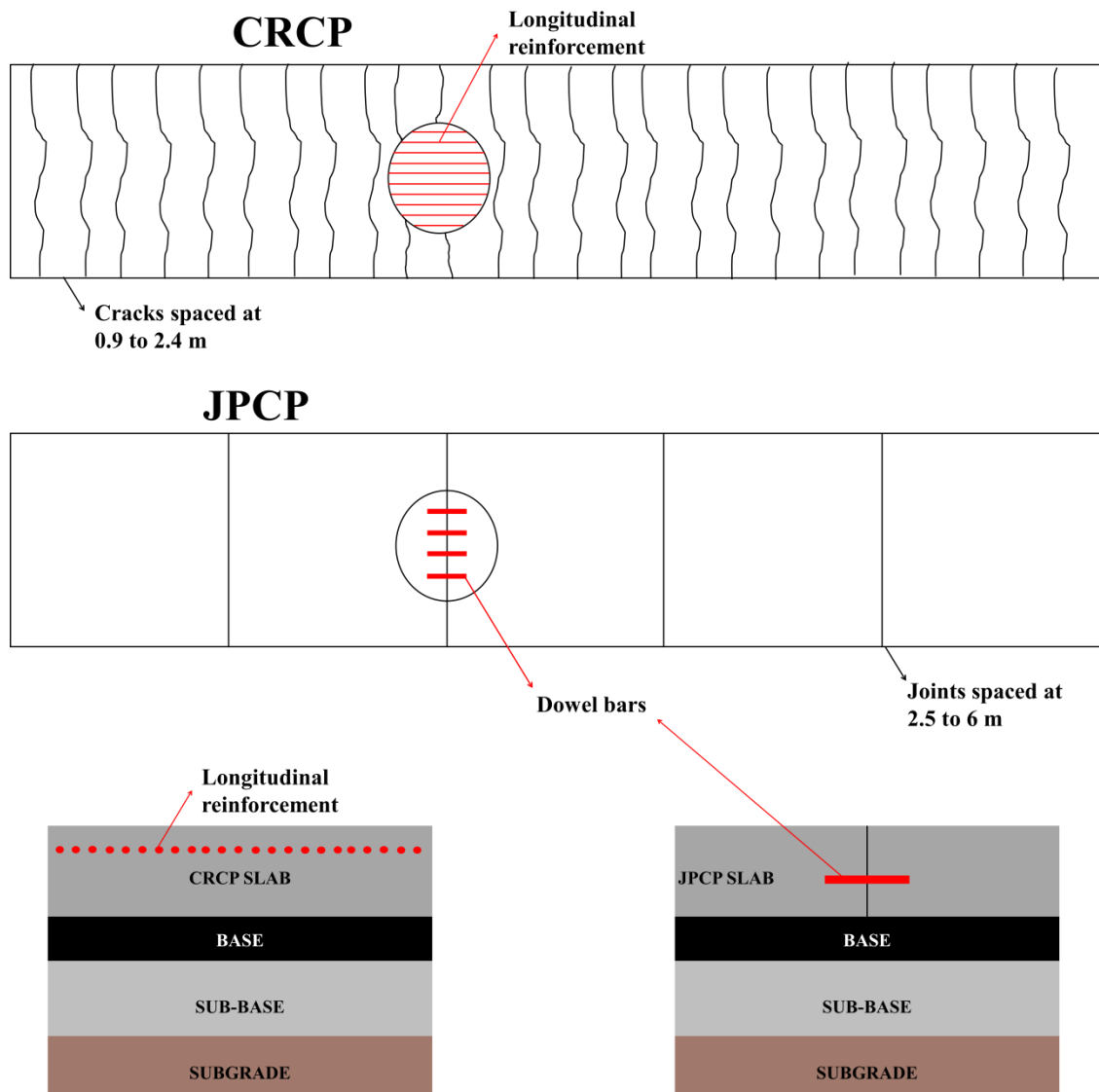


Figure 1. 1– Basic design and structural differences between CRCP and JPCP (Adapted from SALLES and BALBO, 2015)

In search of a better understanding of this structure behavior in a tropical climate, four CRCP sections were constructed at the University of São Paulo (USP) campus in 2010. The CRCP

sections were designed with only 50 m of length, which is short in comparison to traditional CRCP. The first performance analysis of this “short” CRCP is presented in Salles (2014). The experimental short CRCP showed a unique crack pattern with a long cracking period resulting in fewer cracks than expected. It was assumed that the short structure length along with the lack of anchorage at the slabs longitudinal edge made the crack development slower preventing cracks from appearing at the slab surface. However, falling weight deflectometer (FWD) and dynamic load testing showed a typical CRCP performance, i.e., high LTE, low deflections (save for the longitudinal edges), and low stresses.

The thesis described here presents the final approach of this research project. In order to reasonably apply the short CRCP technology in bus corridors, it was necessary to develop specific design recommendations for the structure. In spite of this need, a complete characterization of the existing sections was performed with an ultrasonic non-destructive device (MIRA). Data on thickness variation, concrete condition, and reinforcement location were fully analyzed. Also, as most CRCP design models are focused on transverse crack characterization (spacing and width), MIRA was applied to characterize surface visible cracks and to discover non-visible cracks.

With the complete knowledge of several structure parameters it was possible to numerically simulate the short CRCP with the concrete pavement finite element software ISLAB. ISLAB was used to determine a shift factor between field stresses obtained through a dynamic-load testing and theoretical stresses. Furthermore, critical environmental and vehicle loadings coherent with São Paulo’s climate and bus traffic were explored to determine the best combination of design aspects for the short CRCP. Finally a design procedure in a chart format was proposed and discussed.

## **1.2 Research Objective**

The main objective of the proposed thesis described herein is to propose reasonable, intuitive and reliable design recommendations for short CRCPs to be applied in bus corridors, stops and terminals. These design recommendations will be offered in a simple format ready to be absorbed by the Brazilian pavement community. Due to the clear differences between JPCP and CRCP, the current international CRCP design methods and studies present a singular ideal of avoiding the use of classic JPCP design and performance models for CRCP design.

Regarding this idea, the development of proper design recommendations for the short CRCP not based on existing Brazilian design methods for JPCP, but in compliance with Brazil's climate and bus traffic is imperative for the large-scale implementation of this structure. In order to successfully achieve the main objective described above, several research goals (steps) were proposed as follows:

- Review crucial aspects of modern CRCP design and construction as well as the state of the art of non-destructive testing of concrete pavement;
- Determine several slab parameters thought the use of a non-destructive ultrasonic technique (MIRA);
- Calibrate and test a MIRA simulation software for thickness, inclusions (reinforcement) and cracks;
- Develop a procedure for signal interpretation to visualize incipient cracks;
- Investigate the structural effect of transverse cracks based on LTE, ultrasonic signals and stresses theoretical simulations;
- Establish a reliable shift factor between field and theoretical stresses;
- Analyze critical environmental and vehicle loads for the short CRCP concerning fatigue models;
- Developed short CRCP design guidelines including several slab parameters with focus on bus corridor traffic;
- Analyze the experimental short CRCP performance regarding the design chart proposed for this structure.

By the end of this research project, it is expected to present design recommendations in an chart format regarding pavement parameters like slab thickness, axle load, thermal gradient and concrete modulus of rupture.

## **1.2 Thesis structure**

Contents of this thesis are presented as follows:

- **Chapter 1:** The research contextualization and objectives are presented in the first chapter;

- **Chapter 2:** The literature review of the newest CRCP research along with concrete pavement non-destructive testing with focus on the MIRA device is presented in the second chapter. Additionally, critical CRCP design characteristics such as load transfer efficiency and design models are discussed. Finally, the experimental short CRCP sections are presented;
- **Chapter 3:** Ultrasonic data collection and processing for the short CRCP sections are given in the third chapter along with the analysis and signal simulation for thickness, reinforcement and transverse cracks. Furthermore, the signal interpretation for non-visible cracks is proposed and analyzed;
- **Chapter 4:** The updated crack pattern analysis with the inclusion of non-visible cracks is discussed in the fourth chapter. Moreover, deflection data and LTE values for every crack are analyzed;
- **Chapter 5:** Four short CRCP structure models are proposed for field/theoretical shift factor in the fifth chapter. Finally, the shift factor is calculated and discussed;
- **Chapter 6:** In the sixth chapter, the design recommendations for the short CRCP are proposed based on theoretical simulations of several pavement parameters and fatigue models. Additionally, the performance of the experimental short CRCP is evaluated regarding the proposed design charts;
- **Chapter 7:** The thesis conclusions and recommendations for future studies can be found in the seventh chapter.

## 2. LITERATURE REVIEW

In previous work (masters dissertation), the same author of the thesis presented here analyzed, through an extensive literature review, the classic CRCP concepts (SALLES, 2014). Table 2.1 presents the result of this review with a compilation of conclusions and recommendations regarding traditional CRCP knowledge.

Table 2. 1 – Classic CRCP performance aspects regarding basic design parameters

Parameter	Performance Indicator				
	Cracking	Crack Spacing	Crack Width	Punchout	Long-Term Performance
Long. Steel Percentage	The higher the steel percentage, more cracks will develop	Smaller crack spacing	Smaller crack width	fewer punchouts	Slabs with high steel percentages present less distress and higher durability
Long. Steel Depth	The deeper the steel position, more cracks will develop	Smaller crack spacing	Bigger crack width	More punchouts	It is recommended a minimum 76 mm concrete cover for the longitudinal steel to avoid corrosion. Steel placed at higher depths is detrimental to pavement performance
Transverse bars	The presence or absence of transversal reinforcement does not have an impact on the number of cracks	Not analyzed	Not analyzed	Not conclusive	Transverse cracks have a tendency to develop at the transverse bars location. Transverse bars have no influence on long-term performance
Slab thickness	Not analyzed	Not analyzed	Not analyzed	The thicker the slab, fewer punchouts	Thicker slabs present better performance and suffer less influence from other variables
Coefficient of Thermal Expansion (CTE)	Concretes with high CTE increase the number of cracks resulting in a great number of wandering cracks	Smaller crack spacing	Not analyzed	More punchouts	High cement content mixtures must be followed by a strict curing process regarding the relation between CTE and slab cracking.
Base Type	Pavements with granular bases present greater number of cracks, smaller crack spacing and bigger crack width resulting in a greater number of punchouts.				For long term performance, asphalt bases are considered slightly better than cemented bases both being more recommended than granular bases due to erosion potential

However, several studies and analyses have only been published in recent years, making knowledge updating an essential activity for the purposes of the thesis described herein. In this chapter, reflections about the latest CRCP research focusing on performance, load transfer-efficiency (LTE) and design are presented along with a section on modern non-destructive testing for concrete pavements. Furthermore, the short CRCP experimental sections that were used in this research are described with results from previous publications.

## **2.1 Continuously reinforced concrete pavement (CRCP): state of the art**

Due to the CRCP being a robust structure because of its Portland cement concrete (PCC) slab thickness and amount of longitudinal steel, several authors focus their analysis on environmental loads rather than traffic loads, since the former will dictate the slab behavior at young ages. Because of the movement restriction provided by the longitudinal reinforcement and by the pavement's transversal and longitudinal edges, the CRCP faces greater tensile stresses due to temperature changes and concrete shrinkage than jointed plain concrete pavement (JPCP) (ZHANG *et al.*, 2010).

Exploring the comparison between JPCP and CRCP against climatic effects, Ryu *et al.* (2013) state that the design and structural behavior of both pavements is very different and it should be considered as such in design guides and performance evaluations. In JPCP, concrete volume changes are allowed and design details are projected to ensure adequate load transfer in physical discontinuities, i.e. transverse contraction joints. On the other hand, the CRCP concrete volumetric changes are heavily restricted by the longitudinal reinforcement and slab/base friction. Due to this different behavior, concrete with high coefficients of thermal expansion (CTE) are not ideal for CRCP due to the early development of crack spalling.

Liu *et al.* (2013) comparing a CRCP in which part of the extension was inside a tunnel - where the temperature is more uniform and lower and the humidity is higher (features of a proper curing process) than in an open environment - concluded that the CRCP inside the tunnel showed a better performance (crack pattern) than the CRCP outside the tunnel. Ren *et al.* (2012) stress the importance of an adequate curing process stating that the concrete slab temperature variation is a dominant factor on the slab cracking during the first year. With this, a sufficient curing time should be provided to prevent undesirable cracking patterns.

Moreover, Zhang and Liu (2012) showed that, due to the great thickness, the slab deformation is contained by the foundation and by the slab's self-weight and claim that the thermal gradient between the slab bottom and the top can cause up to 30% stress variations. In Figure 2.1 it is clear the aggravating effect of a nonlinear thermal gradient particularly in the slab half-height in which the longitudinal steel is located (CHOI *et al.*, 2011).

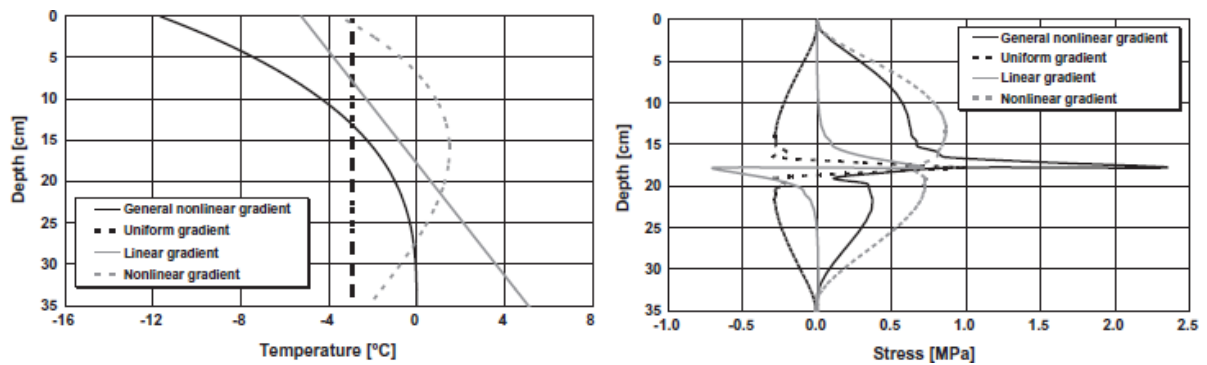


Figure 2. 1 - Effect of differential thermal gradients in slab stresses (CHOI *et al.*, 2011)

### 2.1.1 Improvements and changes in CRCP design concepts

Several studies indicate that if the initial pavement performance, i. e., young age performance, is appropriate, the structure's chances of success throughout the life project will be higher. Concerning this, attention should be paid to the functionality of some features shown in Figure 2.2. Zhang *et al.* (2012) state that the CRCP fatigue process is due to aggregate interlocking loss at the crack. The load transfer loss in transverse cracks increases tensile stress at the slab's top which eventually leads to punchouts development. Load transfer efficiency (LTE) is controlled mainly by crack width (interaction between aggregates) and by slab thickness (contact area). According to Lou *et al.* (2011), CRCP guide specifications in China regulate crack width up to 1 mm, which is consistent with the AASTHO guide (1993). However, as noted by Vandeboussche *et al.* (2012), the crack transferring load performance will drop significantly when the crack width is greater than 0.5 mm. Nevertheless, international CRCP literature still lacks a clear width regulation that is correlated to the air temperature. A width of 1 mm at 32°C does not imply in a similar performance at 10°C. The natural expansion of the concrete at high temperatures causes cracks to become more closed

providing greater interlocking. This can be one tropical climate benefit to the pavement's performance after the full development of the cracking pattern.

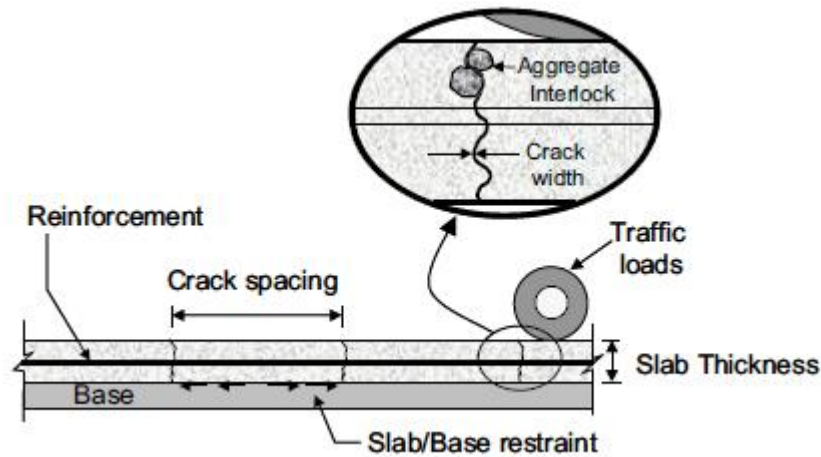


Figure 2. 2 - Illustration of the major factors affecting CRCP performance (RASMUSSEN *et al.*, 2009)

According to Roesler and Hiller (2013), the new AASHTO design method based on the Mechanistic-Empirical Pavement Design Guide (MEPDG) takes into account factors influencing punchout development and increase in surface roughness, such as loss of foundation and support on the edges, excessive crack spacing and width and high temperatures during construction. The method indicates that when properly designed, CRCP offers a long service life, perfect rolling surface and minimal maintenance needs. Still analyzing the new guide, Vandenbossche *et al.* (2012) showed, based on a sensitivity analysis, the effect of project inputs variations on the punchout number (Figure 2.3).

The main factors are slab thickness, base type, concrete tensile strength and longitudinal reinforcement percentage. Although not mentioned in the paper, the sensitivity analysis does not always meet the maximum recommended values of punchout per mile of 6 to 13.

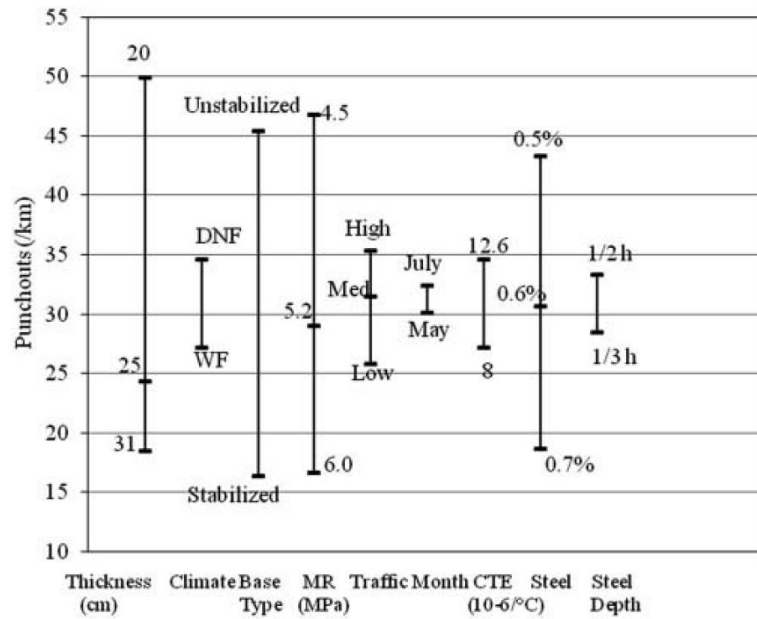


Figure 2. 3 - Sensitivity analysis of the MEPDG prediction model (VANDENBOUSSCHE *et al.*, 2012)

A key aspect that has become the rule in the CRCP design is the use of stabilized bases with low erosion potential. Roesler and Miller (2013) attest to this criterion when comparing bases stabilized with cement (CTB), with asphalt (ATB) and granular. In Figure 2.4 the performance difference regarding punchouts and IRI is notable. For several US transportation departments, the maximum number of per mile punchouts ranges from 6 to 13 and the maximum IRI is set at 2.7 m/km (170 inches/mile). Although the authors did not compare the type of stabilization, through Figure 2.4 it is possible to intuit that the cement stabilized material presents similar performance to the asphalt material. This only occurs in stabilizations with low binder percentage. Several authors have demonstrated the asphalt base superiority in other studies (LEE and DARTER, 1995; GHARAIBEH *et al.*, 1999; JOHNSTON and SURDAHL, 2006)

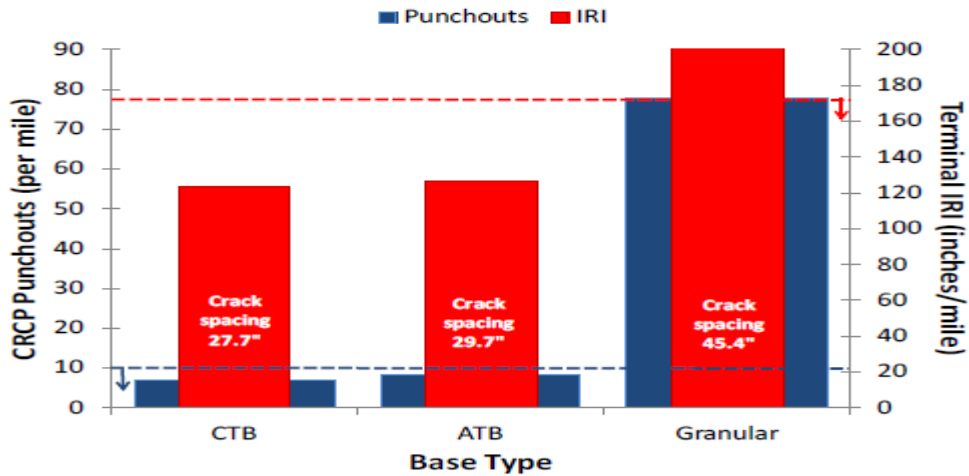


Figure 2. 4 - Effect of stabilized bases in CRCP performance (ROESLER e HILLER, 2013)

The stabilization benefits are understandable. In addition to prevent the inner layers erosion, stabilized bases can increase tensile strength introducing greater rigidity (Zhang, 2012). This also goes in agreement with the sensitivity (MEPDG) study performed by Vandebossche *et al.* (2012). According to the authors, using a stabilized base or no is more influential in damage potential with low crack LTE. However with high LTE, base stabilization does not seem so important, as shown in Figure 2.5

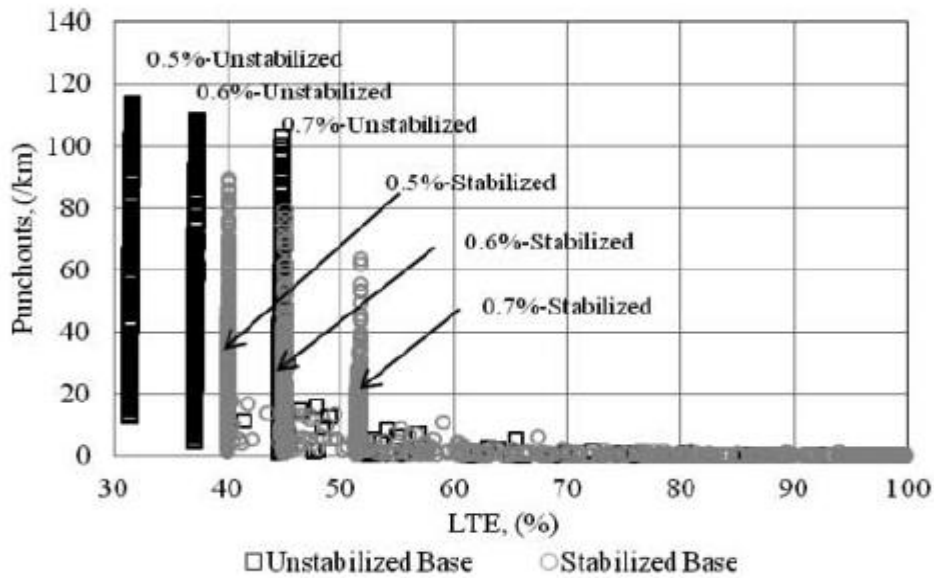
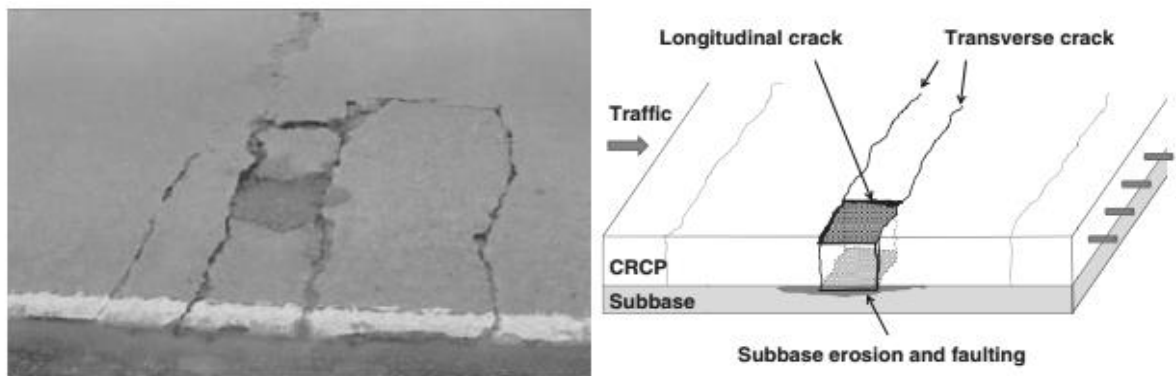
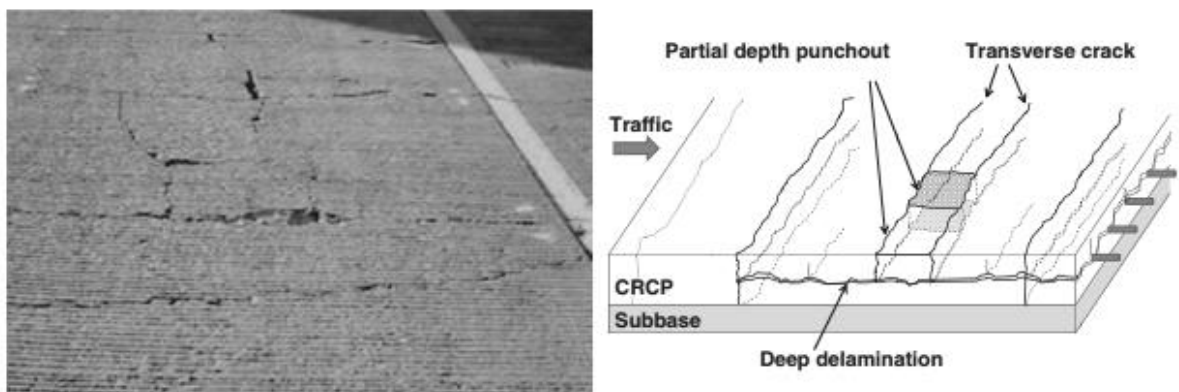


Figure 2. 5 - Effect of base type and LTE in CRCP performance (VANDENBOSSCHE *et al.*, 2012)

The use of more rigid non-erodible bases helped mitigate the punchouts problem - usually connected to slab support loss. However, as reported by Jung *et al.* (2012), in these improved structures, longitudinal cracks started to appear at the longitudinal reinforcement position connecting two closely spaced cracks. To this problem was given the name partial punchout. Figure 2.6 presents the basic differences between deep and partial punchouts.



(a)



(b)

Figure 2. 6 - (a) Deep punchout and (b) partial punchout (JUNG *et al.* 2012)

Partial punchout, although also involving the loss of carrying capacity, hardly presents crack spalling and slab settlement, which are the critical points of the original punchout. Partial punchout probably occurs due to a delamination that divides the slab into two pieces during the first period of concrete strength gain. This happens because the strong friction between the slab and base and also due to the tying effect of the longitudinal steel. This interaction forms two concrete slabs with different strength values and lower thickness and stiffness when

compared to the original designed slab. As a result the stresses inflicted by vehicle loads are much greater than the design predicted, causing a decline in the fatigue life, especially at the slab's top. The delamination occurs due to differences between the material strength and thermal stresses that develop during the concrete shrinkage. Temperatures at early ages and thermal gradients to which the slab is subject are considered factors with delamination potential.

Another interesting aspect of the same work is the role given by established models to the subgrade reaction modulus ( $k$ ). More rigid support conditions reduce deflections resulting in lower shear stresses at the interface which *per se* reduces erosion. However MEPDG indicates that high  $k$  values lead to more punchouts because for the MEPDG model, the problem is treated analogously to longitudinal fatigue cracks. Stiffer bases may increase tensions generated by warping and curling which supposedly increases the chances of fatigue cracking. However, as mentioned before, several studies have positively correlated bases less susceptible to erosion with a smaller number of punchouts. Figure 2.7 shows a comparison between the MEPDG (a) and a model created by the authors (b). Results are very conflicting, indicating MEPDG ineffectiveness to consider the non-erosion potential of stiffer bases (JUNG *et al.*, 2012).

Momeni (2013) also points out additional advantages of having stabilized bases with more uniform material. According to the author, in the early stages of concrete contraction, changes in the friction coefficient between slab and base may cause direction variations of the stresses that are under development. This is a potential cause of shift in the cracks formation, originating meandering and “Y” cracks which are considered undesirable due to the highly likelihood of crack intersection.

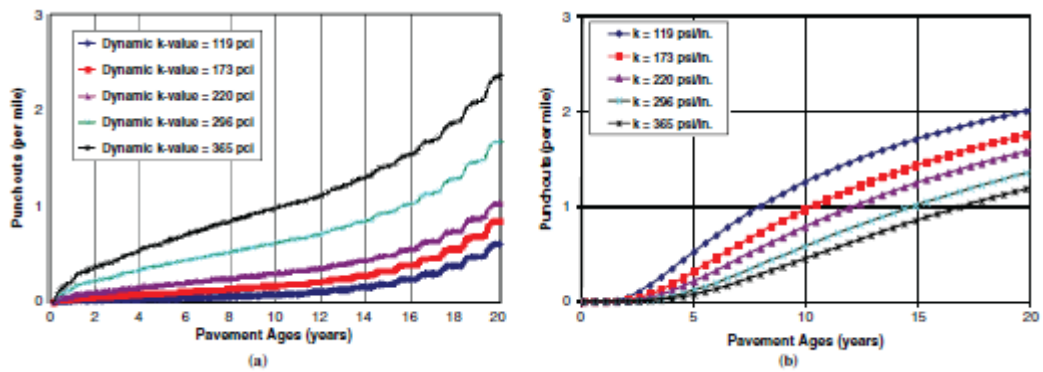


Figure 2. 7 – Punchout predictions according to (a) MEPDG and (b) erosion based model  
(JUNG *et al.*, 2012)

Regarding slab thickness it is intuitive to think that the thicker the slab, more resistant is the structure. Roesler and Hiller (2013) state that due to the sensitivity of the tensile strength and thickness relation, even the smallest change in this parameter radically modifies the pavement behavior as evidenced in Figure 2.8a. Furthermore, a greater thickness, logically, provides a greater area of contact between aggregates, which increases LTE. As for the steel percentage, it is an established CRCP knowledge that the greater the steel amount, the greater the number of cracks, the smaller the crack spacing and width and the better the performance (Figure 2.8b). Although some authors have not found a relationship between large crack spacing and low crack LTE, most design models adopt this criterion. The fact is that the crack width influences the crack’s behavior much more than the spacing between them. However care must be taken when approaching excessive steel percentages (greater than 1%) which can generate an abnormal number of cracks. These cracks, although having minimum widths can intersect each other facilitating punchout development. According to MEPDG recommendations, cracks should not be spaced more than 1.8 m to ensure tighter cracks.

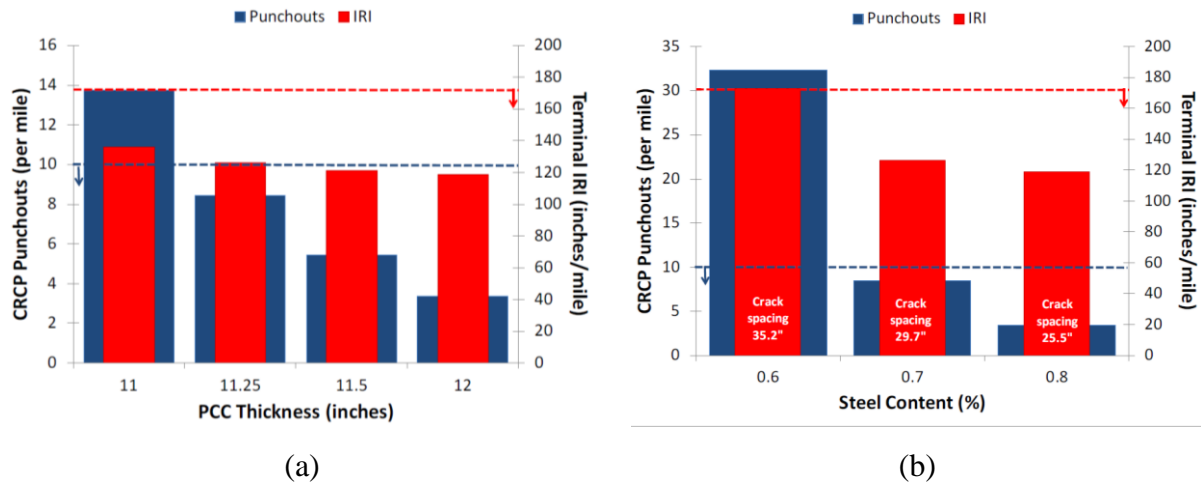


Figure 2. 8 – Punchout number regarding: (a) slab thickness and (b) steel amount (ROESLER and MILLER, 2013)

The steel depth regulates crack width which affects LTE. Consequently the closer to the surface the steel is, the tighter the cracks will be. In addition, steel positioned close to the surface displaces the slab neutral axis up, decreasing tensile stresses at the top. Still, some US state transportation departments have observed great CRCP performances with longitudinal steel positioned at the slab's half height (TAYABJI *et al.*, 1998a).

Regarding the concrete mix, the major research focus has been the coefficient of thermal expansion (CTE) of coarse aggregates. An aggregate with high CTE levels makes the concerns about temperature and hydration heat mentioned in the opening paragraphs of this review more alarming. Ryu *et al.* (2013) report, based on field tests, that the use of concrete with greater CTE than 5.5 microstrain/°F is a high design risk for CRCP.

Another problem with high CTE levels is that this parameter is closely related to development of longitudinal cracks. Choi *et al.* (2011) found that the longitudinal reinforcement resists warping stresses caused by the temperature gradient as shown in Figure 2.9. This resistance causes vertical stresses in the concrete and tensile stresses in the vicinity of the concrete-reinforcement bound. Longitudinal cracks are initiated at the transverse crack and follow along the longitudinal reinforcement. According to the authors, high levels of CTE, high modulus of elasticity and specific nonlinear thermal gradients potentiate the development of longitudinal cracks.

Longitudinal cracks can also be reduced with better curing methods and the use of two-mat placement of longitudinal reinforcement compared to one-mat placement as shown in Figure 2.10. Furthermore, greater steel diameter raises vertical stresses because it increases the concrete-steel contact area and the motion restraint exerted by the latter.

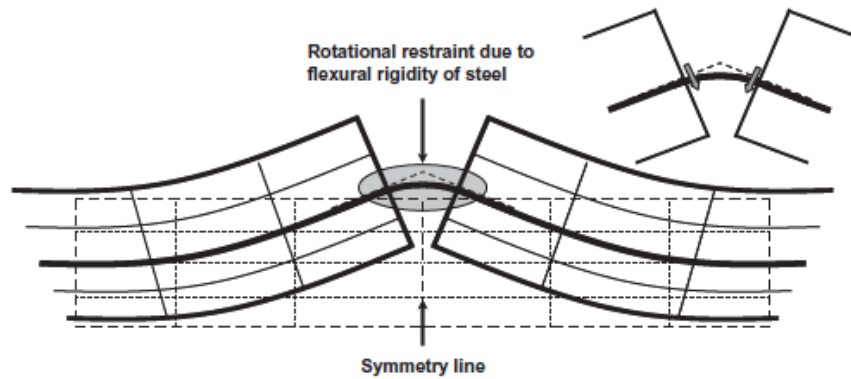
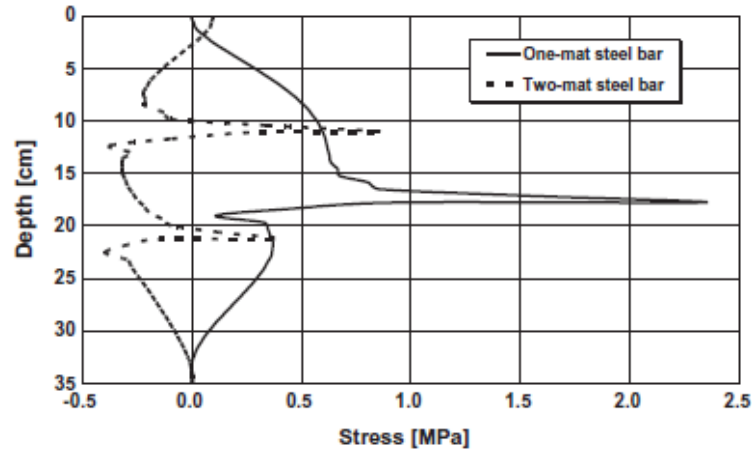


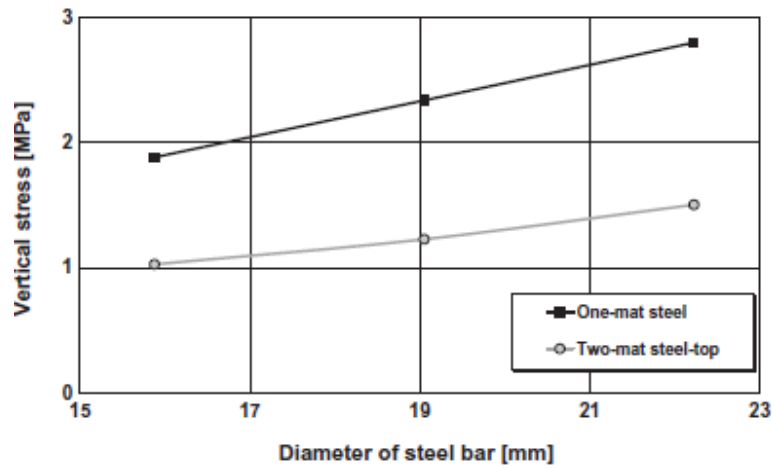
Figure 2. 9 – Steel restraint on concrete subjected to a linear temperature gradient (CHOI *et al.*, 2011)

Al-Qadi and Elseif (2006) statistically demonstrated that the probability of a transverse crack appearing on the transverse reinforcement position is 60%. The authors also confirmed by finite element modeling two major mechanisms controlling the occurrence and propagation of transverse cracking, namely: uniform and severe increase of longitudinal compressive stress at the pavement surface in between two transverse bars and tensile stress concentration near the transverse reinforcement.

One of the most concise examples of advances in CRCP design projects is the Belgian case, explained here through the studies of Ren *et al.* (2013). The basic design of Belgian CRCP between 1970 and 1977 (Project 1) was a 200 mm slab with reinforcement percentage fixed at 0.85% at 60 mm depth, over a 60 mm concrete asphalt base laid on a 200 mm lean concrete sub-base. The resulting crack pattern was a small crack spacing.



(a)



(b)

Figure 2. 10 – Comparison of one-mat to two-mat placement of longitudinal steel regarding (a) vertical stress distribution and (b) effect of the bar diameter (CHOI *et al.*, 2011)

To address the small crack spacing problem (CRCP research focus was only shifted to crack width in the early 1990s), project designs between 1977 and 1991 were altered, creating project 2, composed of the same slab thickness, now with a 0.67% steel percentage at a depth ranging between 60 and 90 mm and 200 mm lean concrete base. Result: better distribution of cracks and greater spacing (between 1.4 and 2.4 m) – suitable for most publications at the time. However, the CRCP project 1 still presented a great performance despite the cluster cracking, while project 2 exhibited punchouts at very young ages caused mainly by the erosion of base material and great crack widths.

Thus, Project 3 was developed in 1991, reintroducing the concrete asphalt base (60 mm), increasing the slab thickness to 250 mm with reinforcement percentage at 0.75% positioned in a depth between 80 and 90 mm. As a result, the average crack spacing was in between 1.36 and 1.69 m six months after construction and around one meter after two years; small but within the levels recommended by AASTHO (1993). The crack width returned to satisfactory patterns, i. e., smaller than 1 mm.

### 2.1.2 Joint-related issues in CRCP

Despite the concept of being a jointless slab, the CRCP still has three types of joints, the longitudinal ones, tying the slab with the edge or with another slab, the transition ones at the slab end and the construction ones when the concreting process is interrupted. Evidently, the ideal CRCP construction is continuous, but depending on the road length or the concrete volume, stoppages are necessary.

- Longitudinal joints: According to Sun *et al.* (2011a), the lane's longitudinal separation can increase water penetration and decrease the load transfer at the longitudinal joints which favors the punchouts development in CRCP. The design method for tie bars does not take into account the effects of temperature variation, hydraulic retraction and load configurations. During concrete hydration, the temperature development is the sum of heat generated by the cementitious materials and the heat exchange between structure and environment. With the thermal gradient variation, the concrete has the potential to expand and contract and to bend the slab up or down. Some factors restrict the CRCP movement, such as steel reinforcement, tie bars and base layer.

In a study conducted in six lanes (180 mm thick slabs) instrumented with Vibrating Wire Strain Gages and Steel Strain Gages, the authors observed that the deformations are larger near the longitudinal edge. Rises in temperature increase deformations. Over time, the tendency is the same but the deformation levels are smaller. The air temperature influences the concrete temperature mainly on the surface as shown in Figure 2.11.

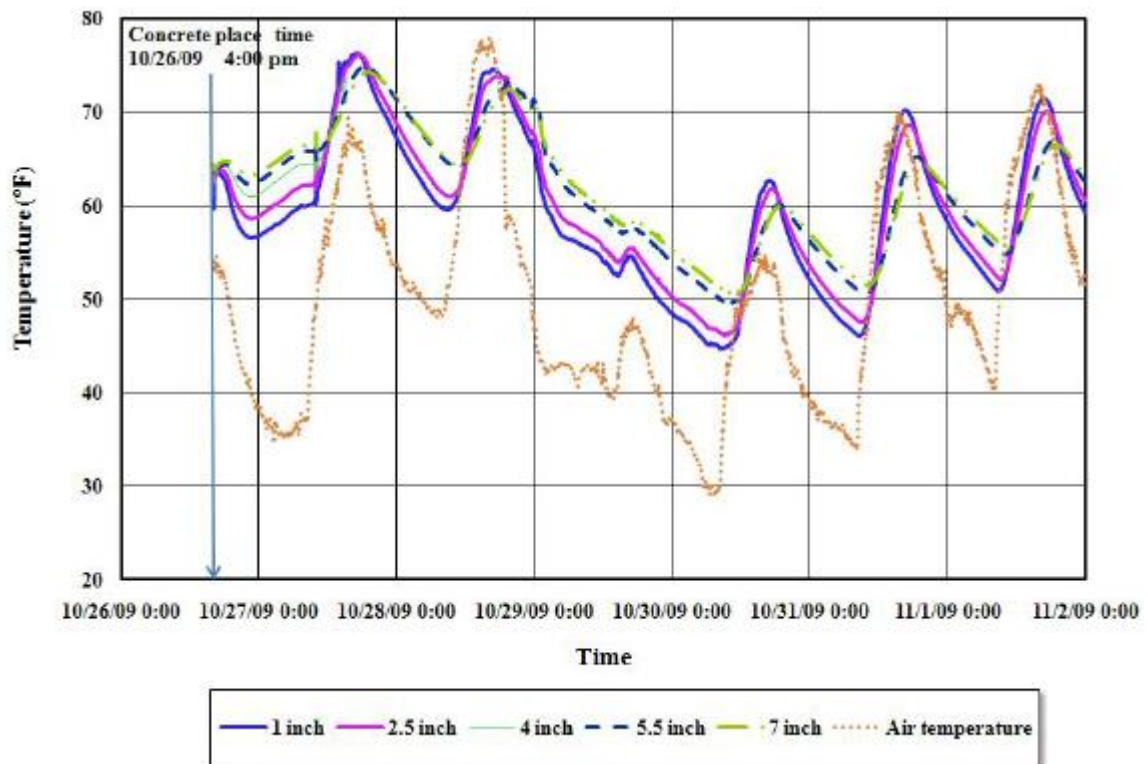


Figure 2. 11 – Temperature variations near the edge (SUN *et al.* 2011a)

As for steel, the authors state that the bars movement is greater near the joint. The steel deformation in the vicinity of the edge is very similar to concrete deformation in that position; this may be a good indicator of steel-concrete boundary conditions.

- Construction joints: Zhou *et al.* (2014) collected data from CRCP distresses in Texas and concluded that about 20% of those are located in construction joints. Volume changes due to temperature and moisture changes are almost entirely suppressed by the longitudinal reinforcement and by slab friction, save the areas at the slab end where random cracks are more likely to happen in order to relieve the stresses. Experiments showed that in construction joints the tie bars behave differently from continuous longitudinal bars. When the temperature increases, the tie bars may be in compression in what can potentially cause longitudinal cracks in these positions. The presence of more steel near the construction joint affects the concrete mass consolidation resulting in the formation of air voids and surface distresses. It is the authors' recommendation to not use tie bars in CRCP construction joints.

- Transition joints: reliable research studies on transition joints performance for CRCP were not found. The newly published CRCP guidelines of the Federal Highway Administration (FHWA) mentions that use of anchors lugs has been avoided by most road agencies due to financial and performance issues (ROESLER *et al.*, 2016). The same manual recommends, based on information from a “tech brief” developed by Zollinger and Jung (2013), four options of transition joints from CRCP to JPCP while also indicating options for transitions between CRCP and asphalt pavement. Unfortunately, neither manual presents reflections on these transition joints alternatives’ performance.

### 2.1.3 CRCP overlay

A very opportune CRCP feature is the fact that at the end of its designed life, the structure can easily receive asphalt or concrete overlays working as a powerful base layer (ROESLER and HILLER, 2013).

Moreover, studies from Ryu *et al.* (2013) and Sun *et al.* (2011b), analyzing theoretical models and field examples, indicate CRCP as a great solution for pavement resurfacing. Overlays of JPCP with asphalt pavements, although widely used, suffer from the reflection of the old pavement cracks. It is known that the CRCP performs adequately as long as the sub-base conditions are appropriate, i. e., not subject to erosion. JPCP, even cracked, meets these requirements.

In the case study presented by Ruy *et al.* (2013), the old JPCP consisted of a 254 mm slab with joints spaced every 4.6 m, under a 152 mm granular base. The slab presented many problems due to over 30 years of traffic exposure, such as longitudinal and transversal cracks along with joint faulting. Analysis showed that about 43% of the slabs had cracks due to loss of base support (uneven support) and to heavy vehicles loading. FWD tests indicated high deflections and consequent low joint LTE. The CRCP resurfacing was designed as a 178 mm slab with 0.7% of longitudinal reinforcement positioned 102 mm from the surface. The CRCP concrete in the slab bottom moved in the tensile stress direction during the morning and in the compression direction during the afternoon. This, according to the authors, shows that the CRCP was satisfactorily adhered to the JPCP slabs.

Variations of crack width regarding slab thickness were different than in traditional CRCP, where crack width variation has the opposite direction at the slab top indicating a slab bend that matches a slab with a neutral line close to its half height. On the other hand, the overlay presents variations in the same direction, indicating a neutral line below the slab half height in a clear demonstration of the perfect integration between the old and new slabs. The crack spacing was 1.45 m; 81% of the CRCP transverse cracks occurred above the transverse reinforcement; 9% in the position of the old JPCP transverse joints. This proves that there was no reflection of cracks and joints of the JPCP. FWD tests showed a significant improvement in LTE and a decrease in deflections. No information was found on the geometry elevation of this new section regarding the remaining of the highway. It was expected a vertical step at the end of the section due to increase in the overall pavement thickness, however, the geometry adjustment was not described in this paper.

## **2.2 Modern non-destructive evaluation techniques for concrete pavements**

Nondestructive evaluation methods, as the name implies, are structure analysis techniques where it is not necessary to physically intervene in the structure. It is possible to observe several parameters within the material without actually having inside contact. The greatest advantage of this type of study is, clearly, its not harmful aspect. For pavements, one of the great problems in layers analysis and characterization is material heterogeneity. When extracting a specimen (coring) or carrying out a trench, one causes a damage degree of greater or lesser impact and the eventual replacement of that removed material will not present the same properties as the original layer. Additionally, the extraction vicinities are known locations of distresses such as cracks and rutting because the stresses in such points are not the same as in the continuous structure. Adherence problems between the recomposed and the original material aggravate this issue. In addition to the structural details, forensic extraction of materials is costly, laborious, unproductive and potentially not representative of the structure as a whole, noting the aforementioned heterogeneity issue. The labor and financial factors are also mentioned as destructive methods disadvantages in Nasief *et al.* (2011). Non-destructive methods, if properly performed and interpreted, can assess a specific point much more quickly and without creating damage. However, one should be aware that all methodologies have simplifications which can lead to errors.

Currently, the combined use of destructive and non-destructive techniques has become the primary means of pavement structures evaluation. First, non-destructive equipment is applied in a comprehensive and fast assessment. After the data interpretation, for locations presenting distresses or where there is doubt in the results, physical material extraction is performed. As pavement structures usually extend for several kilometers, the combination of methods seems to be the key point in the post-construction assessment (thickness check, bars presence and positioning, distresses, etc.) and the maintenance feasibility approaches (distresses, water presence, voids, etc.). In addition to these tasks, unlike the destructive methods, nondestructive methods can be quality control tools used during construction and not only distress assessment tools and/or maintenance and rehabilitation indicators (HOEGH *et al.*, 2011). It is intuitive to think that in both cases, if the desire is to perform pavement maintenance or evaluate new constructions, the destructive material removal must be performed only if needed. Considering the pavement rehabilitation, the sub surface distresses inspection without causing further damage or destruction to the layer can greatly assist maintenance decisions, such as the necessity or not to make a full or partial recovery as discussed by Hoegh *et al.* (2012a).

In this chapter, a comparatively review of the most modern non-destructive methods in operation by the main US transportation departments focusing on concrete pavements evaluation is presented.

### 2.2.1 Ground Penetrating Radar (GPR)

According a compilation by Olhoeft and Smith III (2000), at the end of 1999 there were more than 260 articles, patents and standards related to the use of the GPR technology to evaluate concrete and asphalt pavements. Applications are the most diverse, ranging from distress analysis during construction to the collapse causes investigation at the end of the designed life.

GPR is an electromagnetic method of investigation. The basic principle of the method is the reflection in which a signal is sent by an antenna to the structure and energy reflections caused by changes in material properties are recorded. Complementing the latter idea, Olhoeft and Smith III (2000) state that concrete and asphalt layers are heterogeneous materials, influenced both by the mix materials type and composition as by the interaction with the

environment and the construction method. Thus, the electrical properties of the layer may range from highly conductive to highly resistive in millimeters. Furthermore, the introduction of metal for reinforced structures expands this range of electromagnetic properties. All these matter eccentricities result in significant percentage of simplification for this kind of assessment, although comparative results with samples have shown acceptable errors.

Grote *et al.* (2005) state that GPR can be equipped with antennas for sending and registering different frequency classes. By using high-frequency antennas, the results appear in high resolution, however the depth range is low. On the other hand, low frequency antennas provide deeper penetration with a consequent lower resolution. Most commercial GPR offer antennas with frequencies between 50 MHz and 1.5 GHz (DANIELS, 1996).

The GPR primary evaluative function evidenced in international studies was for determining the layer thickness of both asphalt and concrete pavements (TOMPKINS *et al.*, 2008). The possibility to carry out surveys with the unit coupled to a vehicle makes this type of evaluation very productive and almost continuous with minimal traffic interruption (OLHOEFT and SIMTH III, 2000 and HUGENSCHIMDT, 2002).

Hugenschmidt (2002) further states that the calibration is normally done with the use of cores comparing the travel time to the specimen's exact thickness. In the same study thickness differences between 50 and 150 mm were found comparing cores and GPR results – what the author regards as an acceptable error margin. However for concrete slabs such differences can imply in performance issues. It should be noted that other studies, such as Grote *et al.* (2005) found major errors due to erroneous estimates of the dielectric constant, which intensifies the need for a thorough study of this parameter. Figure 2.12 shows an example of steel coating depths on a bridge. The reflections caused by the asphalt layer bottom (gray arrow), by the top of the bars (white arrow) and finally, by the bottom of the concrete layer are visible. The graph below shows the steel coating results in the evaluated section. Comparison with 15 cores showed an average difference of 6 mm for the analyzed sections (HUNGESCHMIDT, 2002).

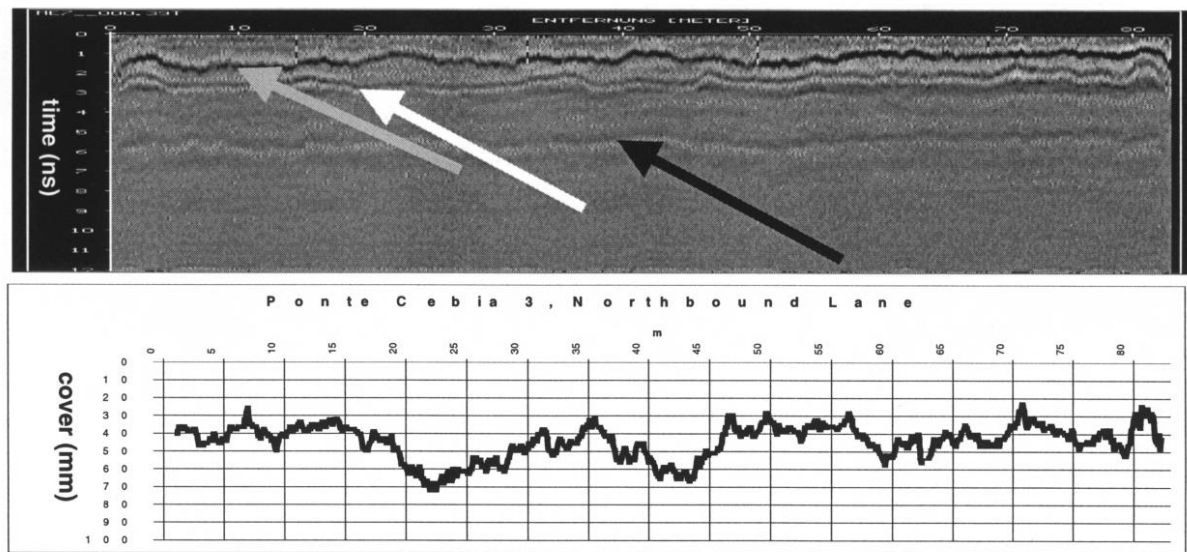


Figure 2.12 – Steel coating analysis in a bridge (HUNGESCHMIDT, 2002)

Hugenschmidt and Mastrangelo (2006), also testing bridges, were able to measure the steel coating of 77% of the cases inspected. The average difference between the results of GRP and the actual data (cores) was 10 mm. For concrete thickness, 95% of the measurements were successful with a 9 mm average error. These range of errors would be more acceptable for pavement evaluation.

In pavement analysis, Saarenketo and Scullion (2000) were able to assess with a certain precision the subgrade soil, the layers thickness, the granular base quality, the presence of sub-surface distresses, asphalt pavement voids and mixture segregation through the dielectric response of the studied material. In the research of Scullion (2006), it was possible to identify voids filled with water (red reflection in Figure 2.13) and with air (blue reflection). Hoegh *et al.* (2015) developed a procedure to better identify areas with air voids in asphalt pavements.

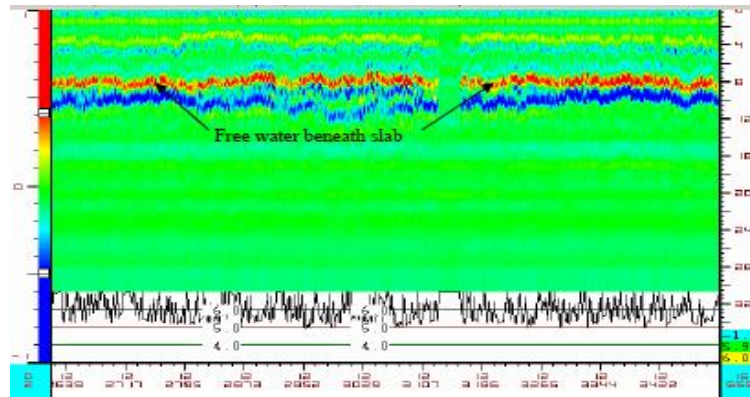


Figure 2.13 – Presence of free water beneath slab (SCULLION, 2006)

However, despite the results discussed, several studies point out difficulties and failures in GPR evaluation. Hoegh *et al.* (2012a) admits that the GPR returns accurate information but only for shallow thicknesses. According to the authors the extent to which the evaluation deepens, the readings become confused; furthermore, the visualization of non-uniform cracks is considered difficult. Haza *et al.* (2011) also points problems in voids and cracks observation with GPR, in the same way that Hoegh and Khazanovich (2012), whom could not measure the thickness and find delamination areas with the device. Maierhofer (2003) found that when the moisture level is too high, the electromagnetic waves are absorbed rapidly losing its potential. So it is practically impossible to investigate fresh concrete or during the early curing stages. Scullion (2006) notes that due to concrete having a mitigation action on GPR waves, data from base and sub-base materials are lost, which does not occur in asphalt pavements. This indicates that if strong signal reflections appear below the slab, the distress severity or impaired area is quite alarming. Yet, according to the author, in some places, strong reflections were not water related problems, but saturated base clays without voids. This, according to the author, compromises the method, requiring the destructive verification to certify the distress presence. Therefore, although productive and useful for several applications, GPRs can produce a certain degree of doubt that is not desirable for precise pavement evaluations.

### 2.2.2 Infrared tomography

According to Clark *et al.* (2003), most materials absorb infrared radiation which causes an increase in their temperature. All objects with temperature above absolute zero emits infrared energy. For this type of data to be visible and understandable, the thermal imaging technique

is utilized to convert the thermal radiation pattern into a visual image. To this end, an infrared camera is used. Not having the need for direct contact with the object being analyzed, high productivity readings (rapid response), high resolution and portability (camera) are some of the technique highlights.

However, evaluations are dependent on several factors such as the materials temperature, atmospheric temperature and climate conditions. According to the aforementioned authors, sunlight highlights objects more clearly when it increases their temperature, improving the results, what goes in agreement with the findings of Park *et al.* (2004). The authors state that the infrared techniques are adversely affected by sunlight incidence in the analyzed object. Hoegh and Khazanovich (2012) point out the technique's potential to find concrete delaminations, though, again, attention must be drawn to the climatic conditions interference in results. Furthermore, the influence of temperature on the readings is much more concise on the material surface, thus deeper assessments are difficult to interpret.

Additionally, regarding the infrared tomography disadvantages, Clark *et al.* (2003) affirm that when it is desired to know the object temperature, it should be noted that the measurements are related to the object temperature as well as to temperature emitted by the object. Thus materials which transmit more heat can influence the readings of other nearby materials.

In the example in Figure 2.14, delamination areas have a different temperature from those where the concrete is flawless. With an image amplification, it is possible to note (highlighted in green) those areas. The temperature difference in the areas with and without delamination was about 0.2 to 0.3 ° C. Forensic testing conducted in the same sites showed the distress presence (Clark *et al.*, 2003).

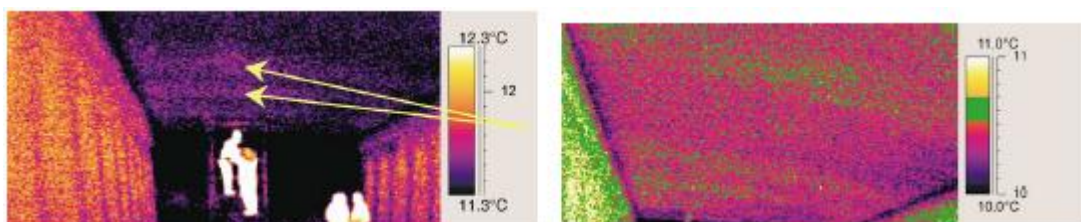


Figure 2. 14 – Delamination areas identification with infrared tomography (CLARK *et al.*, 2003)

### 2.2.3 Magnetic tomography (MIT Scan 2)

Magnetic tomography is an evaluation technique that applies pulse induction principles to find metal parts inside objects. In pavements, the Magnetic Imaging Tools (MIT Scan 2) is often used to check dowel and tie bars placement in joints.

The equipment emits a pulsing magnetic signal of low intensity and measure the transient signal induced in steel bars inside the concrete. These signals contain information about the distribution of electrical conductivity and magnetic properties, which allows not only determining the position but also the size, shape, orientation and type of the steel element.

An example of MIT Scan 2 reading extracted from the work of Hossain and Elfino (2006) is shown in Figure 2.15.

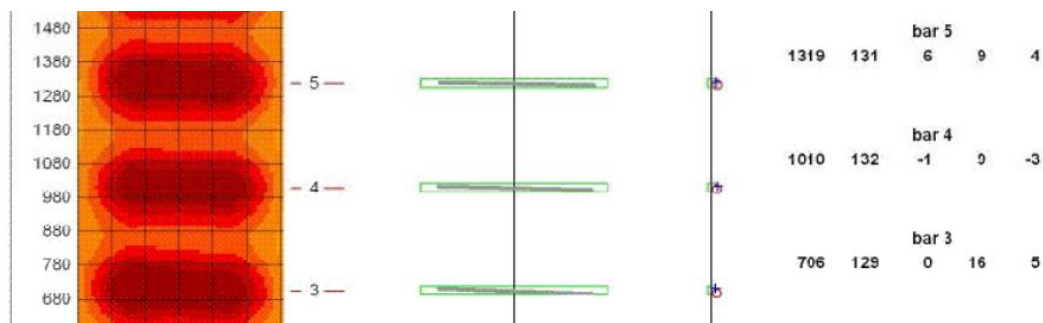


Figure 2. 15 – MIT Scan 2 application results for dowel bars (HOSSAIN and ELFINO, 2006)

The interpretation of the numbers below the bar is made from left to right as follows (4 bar example):

- Position X = 1010 mm. Bar 4 is 1010 mm from the scanning starting point (in this case, slab edge);
- Depth = 132 mm. Regarding the concrete surface;
- Lateral displacement = -1 mm. Bar's middle is 1 mm to the left of the transverse joint (positive values indicate a shift of the joint right side);
- Horizontal misalignment = 9mm. Bar 4 is skewed 9 mm from one end to the other in clockwise direction (negative value means counterclockwise);

- Vertical misalignment = - 3 mm. The right end of the bar is 3 mm higher than the left end (positive sign would indicate that the right end would be lower than the left).

The study findings point out results that present disagreement with reality, with high misalignments indications that did not occur. This, according to the authors, is due to the fact that the MIT Scan 2 readings are highly susceptible to the presence of nearby other steel materials not calibrated in the experiment. Nevertheless, Rao *et al.* (2009) suggested several changes in construction methods and distresses thresholds of US transportation departments after analyzing more than 60 pavements with MIT Scan 2.

Despite the technique effectiveness in detecting steel elements in the structure also proven by Prabhu *et al.* (2006), Hoegh and Khazanovich (2012) point out that its operation is limited to this material type. Nasief *et al.* (2011) complements the restriction stating that to estimate the layer thickness it is necessary to place a steel at the top of the base at each measurement point which is evidently unrealistic and unproductive for constructors.

#### 2.2.4 Modern ultrasonic techniques

According to Hoegh *et al.* (2011), ultrasonic techniques utilize high frequency waves (greater than 20,000 Hz) to characterize materials' properties and detecting distresses. Sound waves are generated by transducers; they travel through the material and are received by receptors on the surface. Signal analysis allows discovering information about the means by which the signal had traveled. This technique has been used successfully for many years in medicine and evaluation of metallic and composite materials. However, application of this method in typical pavement materials such as concrete and asphalt has been problematic due to the need for a signal coupling liquid and the difficulty in reaching the required thickness, because of the different layers which may cause wave attenuation. These difficulties led to the use of rudimentary methods such as chain dragging and impact echo. Hoegh and Khazanovich (2012) argue that the former is much influenced by the operator and the latter only inspects properly plain and uniform structures and distresses. Moreover, both are considered slow and unproductive. More recently, ultrasonic testing has been used for detection of inclusions, estimation of compressive strength, elastic modulus and crack propagation in concrete specimens producing interesting results (CARNONARI *et al.*, 2010; DIOGENES *et al.*, 2011; PERLIN and PINTO, 2013). However, most methods require the coupling of transducers and

sensors in at least both sides of the specimen which assumes the use of specimens therefore impairing the non-destructive goal of the test for pavement evaluations.

In order to overcome these problems, transducers with dry contact point with the capacity to emit shear waves of low frequency (50 kHz) were created making it possible to effectively penetrate at greater depths. MIRA is an example of this novel technique. The device has a linear array of ten channels spaced 40 mm apart containing 4 transducers each for a total of 40 transducers (Figure 2.16). This arrangement makes each group of four transducers (channel) to produce shear waves that are centered between the four transducers with a perpendicular focus to the surface (SHEVALDYKIN *et al.*, 2002; BISHKO *et al.*, 2008).

Therefore each channel acts like an emitting and receiving transducer where the first transducer emits shear wave to all the remaining transducers being followed by the other transducers sequentially up to the tenth transducer which only receives the emitted signal. Figure 2.17 provides an illustration for this arrangement that originates 45 pairs of emitting and receiving transducers. The enormous amount of data is interesting as there is a perfect image compilation, especially for heterogeneous materials.



Figure 2. 16 – MIRA device and transducers (BISHKO, *et al.* 2008; RAPAPORT, 2011)

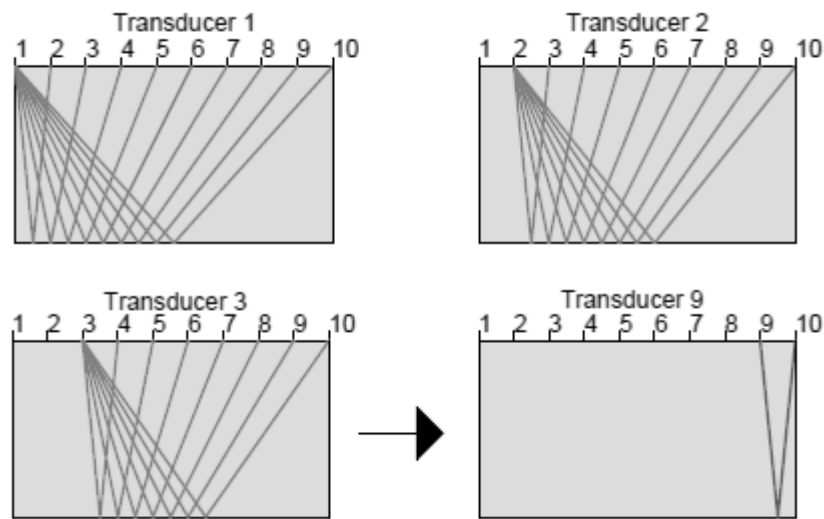


Figure 2.17 – Transducer interaction in MIRA's linear array

Concerning measurements, although the analyzed surface must be plane, it does not need to be smooth as each transducer has a spring system that allows for readings in slightly irregular surfaces avoiding the transducer to be in contact with air which may impair the measurement. Also, as mentioned by Haza *et al.* (2011), testing in rough surfaces is possible due to wear-resistant ceramic tip that each transducer is built with. A survey takes less than 2 seconds. According Vancura *et al.* (2013), low frequency wave (typically 50 kHz) allows the signal to navigate through the concrete despite the material heterogeneous characteristics. The signals are reflected once an acoustic discontinuity takes place, which is defined as the interface between a medium wherein the impedance of the following medium is different. The acoustic impedance is a material property and is the product of sound velocity and material density. The device is linked to a portable computer which carries the MIRA software. Through the software operation, it is possible to perform calibrations, readings and changes in the device's original configuration. The software also allows for a 2D image view of the current reading. Figure 2.18 shows again the device and its operation principle compared to the impact echo.

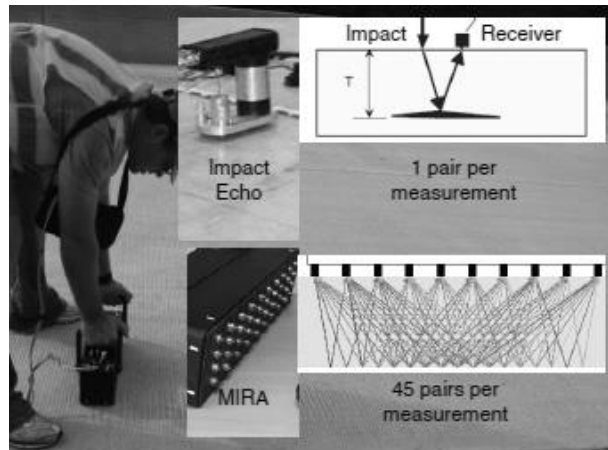


Figure 2. 18 – Impact echo *versus* MIRA (VANCURA *et al.* 2013)

A clear example of using MIRA to CRCP analysis, extracted from Hoegh *et al.* (2011), is shown in Figure 2.19. The three reflections of the longitudinal reinforcement at the slab half-height and the lower reflection corresponding to the interface between the slab and base (backwall) can be easily identified. Note that the backwall does not extend to image limits; this should not be considered a problem or lack of continuity in the layers bonding, as it is the result of the device’s small aperture scan. As seen in Figure 2.18 the transducers’ arrangement in MIRA is such that the greater information amount is located at the scan center and not in its borders. The study shows a strong correlation between MIRA results for steel coatings and slab thickness and cores extracted at the same position.

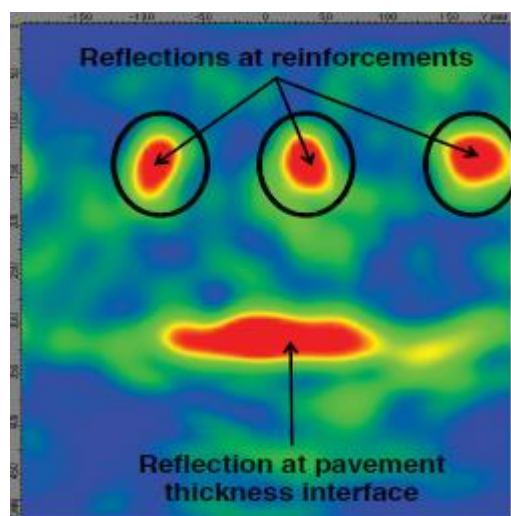


Figure 2. 19 – MIRA reading example (HOEGH *et al.* 2011)

Once on MIRA, the data obtained by the transducers is processed with the synthetic aperture focusing technique (SAFT), which rebuilds the information from all transducers pairs (HAZA *et al.* 2011). According to Bishko *et al.* (2008), the SAFT algorithm implementation enables the creation, by readings superposition, of 3D images. The complete reading and interpretation equations of ultrasonic waves by MIRA can be found in Samokrutov *et al.* (2006). More details on SAFT and its modifications performed by Hoegh (2013) will be provided on the next chapter.

For example, with the compilation of various readings it is possible to reconstruct in a 2D image the exact position of a distress (Figure 2.20). Forensic analysis of the slab shows the device accuracy which was also able to correctly indicate the slab thickness of approximately 230 mm (9 in.). Compared with other methods, ultrasonic evaluation with MIRA showed the best correlation with the destructive forensic studies (HOEGH *et al.*, 2013).

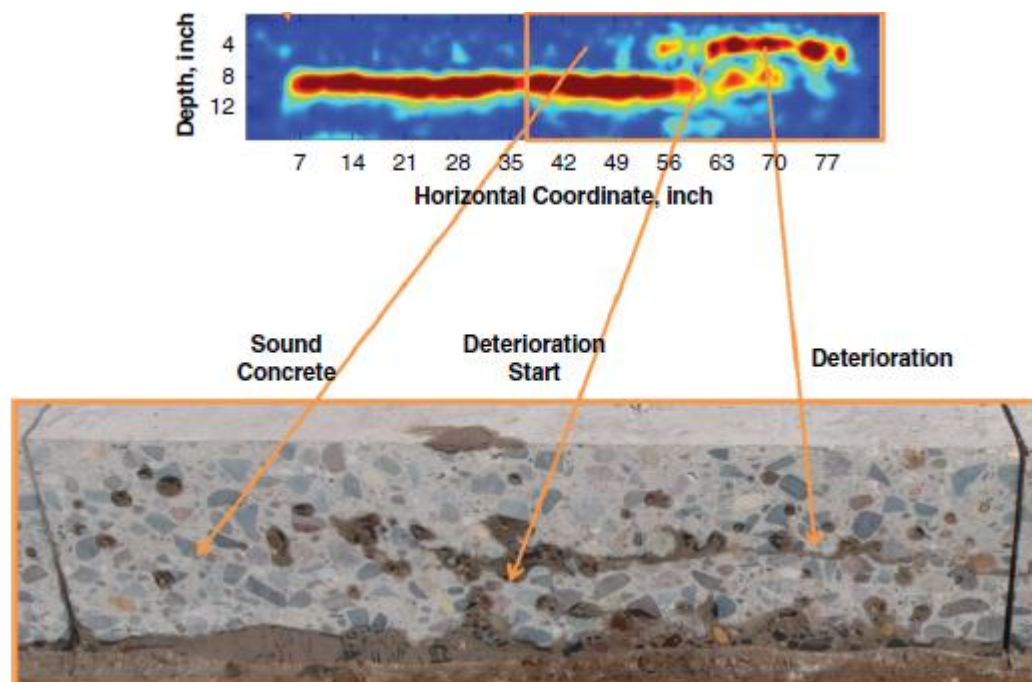


Figure 2. 20 – Forensic evidence of delamination presence in a concrete slab (HOEGH *et al.*, 2013)

A combination of several studies, collected by Vancura *et al.* (2013) certifies MIRA results as seen in Figure 2.21. Hoegh *et al.* (2011) and Edwards (2012) also found a high correlation between MIRA results and cores in concrete pavements as shown in Figure 2.22.

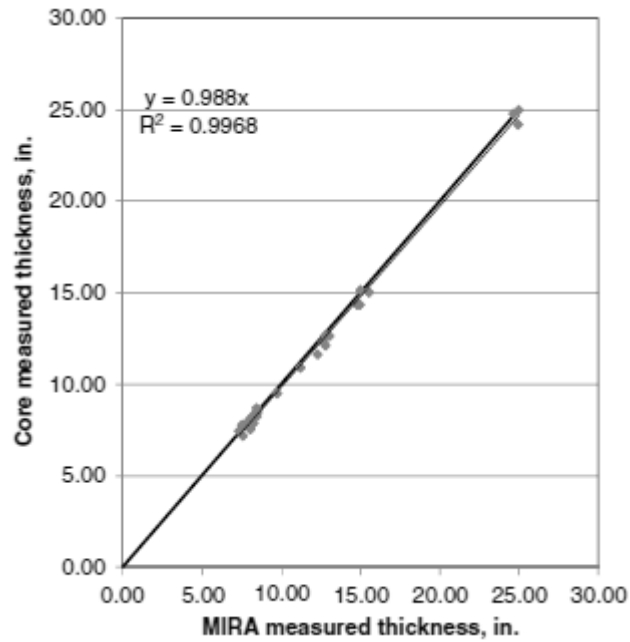


Figure 2. 21 – MIRA sensitivity analysis (VANCURA *et al.*, 2013)

Vancura *et al.* (2013) was not conclusive on how many surveys should be made to correctly measure pavement thickness. But the authors stress that the core extraction every 300 m - standard procedure – does not characterize the thickness in a section. For the first JPCP section, correlation analysis indicated a measured needed every 14 m, while for the second section the interval was 80 m. Salles *et al.* (2017) applying MIRA thickness surveys in a large segment of an US highway were able to observe great thickness variation in both transverse and longitudinal directions.

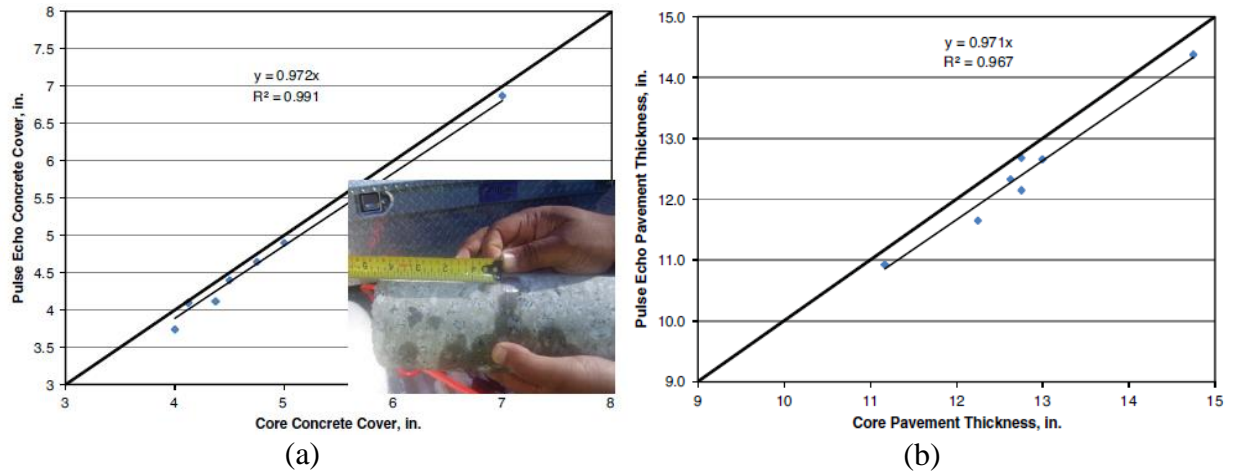


Figure 2. 22 – Correlation index between the cores and MIRA of (a) concrete cover and (b) slab thickness (HOEGH *et al.*, 2011)

Moreover for Hoegh *et al.* (2011), observation of deteriorated concrete near the constructive joint was possible with MIRA. In Figure 2.23a a sound concrete with a slab/base interface reflection is visible. This scan was held in the right wheel track. In Figure 2.23b (joint middle) there is a reflection closer to the surface and no reflection indicating the slab end. This is due to the concrete in Figure 2.23b being deteriorated making the distress reflection to creates a "shadow" that prevents the slab/base backwall reflection to be visible. In Figure 2.23c, forensic photographs prove MIRA's precision.

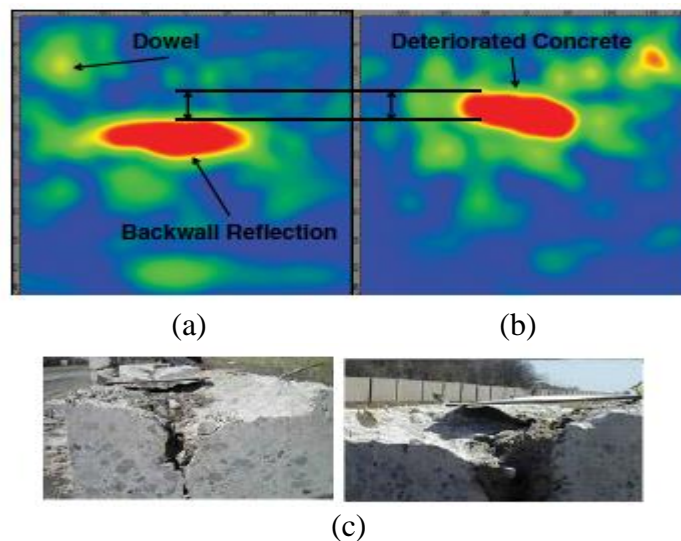


Figure 2. 23 – MIRA scan (a) at the joint right side, (b) at the joint middle and (c) trench proving (HOEGH *et al.*, 2011)

In Hoegh and Khazanovich (2015), the development of software (SAFT-PAN) able to analyze and unite MIRA overlapping readings creates more complete pavement images. According to the authors, it is possible to observe very small and occasional failures as cracks by the shading effect they cause in the backwall reflections. Figure 2.24 shows clearly the two discontinuities in the reflection "backwall" between the slab and base. These two spots are two vertical cracks (CR1 and CR2). More information on SAFT-Pan will be given in the next chapter.

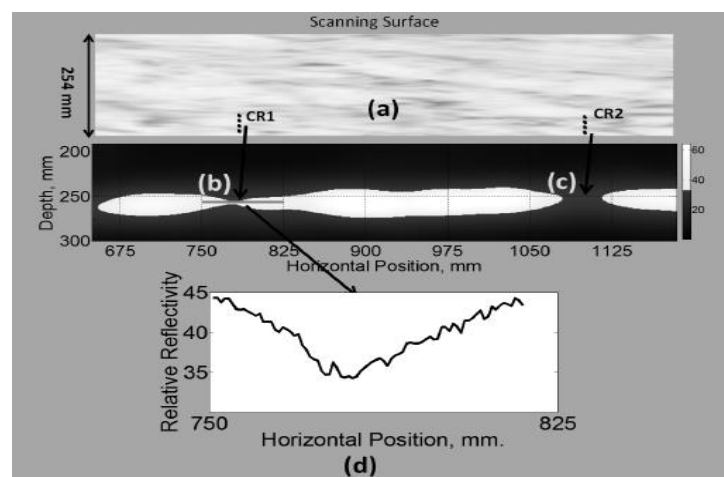


Figure 2. 24 – Example of SAFT-Pan utilization to visualize cracks (HOEGH and KHAZANOVICH, 2015)

For Hoegh *et al.* (2012b), MIRA was also proved efficient in investigations of boundary between two layers of asphalt (Figure 2.25). Reflections in blue represent a sound uniform material, while green spots are reflections of consolidation issues caused by voids or distresses. The more yellowish (greater reflection) is the top layer detachment over the bottom. Bishko *et al.* (2008) states that the device can provide clear results in thicknesses of up to 2 m.

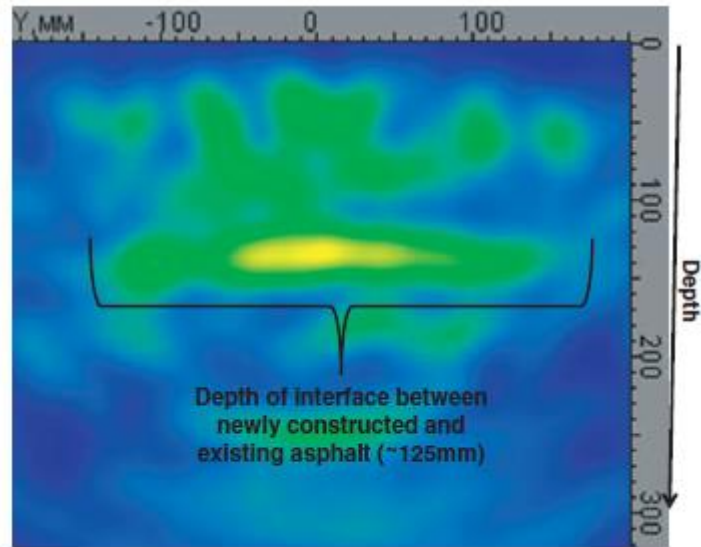


Figure 2. 25 - Detachment between two asphalt layers (HOEGH *et al.* 2012b)

As the ultrasonic linear array used in this study (MIRA) is based on shear waves, it is also possible to determine shear wave velocity at the slab surface, an important indicator of material properties that is applied in the MIRA scans reconstruction to transform time into distance. The shear wave is one of the three modes of wave propagation caused by external impact in concrete which behaves like an elastic solid medium. The movements inside the concrete subsequent to the impact can be characterized by the direction of the particle motion regarding the propagation direction. The compression (longitudinal) P-waves presents particle motion parallel with the wave propagation direction whereas the transverse (shear) S-waves are perpendicular to the wave propagation direction. In the R-wave (Rayleigh), the particles move in a retrograde elliptical direction being a combination of P and S waves (GRAFF, 1991).

MIRA allows shear wave velocity computation from analysis of the direct (un-reflected) first arrival of shear waves at the concrete surface. According to Heisey *et al.* (1982), shear wave velocity is a function of Young's modulus, Poisson's ratio, and pavement density and can be used to compute compressive strength (AN *et al.*, 2009). Multiple studies have found strong correlations between compressive strength and shear wave velocity (CHO *et al.*, 2007; AN *et al.*, 2009; FREESEMAN *et al.* 2016). From the studies mentioned above, only Freeseaman *et al.* (2016) applied MIRA. Salles *et al.* (2017) also applying MIRA was able to discover changes in construction of a US highway at the end of its service life when analyzing the

shear wave velocity. Alterations in shear wave velocity were statistically related to a greater presence of distresses – sections with higher shear wave velocity presented a better performance. Cores and additional data from other highways will soon be added to this research project.

### **2.3 Load transfer efficiency (LTE) in joints and cracks**

JPCP and CRCP structures have a surface layer made by concrete slabs which present discontinuities. Unlike asphalt layers, concrete slabs undergo natural shrinkage of the mixture's cementitious components that causes a high stress state at a young age - when the concrete has not yet developed its complete strength. To ease these tensions, micro cracks develop in the structure and then are combined with other micro cracks until a sharp break takes place, originating shrinkage cracks. Due to this known problem, joints are designed in JPCP to induce cracking in a known location and to keep the slabs interconnected by a load transfer system (dowel transfer bars). On the other hand, for CRCP there is no cracking induction, the cracks develop randomly but are kept strongly tightened by the longitudinal reinforcement positioned above the slab half-height. In JPCP the load transfer between slabs occurs both by the dowel bar and by the aggregate interlocking; for CRCP it is considered that only the last component operates in LTE. Temperature affects LTE in both structures, as on colder days there is a concrete contraction trend which results in larger joints and cracks widths potentially lowering the aggregate contact.

LTE is best known mathematically as the deflection ratio of the unloaded slab and the loaded slab. Two equations (Equations 1 and 2) developed by Shahin (1984) are most commonly used to calculate the LTE (LTE \* is referred by some authors as the crack efficiency), as follows:

$$LTE = \frac{\delta_2}{\delta_1} \times 100\% \quad (1)$$

and

$$LTE^* = \frac{2\delta_2}{\delta_1 + \delta_2} \times 100\% \quad (2)$$

being both reunited by Equation 3, as follows:

$$LTE^* = 2 \times \left( 1 - \frac{1}{1 + \frac{LTE}{100}} \right) \times 100\% \quad (3)$$

where:

$\delta_1$  = loaded slab deflection;

$\delta_2$  = unloaded slab deflection.

The direct relation between the deflections mentioned above assumes that if the joint/crack has a weak ability to transfer load from one slab to the other, i. e., the deflection in the loaded slab is much higher than in the unloaded slab, LTE will be lower, close to 0%. Conversely, if the load transfer capacity is high (similar deflections in both slabs), LTE will be closer to 100%. LTE can also be calculated based on stress data, as shown in Equation 4:

$$LTE_\sigma = \frac{\sigma_2}{\sigma_1} \times 100\% \quad (4)$$

where:

$\sigma_1$  = crack/joint stress in the loaded slab;

$\sigma_2$  = crack/joint stress in the unload slab.

Khazanovich and Gotlif (2003) report difficulties when comparing LTE measurements from deflections and stresses. Due to the greater difficulty of measuring stress in a concrete slab, LTE based on stress is much more dependent on the load dimensions.

According to Ioannides *et al.* (1996) there are two stiffening components in a joint: the dowel bar component (D) and aggregate interlock component (AGG). The same research group, in previous publications, characterized these two components as dimensionless parameters governing the joint stiffness performance according to Equations 5 and 6 (IOANNIDES and KAROKEVICS, 1990; IOANNIDES and KAROKEVICS 1992):

- Pavements without dowel bars:

$$AGG^* = \frac{AGG}{k\ell} \quad (5)$$

- Pavements with dowel bars

$$D^* = \frac{D}{spk\ell} \quad (6)$$

where,

$D^*$  and  $AGG^*$  = dimensionless joint stiffness of pavement with and without transfer bars, respectively;

$AGG$  = aggregate interlock shear stiffness by unit length;

$D$  = shear stiffness of a single dowel bar;

$\ell$  = slab's radius of relative stiffness;

$k$  = subgrade reaction modulus;

$sp$  = dowel bars spacing.

Unfortunately, the original work does not consider the two dimensionless parameters united action. It is known that even for pavements with dowel bars, part of the LTE is achieved by aggregate interlock. However, it is possible to separate the parameters knowing the overall stiffness of the joint ( $AGG_{TOT}$ ) as calculated by Equation 7:

$$AGG_0 = AGG_{TOT} - D \times sp$$

(7)

where:

$AGG_0$  = joint stiffness corresponding to aggregate interlock;

Enhancing early studies, Croveti (1994) proposed the following relation between the joint total stiffness and LTE (Equation 8):

$$LTE = \frac{100\%}{1 + 1,2 \left( \frac{AGG_{TOT}}{k \ell} \right)^{-0,849}} \quad (8)$$

Zollinger *et al.* (1999) also developed a similar model (Equation 9):

$$LTE = \frac{100\%}{1 + 10 \left[ \frac{0,214 - 0,183 \frac{ar}{\ell} - \log \left( \frac{AGG_{TOT}}{k \ell} \right)}{1,18} \right]} \quad (9)$$

where:

$ar$  = load equivalent radius.

In Figure 2.26 there is a comparative evaluation of the two models with the simulation of LTE with ISLAB2000 software. Despite the equation proposed by Croveti (1994) being simpler

than that of Zollinger *et al.* (1999), the former has better matching with the ISLAB2000 results.

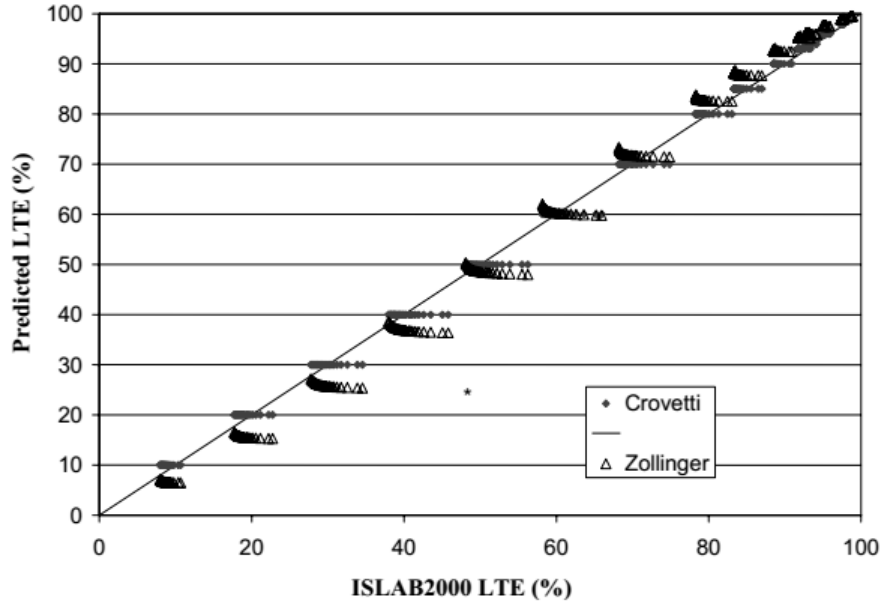


Figure 2. 26 – LTE prediction from Croveti and Zollinger models versus ISLAB2000 LTE (KHAZANOVICH and GOTLIF, 2003)

Selezneva *et al.* (2004) updated the LTE calculation model introduced by Ioannides *et al.* (1996) to include LTE provided by aggregate interlocking, longitudinal reinforcement and base support. Equation 10 presents the new expression.

$$LTE_i = 100 \left\{ 1 - \left[ 1 - \frac{1}{1 + \frac{\log^{-1}\left(0.214 - 0.183 \frac{ar}{\ell_1} - \log(J_{Ci}) - (500P - 3)\right)}{1.18}} \right] \left[ 1 - \frac{LTE_{base}}{100} \right] \right\} \quad (10)$$

where,

$LTE_i$  = total crack LTE due for time increment i (%);

$\ell_1$  = radius of relative stiffness for time increment i (mm);

P = Percent of longitudinal reinforcement expressed as fraction;

$LTE_{Base}$  = LTE contributed by the base layer – 20% for aggregate base; 30% for asphalt treated base or concrete treated base; and 40% for lean concrete base;

$J_{ci}$  = dimensionless aggregate interlock factor for time increment  $i$ .

The dimensionless aggregate interlock factor is determined with Equation 11, as follows (JEONG and ZOLLINGER, 2001):

$$\log(J_{ci}) = ae^{-e^{-\left(\frac{j_s-b}{c}\right)}} + de^{-e^{-\left(\frac{s_i-e}{f}\right)}} + ge^{-e^{-\left(\frac{j_s-b}{c}\right)}} \times e^{-e^{-\left(\frac{s_i-e}{f}\right)}} \quad (11)$$

where,

$a = -2.2$ ;  $b = -11.26$ ;  $c = 7.56$ ;  $d = -28.85$ ;  $e = 0.35$ ;  $f = 0.38$ ;  $g = 49.8$ ;

$j_s$  = lane-shoulder joint stiffness (4 for tied PCC; 0.04 for all other shoulder types);

$s_i$  = dimensionless shear capacity for time increment  $i$ .

The transverse crack dimensionless shear capacity at pavement age  $i$  can be characterized by Equation 12, as follows:

$$s_i = s_{0i} - \Delta S_{i-1} \quad (12)$$

where,

$s_{0i}$  = initial crack shear capacity based on crack width and slab thickness for time increment  $i$ ;

$\Delta S_{i-1}$  = loss in shear capacity accumulated from all previous time increments.

Crack shear capacity deterioration is related to crack width and slab thickness. The loss of shear capacity at the end of a predetermined time increment is calculated by Equations 13 and 14 according to the relation between crack width and slab thickness.

$$\Delta_{Si} = \sum_j \left[ \frac{0.005}{1 + \left(\frac{cw_i}{h}\right)^{-5.7}} \right] \left( \frac{n_{ji}}{10^6} \right) \left( \frac{\tau_{ij}}{\tau_{refi}} \right) ESR_i \quad \text{if } \frac{cw_i}{h_{PCC}} < 3.7 \quad (13)$$

$$\Delta_{Si} = \sum_j \left[ \frac{0.068}{1 + 6 \left(\frac{cw_i}{h} - 3\right)^{-1.98}} \right] \left( \frac{n_{ji}}{10^6} \right) \left( \frac{\tau_{ij}}{\tau_{refi}} \right) ESR_i \quad \text{if } \frac{cw_i}{h_{PCC}} > 3.7 \quad (14)$$

where,

$cw_i$  = crack width for time increment  $i$  (mm);

$h$  = slab thickness (m);

$n_{ij}$  = number of axle load applications for load level j;

$\tau_{ij}$  = shear stress on the transverse crack at the corner due to load j (kPa);

$\tau_{refi}$  = reference shear stress derived from the Portland Cement Association test results found in Jeong and Zollinger (2001) (kPa);

ESR = equivalent shear ratio to adjust traffic applications for lateral traffic wander (NCHRP1-37A)

According to Ioannides and Korovessis (1990), due to the questionable longevity of the aggregate interlock system, this load transfer mechanism should not be the only one available for JPCP. Factors such as aggregate abrasion with time added up to temperature variations that generate divergence of the two joint faces may decrease the load transfer. For CRCP, the tying effect of the longitudinal reinforcement mitigates these losses.

In Figure 2.27 the correlation of LTE with the dimensionless joint coefficient regarding aggregate interlock (AGG \*) is presented. With knowledge of the slab's radius of relative stiffness and subgrade reaction modulus it is possible to backcalculate the joint stiffness relative to aggregate interlock (AGG).

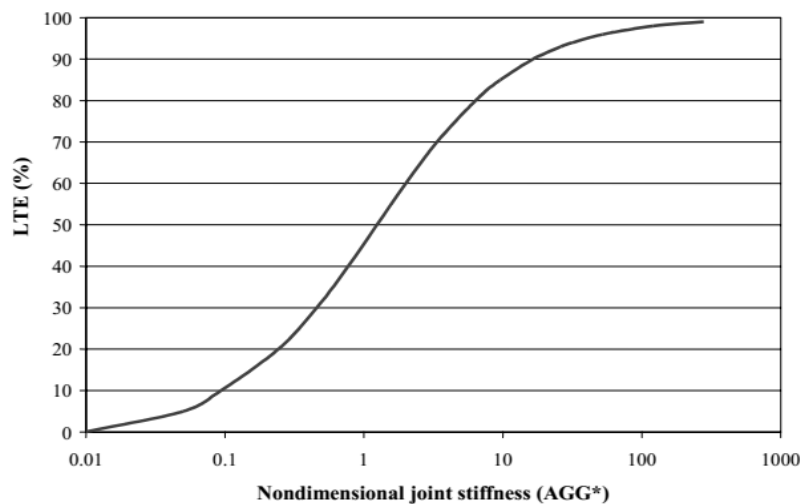


Figure 2. 27 – LTE as function of joint stiffness by aggregate interlock (KHAZANOVICH and GOTLIF, 2003)

Maitra *et al.* (2010) also developed, by finite element modeling, a model for the characterization of what the authors call "interlocking modulus" ( $K_j$ ). The  $K_j$  is a function of crack width and maximum diameter of coarse aggregate, as suggested by Equation 15:

$$K_j = 0.4568 \times cw^{-0.7493} \times \exp(0.0643 \times \frac{agg}{cw}) \quad (R^2 = 0.995) \quad (15)$$

Where:

$K_j$  = Interlocking modulus (MPa/mm)

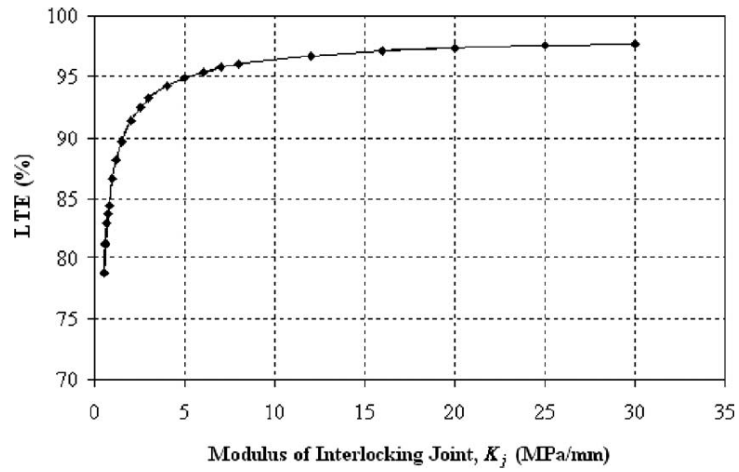
$cw$  = crack width (mm);

$agg$  = nominal size of 20% of coarse aggregates in concrete mix (mm)

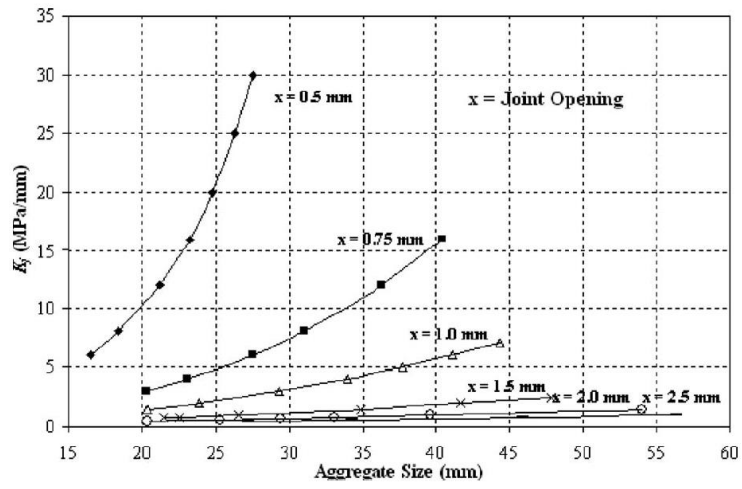
The greater the interlocking modulus, the greater will be the LTE as shown in Figure 2.28a. In Figure 2.28b is possible to observe the crack width effect in the interlock module. For very open cracks ( $cw > 1.0$  mm), the effect of greater aggregates is insignificant.

Jeong and Zollinger (2001) present discussions about the aggregate interlock impact on LTE. For the authors, based on the equations developed by Ianonides and Hammons (1996) and Zollinger *et al.* (1999), the separated effect of dowel bars and aggregate interlock can be seen in Figure 2.29.

In the graph it is visible that great crack or joint widths have bigger impact on load transfer by aggregate interlock (JHA - LTE) than by dowel bars (JD-LTE). This is intuitive because the contact between the crack/joint walls is needed for high LTE levels. The joint/crack total stiffness (J) decreases considerably with crack/joint width following the fall of joint stiffness by interlock (JHA) until the crack/joint has a width of 25 mils (0.65 mm) where the joint becomes equal to the joint stiffness by the dowel bar (JD). Through the theoretical basis it is possible to conclude that for JPCP interlock aggregated accounts for slightly less than 20% of LTE. With very open joints, LTE is around 80%. Several authors and manuals specify this value as a minimum for adequate JPCP behavior, which of course implies the perfect positioning and operation of all dowel bars in the joint. This explains the importance of adequately executed JPCP joints and the need to maintain CRCP cracks tight.



(a)



(b)

Figure 2. 28 – Interlocking modulus versus (a) LTE and (b) aggregate size with different crack widths (MAITRA *et al.*, 2010)

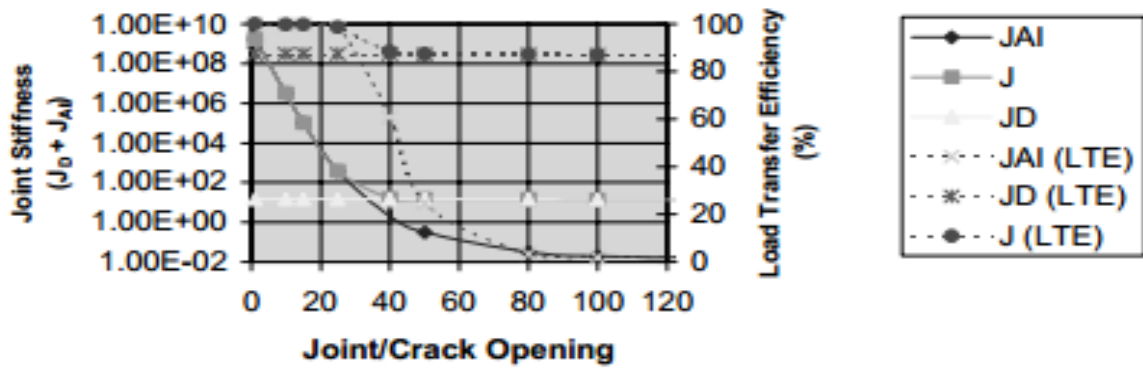


Figure 2. 29 – Load transfer and joint stiffness relation to joint opening (JEONG and ZOLLINGER, 2001)

Figure 2.30, according to Jeong and Zollinger (2001), presents crack width and slab thickness combinations to maintain a level of crack stiffness in order to avoid excessive wear out and loss of aggregate interlock.

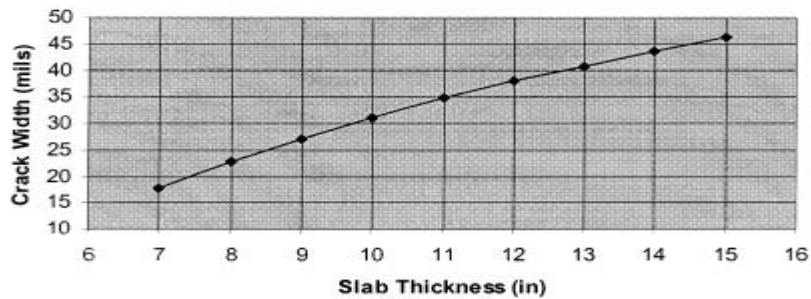


Figure 2. 30 – Suggested crack width for a given slab thickness to achieve an 91% LTE (Jeong and ZOLLINGER, 2001)

It is essential to note that the limits indicated in Figure 2.30 are among the recommendations of the Permanent International Association of Roads Congresses (0.5 mm or 20 mils) and the 1993 AASHTO design guide (1 mm or 40 mils) (PIARC, 1994; AASHTO, 1993).

For LTPP data, the stiffness variations in CRCP cracks and JPCP joints are shown in Figure 2.31. Average stiffness for cracks and joints was 1240 and 730 MPa, respectively.

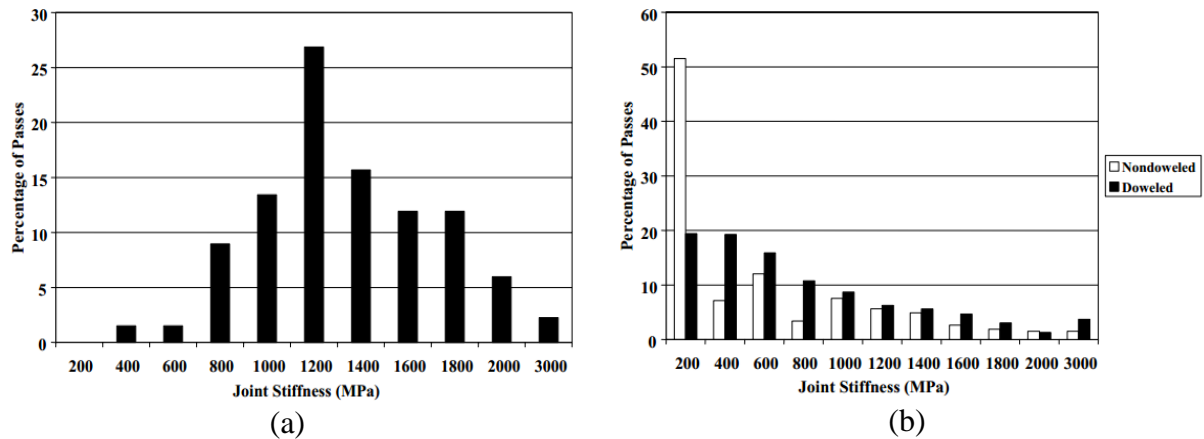


Figure 2.31 - Stiffness distribution of (a) cracks and (b) joints (KHAZANOVICH and GOITLIF, 2003)

The same authors recommend the use of stiffness values for cracks and joints in performance prediction software in accordance with Table 2.2. Values for CRCP cracks are greater than for JPCP joints indicating a more stable physical discontinuity (crack/joint) for the former pavement.

Table 2.2 – Recommended joint/crack stiffness (KHAZANOVICH and GOITLIF, 2003)

Pavement Type	Recommended Ranges (MPa)
Nondoweled JCP	100-500
Doweled JCP	400-1000
CRCP	800-1400

The FWD position also impacts LTE as demonstrated by Khazanovich and Gotlif (2003). In Figure 2.32, results of joints and cracks deflection data from LTPP are presented. When the load is applied in the second slab relative to traffic direction, LTE is lower than when the load is applied to the first slab. This outcome is more influential in JPCP joints than CRCP cracks. The authors could not explain this difference, but the finding is important to standardize the survey methodology. Also notable is the worst performance of JPCP joints when compared to CRCP cracks.

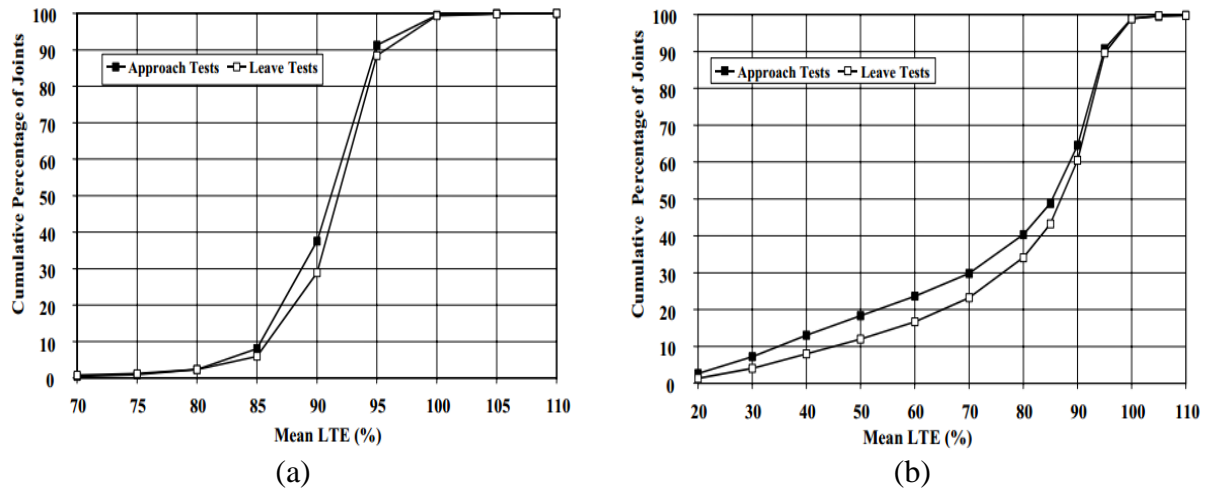


Figure 2. 32 - Distribution of LTE mean values in (a) cracks and (b) joints (KHAZANOVICH and GOITLIF, 2003)

On the variability issue of LTE measured in a same joint or crack, Kazhanovich and Gotlif (2003) stated that LTE variability in cracks is lower than in joints, being both below 2%, which is satisfactorily low. Joints without transfer bars have higher variability of LTE than joints with the device. Also, the variability of LTE in the same section is much larger in JPCPs than in CRCPs (10% *versus* 5 on average). The relationship between joints with and without dowel bars remained equal. Dowel bars, if well positioned, diminish the individual characteristic of the joint avoiding a greater variation of results in the same segment.

As expected the LTPP LTE results show that joints without dowel bars exhibit lower LTE than joints with the device (Figure 2.33). However, an increase in bar diameter does not have the expected effect. Intuitively, a thicker bar would carry a greater load percentage, in addition to having greater contact area with the concrete resulting in higher LTE. Yet Figure 2.34 suggests the lack of influence of bar diameter in LTE.

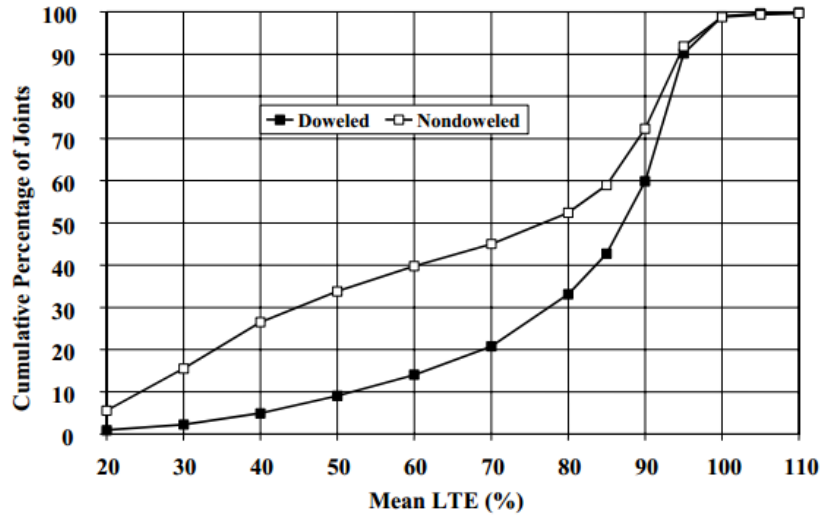


Figure 2. 33 - Doweled and nondoweled joints LTE asses (KHAZANOVICH and GOITLIF, 2003)

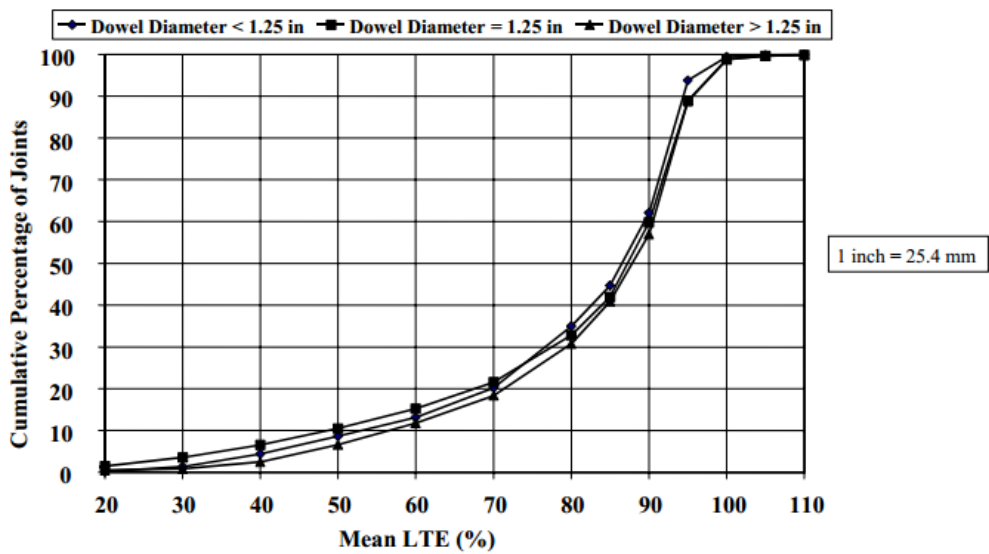


Figure 2. 34 – LTE versus dowel diameter (KHAZANOVICH and GOITLIF, 2003)

The base type seems to have more influence in joints without dowel bars as can be seen in Figure 2.35. Strangely for joints without dowel bar, bases with lean concrete showed the worst LTE performance. It is known that stabilized bases have better performance, however, the high cement content of the lean concrete can increase slab stiffness potentiating warping. Furthermore, the lean concrete shrinkage crack usually appears exactly in the JPCP joint

position. These two factors reduce the LTE of joints without dowel bars. The report does not provide comparative data for CRCP.

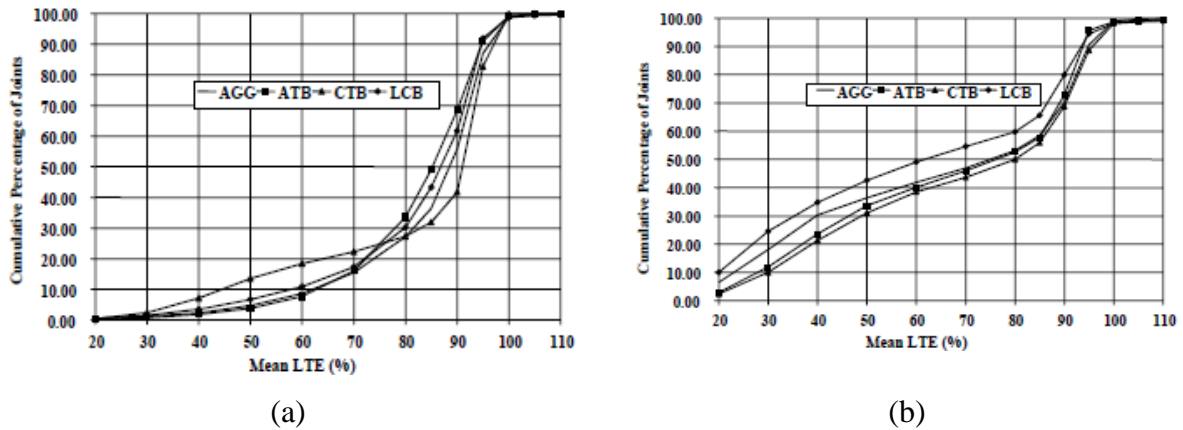


Figure 2.35 – Distribution of joint LTE versus base type in (a) doweled joints and (b) non-doweled joints (KHAZANOVICH and GOITLIF, 2003)

Regarding the subgrade type, there was a slight performance superiority in pavements over fine soils than over coarser soils. This is explained by Equation 4 described before, a stiffer subgrade implies higher  $k$  values that can decrease the dimensionless joint stiffness (AGG \*). In the same report there was no influence of slab thickness in LTE for JPCP and CRCP. The same applies to concrete compression strength. This parameter variations promoted insignificant changes in load transfer.

The effect of longitudinal reinforcement percentage in CRCP also had no influence on LTE. Steel percentages ranging between 0.5 and 0.75% have proven effective in maintaining the average LTE above 90%. The effect of cracks/joints spacing in LTE was virtually nil. It is assumed that the little variability CRCP LTE explain the results. Practically all cracks had an LTE above 90%.

Measurements in the same joint/crack at various periods of the day resulted in higher LTE in the afternoon due to higher temperature causing concrete natural expansion what increases aggregates contact. Consistently, season also influences the LTE, with warmer seasons favoring the joint/crack performance. The authors recommend standardized tests always on

the first morning period for the most critical parameter value. But for tropical countries such as Brazil, where temperature varies widely on the same day from one region to the other, the ideal remains always to record and discuss the results based on the temperature at the exact testing time.

Also, JPCP joints were considered more dependent on the applied load level than CRCP cracks. However, likewise variability, this dependency was small. The study reports for these two experiments that the surveys were conducted in the same locations on different days, but the temperature is not described in the report and certainly varied during the various tests. As mentioned, the parameter has a great effect on LTE (KHAZANOVICH and GOITLIF, 2003).

## **2.4 CRCP design models and equations**

CRCP design methods are based on the design of two basic structural elements: slab thickness and longitudinal reinforcement percentage. Both elements are well-known to be interconnected, but only in the newest MEPDG version, both design models were developed conjointly.

The first CRCP design methods date from 1972 (AASHTO, 1980) and were based on experimental data provided by the AASHO Road Test, which was performed over JPCP sections. The main pavement distress pointed out by the method was the development of cracks in the wheel track. As acknowledged, the CRCP cracking is not considered a distress and therefore the concepts of the first method are not applicable to this structure. The 1984 PCA guide, in the same way, did not involve the CRCP different structural aspects. The analysis of critical stresses and deflections were based solely on JPCP.

The first method to separate CRCP from JPCP was the 1993 AASHTO method. In it considerations of load transfer between cracks were noted. However, the slab thickness design criteria adopted parameters from the AASHO Road Test, i. e., with little regard to CRCP. Only in 2004 with the new MEPDG method that the AASHO Road Test failure criteria were not considered, being replaced by IRI (International Roughness Index) and punchout number. In designing the slab thickness it was assumed that IRI depends on the punchout number that the pavement would present in a given design time. Therefore, punchouts are the main failure

evidence to the most modern design method applied in the US. According to the method original report (ERES, 2004), the punchout mechanism is described as follows:

- 1) With the continuous concrete shrinkage, crack width increases with time;
- 2) With the increase of crack width, LTE decreases. Repetitions of heavy vehicle loads magnifies the LTE drop by aggregate interlock loss;
- 3) A low LTE combined with fine pumping through the base material results in high levels of stress on the slab top at about 1 meter from the edge;
- 4) When the fatigue damage on the slab top becomes greater than the material strength, a longitudinal crack follows, uniting two or more transverse cracks, delineating the punchout.

Ha *et al.* (2012) tested the MEPDG sensitivity to CRCP based on crack width and LTE variation for two construction temperatures. Figure 2.36 shows the results. Pavements built at higher temperatures (100°F = 38°C) have more open cracks and therefore a lower initial LTE. With time this difference worsens to the point where, after 20 years, there is a 20% LTE gap between the two temperatures. However, the authors state that LTPP and Texas Department of Transportation data indicate LTE high values (above 90%) for CRCP with over 30 years of traffic exposure. Tests conducted in the summer and winter in the same cracks showed no differences.

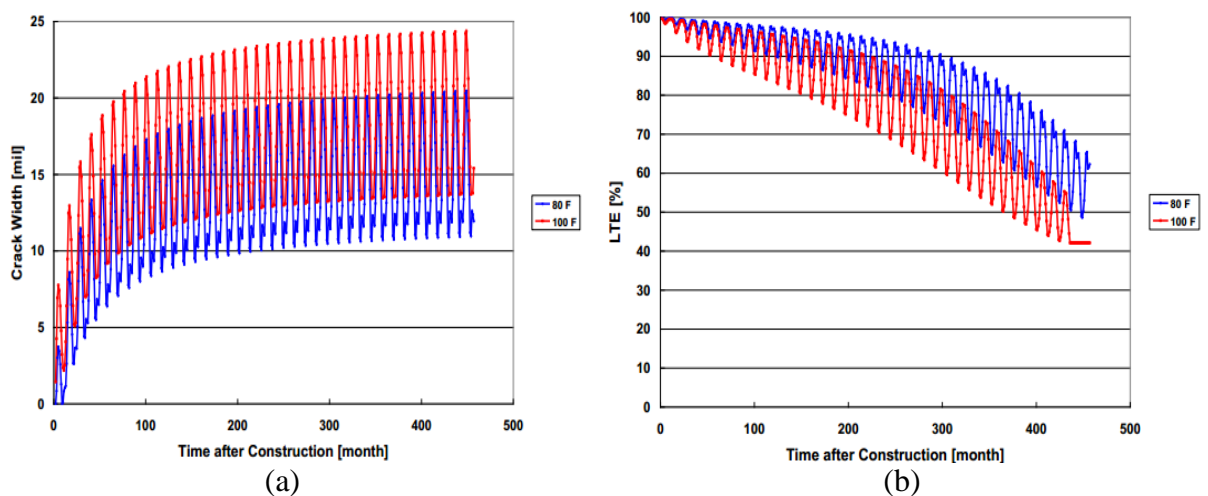


Figure 2. 36 – (a) Crack width and (b) LTE variation over time for two temperature settings  
(HA *et al.* 2012)

This section presents the in-depth analysis of the most well-known CRCP models and design equations. It is important to note that the CRCP state-of-the-art design is shifting away from JPCP design as both structures are quite dissimilar presenting diverse performance criteria and structural components.

#### 2.4.1 1986 AASTHO design guide

The 1986 AASHTO Guide (1986) features three separate mathematical formulations for determining the longitudinal reinforcement percentage, considering the crack spacing (Equation 16), crack width (Equation 17) and the steel stress at the crack (Equation 18):

$$L = \frac{1.32 \left(1 + \frac{ft}{1000}\right)^{6.70} \times \left(1 + \frac{\alpha_s}{\alpha_c}\right)^{1.15} \times (1 + \emptyset)^{2.19}}{\left(1 + \frac{\sigma_w}{1000}\right)^{5.20} \times (1 + P)^{4.60} + (1 + 1000Z)^{1.79}} \quad (16)$$

$$CW = \frac{0.00932 \left(1 + \frac{ft}{1000}\right)^{6.530} \times (1 + \emptyset)^{2.20}}{\left(1 + \frac{\sigma_w}{1000}\right)^{0.491} \times (1 + P)^{4.55}} \quad (17)$$

$$\sigma_s = \frac{47300 \left(1 + \frac{DTD}{100}\right)^{0.425} \times \left(1 + \frac{ft}{1000}\right)^{4.09}}{\left(1 + \frac{\sigma_w}{1000}\right)^{3.14} \times (1 + P)^{2.74} + (1 + 1000Z)^{0.494}} \quad (18)$$

Where,

L = crack spacing (feet);

cw = crack width (inches);

$\sigma_s$  = steel stress (psi);

ft = concrete tensile strength (psi);

$\alpha_s$  = thermal coefficient of steel (inch/inch/°F)

$\alpha_c$  = thermal coefficient of concrete (inch/inch/°F)

$\emptyset$  = rebar diameter (inches);

$\sigma_w$  = wheel load tensile stress (psi);

P = percent steel reinforcement;

Z = concrete shrinkage (inch/inch);

DTD = design temperature drop (°F).

The three parameters are pre-selected according to minimum and maximum criteria and the three equations are solved. The longitudinal reinforcement percentage that best meet the three

parameters is chosen. As pointed out by Ha *et al.* (2012) the model used in the above equations does not consider the temperature variation effects along the slab thickness. The authors also comment that the resulting percentage is low, in a clear evidence that the method prioritizes fewer cracks and larger crack spacing over more tight cracks which nowadays is not considered appropriate.

The AASHTO guide updated version in 1993 determines slab thickness and amount of longitudinal reinforcement. However, the thickness is calculated from equations developed to JPCP with some changes in load transfer coefficients indicating a yet not accurate link to CRCP's very particular aspects.

#### 2.4.2 Other studies

The 1984 design method of the Portland Cement Association (PCA, 1984) – which is widely applied for JPCP design in Brazil (DNIT, 2004) – for CRCP suggests the use of the concrete slab thickness calculated for JPCP when the design data traffic is identical. The guide advises that while CRCP stresses are smaller (considering an ideal spacing between cracks) than JPCP ones for the same load, the former suffers from higher deflections in corners and edges. This information was assessed with a study using the finite element software JSLAB, according to PCA (1984) - information on this simulation are not clearly detailed in the guide. Besides the information missing in the guide, it is common knowledge in the international concrete pavement community that the PCA methods (1966 and 1984) are problematic due to the lack of temperature and temperature gradient effect on design (BALBO, 2003).

The Illinois Department of Transportation guide specifies an empirically equivalent thickness for CRCP of 80% of the thickness calculated by mechanical-empirical principles to JPCP which again presents problems due to the association between two different structures. However, the state is developing an update of the guide based on MEPDG results. (BEYER and ROESLER, 2009).

The study developed by Khazanovich, *et al.* (2001) used the equivalent concept to decrease the number of variables to be tested without impairing the experiment. The equivalent concept for slab thickness developed by Ioannides and Karokevics (1992), was used to solve Equation

19. It should be noted that Equation 19 is valid only for the application of a vehicle load without consideration of environmental effects.

$$\sigma_{PCC} = \frac{h}{h_{eff}} \sigma_{eff} \quad (19)$$

where,

$\sigma_{PCC}$  = Top PCC stresses;

h = Slab thickness;

$h_{eff}$  = Equivalent slab thickness;

$\sigma_{eff}$  = Top stress in the equivalent slab.

The concept of equivalent temperature linear distribution was introduced by Thomlinson (1940) and most recently updated by Mohamed and Hansen (1997). The concept may be applied as shown by Khazanovich *et al.* (2001) to estimate the tension at the slab top following Equation 20.

$$\sigma_{PCC} = \frac{h}{h_{eff}} \sigma_{eff} - \frac{E}{1-\mu} \alpha \times \left[ \frac{T_{top} + T_{bot} - 2T_m}{3} + \frac{h_{eff}^3 - h^3}{2h_{eff}^3} (T_{top} - T_{bot}) \right] \quad (20)$$

where,

$\sigma_{PCC}$  = Top PCC stresses;

h = Slab thickness;

$h_{eff}$  = Equivalent slab thickness;

$\sigma_{eff}$  = Top stress in the equivalent slab;

$\mu$  = PCC Poisson's ratio;

$\alpha$  = PCC coefficient of thermal expansion;

E = PCC modulus of elasticity;

$T_m$  = Temperature at half-height;

$T_{top}$  = Temperature at PCC top;

$T_{bot}$  = Temperature at PCC bottom.

The work also assigns concepts developed by Korenev and Chernigovskaya (1962, Apud KHAZANOVICH *et al.*, 2001) for the combined effects of vehicular and environmental loads on a given geometry slab. Equation 21 governs the structural equivalence concept, as follows:

$$\sigma_{PCC1} = \frac{h_1^2 h_2 \gamma_1}{h_{eff}^3 \gamma_2} \sigma_{PCC2} - \frac{E_1}{1-\mu_1} \alpha_1 \times \left[ \frac{T_{top} + T_{bot} - 2T_m}{3} + \frac{h_{eff}^3 - h^3}{2h_{eff}^3} (T_{top} - T_{bot}) \right] \quad (21)$$

where,

h = slab thickness;

$\gamma$  = slab unit self-weight;

1 and 2 = slab1 and 2, respectively.

As Figure 2.37 shows, there is a perfect correlation of the equivalency model with simulations from ISLAB2000.

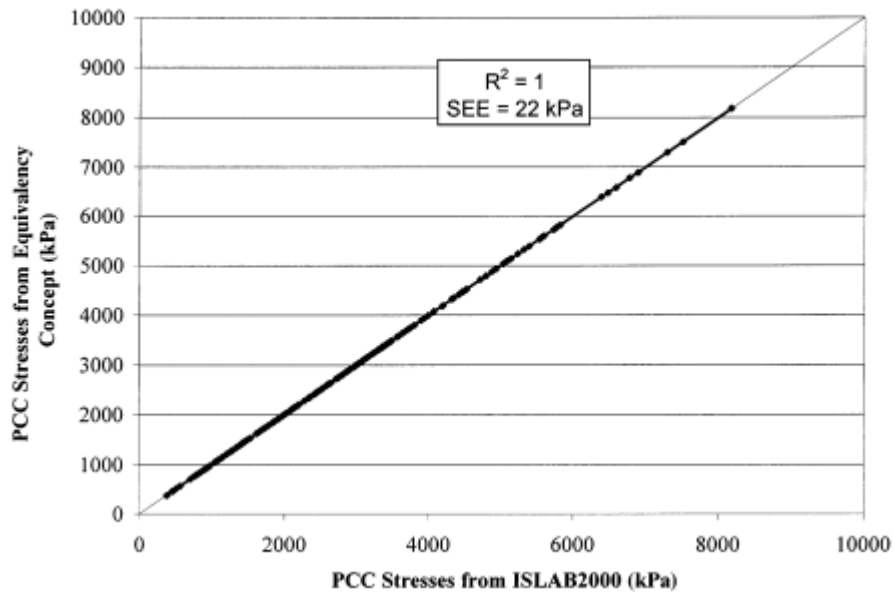


Figure 2. 37 – CRCP top surface stresses obtained from ISLAB2000 and by using equivalent structure concept (KHAZANOVICH *et al.*, 2001)

Selezneva *et al.* (2004) calculated the average crack width at steel depth which is determined based on the findings of Reis *et al.* (1965) using Equation 22 which correlates crack spacing with crack width.

$$cw = L(\epsilon_{shr} + \alpha \Delta T) - L \frac{C_2}{E} \left[ \frac{LU_m P}{c_1 \phi} + C \sigma_0 \left( 1 - \frac{2s_d}{h} \right) + \frac{L}{2} f \right] \quad (22)$$

L = crack spacing (mm);

$\epsilon_{shr}$  = unrestrained concrete drying shrinkage at the steel depth;

$\alpha$  = concrete coefficient of thermal expansion (CTE) ( $^{\circ}\text{C}^{-1}$ );  
 $\Delta T$  = drop in PCC temperature at the steel depth;  
 $c_1$  = first bond stress coefficient;  
 $c_2$  = second bond stress coefficient;  
 $E$  = concrete modulus of elasticity (kPa);  
 $P$  = percent of longitudinal reinforcement (fraction);  
 $\phi$  = steel bar diameter (mm);  
 $U_m$  = peak bond stress (kPa);  
 $h$  = slab thickness (mm);  
 $sd$  = steel depth (mm);  
 $f$  = base friction coefficient;  
 $C$  = Bradbury correction factor for slab size;  
 $\sigma_0$  = Wastergaard nominal environmental stress factor (kPa);

Selezneva *et al.* (2004) also based on Reis *et al.* (1965) developed Equation 23 used to predict the mean transverse crack spacing:

$$L = \frac{(f_t - f_\sigma)}{\frac{f_t}{2} + \frac{U_m P}{c_1 d_b}} \quad (23)$$

where,

$f_t$  = concrete tensile strength (kPa);  
 $f_\sigma$  = maximum concrete stress at steel depth (kPa);  
 $P$  = percent of longitudinal reinforcement;

The simulation of a known load over a CRCP lane is illustrated in Figure 2.38. It can be seen that the location of maximum tensile stresses on the surface is in the middle of the load application points (axis). This, in a single lane, represents the distance of 1 to 1.4 m from the lane edge which thus confirms the distance to the vast majority of longitudinal fatigue cracks in punchouts, as reported by Selezneva *et al.* (2004).

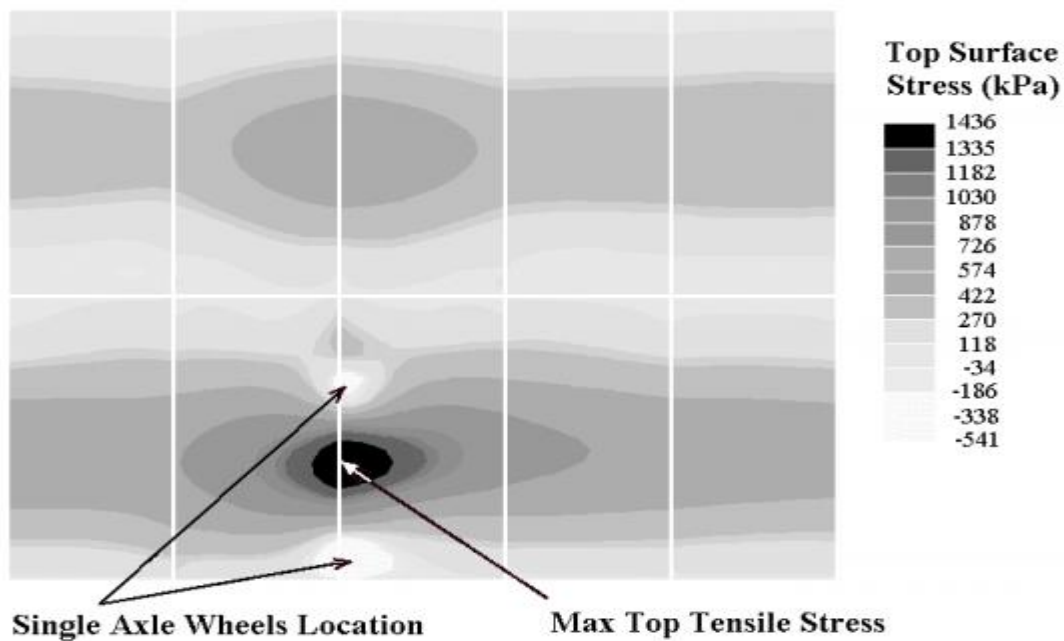


Figure 2.38 – Stress output example of mechanist model (SELEZNEVA *et al.*, 2004)

#### 2.4.3 MEPDG

The MEPDG (USA) offers a choice of three levels of input data: Level 1 requires properties and parameters of the materials acquired through field tests or with the same material to be used in future construction; Level 2 also requires test results, but with a lower degree of precision, accepting also correlations between variables; finally, Level 3 already provides the initial information from an extensive internal database.

Elfino *et al.* (2011) conducted a very practical study to demonstrate the differences between the results of the projects designed with the three levels and also comparing the original project designed with the 1993 AASTHO method. The results show a 10-year difference in the durability of the pavement when MEPDG level 1 is applied compared with the original design (AASTHO, 1993). The difference from level 1 to level 3 was a 15-year longer durability when the first level is used. Intuitively, the higher the knowledge level of structural materials and concepts that will be used, the higher the pavement quality. However, the authors did not write about the reliability coefficients which are used at each level. Furthermore, various projects are designed years in advance of the construction and this can compromise the quality of tests.

The MEPDG calculation according to ARA (2003) is presented in the following sequence to analyze which are the most fundamental design criteria adopted in this method. However, it is known in the technical community that the models developed in ARA (2003) were modified prior to their inclusion in the MEPDG guide. Nonetheless, the MEPDG is closed and no information could be found on those modifications. The estimation of crack spacing is determined by Equation 24:

$$L = \frac{f_{t28} - C\sigma_0 \left(1 - \frac{2S_d}{h}\right)}{\frac{f}{2} + \frac{U_m P}{C_1 \phi}} \quad (24)$$

where,

L = crack spacing (in.)

C = the Bradbury coefficient;

$\sigma_0$  = Westergaard's nominal stress factor;

$S_d$  = steel depth (in.)

h = concrete slab thickness (in.)

f = base friction coefficient;

$U_m$  = peak bond stress (psi);

P = steel percentage (fraction);

$C_1$  = first bond stress coefficient;

$\phi$  = steel bar diameter (in.)

The Bradbury coefficient corrects the curling stress for finite slabs. The Bradbury coefficient is calculated with equations 25 and 26, as follows:

$$C = 1 - \frac{2\cos\lambda\cosh\lambda(\tan\lambda + \tanh\lambda)}{\sin 2\lambda + \sinh 2\lambda} \quad (25)$$

$$\lambda = \frac{l}{\ell\sqrt{8}} \quad (26)$$

where,

l = slab length (in.);

$\ell$  = radius of relative stiffness (in.);

The Westergaard Nominal stress factor is calculated by Equation 27:

$$\sigma_0 = \frac{E\varepsilon_\Delta}{2(1-\mu)} \quad (27)$$

where,

E = concrete modulus of elasticity (psi);

$\varepsilon_\Delta$  = equivalent total strain difference between slab surface and bottom;

$\mu$  = concrete Poisson's ratio;

The equivalent total strain difference between slab surface and bottom is calculated by Equation 28.

$$\varepsilon_\Delta = \alpha\Delta t_{eqv} + \varepsilon_\infty\Delta(1 - rh^3) \quad (28)$$

where,

$\alpha$  = concrete coefficient of thermal expansions (1/°F);

$\Delta t_{eqv}$  = equivalent temperature (°F);

$\varepsilon_\infty$  = concrete ultimate shrinkage (strains);

$\Delta(1 - rh^3)$  = relative humidity difference between slab surface and bottom;

The equivalent temperature is calculated by Equations 29 and 30.

$$\Delta t_{eqv} = \frac{R_0}{2CF} \left( 1 - e^{-\frac{h}{12}\sqrt{\frac{2\pi}{y^2}}} \right) \quad (29)$$

$$CF = 1 + 0.116h^{3/2} - 0.565h + 0.685h^{1/2} \quad (30)$$

where,

$R_0$  = effective range in temperature

y = concrete thermal diffusivity (ft<sup>2</sup>/day);

The effective temperature ranges for the minimum seasonal ambient temperature are displayed in Table 2.3.

Table 2. 3 – Effective temperatures ranges (ARA, 2003)

Minimum Seasonal Ambient Temperature (°F)	R <sub>0</sub>
< 40	21.5
40 to 60	23.4
60 to 80	25.7
> 80	30.1

The relative humidity difference between the slab surface and bottom is calculated through Equation 31. It must be noted that this equation was developed for a wet/freezing climatic zone with an ambient humidity range of 50 to 95 %.

$$\Delta(1 - rh^3) = 0.2(0.0028h^2 - 0.107h + 1.4292) \quad (31)$$

The peak bond stress ( $U_m$ ) is calculated with Equations 32 and 33.

$$U_m = 0.0020k_1 \quad (32)$$

$$k_1 = 117.2f_{c28} \quad (33)$$

where,

$k_1$  = bond slip coefficient;

$f_{c28}$  = concrete compressive strength at 28 days (psi);

The first bond stress coefficient is calculated by Equation 34 or 35 depending on the crack spacing seed, as follows:

$$C_1 = L_{seed} \text{ if } L - L_{seed} < 0.01 \quad (34)$$

$$C_1 = 0.577 - 9.499 \times 10^{-9} \frac{\ln \varepsilon_{tot-sd}}{\varepsilon_{tot-sd}^2} + 0.00502L_{seed}(\ln L_{seed}) \text{ if } L - L_{seed} > 0.01 \quad (35)$$

where,

$L_{seed}$  = seed crack spacing (in.);

$\varepsilon_{tot-sd}$  = total maximum strain at steel depth (strains).

The total maximum strain at steel depth is calculated by Equation 36:

$$\varepsilon_{tot-sd} = \Delta T_{sd} \alpha + \varepsilon_{shr} \quad (36)$$

where,

$\Delta T_{sd}$  = maximum concrete temperature difference from the concrete set temperature at steel depth (°F);

$\varepsilon_{shr}$  = unrestrained concrete drying shrinkage at steel depth (strains);

The maximum concrete temperature difference from the concrete set temperature at steel depth is determined following Equation 37:

$$\Delta T_{sd} = T_{set} - T_{steel,min} \text{ if } T_{set} > T_{steel,min}, \text{ else } 0. \quad (37)$$

where,

$T_{set}$  = concrete set temperature at steel depth (°F);

$T_{steel,min}$  = lowest average seasonal temperature at steel depth (°F);

The concrete set temperature at steel depth is the temperature at which the concrete layer shows zero thermal stress. This value is calculated by Equations 38 and 39. The allowable temperature range for the use of these expressions is 60 to 120°F.

$$T_{set} = 0.20225CCH + T_{cons} \quad (38)$$

$$H = -0.0787 + 0.0007T_{cons} - 0.00003T_{cons}^2 \quad (39)$$

where,

CC = mixture cement content (lb/yd<sup>3</sup>);

H = heat of hydration (KJ/g);

$T_{cons}$  = the average seasonal ambient temperature for the construction period (°F).

The unrestrained concrete drying shrinkage at steel depth is calculated by Equation 40, as follows:

$$\varepsilon_{shr} = \varepsilon_{\infty} \left[ 1 - \left( \frac{rh}{100} \right)^3 \right] \quad (40)$$

where,

$\varepsilon_{\infty}$  = concrete ultimate shrinkage (strains)

rh = relative concrete humidity at steel depth (%)

According to ARA (2003) the crack width at steel depth is calculated by Equation 41, as follows:

$$cw = \max \left[ L \left( \varepsilon_{shr} + \alpha \Delta T_{sd} - \frac{c_2 f_\sigma}{E} \right) 1000 C_c, 0.001 \right] \quad (41)$$

where,

$cw$  = crack width (mils);

$c_2$  = second bond stress coefficient;

$f_\sigma$  = maximum longitudinal tensile stress in the concrete at steel depth (psi);

$C_c$  = crack width calibration constant (1.0)

The second bond stress coefficient is determined by Equations 42 to 45:

$$c_2 = a + \frac{b}{k_1} + \frac{c}{c_s^2} \quad (42)$$

$$a = 0.7606 + 1772.5 \varepsilon_{tot-sd} - 2 \times 10^6 \varepsilon_{tot-sd}^2 \quad (43)$$

$$b = 9 \times 10^8 \varepsilon_{tot-sd} + 149486 \quad (44)$$

$$c = 3 \times 10^9 \varepsilon_{tot-sd}^2 - 5 \times 10^6 \varepsilon_{tot-sd} + 2020.4 \quad (45)$$

The maximum concrete longitudinal tensile stress at steel depth is calculated by Equation 46

$$f_\sigma = \frac{LU_m P}{c_1 \phi} + \sigma_{env} + \frac{L}{2} f \quad (46)$$

where,

$\sigma_{env}$  = environmental tensile stress (psi)

$f$  = base friction coefficient.

The environmental tensile stress is calculated by Equation 47:

$$\sigma_{env} = C \sigma_0 \left( 1 - \frac{sd}{h} \right) \quad (47)$$

where,

$C$  = Bradbury coefficient;

$\sigma_0$  = Westergaard nominal stress factor (psi);

$sd$  = steel depth (in.)

$h$  = slab thickness (in.)

The critical top stresses are computed with a Finite element model in a location 1.21 m from the pavement edge. Crack width enables the calculation of crack stiffness with Equation 11 and then LTE is calculated applying Equation 10 using crack stiffness. As crack width is a function of crack spacing as seen in Equation 41 it is notable that a great concern of the method relies in the crack spacing and crack width determination.

Also, it is possible to observe that the current version of MEPDG brings considerable improvements incorporating a punchout prediction model based on fatigue damage associated with the formation of longitudinal cracks between closely spaced transverse cracks (less than 0.8 m crack spacing). However, according to Jung *et al.*, (2012), the punchout model does not consider directly the base erosion as a variable. The authors state that the MEPDG provides a greater number of punchouts when the subgrade reaction modulus (k) is increased due to the punchout the model being analogous to fatigue longitudinal crack development. The consequence of this guide simplification is that very stiff bases (high value of k) may present more predicted punchouts.

It is well established in the technical community that the quality and performance of the base material has a direct effect on the development of punchouts. In accordance to this, the authors developed an empirical model to predict the erosion width of the base layer. This model is described in Equation 48.

$$\epsilon = AGE \frac{(-7.4+0.342P_{200}+1.557_{berod}+0.234_{precip})}{12} \quad (48)$$

where,

$\epsilon$  = maximum width of eroded base or subbase measured inward from the slab edge during 20 years (in.)

AGE = pavement age (month);

$P_{200}$  = percentage of subgrade soil passing the No. 200 seive

precip = mean annual precipitation (in);

berod = base erosion index based on Jeong and Zollinger (2001) [1 for LCB. 2 for CTB with 5% cement, 3 for ATB and CTB with <5% cement, 4 for GRA with 2.5% cement and 5 for untreated GRA].

The fatigue model developed by Jung *et al.* (2012) is presented in Equations 49 e 50, as follows:

$$Fd = \sum_i \frac{N_i}{N_{fci}} \quad (49)$$

$$N_{fci} = 10^{2\left(\frac{MR_i}{\sigma_i}\right)^{1.2} + 0.4371} \quad (50)$$

where,

$Fd_i$  = maximum accumulated fatigue damage for the  $i$ th time increment;

$N_i$  = number of ESALs applied during time increment  $i$ ;

$N_{fci}$  = number of allowable loads to failure for time increment  $i$ ;

$MR_i$  = modulus of rupture during time increment  $i$  (psi);

$\sigma_i$  = design stress for conditions over time increment  $i$  (psi).

Friction between slab and base has a direct impact on crack spacing as comment by Rao *et al.* (2004). Table 2.4 shows the variation of the slab/base friction coefficient for different materials. These data are the result of backcalculation of values indicated by the AASTHO Guide (1993) based on crack spacing observations in real CRCP.

Table 2. 4 – Backcalculated friction values (RAO *et al.*, 2004)

Base Type	Mean friction	Min. friction	Max. Friction
Asphalt Treated	7.6	2.5	15.0
Cement Treated	9.5	3.5	23.0
LCB	8.5	3.0	20.0
Granular	2.5	0.5	4.0
Fine-grained soils	1.15	0.5	2.0

Kohler and Roesler (2006) modified Equation 41 in order to determine the crack width at any slab depth. To this end, the authors considered that concrete stresses caused by the reinforcement movement restrictions are uniform along the slab thickness. A new expression (Equation 51) where  $z$  is the desired depth is presented below:

$$cw(z) = CcL \left\{ \varepsilon_{shr} + \alpha \Delta T_z - \frac{c_2 f \sigma}{E} \left[ \frac{LU_m P}{c_1 \emptyset} + C \sigma_0 \left( 1 - \frac{zz}{h} \right) + \frac{L}{s} f \right] \right\} \quad (51)$$

#### 2.4.4 2008 AASTHO Guide

The update of the AASHTO design method made available in 2008 (AASHTO, 2008), incorporated some factors that were not fully addressed in the 1993 guide (AASHTO, 1993). Among such factors include the materials' durability, positioning and amount of longitudinal reinforcement, base layer erosion and different construction methods.

The two fundamental criteria of CPRP evaluation according to the guide are the punchout number and ride quality - international roughness index (IRI). Concluding the design, the design engineer stipulates the maximum number of desirable punchouts at the end of the pavement life (usually 6 to 13 per mile). It is also observed the value of IRI in any design time. For most US transportation departments CRCPs, the value of IRI should be below 2.7 m/km. The guide also incorporates parameters such as cracks spacing between 0.9 and 1.8 m and crack width smaller than 0.5 mm for the design of a CRCP with adequate performance.

The AASHTOWare ME Pavement Design was created from the development of MEPDG resulting from project NCHRP 1-37A (2004) described in the above section and AASHTO Manual of Practice (AASHTO, 2008). Again, there were considerable alterations in models from project NCHRP 1-37A (2004) to the ME Pavement design that are not computed in any available document.

### 2.5 Experimental short CRCP sections (current research)

The experimental CRCP sections were constructed (Figure 2.39) between July and September 2010, during the dry winter season in the São Paulo campus of University of São Paulo. Geographically, the sections are located at parallel -23°33'01" (South American Datum 69). As the initial goal was to simulate a bus stop, the sections length was 50 meters – short compared to traditional CRCP that can reach more than 400 m, depending on the continuous concreting process. There is no anchorage at the sections end, giving freedom to the longitudinal displacement of the concrete slabs, as it would be the case of bus stops in urban corridors (without transition slab or anchor).



(a) Longitudinal reinforcement (Section 1)



(b) Concreting (Section 2)



(c) Surface texturing (Section 1)



(d) Curing (Sections 3 and 2)



(e) Transaction joint between Section 1 and the interlocked pavement



(f) Sections in operation (Section 4)

Figure 2. 39 – Construction details of the experimental short CRCP sections

The daily traffic (unidirectional) consists in about 378 buses and 145 medium sized trucks and 750 cars. The old asphalt pavement, which was built almost 40 years before the CRCP construction, was completely removed due to severe rutting and cracking distresses. The sections have constant width of 5.5 m and are composed of 240 mm thick concrete slabs. The thickness was defined based on traffic and also with international experience of using this pavement on urban streets. The concrete designed tensile strength was set at 4.5 MPa (28 days); the commercially available concrete employed granite aggregates and cement content of 350 kg/m<sup>3</sup>.

The only difference between sections is the longitudinal reinforcement percentage as shown in Table 2.5. All layers described in Table 2.5 were new layers constructed for the experimental section.

Table 2. 5 –Short experimental CRCP design features

	Section 1	Section 2	Section 3	Section 4
Concrete Slab (mm) *	240	240	240	240
Asphalt Base (mm) *	60	60	60	60
Dry-Macadam Sub base (mm) *	300	300	300	300
Steel Reinforcement (%)	0.57	0.44	0.77	0.67

\* Layer thickness

The transverse reinforcement consists of bars spaced 0.9 m apart, with 20 mm diameter bars. All applied steel was the CA-50 type. The design decision of different steel percentages was made with reference to the CRCP mentioned in the technical literature. It is known that greater steel amount causes more cracking, decreasing the spacing which can be harmful due to increase in cracks' intersecting potential (MA and MCCULLOUGH, 1978; VERHOEVEN, 1992; KIM *et al.*, 1998). However, high reinforcement percentages also provide tighter cracks (ZOLLINGER, 1989; SUH and MCCULLOUGH, 1994; KOHLER and ROESLER, 2006). As previously discussed, in the early 1990s there was a shift in the focus of CRCP performance analysis; before, most of the design was based on cracks spacing (ideally between 0.9 and 2.4 m), thus, the steel percentages were 0.5 and 0.6%, however it was observed that although cracks were more well-spaced, the load transfer between them was

unsatisfactory leading to stresses accumulating on the edge causing longitudinal cracks due to fatigue. Therefore, the design focus was aimed to minimize crack width (maximum 1 mm) using greater steel percentages (between 0.7 and 0.8%).

The longitudinal reinforcement position is also a point of great interest; it is known when the steel is nearer the surface cracks are tighter and load transfer is higher. However, researchers indicate a minimum coating 76 mm to prevent corrosion by water infiltration (GHARAIBEH *et al*, 1999). Regarding the steel loss by oxidation, Verhoeven (1992) found no significant corrosion in an extensive CRCP survey. For the short CRCP, the designed steel depth was 110 mm from the surface, 10 mm from the slab half-height. More detailed construction practices can be found in Balbo *et al* (2012) and in Salles (2014).

\

### **3. ULTRASONIC TESTING**

This chapter describes the whole process of the non-destructive ultrasonic testing of the experimental short CRCP. Survey methodology, data processing and analysis are presented. All figures and tables presented in this chapter, if not referenced, are result of the current study.

#### **3.1 Ultrasonic data collection procedure**

For steel characteristics and slab thickness the readings were made on five measuring stations per section. Stations were distanced 5 meters from the edge (stations 1 and 5) and 10 meters from each other (2, 3 and 4). At each station two lines of measurements (A and B) were drawn and at each line readings were made at the right (40 mm from longitudinal edge), center and left (40 mm from longitudinal joint) positions. Lines A and B were distanced at 40 mm to avoid placing the device above a transversal bar where it would be difficult to measure the slab thickness. The stations number and the position of the A and B lines were defined considering the traffic direction on each section (arrows in Figure 3.1). Firstly, readings were held in the transversal direction in order to find the longitudinal bars position, which then were marked on the pavement surface. Three readings were made for all locations moving the device (MIRA) 60 mm after each reading. Subsequently to this, the thickness was measured in between bars in the longitudinal direction. Three readings were made beginning at the MIRA center and moving it forward and back for the next two readings. Thickness measurements locations were marked with an X and a V for the measurements lines A and B, respectively. New calibrations were made whenever the measurement changed from steel depth and position to slab thickness. Calibration consisted of a measurement to determine the shear wave velocity at the slab surface in each location. It is recommended a new calibration for each new set of readings. Figure 3.1 displays the measurement stations and locations.

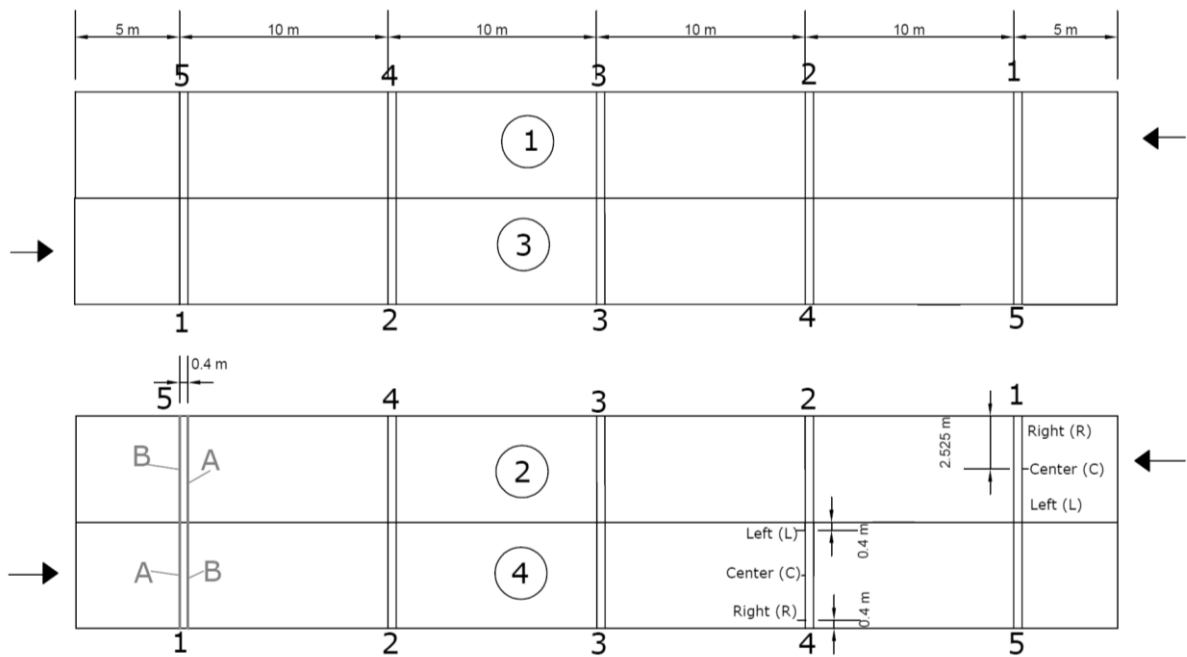


Figure 3.1 – Steel depth and location and slab thickness measuring stations

For visible cracks, measurements were taken regarding the March, 2015 crack map (Figure 3.2). Measurements were held in every visible crack in three positions: right (40 mm from the longitudinal edge), center and left (40 mm from the longitudinal joint). There readings per position were made, moving the device 45 mm from one reading to the other. One crack per section received a more in-depth evaluation with five readings on each position. Cracks F1.3, F2.3, F3.6 and F4.7 were selected for this procedure. Calibration was performed every time the device was moved to a new crack.

Non-visible cracks evaluation was performed in panels between two cracks or between crack and transversal edge. The device was placed longitudinally at the lane center and successive readings took place every 90 mm. Calibration was performed for every panel and whenever the images showed unreliable reflections near the surface. Those unreliable reflections (strong red reflections) could be seen as a change in the concrete properties. As the non-visible cracks measurements were taken in straight lines through great lengths such changes were expected to happen.

The device operation was uncomplicated and the readings and calibrations were quickly done (approximately 2s for each reading) making it a productive testing. On two occasions over the

four days of survey, the Wi-Fi signal between the computer and the MIRA device was lost making it necessary to restart the device.

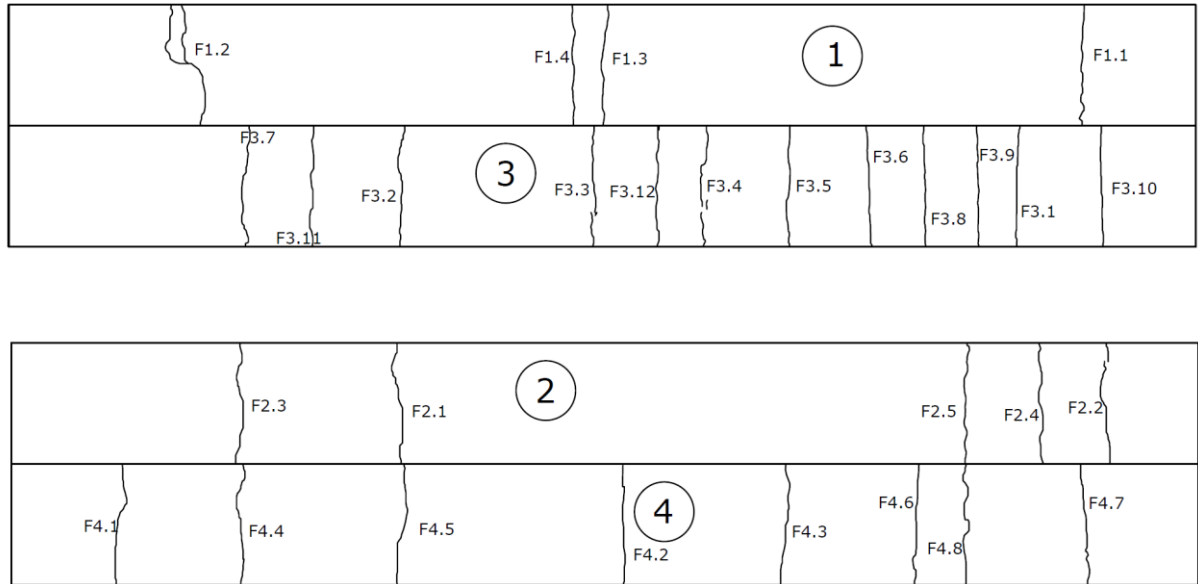


Figure 3. 2 – Short CRCP March, 2015 crack map

### 3.1.1 Ultrasonic data processing

Ultrasonic readings were processed using the technique for ultrasonic linear array evaluation developed by Hoegh (2013) where a much more detailed approach can be found. In brief, the ultrasonic time-history data provided by MIRA’s 45 transducers pairs at various incident angles was processed using an adaptation of the instantaneous amplitude-based synthetic aperture focusing technique (SAFT). The SAFT is applied in the MIRA software to provide 2D images of the readings; however the algorithm adaptations performed by Hoegh (2013) were able to improve the original images. The information received by transducers pairs at spatially diverse locations allowed for reconstruction of the relative reflectivity amplitude within the region of interest (ROI) creating a B-scan of the area by addressing a specific reflection color for each level of amplitude showed by the ultrasonic signal. For this, information on the time of flight of the signal emitted by a transducer, going through the target (reflection point) and being received by another transducer (Figure 3.3) and shear wave velocity for all transducers pairs were applied in Equations 52 and 53.

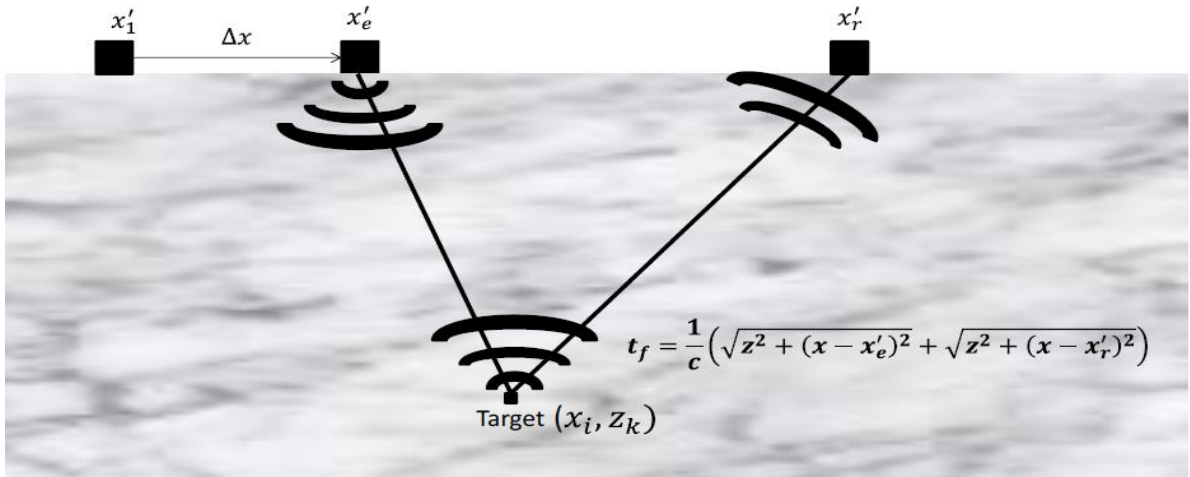


Figure 3. 3 – Illustration of MIRA linear array and signal time of flight equation (HOEGH and KHAZANOVICH, 2015)

$$\hat{o}_{i,k} = \sum_{e=1}^{T-1} \sum_{r=e+1}^T A(x_r, x_e, x_i, z_k) \Psi_{e,r}(x_i, z_k) \quad (52)$$

$$\Psi_{e,r}(x_i, z_k) = s \left( x_r, x_e, \frac{1}{V} \left( \sqrt{z_k^2 + (x_i - x_e)^2} + \sqrt{z_k^2 + (x_i - x_r)^2} \right) \right) \quad (53)$$

Where,

$\hat{o}_{i,k}$  = the image reflectivity of each position inside the ROI;

T = number of transducers positions;

e, r = index of the emitting and receiving transducers;

V = shear wave velocity;

i, k = index of the ROI's horizontal and vertical positions;

s = the response magnitude at the evaluated time for given transducers;

A = apodization coefficient, which is related to the various incident angles of the signal (BALMER, 1992 apud HOEGH and KHAZANOVICH, 2015).

Therefore, the shear wave velocity is applied to transform the time of flight information into distance information (depth). This distance is the depth of the reflection point in the ROI. It must be noted that this implies in a simplification of the reconstruction method in both the original SAFT and in the adaptation performed by Hoegh (2013) as shear wave velocity is estimated only in the slab surface but applied for image reconstruction through all the slab thickness.

The Hilbert transform is used to calculate instantaneous attributes of a time series being of special interest to estimate amplitude and frequency. The Hilbert transform, of a given function  $\kappa(z)$ , is defined by Equation 54 and the complex analytic signal  $Z(z)$  is given by Equation 55. The complex analytic signal is applied to essentially filter out all the negative signal frequencies from the original signal frequency.

$$HT(z) = \frac{1}{\pi} P \int_{-\infty}^{\infty} \frac{\kappa(s)}{z-s} ds \quad (54)$$

Where,

P = principal value of the singular integral

$$Z(z) = \kappa(z) + jHT(z) \quad (55)$$

To allow for the instantaneous amplitude determination, the absolute value of the complex signal ( $Z$ ) is estimated for each horizontal coordinate of the SAFT reconstruction (Equation 52) using Equation 56:

$$\hat{\sigma}^{IA}(x, z) = \sqrt{(\hat{\sigma}(x, z))^2 + \left(\frac{1}{\pi} P \int_{-\infty}^{\infty} \frac{\hat{\sigma}(x, s)}{z-s} ds\right)^2} \quad (56)$$

Where,

$\hat{\sigma}^{IA}(x, z)$  = instantaneous amplitude-based SAFT reconstruction

The SAFT B-scan procedure was utilized in this thesis concerning three basic applications:

- Concrete slab thickness: in order to identify the division of two materials (two layers), the highest reflection captured by MIRA is considered. As slab and base materials are expected to have diverse properties, the shear wave velocity propagation in such materials must be different. The simple geometry of pavement structures also helps the depth identification of such reflections. However, according to Hoegh (2013), the accuracy of this procedure highly depends on the quality data for the shear wave velocity;
- Reinforcement identification: alterations in the acoustic impedance inside the material are automatically recorded by the analytical procedure. As the geometry of the

reinforcement is usually known, it is rather simple to identify the steel bars inside the concrete;

- Distresses: differently from the reinforcement, distresses are unpredictable in both shape and position. Most distresses are identified by strong unshaped reflections and by the shadowing effect they have on the slab\base reflection. As the impedance changes are computed for areas above the slab\base reflection, the reflection between layers is not observable, indicating a heterogeneity problem within the material.

Shear wave velocity which is used in the software calibration and B-Scan reconstructions as previously explained was determined using the impulse time histories by knowing the transducers spacing and the time of direct arrival pulse (Figure 3.4). As the direct arrival pulse is measured at the concrete surface, the shear wave velocity is calculated only in that position. Consequently, as mentioned before, the shear wave velocity used in the reconstructions is an approximation of the real shear wave velocity in each and every location inside the ROI. Equation 57 can be applied in the redundant information provided by the 45 transducers pairs to estimate shear wave velocity.

$$V = \frac{(x_{ij} - x_{ik})}{(t_{i,j} - t_{ik})} \quad (57)$$

Where V is the calculated shear wave velocity, i, j and k are the transducers 1 through 10, x is the distance between transducers i, j and k and t is the time of the direct arrival pulse for the time history related to transducers i, j and k.

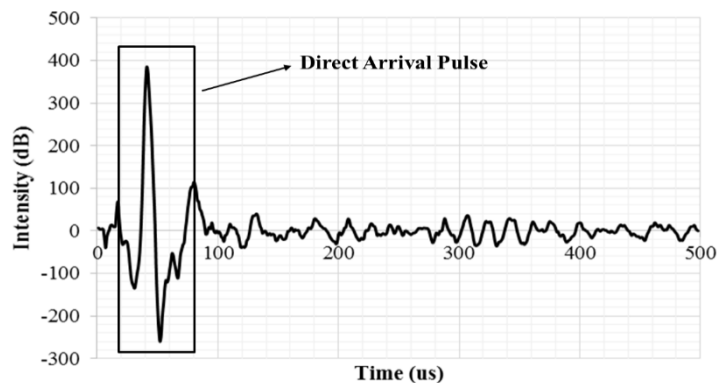


Figure 3. 4 – Direct arrival pulse in a Section 2 thickness measurement

By plotting all the values for  $x_{ij}$  and  $t_{ij}$ , a best fit linear trendline discloses the actual shear wave velocity, removing the time delay from all points because it is a constant for all transducers. Figure 3.5 presents an example of this calculation. In this case the shear wave velocity is 2.438 m/ms. Shear wave velocity is also automatically calculated by the MIRA software during calibration.

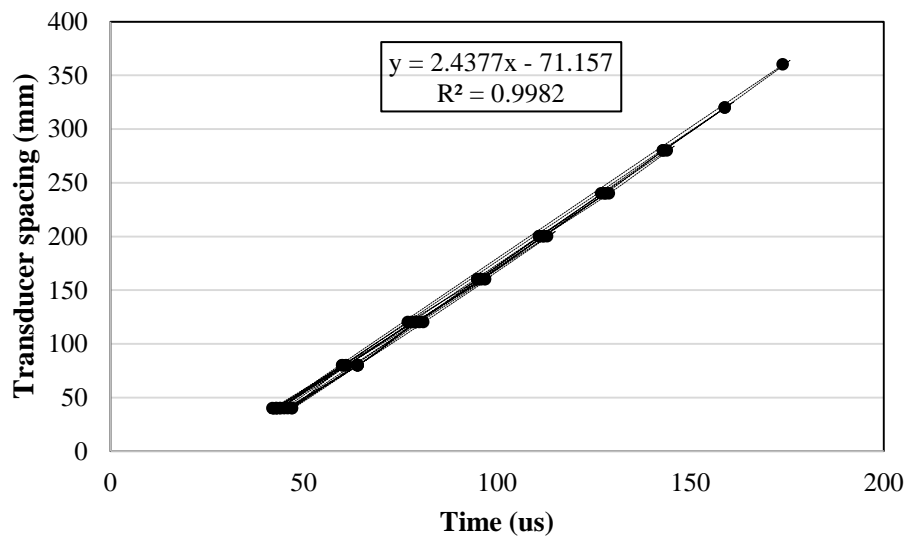


Figure 3. 5 – Shear wave velocity determination for location 1.3-B (3<sup>rd</sup> scan)

### 3.1.1.1 SAFT Panoramic

For some applications, the SAFT B-scans have space limitations when the area of interest is bigger than that presented by a single B-scan (360 mm wide) which can create misunderstandings if the device is not placed directly above the desired distress or design feature. To improve the SAFT evaluation, a reconstruction method of more than one overlapping B-scan was introduced. Two or more B-scans are stitched together regarding common locations of great reflection (great intensity) maintaining the vertical dimensions (k) of the scan while increasing the horizontal dimensions (i) with the precise spacing between the overlapping MIRA readings summarized in Equation 58 (HOEGH, 2013). SAFT panoramic was applied in this thesis to investigate steel spacing and to search for non-visible cracks.

$$\begin{aligned}
\hat{\sigma}_{i,k}^{PAN,m} &= \hat{\sigma}_{k,i-i^*+1}^m \text{ for } i^* \leq i \leq i^* + W - 1 \\
\hat{\sigma}_{i,k}^{PAN,m} &= 0 \text{ for } i < i^* \text{ or } i \geq i^* + W \\
\hat{\sigma}_{i,k}^{PAN} &= \max_m (\hat{\sigma}_{i,k}^{PAN,m})
\end{aligned} \tag{58}$$

Where,

$\hat{\sigma}_{i,k}$  = the image reflectivity of each position inside the ROI;

$\hat{\sigma}_{i,k}^{PAN,m}$  = the image reflectivity of each position of the current SAFT scan considering the dimensions of the panoramic ROI;

$\hat{\sigma}_{i,k}^{PAN}$  = the image reflectivity of each position inside the panoramic ROI;

m = index of the current SAFT scan;

W = maximum number of columns within the ROI;

$i^*$  = horizontal coordinate within the panoramic ROI;

i = horizontal coordinate of the current SAFT scan.

### 3.1.1.2 Hilbert Transform Indicator (HTI)

Each individual MIRA measurement results in 45 data signals ranging in transducer spacing of 40 to 360 mm. Freeseaman *et al.* (2015), analyzing and comparing signals from control and freeze-thaw damaged specimens (Figure 3.6) came up with an indicator that represents the difference from the undamaged specimen to the ones presenting distresses. The research noted a shape variation and an excessive oscillation with damaged specimens' signals.

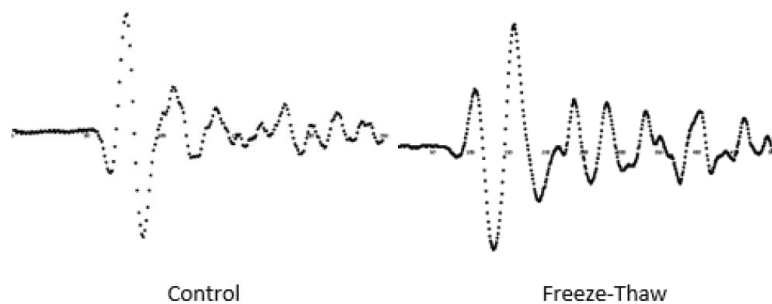


Figure 3. 6 - MIRA signals examples for undamaged and damaged specimens (FREESEMAN *et al.* 2015)

The signal instantaneous amplitude processing through a Hilbert Transform results in a single numerical value which is representative of the signal characteristics. This value was called the Hilbert Transform Indicator (HTI) and is shown below in Equation 59:

$$HTI = \int_0^{500} \frac{HT(t)}{\max(HT(t))} dt \quad (59)$$

Where HT(t) is the Hilbert transform envelope (Blue line in Figure 3.7). Each transmitting and receiving pair allows for the calculation of one HTI. The average HTI of the 45 pairs represents the concrete condition under one MIRA scan. As such, a higher HTI value represents a damaged concrete, while a low value indicates a more sound concrete. The 500 microseconds time window was selected in order to ensure that the signal direct arrival and subsequent scattering was observed which is consistent with the thickness of concrete slabs used in pavements. HTI can also be normalized regarding time, but this action is only interesting when ultrasonic measurements are performed with different frequencies, which is not the case for the data presented in this thesis.

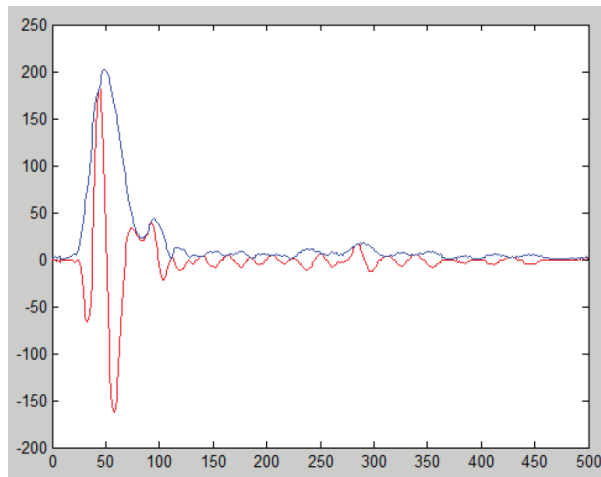


Figure 3. 7– Raw signal (Red) and Hilbert Transform envelope (Blue) (FREESEMAN *et al.*, 2015)

The indicator was able to identify and quantify the level of damage in freeze-thaw specimens. A new study was also able to verify alkali-silica reaction in similar concrete slabs (CLAYTON *et al.*, 2016). For both studies, an HTI above 90 indicates damage existence. In

the present study the HTI was applied to perform a quality assessment of the concrete trough the sections.

Additionally, the HTI of individual pairs was also considered. As can be seen in Figure 3.8 (MIRA simulation grid), each pair of transducers reaches the simulated backwall at a particular position creating 17 locations. Some locations present only one signal (locations 1, 2, 16 and 17) while others have an abundant amount of signals like location 9 (center of simulation) with 5 signals. Table 3.1 presents the number of signals for each location. As the consecutive sensors spacing is constant (40 mm) the locations and its signals will be always the same independent of the analysis depth. By analyzing the individual HTI of each signal, it is possible to infer in a simplistic yet effective analysis on the condition of each signal and on the path it travelled. If a signal presents a high HTI it could mean that there is a distress on the signal's path. This analysis will be applied to fully investigate cracks along the slab depth and to double check the MIRA simulation software for reinforcement.

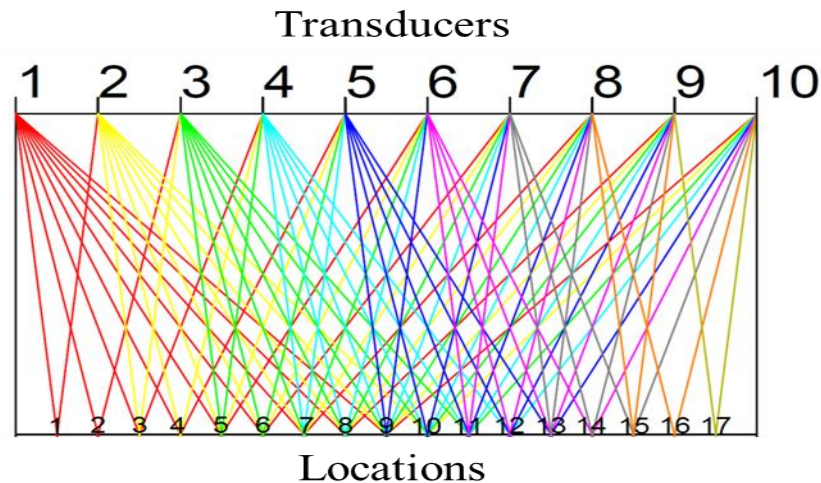


Figure 3. 8 – Locations of backwall signals in a MIRA grid simulation

Table 3. 1 – Signal locations in MIRA grid simulation

Distance from sensor 1		
Location	(mm)	Signal (s)
1	20	1-2
2	40	1-3
3	60	1-4 2-3
4	80	1-5 2-4
5	100	1-6 2-5 3-4
6	120	1-7 2-6 3-5
7	140	1-8 2-7 3-6 4-5
8	160	1-9 2-8 3-7 4-6
9	180	1-10 2-9 3-8 4-7 5-6
10	200	2-10 3-9 4-8 5-7
11	220	3-10 4-9 5-8 6-7
12	240	4-10 5-9 6-8
13	260	5-10 6-9 7-8
14	280	6-10 7-9
15	300	7-10 8-9
16	320	8-10
17	340	9-10

### 3.1.1.3 MIRA numerical simulations

The ultrasonic simulations described here were performed by a simulation software developed at the University of Minnesota (FREESMAN, 2016). The simulation is based on a numerical procedure called Elastodynamic Finite Integration Technique (EFIT). Pfeifer *et al.* (1997) describes EFTI as an adequate numerical approach to analyze ultrasonic wave propagation in concrete pavements due to its success in simulation of strongly heterogeneous, isotropic and anisotropic, linear and nonlinear materials.

In order to generate accurate simulations and maintaining computational efficiency, MIRA horizontal shear waves were simulated using anti-plane deformation and viscoelastic material properties were utilized. Also, Fresseman (2016) has shown better results when simulating the material with viscoelastic properties instead of elastic ones. Moreover the program has features to simulate reinforcement and delamination areas with specific coordinates and properties.

The simulation program was utilized in this thesis to simulate thickness and reinforcement cases as well as to calibrate the software giving a better understating regarding transverse

cracks in CRCPs. As the simulation produces an output similar to MIRA's original output, the same analysis process described above can be applied to the simulation results.

### **3.2 Experimental short CRCP ultrasonic survey results**

Tables 3.2 to 3.3 present the thickness results for sections 1 to 4, respectively. Three thickness measurements were performed in each location; if the variation between this three locations was greater than 5%, the measurement was considered as inconclusive and the thickness was not recorded. Along with thickness results, shear wave velocity values for each measurement are given. Some locations like Section 1's location 5 and Section 2's location 4 were not presented due to calibration problems with the MIRA device. Strong red reflections would appear when testing in these locations making the results unreliable. However, the SAFT algorithm adapted by Hoegh (2013) can erase such unreliable features from the original MIRA algorithm. Unfortunately, during the readings, the operators were not aware of this correction property of the adapted SAFT.

The average thickness for Section 1 was 216.10 mm, 23.90 mm thinner than the original designed thickness of 240 mm. For Section 2 the average thickness was 201.25, while for Sections 3 and 4 it was 221.11 and 195.31 mm, respectively. The sections located side by side presented similar thickness (Sections 1 and 3; Sections 2 and 4). All sections presented locations with thickness below 200 mm with some points as thin as 169 mm. Figures 3.9 to 3.12 show a 3D geometry view of the slabs based on the MIRA results for a more comprehensive understanding of the sections layout. Only thickness from the "A" locations were utilized on the 3D views; if a "A" location did not presented results, than "B" location thickness was applied. The red line represents the design thickness of 240 mm.

As can be seen by the 3D images, thickness varies in both directions. Table 3.4 presents the average thickness by position (right, center and left) and by location (1, 2, 3, 4 and 5), according to Figure 3.1. Regarding the position, Sections 2 and 4 have a transversal profile shaped as an inverse triangle, with the center being thinner than the edges. Differently, Sections 1 and 3 present an ascendant (right to left) line. As for location, there is a tendency (save Section 4) of greater thickness in the slab's middle.

Table 3. 2 – Thickness, shear wave velocity and HTI results for Sections 1 and 2

Section 1				Section 2			
Loc.	Avg. Thickness (mm)	Avg. Vel. (m/ms)	HTI	Loc.	Avg. Thickness (mm)	Avg. Vel. (m/ms)	HTI
1B-R	184.2	2.368	70	1A-R	188.6	2.599	58
1B-C	187.8	2.325	71	1A-C	190.0	2.554	58
1B-L	215.8	2.373	58	1A-L	206.2	2.606	57
2B-R	208.6	2.376	63	1B-R	229.4	2.572	64
2B-C	221.8	2.415	56	1B-C	190.0	2.536	61
2B-L	226.6	NC	55	1B-L	197.2	2.535	62
3A-R	217.7	2.473	57	2A-R	202.3	2.561	66
3A-C	215.8	NC	73	2A-C	175.2	2.467	63
3A-L	244.0	2.529	72	2A-L	209.8	2.586	56
3B-R	215.0	2.425	81	2B-R	201.8	2.566	67
3B-C	219.9	NC	65	2B-C	169.8	2.448	65
3B-L	229.4	2.447	55	2B-L	205.2	2.572	59
4A-R	215.2	2.430	55	3A-R	205.3	2.684	62
4A-C	213.4	2.488	51	3A-C	217.8	2.584	54
4A-L	220.6	2.480	53	3A-L	208.8	2.583	64
4B-R	212.4	2.442	53	3B-R	214.0	2.653	60
4B-C	212.2	2.475	55	3B-C	216.6	2.568	58
4B-L	229.0	2.502	53	3B-L	212.6	2.648	63
NC = non-conclusive				5A-R	203.6	2.488	66
				5A-C	187.0	2.437	80
				5A-L	202.2	2.482	64
				5B-R	204.8	2.481	61
				5B-C	183.4	2.342	80
				5B-L	208.4	2.489	59

Regarding the HTI results, average results are 61 (Section 1), 63 (Section 2), 67 (Section 3) and 72 (Section 4). Standard deviation for sections 1, 3 and 4 was around 10, while for Section 2 it was exactly 6. Sections with most cracks present the higher values, however it can be concluded that the pavement in these measurement stations is showing a sound concrete. For single points, only four positions exhibited HTI higher than 90. Location 3B-L in Section 4 was placed at the crack F4.2 (Figure 3.13). For locations 4B (Section 4) and 1B (Section 3) no reasonable explanation at the pavement surface was found. Results from freeze-thaw and ASR damage showed that HTI higher than 90 indicates the possibility of damage in first stages whereas areas with HTI higher than 100 are considered damaged (FREESEMAN *et al.*, 2015 and CLAYTON *et al.*, 2016). As can be seen in the HTI color map (averages between A and B stations) presented in Figure 3.14, only locations 1 (Section 3) and 4 (Section 4) present

values close to 90. Again, examinations of the surface at those stations show no distresses or cracks.

Table 3. 3 - Thickness, shear wave velocity and HTI results for Sections 3 and 4

Loc.	Section 3			Section 4		
	Avg. Thickness (mm)	Avg. Vel. (m/ms)	HTI	Avg. Thickness (mm)	Avg. Vel. (m/ms)	HTI
1A-R	201.2	2.616	72	186.8	2.615	67
1A-C	169.2	2.625	68	190.6	2.560	67
1A-L	182.0	2.343	97	203.4	NC	68
1B-R	NC	NC	95	181.6	2.574	62
1B-C	173.0	2.619	69	186.8	2.564	77
1B-L	200.2	2.597	76	208.4	2.571	69
2A-R	229.4	2.653	59	173.4	2.750	71
2A-C	255.0	2.603	59	199.6	2.724	58
2A-L	233.4	2.645	67	209.0	2.749	67
2B-R	207.4	2.647	59	169.6	2.738	72
2B-C	251.4	2.603	57	200.8	2.701	60
2B-L	228.6	2.622	71	206.6	2.724	63
3A-R	205.9	2.605	89	202.5	2.642	68
3A-C	238.1	2.599	58	184.1	2.608	57
3A-L	244.2	2.594	66	203.6	2.663	71
3B-R	217.8	2.556	67	195.2	2.635	72
3B-C	227.2	2.617	62	178.0	2.492	73
3B-L	256.4	2.640	64	189.4	2.454	95
4A-R	212.9	2.595	60	184.8	2.620	78
4A-C	226.4	2.625	60	203.2	2.620	78
4A-L	243.0	2.688	59	204.4	2.512	78
4B-R	216.8	2.603	59	192.0	2.663	86
4B-C	229.8	2.660	59	192.4	2.486	99
4B-L	241.2	2.667	65	200.2	2.455	80
5A-R	207.4	2.593	67	205.8	2.521	77
5A-C	206.0	2.641	66	196.8	2.508	75
5A-L	254.8	2.681	59	NC	NC	88
5B-R	204.0	2.566	70	207.8	2.563	67
5B-C	201.6	2.617	66	195.8	2.545	57
5B-L	247.6	2.660	59	211.2	2.572	74

NC = non-conclusive

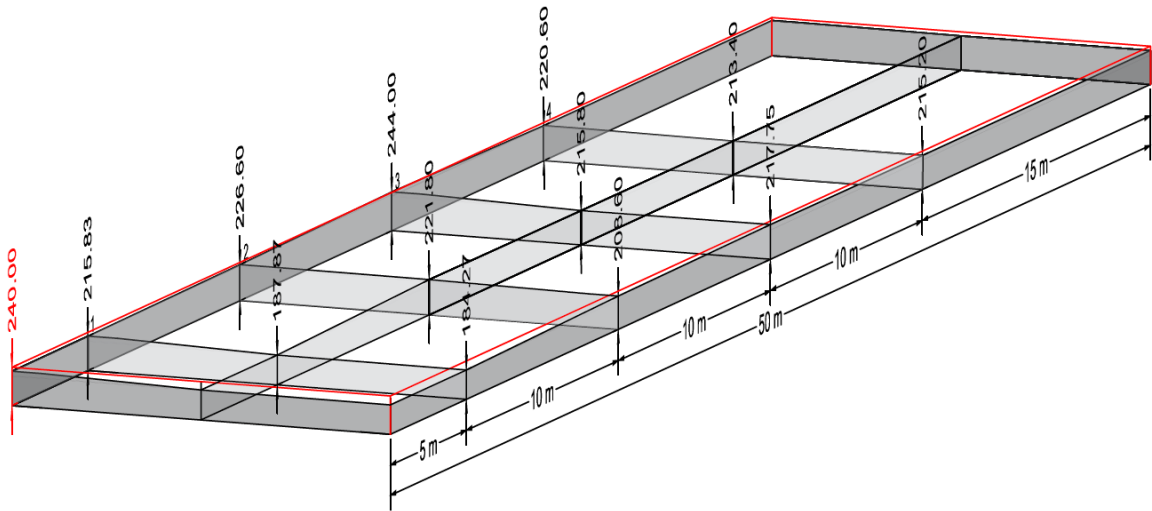


Figure 3. 9 – 3D geometry view of Section 1

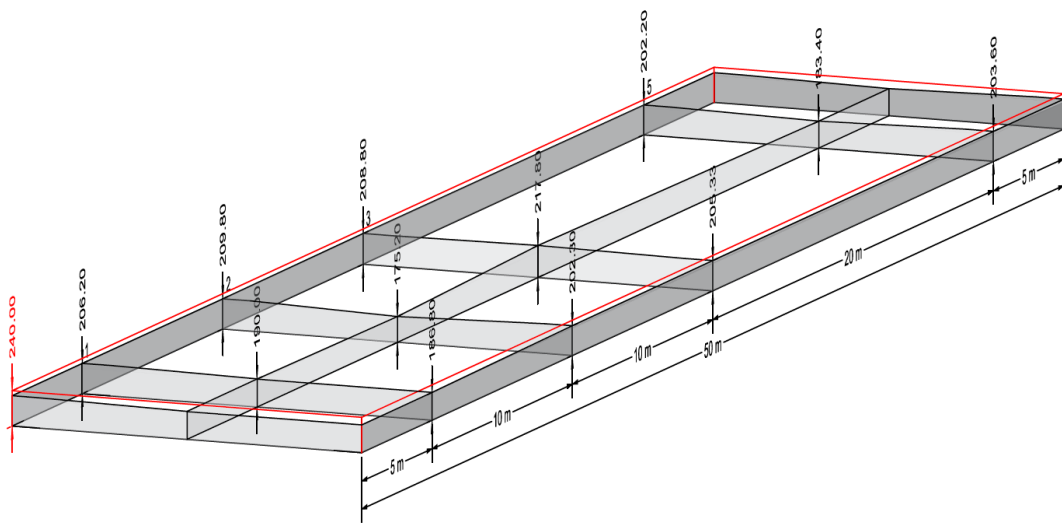


Figure 3. 10 – 3D geometry view of Section 2

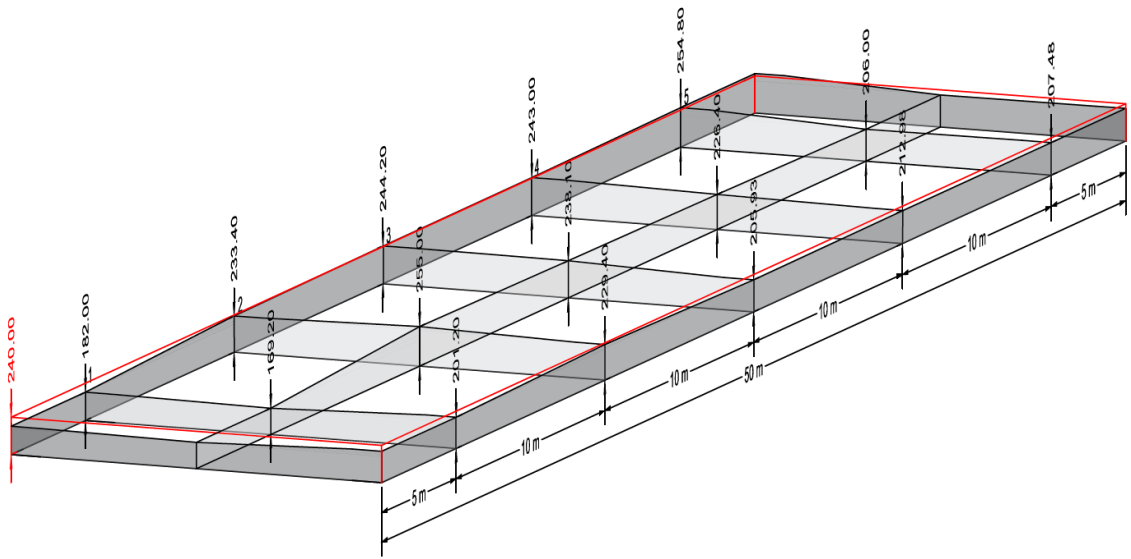


Figure 3. 11 – 3D geometry view of Section 3

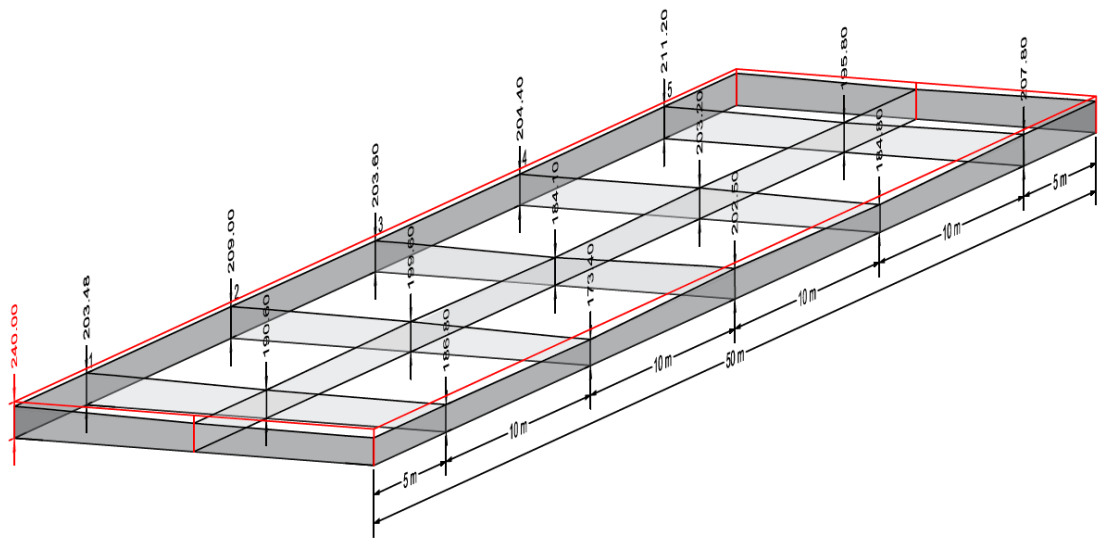


Figure 3. 12 – 3D geometry view of Section 4

Table 3. 4 – Average thickness per position and location

Position	Section			
	1	2	3	4
Right - R	208.8	206.2	211.4	189.9
Center - C	211.8	191.2	217.7	175.2
Left - L	227.5	206.3	233.1	204.0
Location	1	2	3	4
1	195.9	200.2	185.1	192.9
2	219.0	192.3	234.2	193.1
3	223.6	212.5	231.6	192.1
4	217.1	NC	228.3	196.1
5	NC	198.2	220.2	203.4

NC = non-conclusive

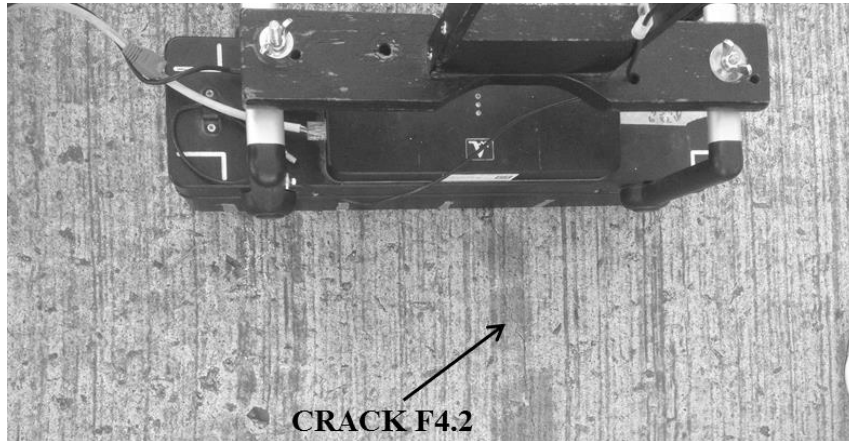


Figure 3. 13 – Crack F4.2 at thickness measurement location 3B-L in Section

As the SAFT algorithm uses shear wave velocity measured by MIRA to create the B-Scans reconstruction which allows for slab thickness determination, it is interesting to visualize this two parameters together. Figure 3.15 provides this information for all thickness measurements. No trend was observed.

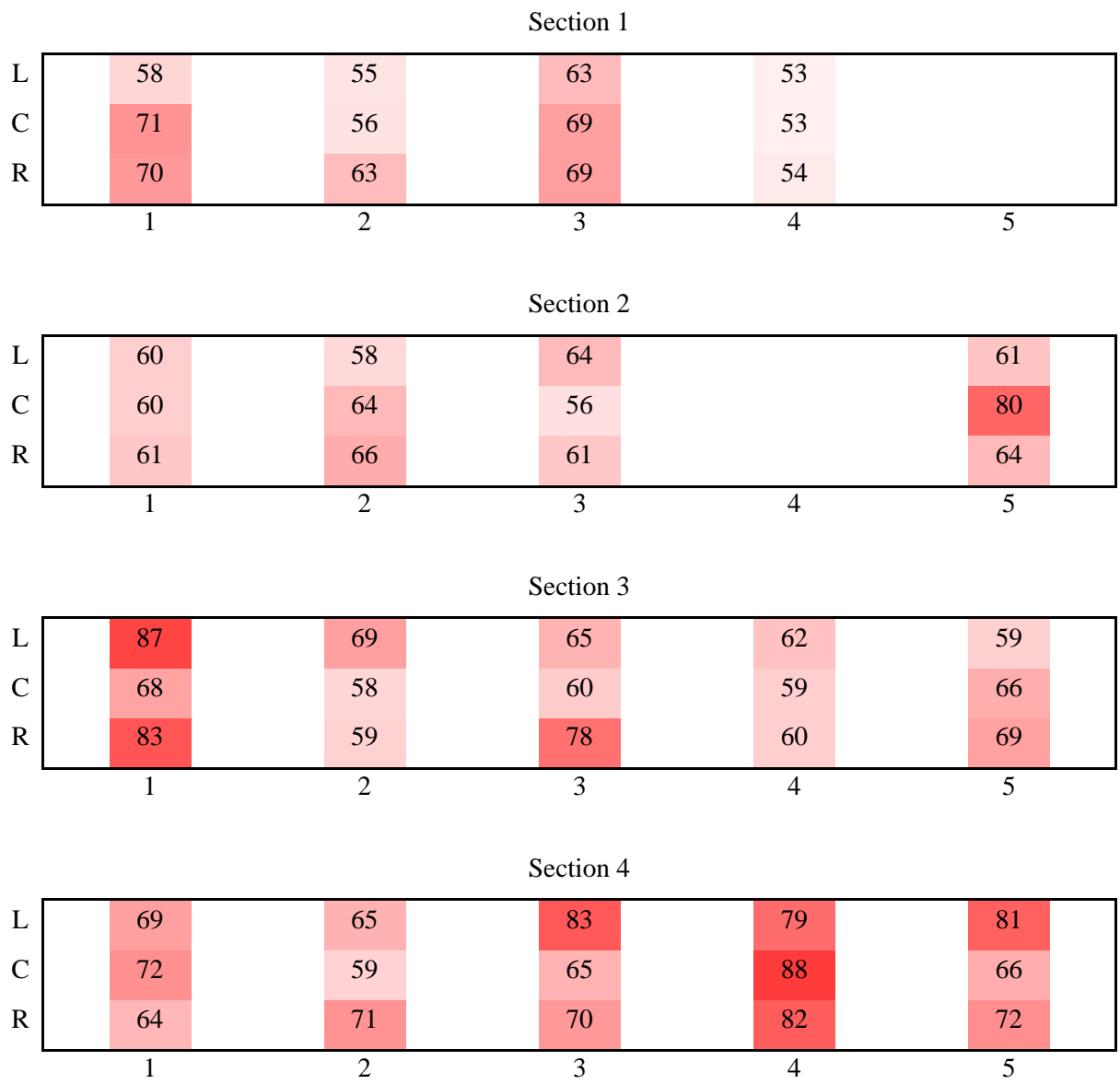


Figure 3. 14 – HTI color map

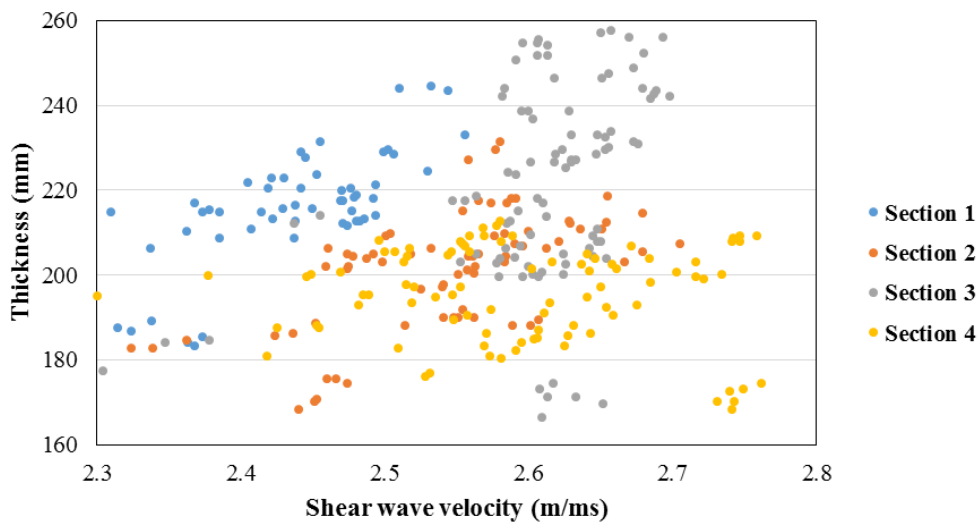


Figure 3. 15 – Thickness *versus* shear wave velocity for MIRA thickness reading

Shear wave velocity *versus* HTI also proved to be inconclusive (Figure 3.16). There is a disproportionate trend, i.e., higher velocity relates to lower HTI values in accordance to several studies that showed higher velocity implies in greater stiffness. Nonetheless, the trend is not statistically significant for these results. Similar to those, relations between thickness and HTI were not conclusive. That happens majorly due to shear wave velocity being measured at the concrete surface, therefore with little relation to deeper locations of the slab.

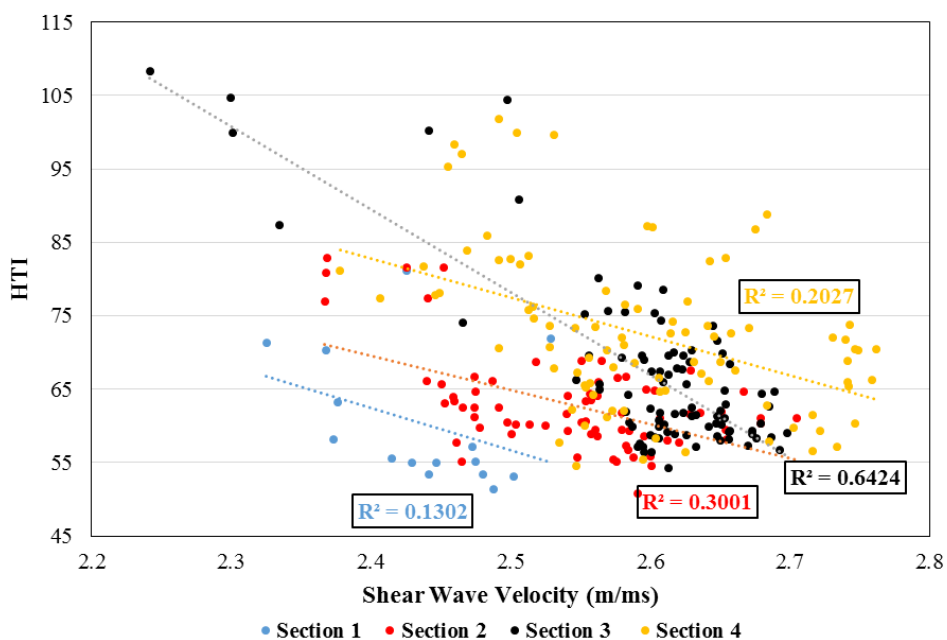


Figure 3. 16 - HTI *versus* shear wave velocity for MIRA thickness readings

### 3.2.1 Longitudinal reinforcement depth and spacing

Tables 3.5 and 3.6 presents the longitudinal reinforcement data extracted from the SAFT-B scans and SAFT-Pan. Figure 3.17 shows examples of B scans where is possible to identify the steel depth, while Figure 3.18 displays two bars enabling the reinforcement spacing determination.

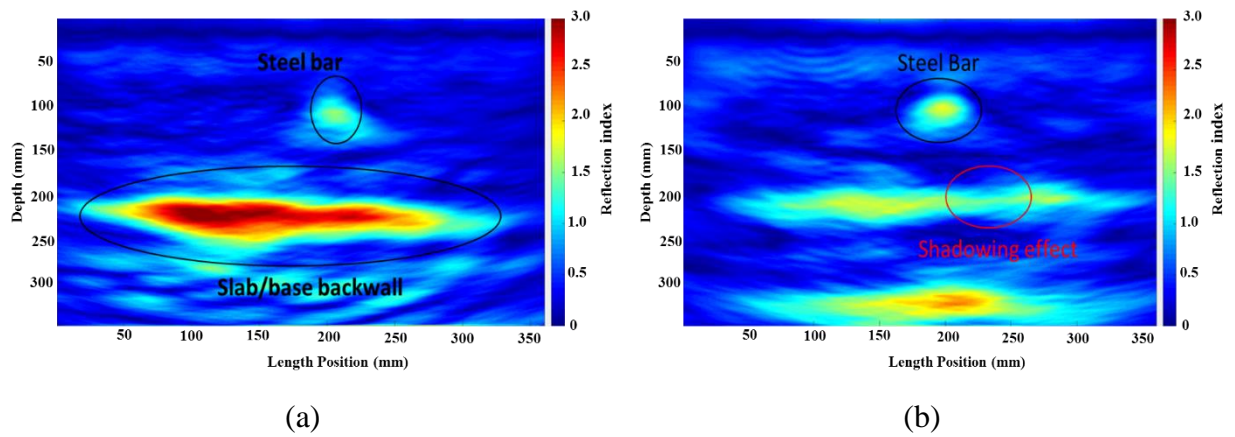


Figure 3. 17 – Steel depth on B scans for (a) Section 1, location 3A, position right and (b) Section 4, location 2A, position center

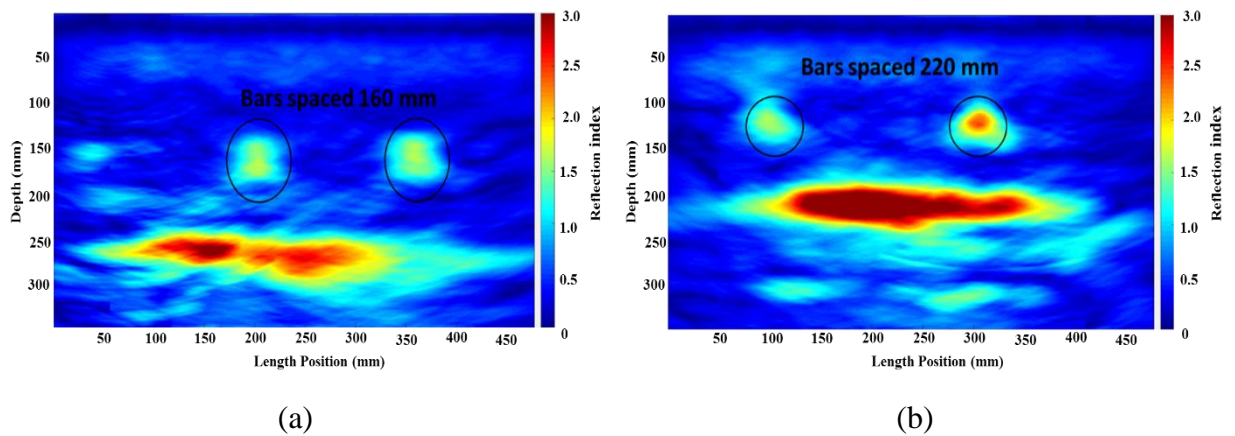


Figure 3. 18 – Steel spacing on SAFT-Pan scans for (a) Section 3, location 3B, position left and (b) Section 2, location 1A, position left

Table 3. 5 – MIRA data for longitudinal steel in Sections 1 and 2

Loc	Section 1				Section 2			
	Avg. Thickness (mm)	Steel Depth (mm)	Steel Depth/Thickness	Steel Spacing (mm)	Avg. Thickness (mm)	Steel Depth (mm)	Steel Depth/Thickness	Steel Spacing (mm)
1A-R	NC	NC	NC	NC	243.2	90	0.37	240
1A-C	NC	NC	NC	NC	190.0	100	0.53	230
1A-L	NC	105	NC	300	206.2	110	0.53	220
1B-R	184.2	NC	NC	NC	229.4	100	0.44	230
1B-C	187.8	NC	NC	NC	190.0	120	0.63	215
1B-L	215.8	130	0.60	NC	197.2	120	0.61	NC
2A-R	NC	120	NC	290	NC	NC	NC	NC
2A-C	NC	125	NC	290	222.6	100	0.45	NC
2A-L	NC	125	NC	NC	209.8	120	0.57	220
2B-R	NC	120	NC	280	201.8	NC	NC	NC
2B-C	208.6	125	0.60	NC	220.5	105	0.48	190
2B-L	221.8	120	0.54	NC	205.2	120	0.58	190
3A-R	226.6	110	0.49	NC	205.3	100	0.49	NC
3A-C	217.7	130	0.60	280	217.8	125	0.57	220
3A-L	215.8	150	0.70	280	208.8	125	0.60	230
3B-R	244.0	110	0.45	NC	214.0	115	0.54	220
3B-C	215.0	135	0.63	300	216.6	125	0.58	220
3B-L	219.9	140	0.64	270	212.6	115	0.54	210
4A-R	229.4	115	0.50	NC	NC	NC	NC	NC
4A-C	215.2	120	0.56	NC	NC	125	NC	220
4A-L	213.4	120	0.56	NC	NC	120	NC	230
4B-R	220.6	110	0.50	NC	NC	100	NC	220
4B-C	212.4	115	0.54	NC	NC	125	NC	200
4B-L	212.2	125	0.59	270	NC	NC	NC	NC
5A-R	229.0	NC	NC	NC	203.6	115	0.56	210
5A-C	NC	NC	NC	NC	187.0	100	0.53	240
5A-L	NC	120	NC	NC	202.2	110	0.54	220
5B-R	NC	NC	NC	NC	204.8	115	0.56	230
5B-C	NC	NC	NC	NC	183.4	100	0.55	200
5B-L	NC	NC	NC	NC	208.4	115	0.55	220

NC = non-conclusive

The designed steel depth was 110 mm from the surface, 10 mm above the slab half-height. The average steel depth observed through MIRA was 122.38 mm for Section 1, 112.12 mm for Section 2, 122.76 mm for Section 3 and 99.50 mm for Section 4. The ratio between steel depth and thickness was supposed to be approximately 0.46, however due to the poor construction practices previously observed in the thickness results, the ratio was increased to approximately 0.55 (Section 1 – 0.57; Section 2 – 0.56; Section 3 – 0.56; Section 4 – 0.51).

One of the classic concepts involving CRCP is the placement of the longitudinal reinforcement slightly above the slab half-height. This new configuration disclosed by the MIRA results can help explain several differences in the crack development and performance of the experimental short CRCP. As the reinforcement is below the slab half-height it had less influence in the crack development. Also, the crack width may be impaired because of the lack of longitudinal reinforcement tightening effect at the slab surface. Additionally, the thickness variation and the mostly incorrect steel placement disclose a deficient construction practice for these slabs. The fact that this is an experimental investigation, i.e., more rigorously controlled than ordinary construction, makes the lack of proper practice in concrete pavement construction in Brazil more evident.

Regarding steel spacing, there were also some deviations from the project design. Sections 1 and 2 (greater spacing) showed a smaller steel spacing than the designed one, while for Sections 3 and 4 the field steel spacing was more similar to the original project. Table 3.7 provides this information, along with the new steel percentage for each section. Since the average slab thickness and the average steel spacing were altered during construction, the steel percentage was recalculated to represent the sections real features. The as built steel percentage was higher than the designed one for all sections. Section 2 has a similar steel percentage as that of Section 4's original project. The major finding of this design assessment is that Sections 3 and 4, due to Section 4's thinner slab, have the same steel percentage. This can help explaining the similar crack behavior of both sections as it will be discussed in the next chapter of this thesis. Moreover, this analysis shows how important it is to know the real field features of a pavement structure, especially for maintenance and rehabilitation decisions since most software and procedures for these processes require accurate design inputs.

Table 3. 6 – MIRA data for longitudinal steel in Sections 3 and 4

Loc	Section 3				Section 4			
	Avg. Thickness (mm)	Steel Depth (mm)	Steel Depth/ Thickness	Steel Spacing (mm)	Avg. Thickness (mm)	Steel Depth (mm)	Steel Depth/ Thickness	Steel Spacing (mm)
1A-R	201.2	120	0.60	170	186.8	90	0.48	190
1A-C	169.2	90	0.53	180	190.6	95	0.50	190
1A-L	182.0	110	0.60	180	203.4	100	0.49	195
1B-R	NC	105	NC	160	181.6	90	0.50	185
1B-C	173.0	90	0.52	170	186.8	100	0.54	200
1B-L	200.2	115	0.57	160	208.4	105	0.50	200
2A-R	229.4	120	0.52	170	173.4	75	0.43	200
2A-C	255.0	120	0.47	180	199.6	105	0.53	200
2A-L	233.4	130	0.56	170	209.0	100	0.48	170
2B-R	207.4	NC	NC	NC	169.6	75	0.44	195
2B-C	251.4	120	0.48	170	200.8	105	0.52	200
2B-L	228.6	115	0.50	170	206.6	100	0.48	180
3A-R	205.9	95	0.46	180	202.5	100	0.49	205
3A-C	238.1	145	0.61	160	184.1	100	0.54	200
3A-L	244.2	150	0.61	160	203.6	95	0.47	215
3B-R	217.8	100	0.46	180	195.2	95	0.49	195
3B-C	227.2	125	0.55	170	178.0	100	0.56	210
3B-L	256.4	150	0.59	160	189.4	100	0.53	195
4A-R	212.9	125	0.59	190	184.8	85	0.46	190
4A-C	226.4	130	0.57	160	203.2	110	0.54	200
4A-L	243.0	145	0.60	180	204.4	100	0.49	185
4B-R	216.8	130	0.60	180	192.0	80	0.42	205
4B-C	229.8	145	0.63	170	192.4	110	0.57	NC
4B-L	241.2	125	0.52	160	200.2	100	0.50	190
5A-R	207.4	120	0.58	180	205.8	110	0.53	190
5A-C	206.0	125	0.61	190	196.8	105	0.53	200
5A-L	254.8	150	0.59	170	NC	115	NC	200
5B-R	204.0	115	0.56	170	207.8	120	0.58	200
5B-C	201.6	115	0.57	170	195.8	105	0.54	195
5B-L	247.6	135	0.55	170	211.2	115	0.54	200

NC = Non-conclusive

Table 3. 7 – Design data *versus* Mira data

	Design Data			MIRA Data				
	Thickness (mm)	Steel Spacing (mm)	Steel Percentage (%)	Avg. Thickness (mm)	Std.	Avg. Steel Spacing (mm)	Std.	Real Steel Percentage (%)
Section 1	240	300	0.44	216.1	10.42	284.4	10.66	<b>0.52</b>
Section 2	240	230	0.57	201.2	10.30	218.5	13.31	<b>0.71</b>
Section 3	240	170	0.78	221.1	16.85	171.7	8.74	<b>0.82</b>
Section 4	240	200	0.67	195.3	10.67	195.9	8.82	<b>0.83</b>

### 3.2.2 Mira Simulations for slab thickness and reinforcement position

Two simulation cases for slab thickness are presented in Figure 3.19. As can be seen, the simulation perfectly captures the backwall reflection at the inputted depth. Small signals attenuations above the backwall for the field data can be explained by the concrete heterogeneous characteristics. The strong reflection at 250 mm for measurement 4.3A-R can be results of the base/sub-base backwall.

A similar analysis was done for the longitudinal reinforcement. Figure 3.20 shows the results. While the simulation captures the backwall attenuation due to the inclusions (steel bars), on the field examples the backwall is clearly weaker. To further investigate the signal interruption and backwall attenuation, signal simulation is illustrated for both cases in Figure 3.21. The complete backwall discontinuity at the end of reconstruction 2.1B-C caused by the second inclusion is perfectly captured by both the field and MIRA simulation. However, for the first inclusion, the middle of the simulated reconstruction presents much higher reflection than the field reconstruction. Apparently, the MIRA simulation software shows greater reflection even than the SAFT reconstruction for points where some signals were lost. This is easily evidenced when comparing the reflection of the second inclusion. It only receives one signal (sensor 9 emitting to sensor 10), yet the simulated reconstruction shows a bigger and more clear inclusion when compared to the SAFT reconstruction.

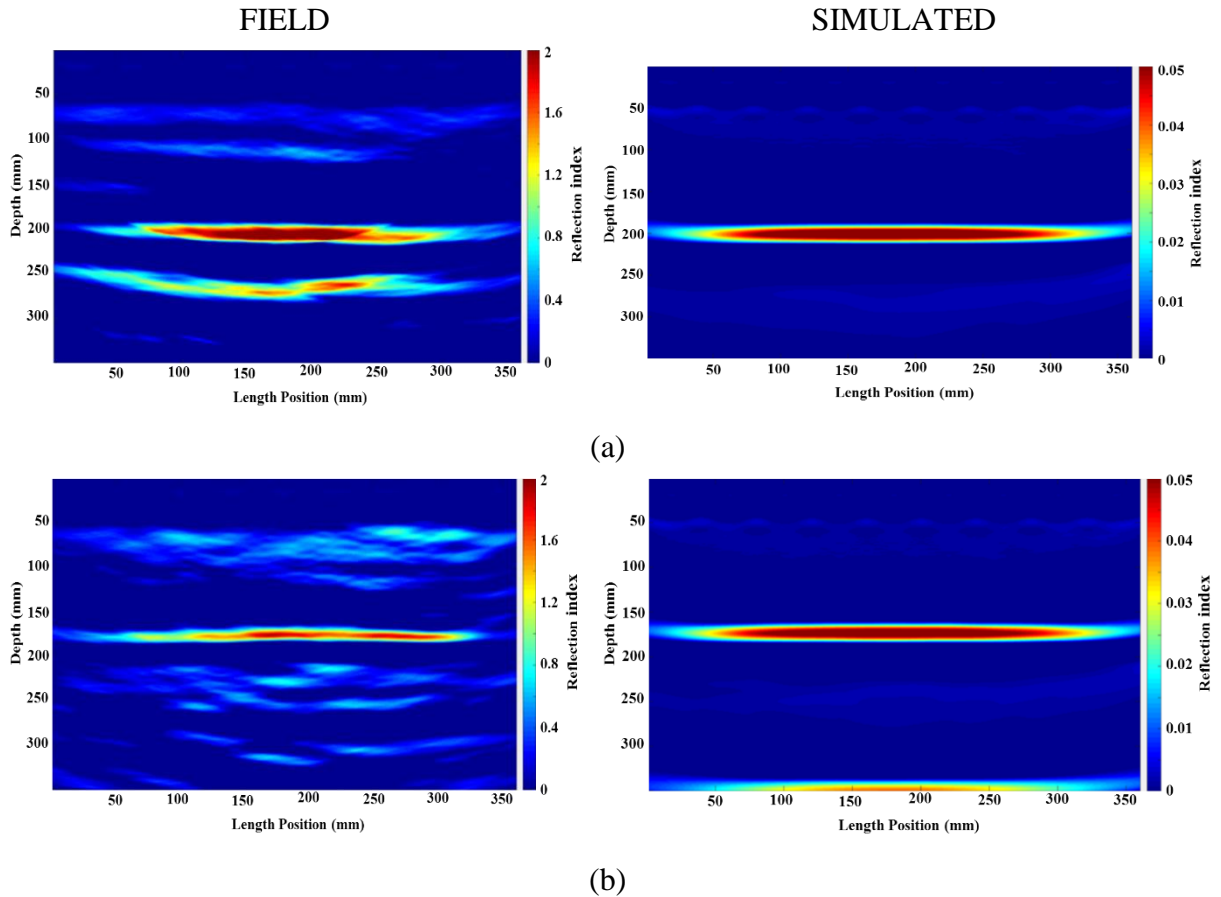


Figure 3. 19 – Thickness simulations for (a) section 4 (4.3A-R) and (b) section 2 (2.2A-C)

Similar observations can be made by the reconstruction case of 1.4B-R. In the signal simulation there is a clear gap below sensor 8 (280 mm). Nonetheless, the MIRA simulation shows a weaker but constant backwall while the SAFT reconstruction displays a break. Both cases were checked for presence of distress which may also attenuate the backwall. HTI resulted in values below 70 for both scans.

Furthermore, signals time history was also analyzed for these four simulations. Figure 3.22 reveals the field data versus simulated data for the thickness measurements. The center signal (sensor 5 to sensor 6) was used in this analysis. As can be seen there is a mostly perfect match between signals with the real data showing more variations as it is expected since as previously mentioned, concrete is a heterogeneous material presenting different properties along the sample's depth and length. For the reinforcement, the goal was to analyze signals reaching the reinforcement bottom and losing strength and signals that reached the reinforcement's top and were reflected to the receiver. For that, signals 2-4 and 9-10 of case

2.1B-C were plotted in Figure 3.23. As can be seen, when the signal hits the inclusion and it is reflected to the receiver (Figure 3.23b) the simulation approach is much more consistent than when the signal is not fully reflected to the receiver. There is an intensity variation after 150 us that is not modeled by the simulator.

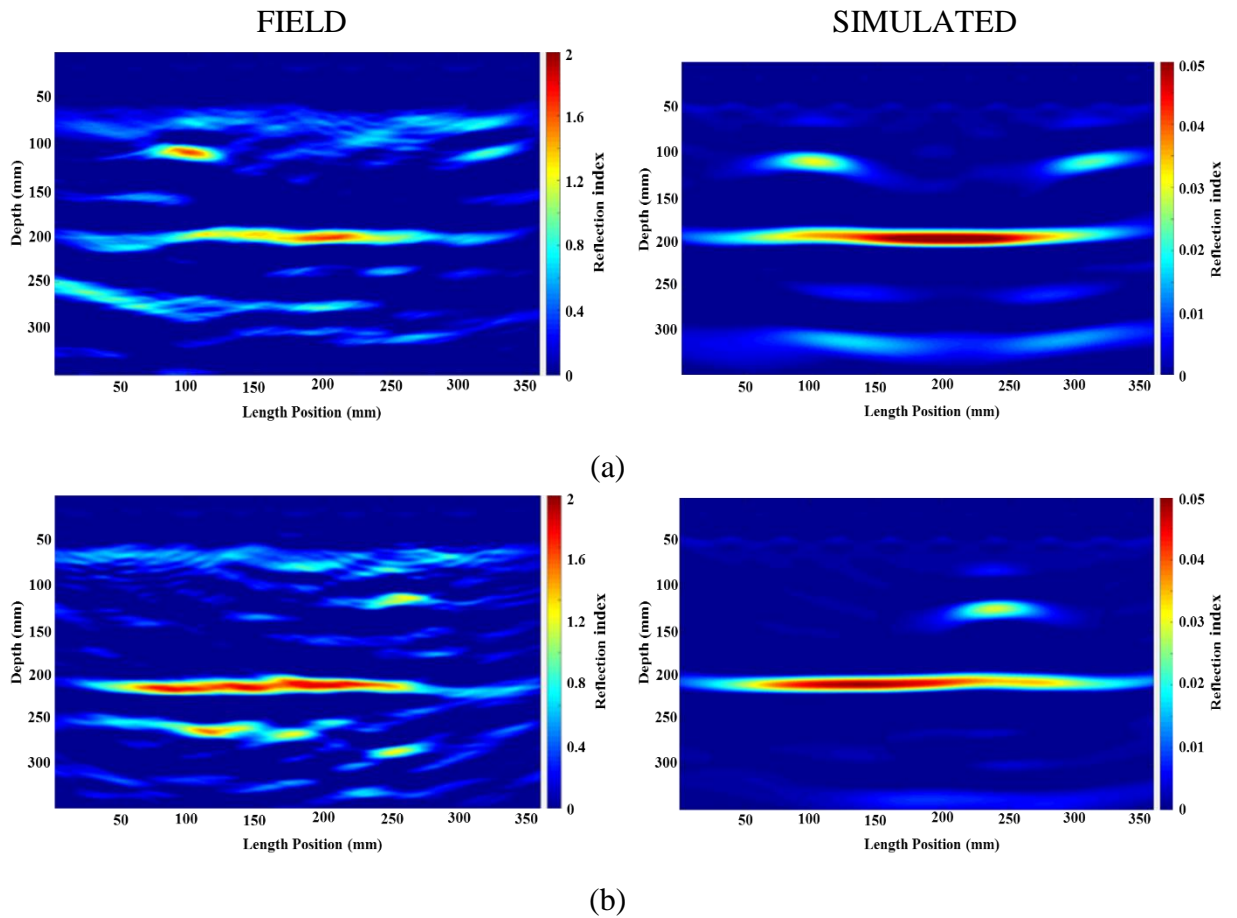


Figure 3. 20 – Reinforcement simulations for (a) section 2 (2.1B-C) and (b) section 1 (1.4B-R)

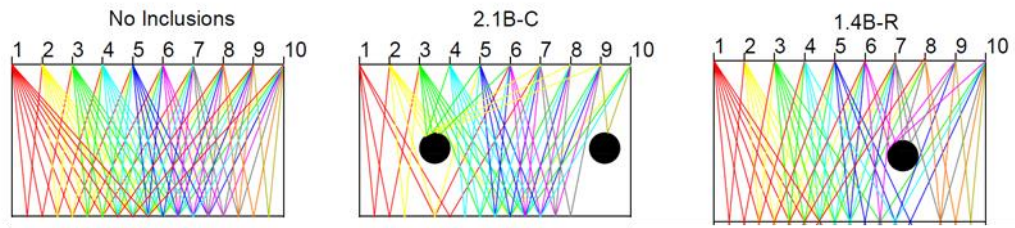
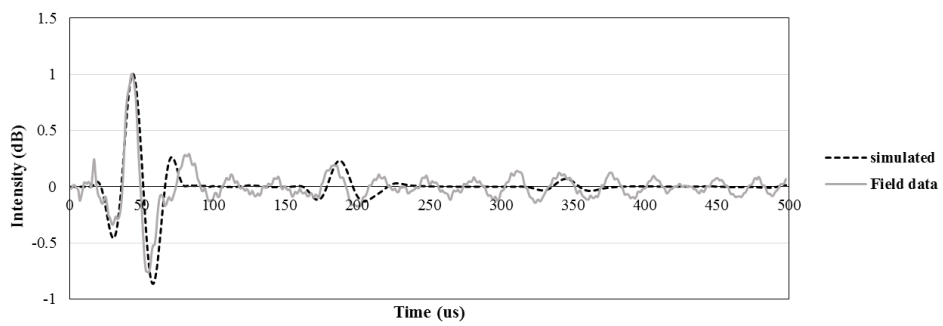
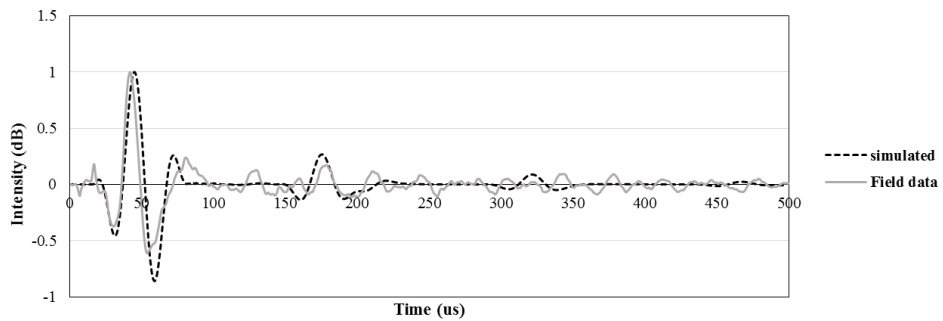


Figure 3.21 – Signal simulation for reinforcement inclusions

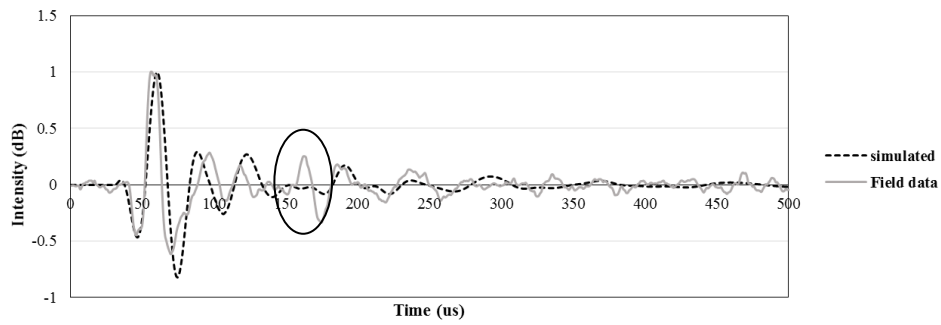


(a)

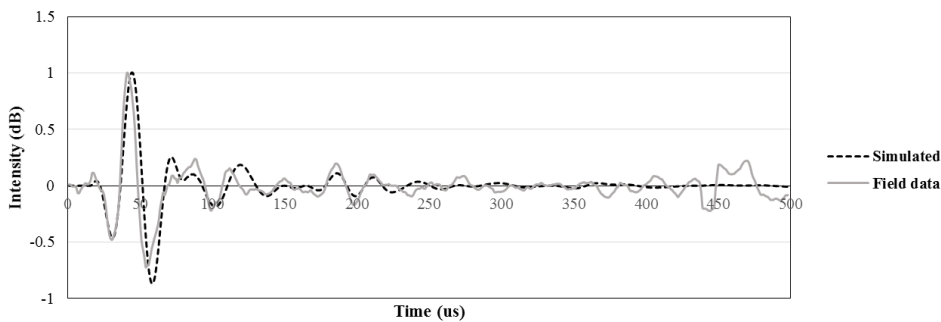


(b)

Figure 3.22 – Field and simulated signals for (a) section 4 (4.3A-R) and (b) section 2 (2.2A-C)



(a)



(b)

Figure 3. 23– Field and simulated signals for (a) loss signal due to inclusion (b) inclusion reflection

### 3.2.3 Core proving

Cores (Figure 3.24) were performed to confirm the thickness ultrasonic measurements. A total of 5 cores were extracted. The thickness results in comparison to MIRA results can be found in Table 3.8. Only the measurement in section 2 presented a difference higher than 20 mm. Investigations on why this measurement presented error was inconclusive; this particular point did not show evidence of damage ( $HTI = 54$ ) however evidence on the slab surface shows that this core was taken 20 mm from the MIRA measurement. A Mira acceptance error has not being yet developed. Edwards (2012) in a broad non-destructive study pointed out average difference of 5%. Additionally, for all cores, the asphalt base was separated from the concrete slab in a clear indication that slab and base are unbounded.

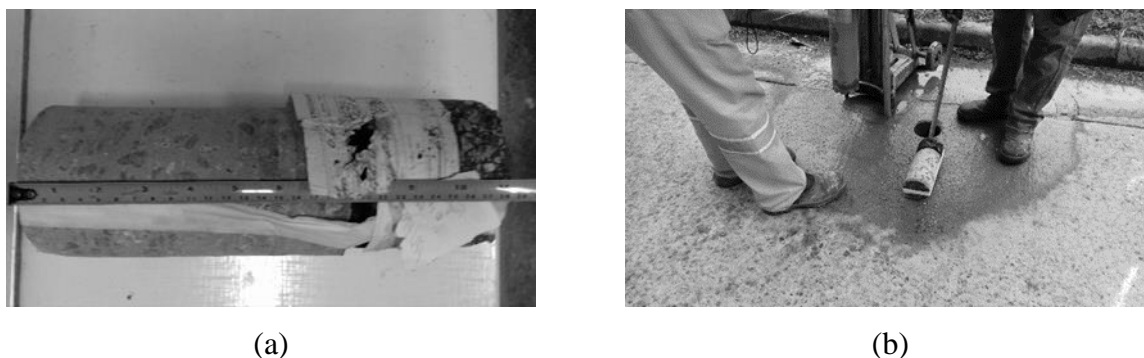


Figure 3. 24 – Core extracted from (a) section 4 (4.3A-C) and (b) section 1 (1.1B-R)

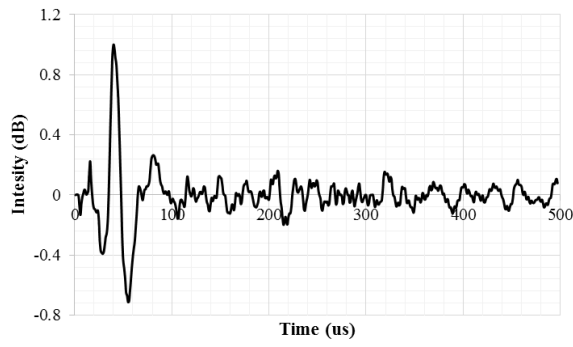
Table 3. 8 – Correlation between MIRA thickness measurements and cores

Section	Location	MIRA Thickness (mm)	Core Thickness (mm)	Difference (mm)
1	1.1B-R	184.2	180	4.27
1	1.3A-L	244	240.6	3.4
2	2.3A-C	217.8	240.2	22.4
3	3.3A-C	238.1	235	-3.1
4	4.3A-C	184.1	190.1	6

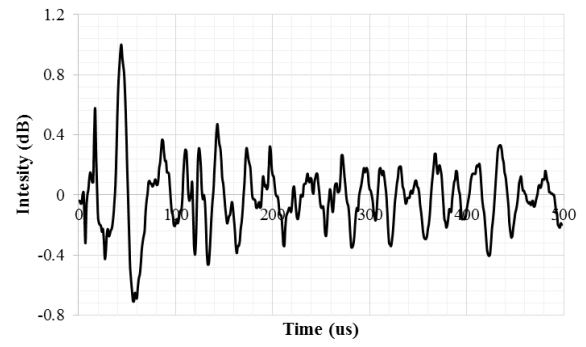
### 3.3 Ultrasonic Crack characterization

The analysis of HTI from the cracks measurement disclosed a high value for most cracks, as seen in Table 3.9. This investigation was the first time that the HTI was applied at transversal shrinkage cracks. As the concrete presents a physical discontinuity on those locations, it is expected that the signal shows differences from sound continuous concrete signal (Figure 3.25). However, some cracks like F4.3 and F2.4 exhibited low HTI values.

SAFT-Pan reconstructions of scans at cracks resulted in two major kinds of features, a continuous slab base backwall with a circular shaped inclusion located at 50 to 100 mm from the surface (Figure 3.26 a and b) or a continuous slab base backwall with another reflection around 150 mm followed by the same circular shaped inclusion described above (Figure 3.26c and d). As seen in the literature review, the mid-depth inclusions can be a transversal bar as it is expected that transverse cracks to be positioned on the top of those. No clear backwall discontinuity was observed unlike the findings of Hoegh and Khazanovich (2015) where the backwall break matched the location of cracks.

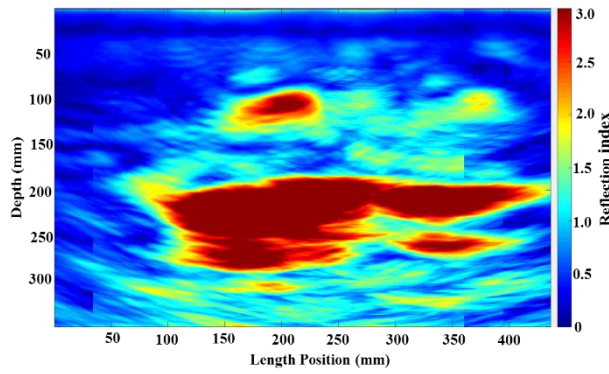


(a)

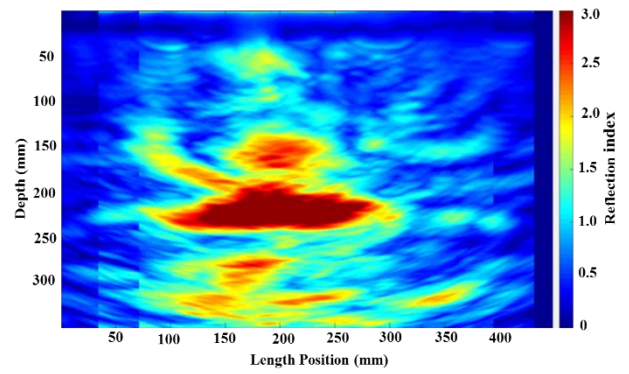


(b)

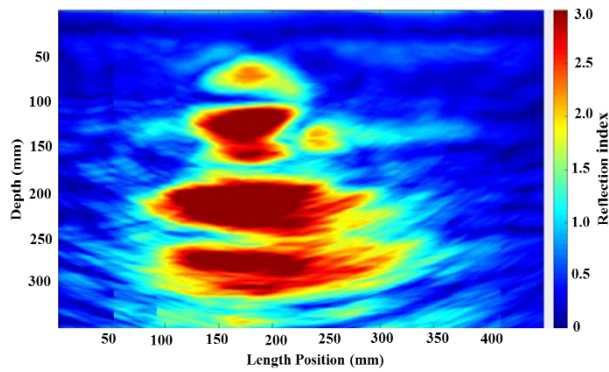
Figure 3. 25 – Signals for (a) thickness measurement (location 3.3B-R) and (b) crack F3.3 (Right).



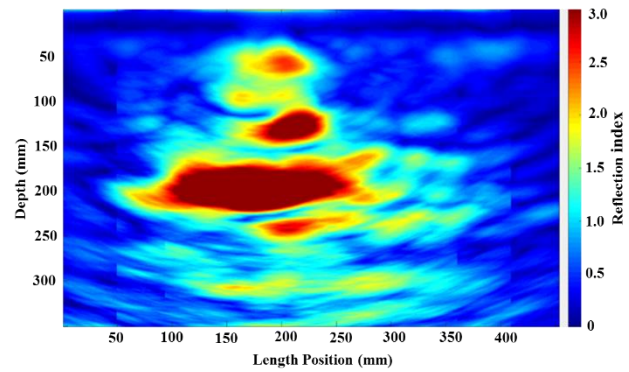
F2.2 - Right



F2.3 - Right



F3.1 - Center



F4.8 - Right

Figure 3. 26 – Examples of typical SAFT-Pan reconstructions at transversal cracks

Table 3. 9 – Crack ultrasonic evaluation

Section 1			Section 2			Section 3			Section 4		
Crack	HTI	Depth	Crack	HTI	Depth	Crack	HTI	Depth	Crack	HTI	Depth
	R	99	F		R	78	P		R	78	P
F1.1	C	81	F	F2.1	C	73	P	F3.1	C	97	F
	L	60	NC		L	77	P		L	74	P
	R	126	F		R	102	F		R	97	F
F1.2	C	117	F	F2.2	C	72	P	F3.2	C	81	P
	L	91	F		L	81	P		L	84	P
	R	106	F		R	98	F		R	100	F
F1.3	C	106	F	F2.3	C	81	F	F3.3	C	104	F
	L	107	F		L	74	P		L	120	F
	R	116	F		R	66	P		R	105	F
F1.4	C	95	F	F2.4	C	73	P	F3.4	C	110	F
	L	62	NC		L	62	P		L	112	F
									R	111	F
								F3.5	C	100	F
									L	112	F
									R	115	F
								F3.6	C	105	F
									L	118	F
									R	98	F
								F3.7	C	103	F
									L	107	F
									R	96	F
								F3.8	C	111	F
									L	111	F
									R	99	F
								F3.9	C	98	F
									L	111	F
									R	86	P
								F3.10	C	86	P
									L	108	F
									R	107	F
								F3.11	C	104	F
									L	110	F
									R	112	F
								F3.12	C	93	F
									L	106	F

NC= non-coclusive  
P = Partial Crack  
F = Full crack

As some SAFT-Pan reconstructions were not as conclusive as the ones featured in Figure 3.26, an investigation of the individual signals HTI was performed. Figure 3.27 displays the normalized HTI (minimum 90) to every signal on crack F2.3 (Right). As can be seen, most signals emitting from sensor 1 and 2 are compromised (high HTI) as well as all signals from sensor 3. Signal (30) from emitter sensor 4 and receiver sensor 10 also yields attention. Crack F2.3 received five overlapping (45 mm offset) scans being the first scan positioned with MIRA’s middle at the crack. The simulation of signal loss due to high HTI (higher than 90) is

presented in Figure 3.28. As can be seen, on the first scan the crack is positioned between sensors 3 and 4, and as the scans are moved the crack also change location accordingly to the predetermined 45 mm scan offset. Moreover, the simulation of the five scans proves that the crack is fully developed along the slab depth. It is also important to note that cracks are usually non-uniform and exhibit wandering shapes across the slab's depth. This helps to explain why this particular crack is positioned below sensor 3 and 4 and not below sensor 5 and 6 (MIRA's center).

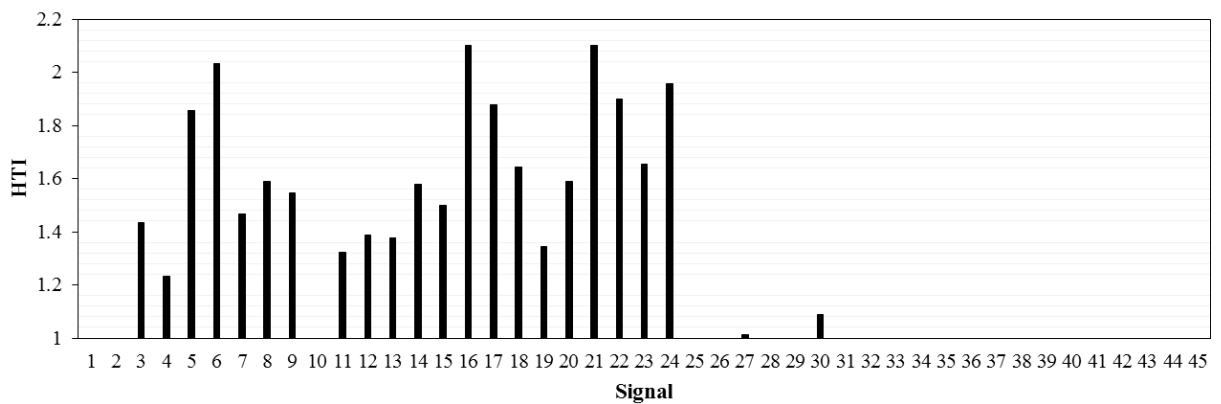


Figure 3. 27 – Normalized HTI for every signal in crack F2.3-R (first scan)

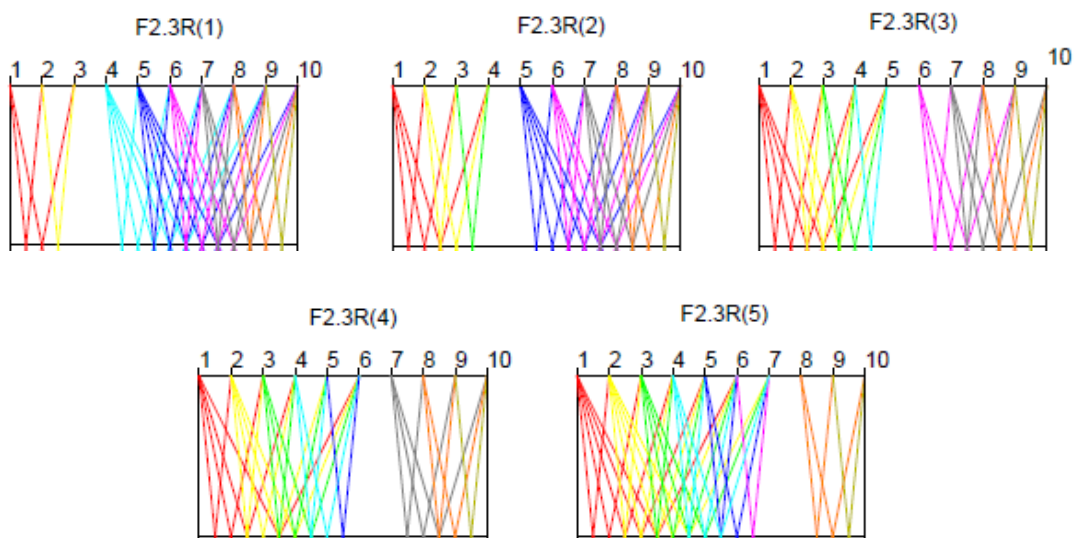


Figure 3. 28 – Simulation of crack F2.5-R scans based on HTI

Figure 3.29 shows another two examples where the crack is not yet fully developed. The presence of low HTI signals in the area near the backwall imply in two situations, a top-bottom partial crack or a crack that originates from the reinforcement location (around the slab half-height). The same simulation of signal loss was attempted to reinforcement MIRA scans to check if signals reaching the inclusion (longitudinal bars) would present high HTI to eliminate the possibility of steel bars to be interpreted as a distress by the HTI method. Results point out low HTI (less than 90) signals at the reinforcement. The assessment of every visible crack into partial (P) or full (F) crack is shown in Table 3.9. There is clear trend in which cracks presenting HTI higher than 93 are full developed cracks while cracks with HTI in between 66 and 92 are partially developed cracks. Cracks with HTI below 65 presented non-conclusive signal loss patterns because most signals exhibited HTI lower than 90 not showing a clear path in the simulations.

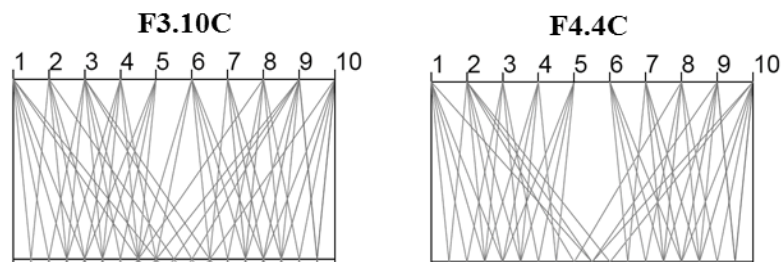


Figure 3. 29 – Signal loss due to high HTI in two partial cracks

### 3.3.1 MIRA simulations of transverse cracks

Transverse cracks were simulated as three different types illustrated in Figure 3.30: a full developed crack (F), partial top-down crack (TP), partial bottom-up crack (BU).. The crack was designed as a delaminated area with a 4 mm width. Unfortunately, due to computational time, 4 mm is the minimal analysis grid inside the MIRA simulation software. This simulated crack width is 4 times higher than the traditional maximum crack width for a good performance CRCP. Also cracks were simulated with low density and low shear wave velocity in an attempt to emulate a void.

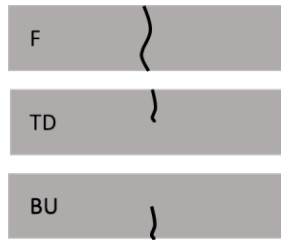


Figure 3.30 – Illustration of crack types

Simulation results are displayed in Figure 3.31. As can be seen, the simulated reconstructions were quite inconclusive. Simulations with a transversal bar showed the same results. There seems to be a backwall displacement for the full and TD cracks (simulated backwall was at 200 mm). The BU crack shows backwall reflection at the center of the reconstruction. HTI values were consistent with the analysis previously performed only for the full crack. The research team at the University of Minnesota currently works on updates to the simulation software

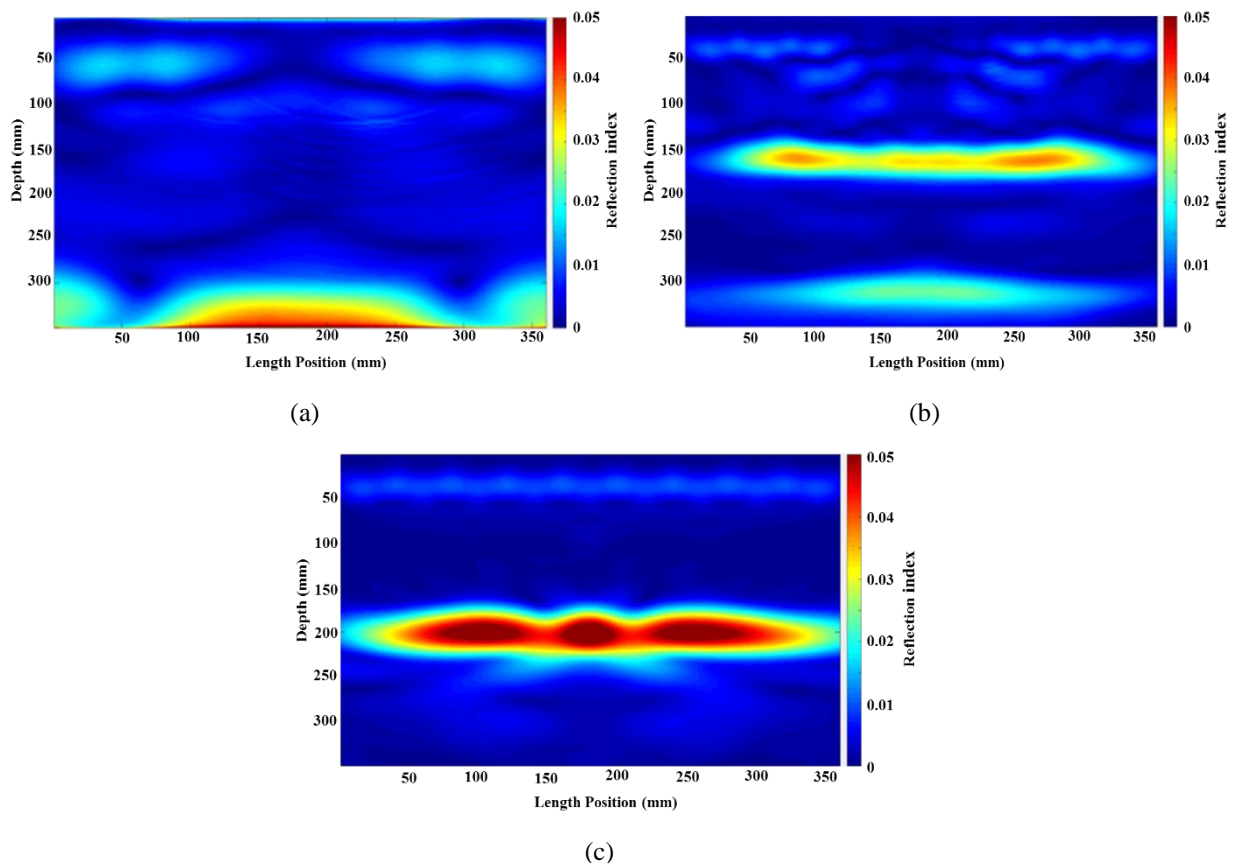


Figure 3.31 – Simulation of (a) Full crack, (b) Top-Down Crack and (c) Bottom-Up Crack

### 3.3.2 Non-visible cracks

SAFT-Pan reconstructions were performed for every slab panel between cracks. Figure 3.32 shows an example (Panel between cracks F4.8 and F4.7 in Section 4). It must be noted that this testing was held before cracks F4.11 and F4.12 were visible at the slabs surface. The scanning began at F4.8 exactly position proceeding in 90 mm steps until F4.7 position. Two regions (red circled) present similar inclusions as that of transversal cracks as discussed before. A crack survey performed one month after the MIRA testing disclosed both cracks now visible on the slab surface. New cracks F1.5, F2.6 (Figure 3.33), F4.9 and F4.10 were discovered in the same way. The first non-visible crack in Figure 3.33 has not yet fully developed to the slab surface, the second one is crack F2.6. However for some panels the non-visible cracks observation was not so easily done. Some mid-depth reflections can be misleading (possible transverse bars or delamination). It should be noted that the stronger backwall reflection may be an indicative of slab/base adhesion, however, no studies were found in that subject. For a more comprehensive analysis of the panels, the HTI was also considered. Figures 3.34 to 3.37 show the HTI variation trough the section's length along with the crack map for each section.

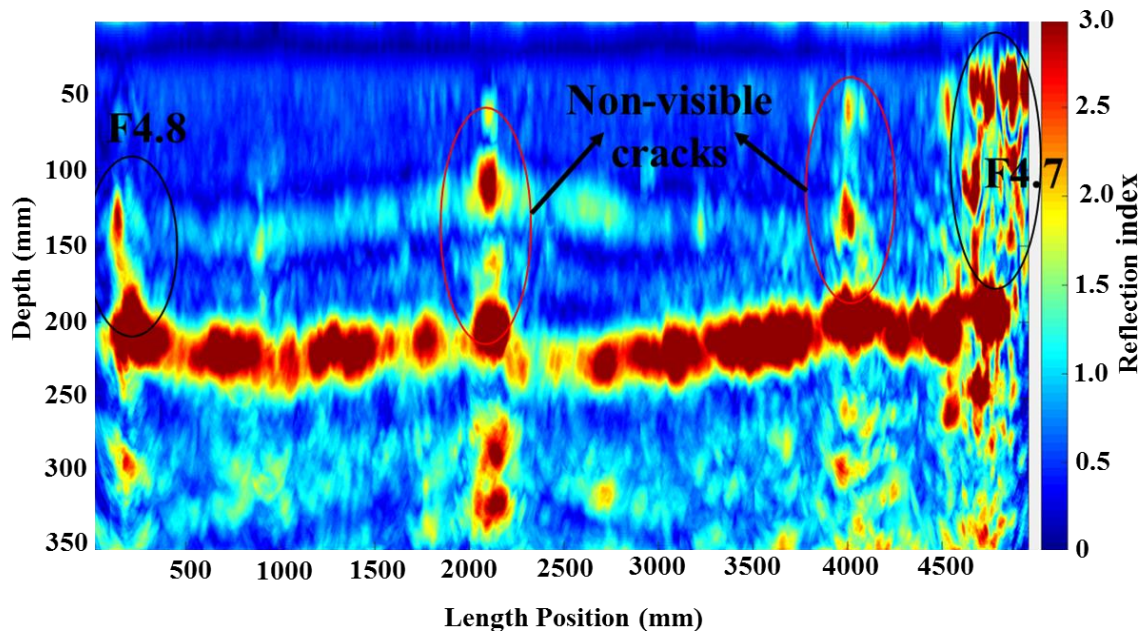


Figure 3. 32 – SAFT-Pan reconstruction of panel between cracks F4.8 and F4.7 in Section 4

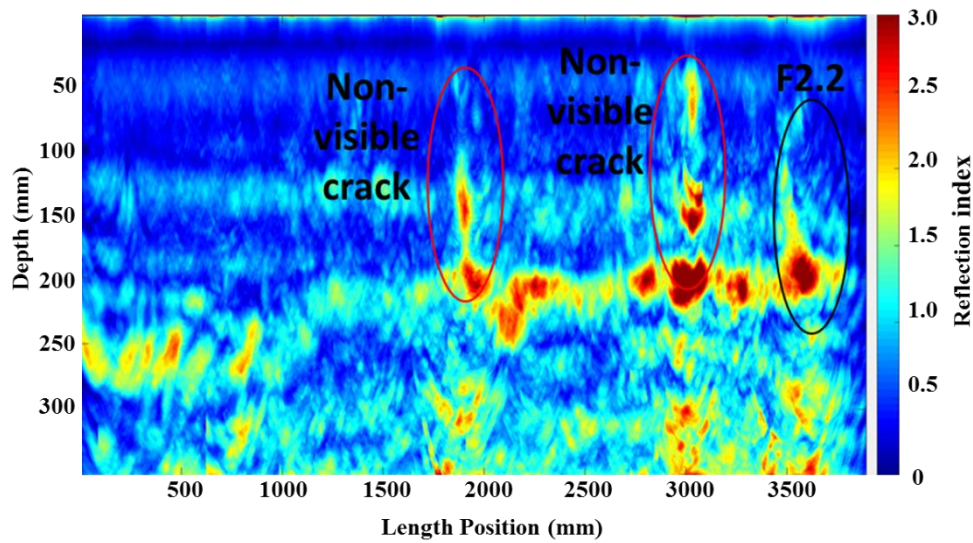


Figure 3. 33 – SAFT-Pan reconstruction of panel between Section 1 and F2.2 in Section 2

Because of the short length, panels between cracks F1.3 and F1.4 (Section 1) and F3.9 and F3.1 (Section 3) were not selected for this evaluation. Also, the section 1's edge and F1.1 panel was not considered for further crack evaluation. As can be seen in Figure 3.34, the panel presents high HTI values through its entire length. This inadequate performance was expected because there is a poor consolidation area in the interlock pavement near the short CRCP joint causing a vertical gap between both pavements. This resulted in abnormal impact by heavy vehicles assessing section 1 which was ensued by joint faulting and corner cracks (Figure 3.38). Additionally, the thickness for that area was deficient presenting values as low as 184 mm what certainly accelerated the fatigue process.

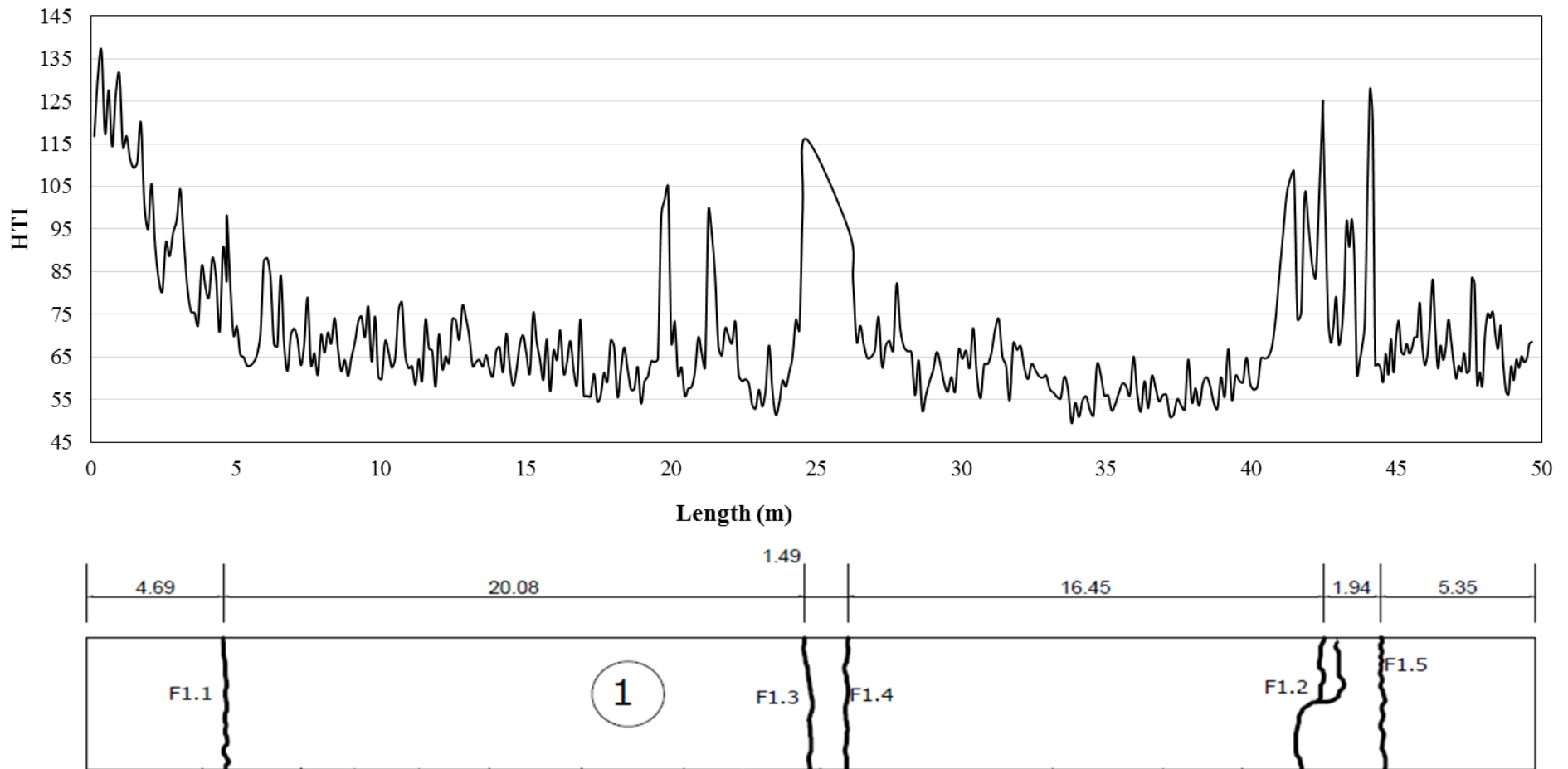


Figure 3. 34 – HTI trough Section 1

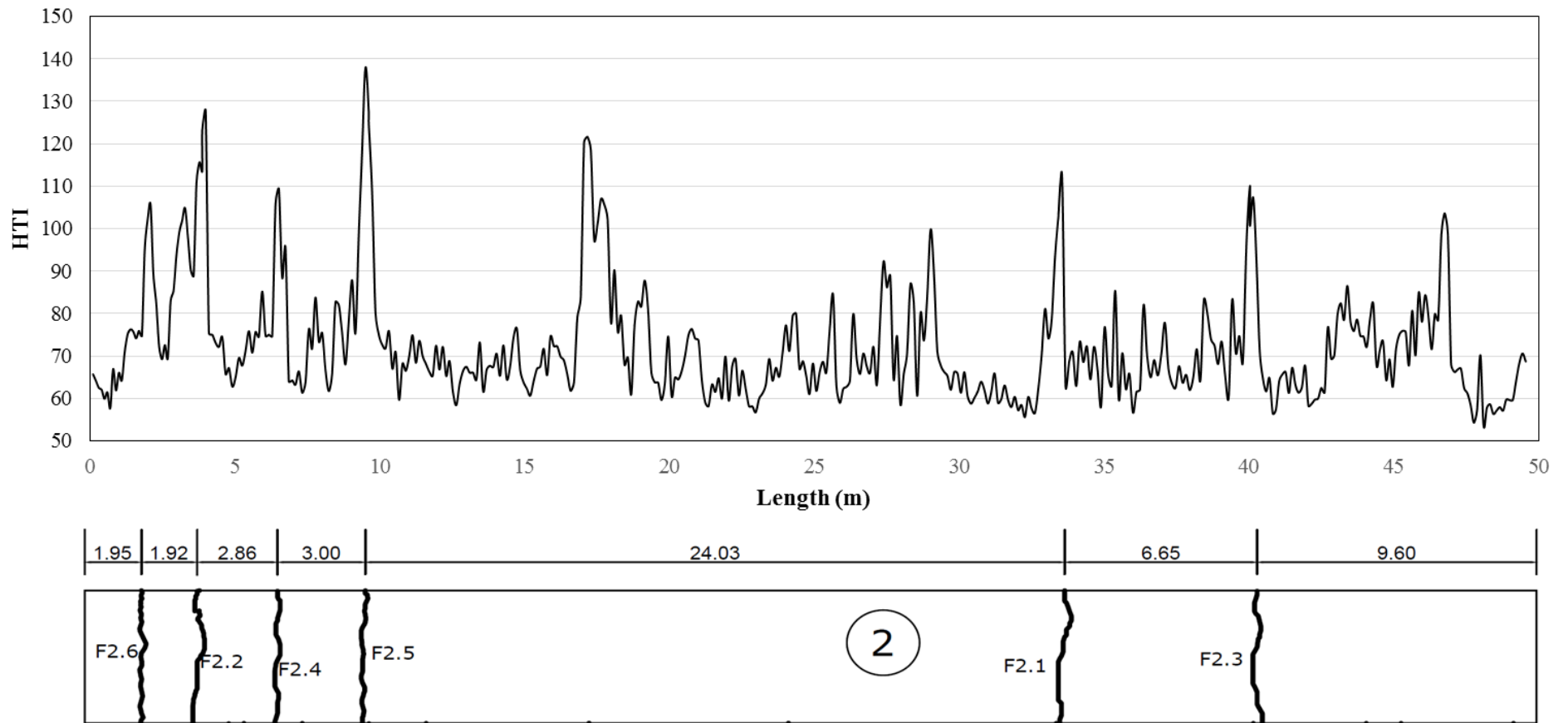


Figure 3. 35 – HTI trough Section 2

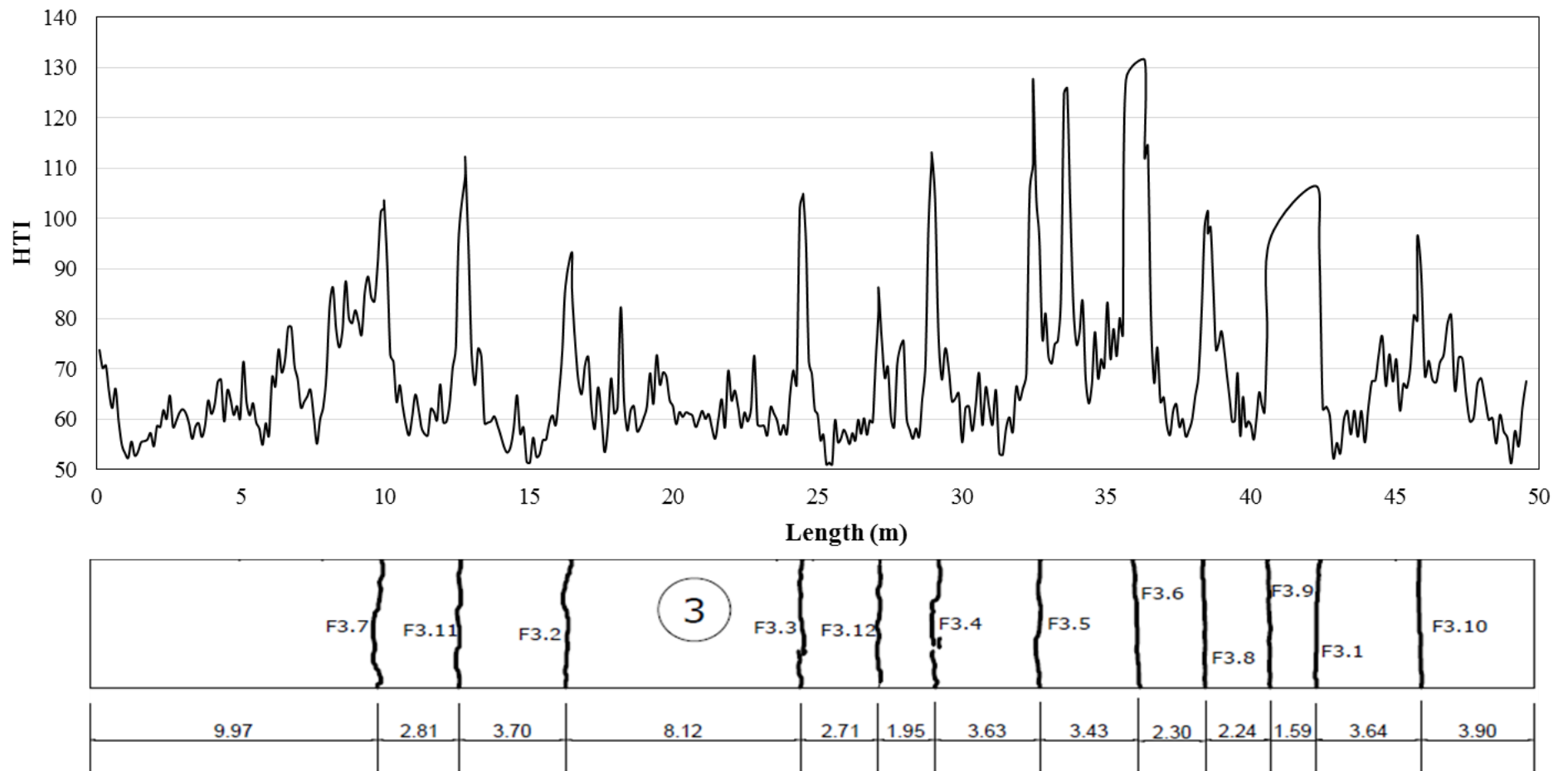


Figure 3. 36 – HTI trough Section 3

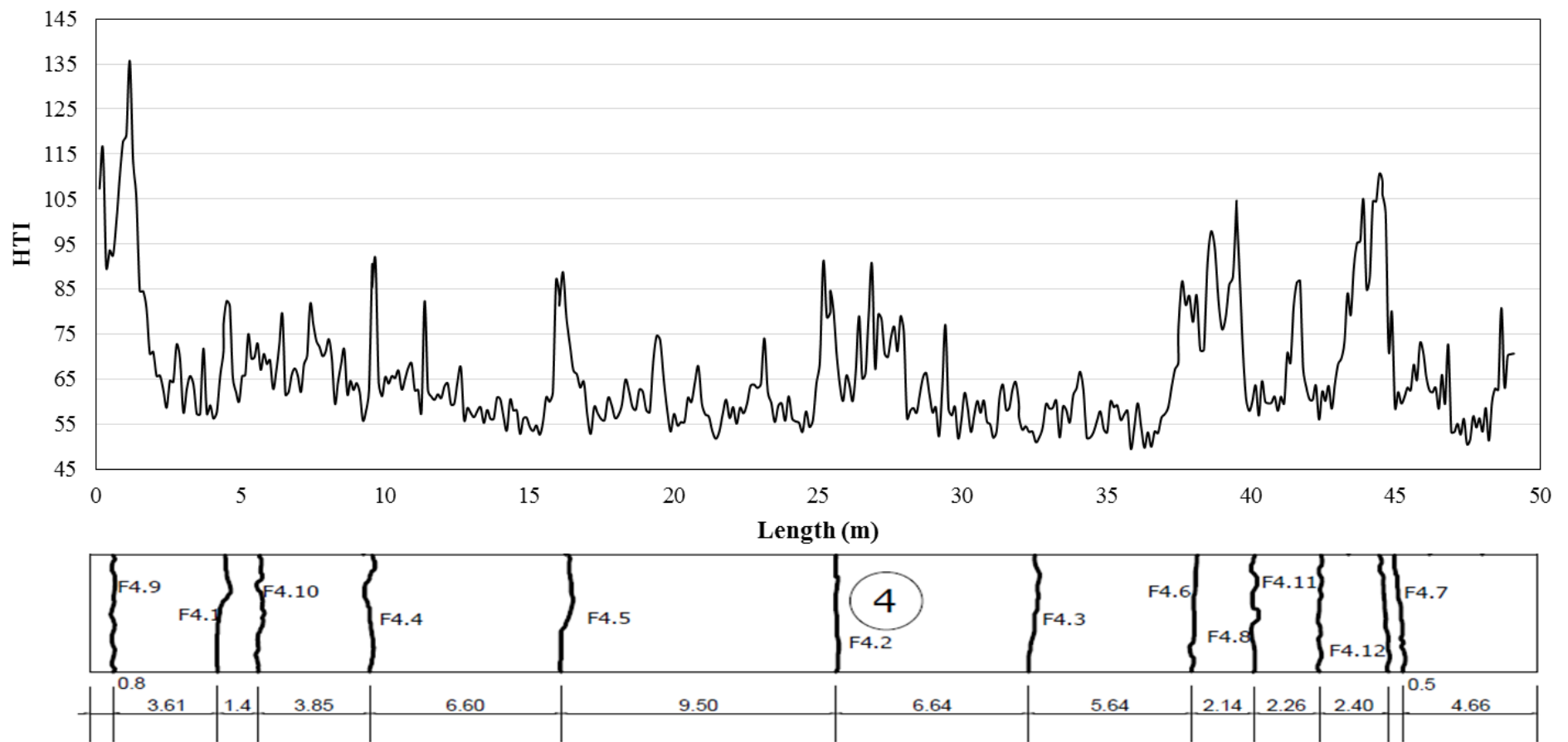


Figure 3.37 – HTI trough Section 4



Figure 3. 38 - Distresses in the transition between interlock pavement and the short CRCP section 1

As can be seen, there is a rise in HTI value at every visible crack, save crack F4.3. However when analyzing crack F4.3 isolated (Figure 3.39), it is possible to see for both set of measurements a rise in HTI at the crack. Concerning this issue, it was established that whenever a point exhibited a peak of HTI the B-Scan of such point was analyzed for having any of the crack features described in the prior section as well as the individual signal loss by means of high HTI. If the crack feature was found along with a coherent signal loss, the location was considered a non-visible crack. The measurement was considered an HTI peak when it presented a value higher than the panel's average HTI and a value higher than the average HTI of the 5 prior and subsequent measurements. Signal loss due to high HTI was investigated by comparison of the three simulations illustrated in Figure 3.40.

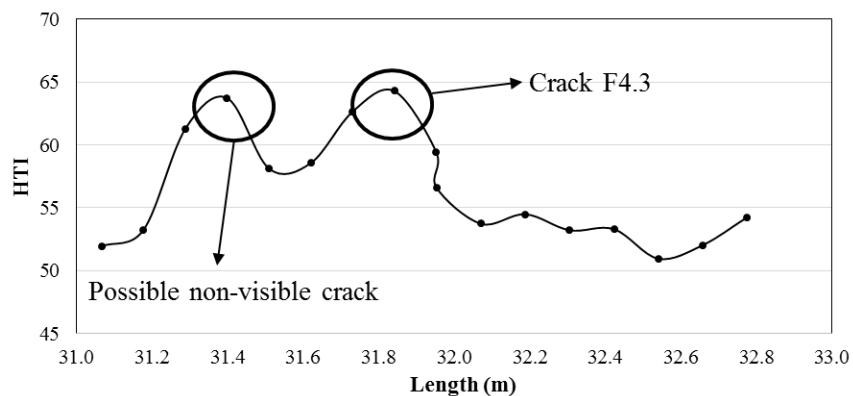


Figure 3. 39 – Crack F4.3 visualization

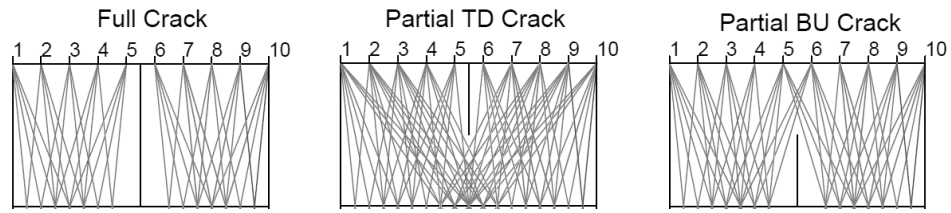


Figure 3. 40 – Signal loss simulation for full, partial top-down (TD) and partial bottom-up (BU) crack

Table 3.10 presents the results for non-visible (IC) cracks analysis. The distance from the section’s edge (traffic direction) and the crack depth based on signal loss are displayed. Unlike the visible cracks, the majority of the non-visible cracks are partially developed, as anticipated since they do not show on the slab surface. However some cracks presented a fully developed signal loss characterization. Those are intuitively expected to show up at the slab surface in the next crack surveys.

Table 3. 10 – Non-visible cracks

Section 1			Section 2			Section 3			Section 4		
Non-visible crack	Dist. (m)	Depth									
IC-1.1	6.08	P	IC-2.1	3.17	F	IC-3.1	6.64	P	IC-4.1	7.41	P
IC-1.2	7.74	P	IC-2.2	8.46	P	IC-3.2	8.19	F	IC-4.2	11.37	P
IC-1.3	8.40	P	IC-2.3	14.72	P	IC-3.3	8.64	P	IC-4.3	19.40	P
IC-1.4	9.79	P	IC-2.4	15.88	P	IC-3.4	19.43	P	IC-4.4	20.85	P
IC-1.5	10.72	P	IC-2.5	17.16	F	IC-3.5	27.85	P	IC-4.5	26.86	P
IC-1.6	16.89	P	IC-2.6	17.74	F	IC-3.6	33.63	F	IC-4.6	27.85	P
IC-1.7	19.89	F	IC-2.7	19.14	P	IC-3.7	34.17	P	IC-4.7	29.40	P
IC-1.8	21.40	F	IC-2.8	24.25	P	IC-3.8	35.24	P	IC-4.8	34.06	P
IC-1.9	27.02	P	IC-2.9	25.64	F	IC-3.9	38.97	P	IC-4.9	38.60	F
IC-1.10	41.34	F	IC-2.10	27.38	P	IC-3.10	44.43	P	IC-4.10	45.84	P
IC-1.11	45.08	P	IC-2.11	28.31	P	IC-3.11	46.81	P	IC-4.11	48.66	P
IC-1.12	46.25	P	IC-2.12	29.00	F						
IC-1.13	48.32	P	IC-2.13	35.38	P						
			IC-2.14	38.43	P						
			IC-2.15	43.27	F						
			IC-2.16	44.28	P						
			IC-2.17	46.07	P						
			IC-2.18	46.86	F						

P = Partial crack  
F = Full crack

For the partial cracks, the most predictable pattern would be a bottom up (BU) crack due to the lack of surface development. However, several types of cracks were observed as can be seen in Figure 3.41. Only crack IC-3.3 presents a configuration that can be described as a BU crack below sensor 6. The majority of the partial cracks show the same characteristics of the visible cracks. This may be an indicative that most non-visible cracks show a similar development pattern to the visible crack, as expected. It is assumed that for the short CRCP, most cracks begin at the reinforcement and develop up and down with time in a similar behavior than traditional CRCP as seen in Jung *et al.* (2012).

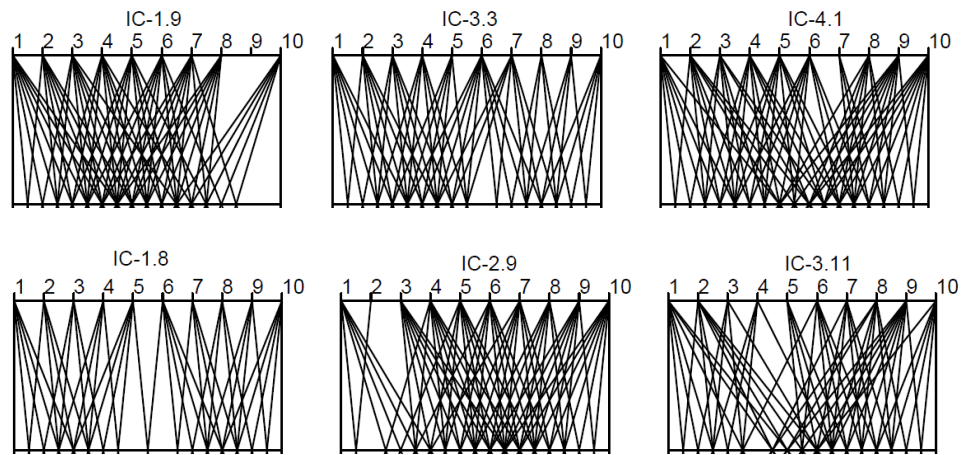


Figure 3. 41 – Signal loss due to high HTI in non-visible cracks

#### 4. CRACK PATTERN ANALYSIS

As seen in Balbo *et al.* (2012), the first crack surveys were performed within two weeks of construction, resulting in non-occurrence of any crack in the four sections; later, surveys were carried out monthly, but with the same result. It was only in October 2011, after a year and two months of construction, that the first crack was visible in section 3 (F3.1 in Figure 4.1). From this first crack five more were found in section 3, and three in Section 4 in January 2012. Due to the more fast cracks development, surveys were carried out every two months. Figure 4.1 shows the updated crack map as of January 2017 while Figure 4.2 displays the crack pattern evolution (every new is crack is presented in red). Cracks evidenced in July 2015 and January 2017 were predicted by the non-visible crack methodology presented in the last chapter.

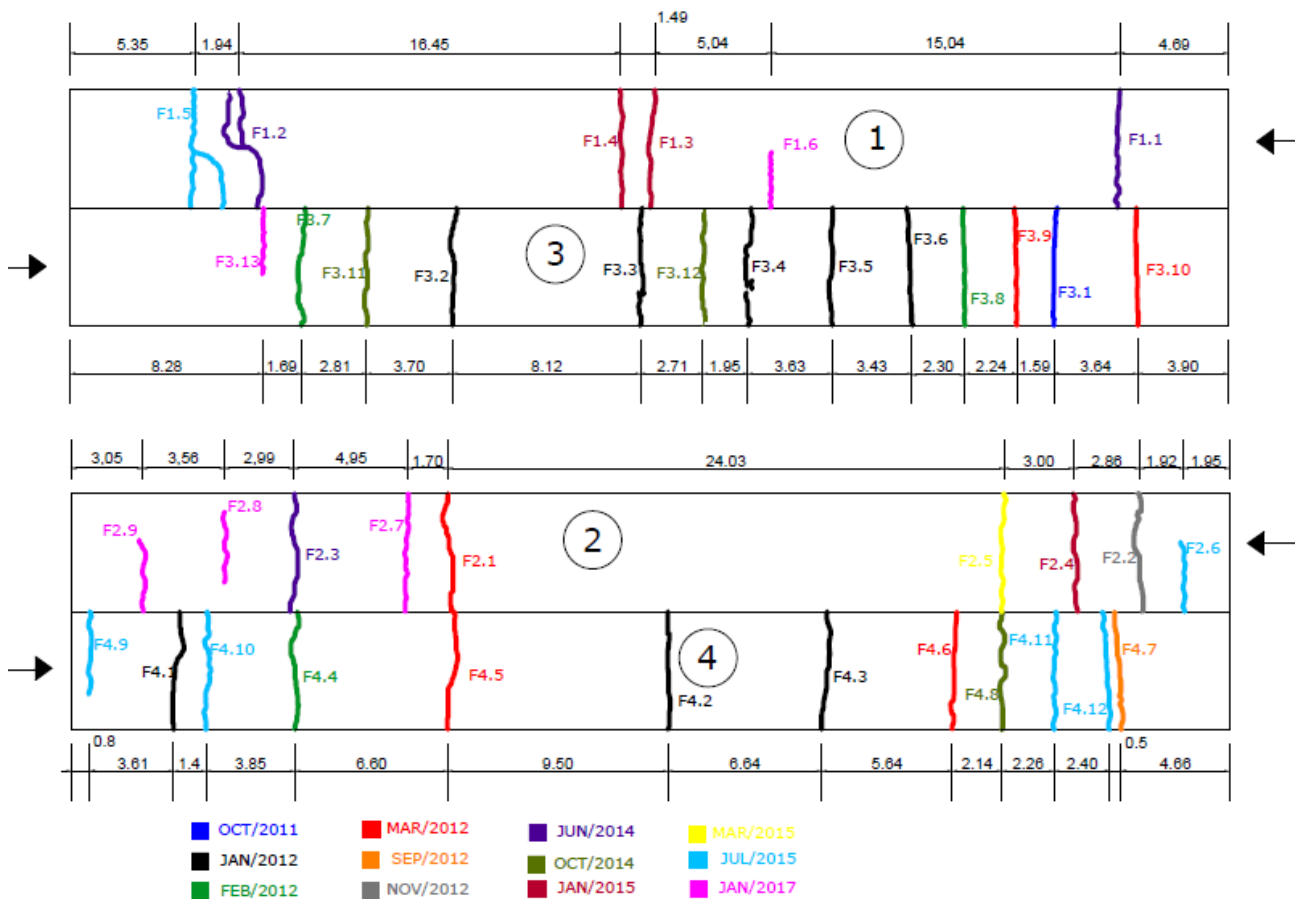


Figure 4. 1 – Updated crack map (June 2015)

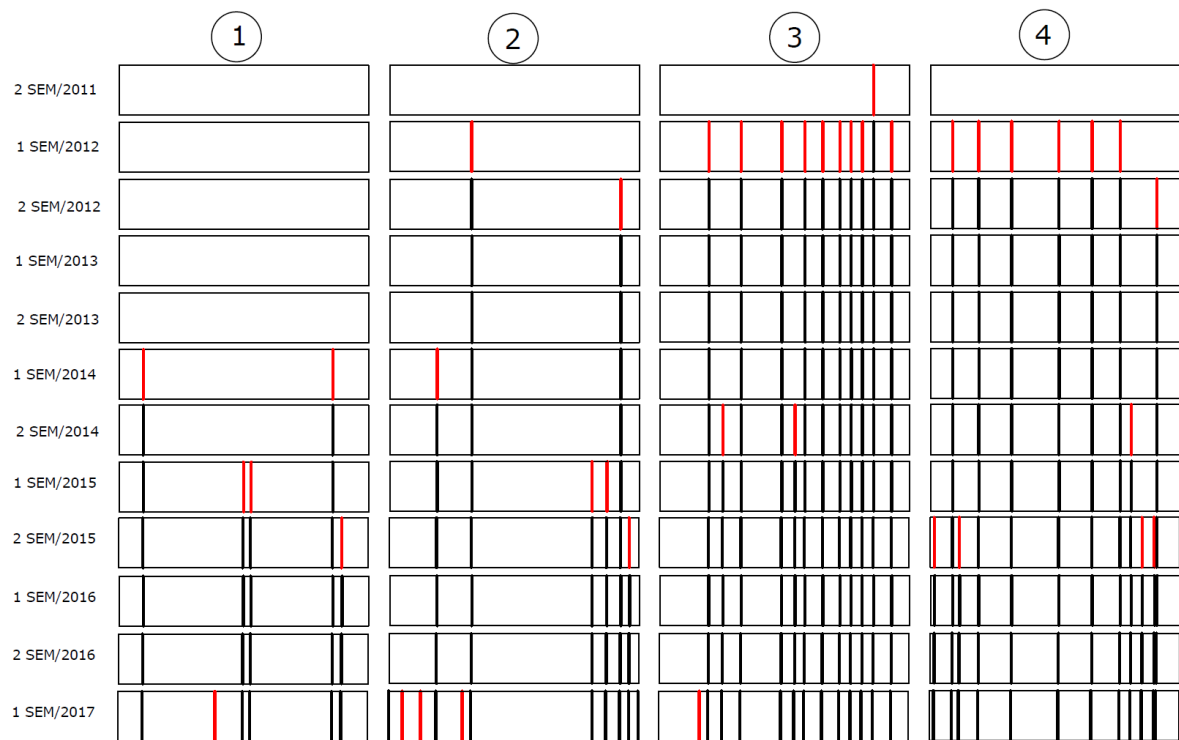


Figure 4. 2– Crack pattern evolution

As can be seen in both Figures 4.1 and 4.2, the major difference presented by the short CRCP cracking regarding traditional CRCP is the cracking time. As observed by several studies, it is expected that the CRCP begins to develop cracks, if not immediately after the construction, in a maximum two-month time; it was also expected that the whole cracking process to last no more than two years (GHARAIBEH *et al.*, 1999; KOHLER and ROESLER, 2004; TAYABJI *et al*, 1998a;. TAYABJI *et al*, 1998b.). The short CRCP first crack took over one year to be visible on the slab surface. For section 1, cracks would only be visible after three years from construction.

As seen in Salles *et al.* (2015), basic knowledge of conventional concrete technology ensures that a 50 m concrete surface without cracks is highly unlikely to occur. Regarding this, cracks are considered to be in the slabs from the construction and curing period, however, these cracks are not visible on the surface due to three main reasons: first, the short length; second, there is no anchoring system at the slabs end, and third, the concrete has been placed over a 60 mm thick asphalt concrete base, creating a strong bond breaker between slab and base interfaces. These three particular design aspects combined allow a more freely concrete

horizontal movement during construction and curing avoiding greater shrinkage stresses. Additionally, the MIRA data analysis disclosed steel depth below the slab mid-height, which makes the reinforcement lose potential in its restriction characteristic. The combination can help hide the retraction mechanism, but does not stop it; the cracks are there, only prevented from appearing at the surface by the longitudinal reinforcement strong tying effect. Additionally, for the more recently discovered cracks (July 2015 and January 2017 surveys), there was some examples cracks not entirely visible along the slab width. This may indicate a slower crack development to the surface with time.

Due to this different cracking process, the resulting crack spacing was greater than the traditional CRCP one. Figure 4.3 presents the cumulative crack spacing for the four sections. The two vertical red lines in Figure 4.3 mark the recommended crack spacing by the AASTHO Design Guide (1993). According to this guide and other studies, cracks should be spaced no more than 2.4 m to avoid loss in load transfer efficiency and no less than 0.9 m prevent crack intersection which can lead to punchout distresses. Experience from traditional CRCP shows that the cumulative crack distribution reaches 100% with crack spacing below 3.0 m for a two-year old pavement and that the AASTHO recommendation range comprehends between 50 and 90% of crack spacing in a CRCP with good performance (MCCULLOUGH and DOSSEY, 1999; TAYABJI *et al.*, 1998a). Only section 4 approaches the criteria regarding cumulative crack spacing. However this same section also presents two spacing with less than 0.9 m which is considered as non-ideal. The new recommended crack spacing by AASTHO (2008) ranges from 0.9 to 1.8 m but it was not plotted against the short CRCP crack spacing due to the lack of studies attesting the recommendations efficacy.

Moreover, the steel percentage had the expected effect in the short CRCP; sections 3 and 4 with more steel presented more visible cracks than section 1 and 2. In the same way section 2 with a higher steel percentage than section 1, presents more cracks.

As for the cracks shape, there are two divided cracks (F3.2 and F3.3) on section 3 and two “Y” cracks (F1.2 and F1.5) in section 1 (Figure 4.4). The “Y” crack was highlighted in black and red in Figure 4b because the crack was very tight making it hard to be visible in the photograph. Those crack types are regarded as non-desired due to their greater potential for

punchouts (ZOLLINGER and BARENBERG, 1990). Despite those four cracks, all the others are straight and uniform presenting no signs of spalling.

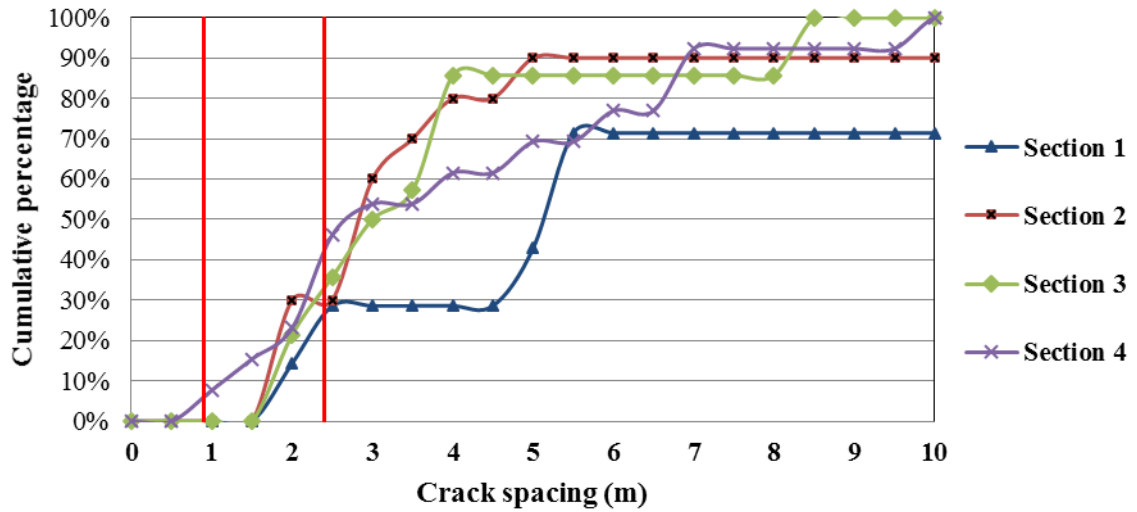


Figure 4. 3 – Cumulative crack spacing regarding visible cracks

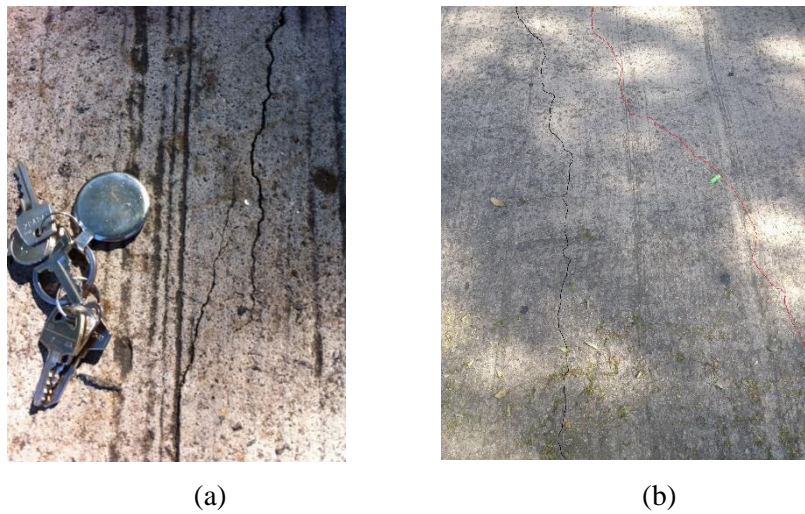


Figure 4. 4 – Divided crack (a) in section 3 and “Y” crack (b) in section 1

#### 4.1 Non-visible crack pattern

Figure 4.5 displays the crack map with the non-visible cracks. Visible cracks are noted by Fx.y and non-visible cracks by Ix.y, where x is the section's number and y is the crack number according to the time in which each crack was observed for the first time for the visible cracks and to the traffic direction for the non-visible cracks. Agreeing to this new map, sections 2, 3 and 4 have the similar number of cracks (24 for section 2 and 23 for sections 3 and 4) while section 1 presents a smaller amount (18). As proven by the MIRA analysis, section 1 has the less steel percentage and therefore was expected to present fewer cracks. Supposedly, the steel percentage difference of 0.1 from section 2 to sections 3 and 4 was not influential in the overall number of cracks but was decisive in the development of cracks to the slab's surface. Moreover, this crack map seems more in accordance with traditional CRCPs. There is only 7 panels with length over 5 m with only one being excessively long (14.32 m). Additionally, several panels present a very small crack spacing (less than 0.9 m). If this potential new cracks are individual cracks or part of a "Y" crack remains to be seen. Nevertheless, this MIRA technique reveals potential for evaluation of cluster cracking or "Y" crack areas before the problem is visible.

Non-visible cracks I1.7 (Section 1), I3.2 (Section 3), I2.13, I2.15 and I2.18 (Section 2) were observed at the slab surface in the January 2017 crack survey proving the ability of the non-visible crack methodology to predict the cracks location. These cracks are now cracks F1.6, F3.13, F2.7, F2.8 and F2.9, respectively, as seen in Figure 4.1. The average difference in location indicated by the MIRA survey and the location in which the crack emerged at the slab surface was 104 mm. This difference can be improved adopting a more precise MIRA survey spacing in future testing.

The updated cumulative crack spacing graph is shown in Figure 4.6. Again, the inclusion of the non-visible cracks results in a much more similar crack spacing as that found in technical CRCP literature. Now all sections comply with the crack spacing recommendation of AASTHO (1993). However, a greater potential for cluster cracking is also observed.

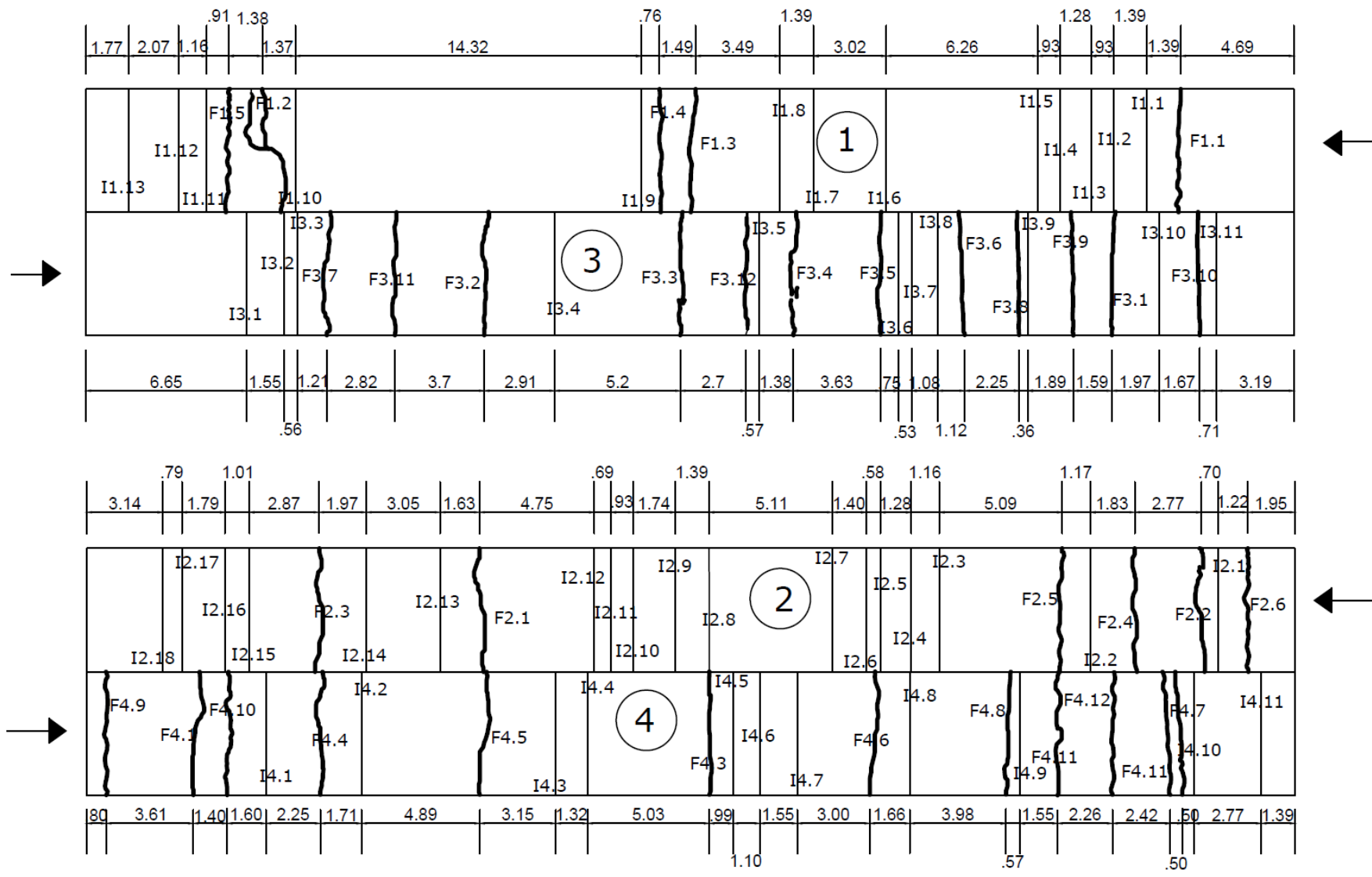


Figure 4.5– Crack map with visible and non-visible cracks

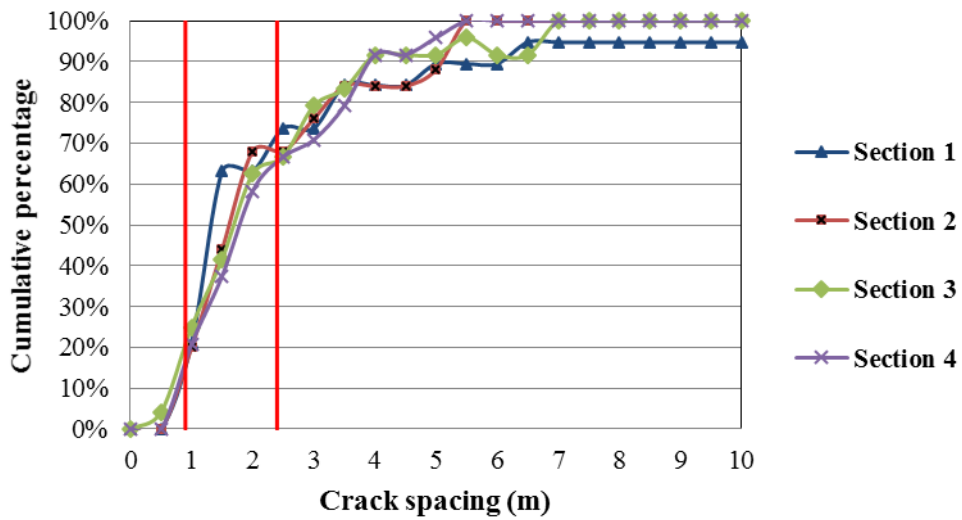


Figure 4. 6 – Cumulative crack spacing for non-visible crack map

#### 4.2 Crack width

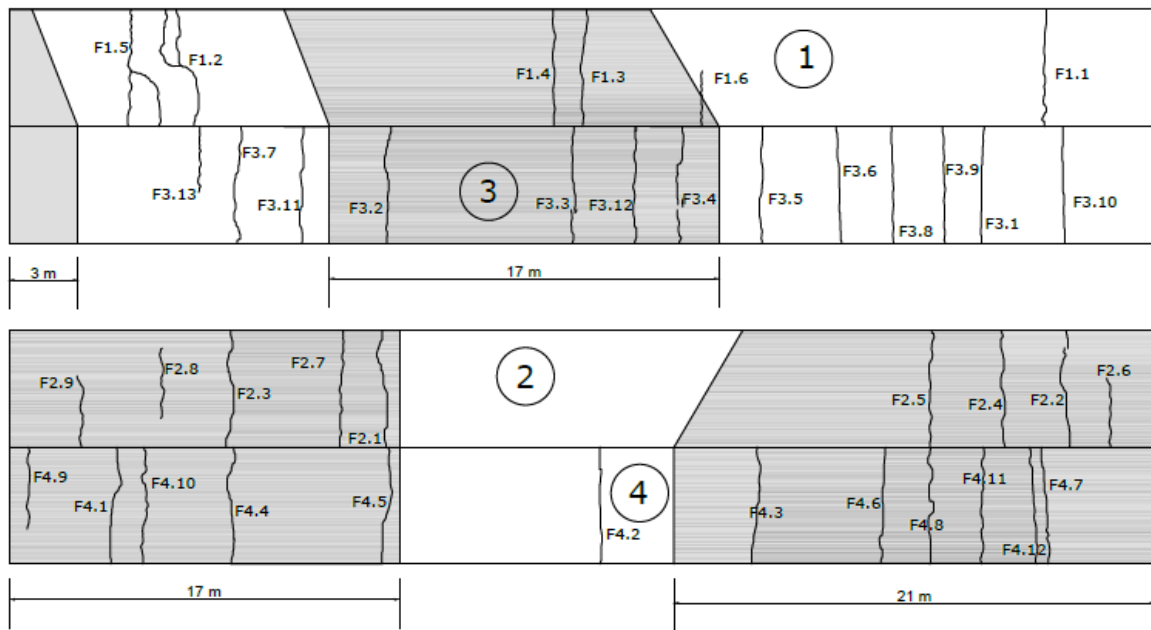
The crack width was determined with a ruler on the slab surface. Although fast, this method only provides the crack width at the surface; it is known that crack width varies with depth (NAM *et al.*, 2006). Table 4.1 presents the crack width for three position, right (R – near the edge), center (C) and left (L - near the center line) along with the average crack width from these three measurements. When the crack is not visible on the position the width value is 0.00. The air temperature during the survey was 24°C.

Most cracks are more wide on the left side (L), near the center line and more tight on the right side (R) near the edge. The traffic is the same in both positions and there is almost no traffic in the lane center, so is reasonable to assume that the traffic plays no role in this disparity of values. The proximity with the edge could explain the smaller crack width on the right side; at this point the slab could be more stable. The left side is more close to the longitudinal joint that separates two slabs making it a weaker position, more suitable to crack opening variations. Sun *et al.* (2011a), as mentioned in the literature review, observed greater deformations and movements in areas close to the longitudinal joint.

Table 4. 1 – Surface crack width in three positions

	R (mm)	C (mm)	L (mm)	Average (mm)		R (mm)	C (mm)	L (mm)	Average (mm)
F1.1	0	0.25	0.10	0.12	F3.1	0.10	0.25	0.25	0.20
F1.2	0.10	0.50	0.75	0.45	F3.2	0.25	0.25	0.25	0.25
F1.3	0.25	0.50	0.75	0.50	F3.3	0.50	0.50	1.00	0.67
F1.4	0.25	0.10	0.10	0.15	F3.4	0.50	0.50	0.50	0.50
F2.1	0.10	0.25	0.25	0.20	F3.5	0.50	0.50	0.75	0.58
F2.2	0.10	0.25	0.25	0.20	F3.6	0.25	0.50	0.50	0.42
F2.3	0.10	0.25	0.10	0.15	F3.7	0.10	0.10	0.25	0.15
F2.4	0	0.10	0.10	0.07	F3.8	0.10	0.25	0.50	0.28
F2.5	0.10	0.25	0.25	0.20	F3.9	0.10	0.25	0.25	0.20
F4.1	0.10	0.25	0.25	0.20	F3.10	0	0.10	0.25	0.12
F4.2	0.25	0.10	0.25	0.20	F3.11	0.25	0.25	0.25	0.25
F4.3	0.25	0.25	0.25	0.25	F3.12	0.10	0.25	0.50	0.28
F4.4	0	0.10	0.25	0.12					
F4.5	0.10	0.10	0.25	0.15					
F4.6	0.10	0.10	0.25	0.15					
F4.7	0.10	0.25	0.25	0.20					
F4.8	0.10	0.25	0.10	0.15					

Also, the condition of sunlight at the slab was observed. The map in Figure 4.7 illustrates the trees' shadow on the short CRCP surface. The data is from 10:30 a.m. in a sunny January day (precisely January 23<sup>rd</sup>). Strangely, for sections 2 and 4, save for crack F4.2, all visible cracks developed in a shadow area. Common knowledge says that areas with sunlight tend to present greater temperature than areas without it, which has a negative impact in concrete curing increasing concrete shrinkage stresses. Yet, for sections 3 and 1, both with less covered area than sections 2 and 4, the lack of sunlight did not created areas with less cracking. Moreover, no effect of extra heating due to sunlight in crack width was observed. Cracks in direct sunlight did not present smaller surface widths as expected regarding the concrete natural expansion.



(a)



(b)

Figure 4. 7 – Sun light condition at the short CRCP surface

To further consider the environmental conditions during the crack width survey, the temperature and relative humidity throughout and before the survey day were investigated. Figure 4.8 presents the data. As can be seen, the days prior to the survey are typical of the São Paulo winter: mild temperatures during the night and morning followed by hotter afternoons.

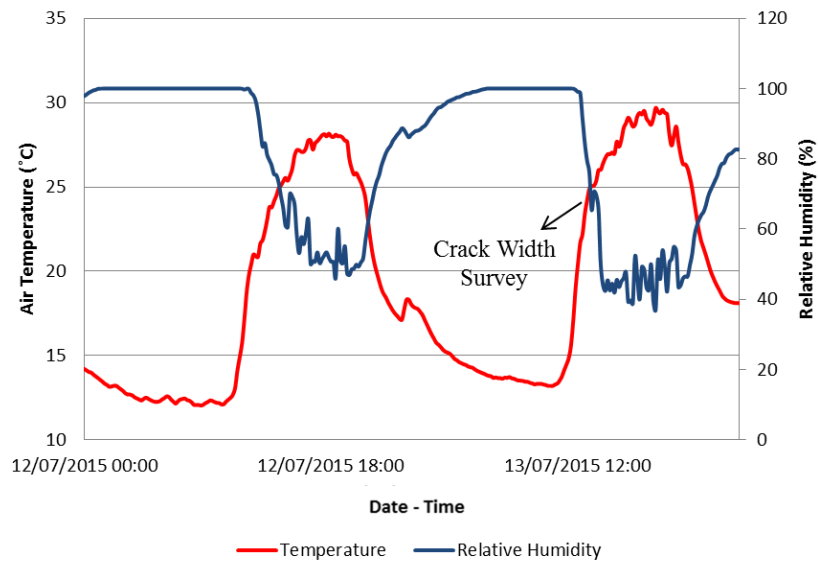


Figure 4. 8 – Climate conditions during and prior to the crack width survey

It was expected that sections with greater steel percentage would present tighter cracks. Table 4.2 explores this correlation. Steel percentage shows reasonable corresponding crack width for sections 1 and 4, whereas for section 2 and especially for section 3 it presents uncoherent results. Observing the other parameters, it is clear that steel depth plays a much more important role on keeping cracks tight than steel percentage or the ratio between steel depth and slab thickness. This conclusion while intuitive and in accordance with previous studies, shows that small changes in steel depth can have a great effect in crack width.

Table 4. 2 – Surface crack width *versus* steel percentage

	Avg. Surface Crack Width (mm)	Steel Percentage (%)	Avg. Slab Thickness (mm)	Avg. Steel Depth (mm)	SD/thickness
Section 1	0.30	0.52	216.1	122.4	0.57
Section 2	0.16	0.71	201.2	112.1	0.56
Section 3	0.33	0.82	221.1	122.8	0.56
Section 4	0.18	0.83	195.3	99.5	0.51

HTI was also related to crack width as, intuitively, a more open crack can be expected to present a higher level of erosion and damage. As revealed by Figure 4.9, tighter cracks can

present several levels of HTI while wider cracks (width over 50 mm) only show damaged indexes (HTI above 90).

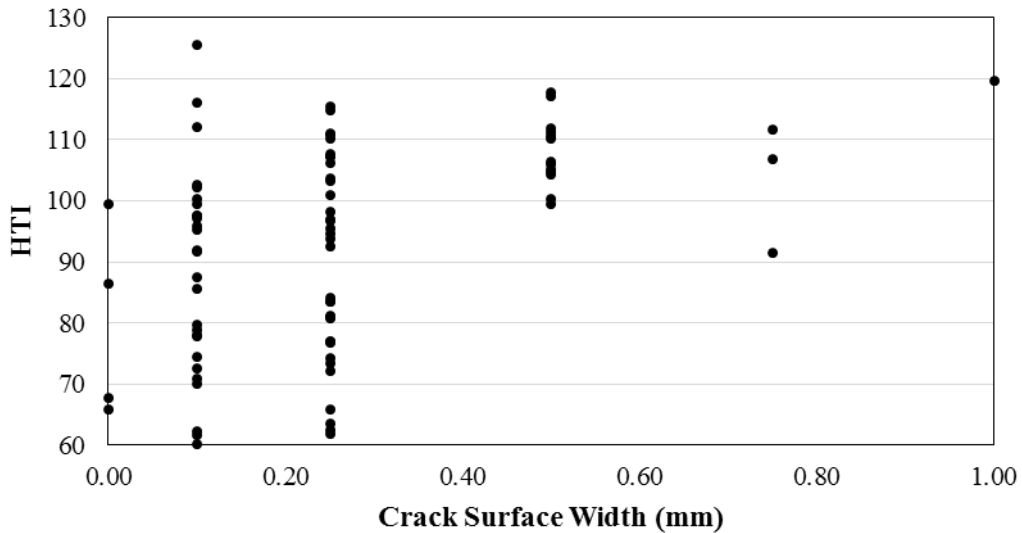


Figure 4. 9 – HTI versus surface crack width

### 4.3 Falling Weight Deflectometer (FWD) testing and previous data

Two deflections surveys with FWD were performed. The first was held in June 2013 with an average air temperature of 20°C, featuring the pavement in the São Paulo winter. On the other hand, the second survey took place in a summer day in February 2015 (average 24°C). Both tests were carried out with a load of 60 kN. Deflection basin analysis and load transfer efficiency (LTE) for the first survey can be found in Salles and Balbo (2014).

For LTE determination, the FWD must be positioned in a way that two sensors become equally distanced from the crack, one in the loaded slab and the other in the unloaded slab as Figure 4.10 illustrates. For basin analysis purposes, the FWD can be positioned anywhere in the slab as long as the position is carefully recorded for future simulations. As a more rational testing scheme, the FWD was placed always in the slab panel middle in-between two consecutive cracks (panel) with the device's vehicle moving in accordance to the traffic direction.

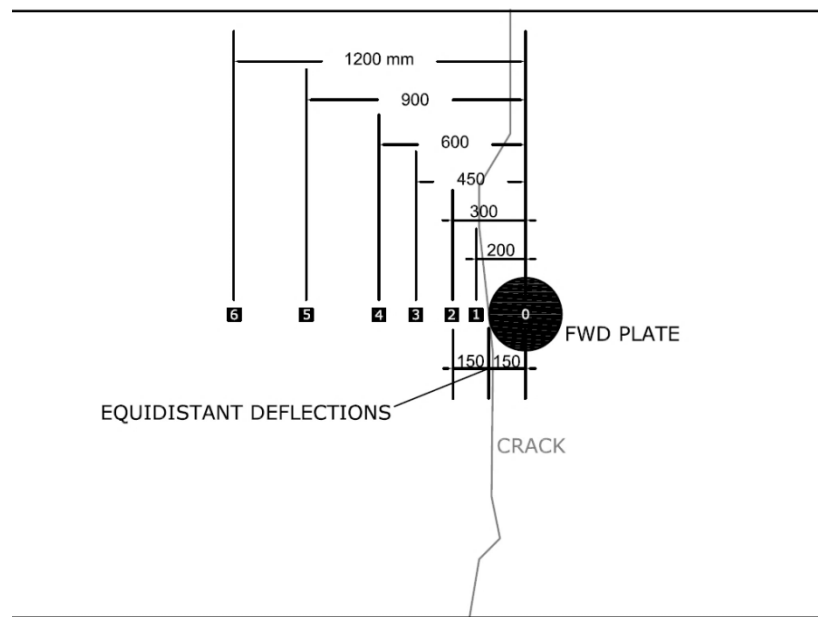


Figure 4. 10 – Illustration of FWD position to evaluate crack LTE

Table 4.3 provides the final results from the analysis of the 2013 winter survey. LTE was calculated based on the classic concept of Equation 1. The backcalculation process was performed by slab simulation through the software EVERFEE, developed by Davids *et al.* (1998), in which the cracks were considered as joints without dowel bars. A quadratic error was calculated between real and theoretical deflection for all six sensors; errors sum below 1.00 were regarded as acceptable. The concrete modulus of elasticity (E) and subgrade modulus of reaction (k) were firstly estimated based on the studies of Hall (1991) and Croveti (1994). It should be noted that the slabs index was based on the crack map of June 2013, presented as reference in Figure 4.11 (cracks in red were yet to be discovered). As Section 1 had not yet showed any visible cracks, the FWD took place 5 m from each transverse edge and 10 m apart for subsequent locations. The complete backcalculation process can be found in Salles and Balbo (2016).

The E variation is reasonable to concrete pavements safe the values presented by locations P1.1 and P2.2. The low E value presented by the former can be explained by the advanced concrete deterioration presented by that region as shown in Figure 3.38 whereas the high value displayed by latter may be an indication of higher stability around that area in accordance to the high k (200 MPa/m). Yet, the abnormal value can also be a result of FWD

testing failure due to imbalanced plate placement. The k high variation can be elucidated by the irregular earthworks that were conducted around the whole area of the University of São Paulo campus during its past implementation. There are several locations where the soft soil was partially replaced by large crushed stone (material retained at the 76 mm sieve) creating an uneven support area<sup>1</sup>.

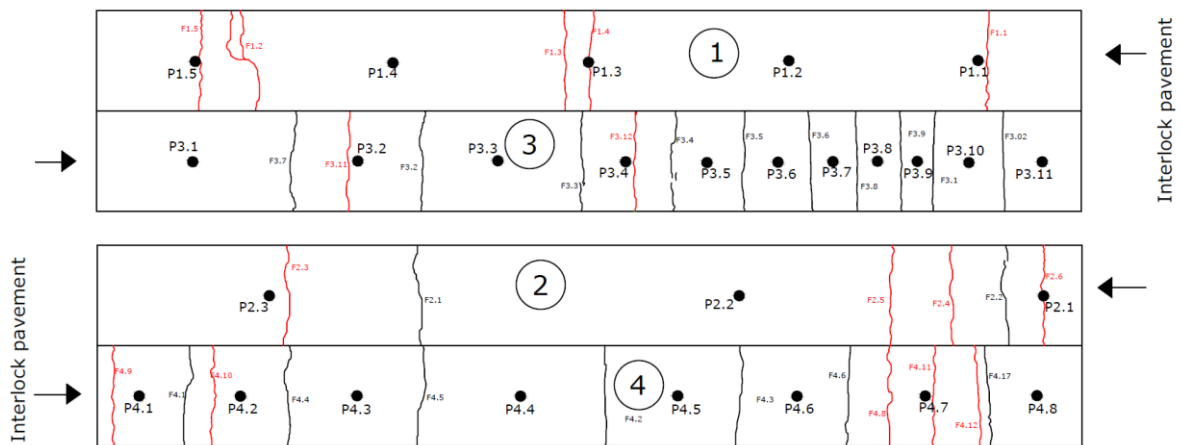


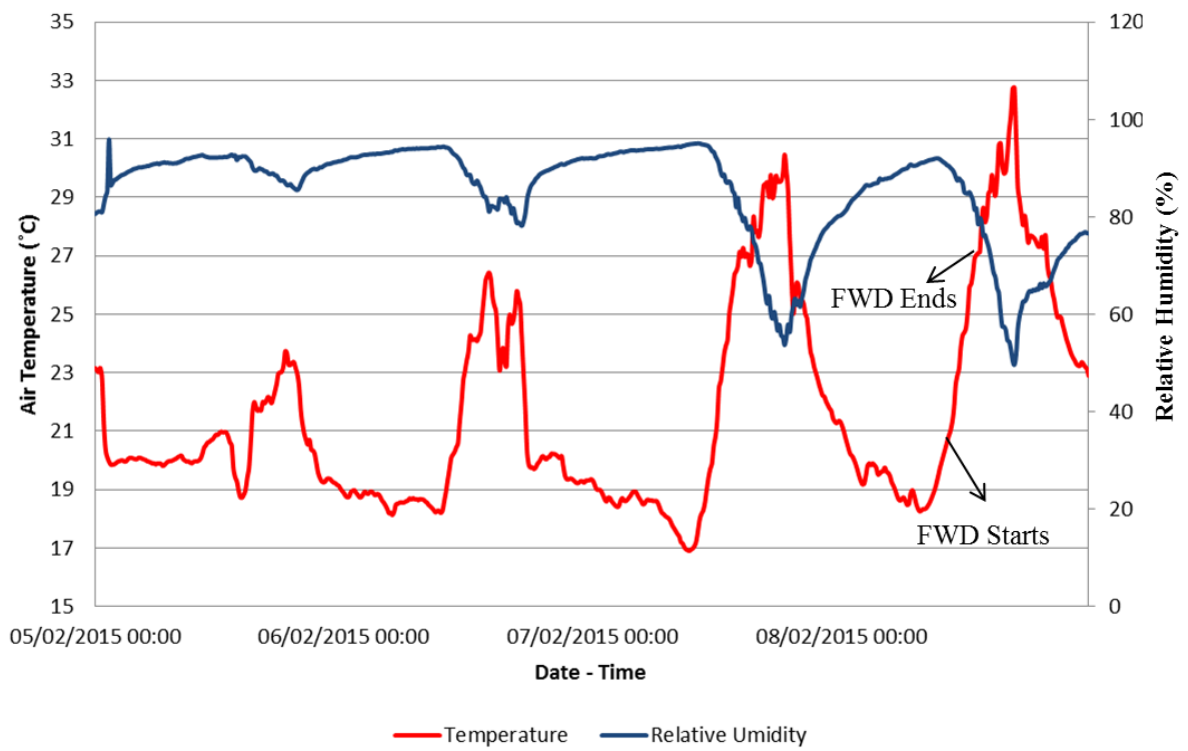
Figure 4. 11 – Winter 2013 crack map (FWD locations)

Tables 4.4 and 4.5 present the deflections for the 2015 summer FWD. It must be noted that the testing began from Section 4 going to Section 3 and then Section 1 and 2, always following the traffic direction. As the test started in the morning (10 a.m.), the air temperature of Section 4 and 3 were milder than for Sections 1 and 2 as also seen in Figure 4.12. The weather condition was of a typical dry sunny summer day although the area experienced some heavy rainfall in the days prior to the FWD testing. Figure 4.13 shows the testing map with all locations. The cracks in red were yet to be discovered in the next surveys.

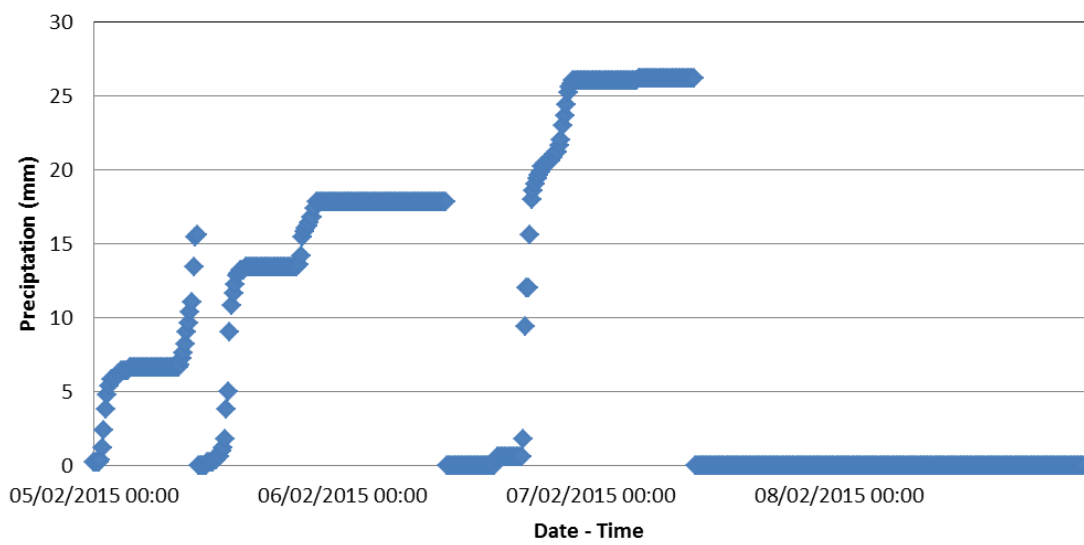
<sup>1</sup> Personal communication with Prof. José Tadeu Balbo.

Table 4. 3 – Backcalculation and LTE results from 2013 winter FWD test

Slab	E (MPa)	k (MPa/m)	$\Sigma$ Error <sup>2</sup>	Crack	LTE
P1.1	12,000	53	17.18	F2.1	94.03%
P1.2	35,000	95	0.53	F2.2	91.58%
P1.3	34,000	120	0.43	F3.1	93.68%
P1.4	38,000	160	0.39	F3.2	94.01%
P1.5	28,000	70	1.12	F3.3	93.24%
P2.1	30,000	80	17.23	F3.4	91.85%
P2.2	60,000	200	0.16	F3.5	92.26%
P2.3	35,000	105	0.11	F3.6	93.17%
P3.1	25,000	95	0.37	F3.7	90.52%
P3.2	25,000	95	0.9	F3.8	92.65%
P3.3	30,000	120	3.6	F3.9	94.47%
P3.4	35,000	130	0.22	F3.10	92.19%
P3.5	42,000	135	0.23	F4.1	95.51%
P3.6	38,000	135	0.2	F4.2	93.01%
P3.7	42,000	115	0.44	F4.3	90.36%
P3.8	42,000	105	0.27	F4.4	94.00%
P3.9	28,000	100	0.44	F4.5	92.67%
P3.10	28,000	85	0.48	F4.6	91.60%
P3.11	25,000	60	0.82	F4.7	91.56%
P4.1	25,000	53	0.96		
P4.2	27,000	70	0.29		
P4.3	45,000	145	0.22		
P4.4	25,000	85	0.21		
P4.5	30,000	85	0.56		
P4.6	28,000	155	0.24		
P4.7	32,000	125	0.29		
P4.8	30,000	115	0.27		



(a)



(b)

Figure 4. 12 -- Climate conditions for (a) air temperature and relative humidity and (b) precipitation during and prior to the FWD testing

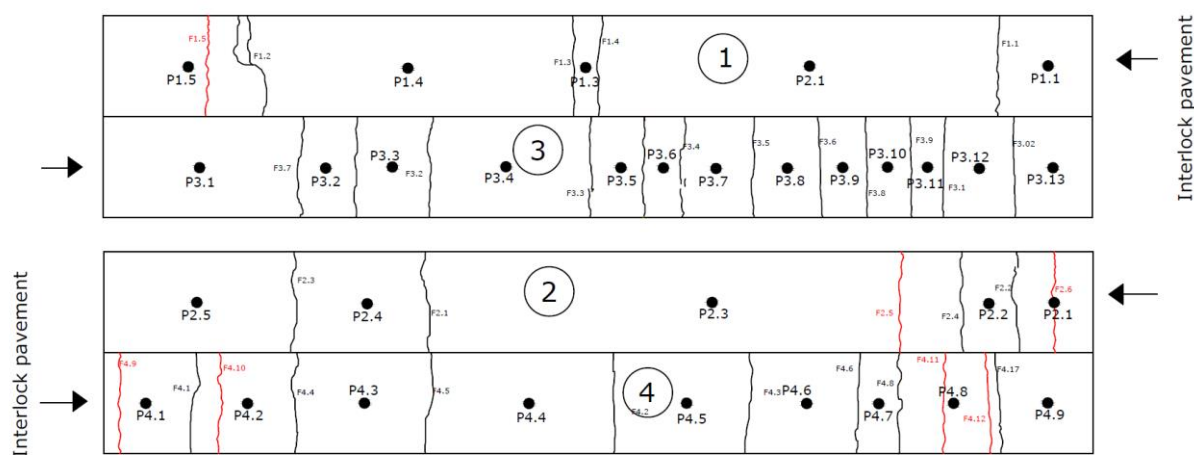


Figure 4.13 – Summer 2015 crack map (FWD locations)

Table 4.4 – Deflection data from February 2015 FWD test

Location	Load (kN)	Deflections (0.01mm)							Air Temperature (°C)
		Df1	Df2	Df3	Df4	Df5	Df6	Df7	
		0	200	300	450	600	900	1200	
P1.1	58.3	37.2	35.6	35.4	34.6	31.3	28.4	24.5	24
F1.2	58.3	37.9	35.4	35.3	32.2	29.2	27.7	22.9	24
P1.1	59.13	19.1	18.4	18.3	17	16.3	13.7	11.8	25
F1.3	59.06	16.5	15.6	15.4	14.9	13.8	11.8	10.4	25
P1.3	59.2	16.3	15.3	15	14.3	13.7	12.3	10.6	25
F1.4	59.48	16.7	15.7	15.2	14.5	13.7	12.5	10.8	25
P1.4	56.5	132.9	73	69.9	69.6	68.7	65.9	62.8	25
F1.2	58.37	32.1	30.9	28.9	28.1	25.7	21.8	18.9	26
P1.5	57.47	30.2	28.1	26.6	24.5	23.1	22.1	18	26
P2.1	58.02	25.7	23.7	22.9	22.7	20.4	17.7	15	26
F2.2	58.09	22.2	21.2	19.9	19.5	18.5	16.7	13.2	26
P2.2	58.3	22.9	22.4	22.1	20.8	19	17.1	15.2	27
F2.4	58.51	26.4	25.4	24.2	24	20.6	17.1	15.1	27
P2.3	58.57	15.2	15	14.4	14	12.6	11.3	9.9	27
F2.1	59.27	16.2	15.1	14.7	14.1	14	11.9	10.5	27
P2.4	58.99	12.4	11.8	11.6	11.3	10	8	7	26
F2.3	58.3	16.3	15.1	14.6	14.1	13.1	11.4	10.2	27
P2.5	58.71	17.9	16.9	15.8	15	12.9	12	10.4	27

Table 4. 5 – Deflection data from February 2015 FWD test: Part II

Location	Load (kN)	Deflections (0.01mm)							Temperature
		Df1	Df2	Df3	Df4	Df5	Df6	Df7	(°C)
		0	200	300	450	600	900	1200	Air
P3.1	58.71	21.6	21.1	20.7	19.3	18	15.2	13.2	21
F3.7	58.37	35.6	34.7	32.6	31.8	29.8	25.6	21.8	21
P3.2	58.71	26.9	26.2	23.9	22.5	20.7	18	16.3	21
F3.11	58.92	23.5	22.3	22.1	21.2	17.5	14.5	13.3	21
P3.3	59.41	21.8	21	19.6	19.1	17.9	16	13.7	21
F3.2	58.78	24.6	23.4	22.5	21.8	18.3	17.5	15.2	21
P3.4	59.27	17	16.5	15.6	15.3	14.4	12.9	11.1	21
F3.3	59.13	18.9	18	17.9	17.2	15.5	13	11.1	21
P3.5	59.34	15.4	14.4	14.2	13.2	12.5	10.9	9.2	21
F3.12	58.78	15.2	14.3	14	13.2	11.5	9.5	8.3	21
P3.6	58.64	14.1	13.2	12.9	12.4	10.9	9.6	8.4	21
F3.4	58.78	15.4	13.8	11.8	11.7	10.7	9.5	8.5	21
P3.7	58.37	14	12.9	12.8	12.1	10.7	9.6	8.5	21
F3.5	58.37	14.1	12.8	12.3	12.2	11.6	9.8	8.4	22
P3.8	58.78	14	13.2	13	12.8	10.6	10.1	8.8	22
F3.6	58.23	15.6	15.1	14.3	14.1	12.4	10.6	9.5	22
P3.9	58.78	14.9	14.2	13.4	13.1	13	11.1	10	22
F3.8	58.3	15.2	14.7	14.2	13.9	13.8	11.9	10.3	22
P3.10	58.85	18.7	17.8	17.2	16.4	14.2	13.1	12.5	22
F3.9	58.92	19.2	19.2	18.9	16.9	15.8	14.7	12.6	22
P3.11	58.51	19.1	18.1	17.7	17.2	16.6	14.5	12.6	22
F3.1	57.95	23.7	22.9	20.8	17.6	16.6	15.5	13.7	23
P3.12	57.19	21.6	21.2	20.7	20.4	19.1	17.3	15	23
F3.10	59.27	27	26.3	25.9	23.9	22	20.2	18	23
P3.13	59.13	31.8	30.3	28.9	26.8	24.6	22.1	19	23
P4.1	59.75	28.3	26.6	25.6	25	23.4	20.6	17.7	20
F4.1	59.41	30.6	30	29.5	29	26.1	24.2	19.5	20
P4.2	58.99	27.5	27	26.5	24.6	23.7	20.4	17.6	20
F4.4	59.48	21.9	21.6	21.1	20.4	19.1	16.1	13.8	20
P4.3	59.41	11.5	11.1	10.6	10.3	9.1	7.6	6.4	20
F4.5	59.2	20.5	20.4	20.2	18.8	17.3	15	13.1	20
P4.4	59.34	21.9	21	20.6	20.4	17.6	15.8	14.3	20
F4.2	58.71	27.2	26.1	24.8	23.6	21.8	18.8	16.1	20
P4.5	58.99	20.9	20.1	20	17.5	17.1	15.2	13.2	20
F4.3	59.41	11.6	11.5	11.4	9.4	8.6	8.2	6.1	20
P4.6	59.75	14.5	14.1	13.7	13.2	12.7	10.8	9.3	20
F4.6	59.41	20.7	20.4	19.8	18.3	12.6	12.1	10.6	20
P4.7	59.61	17.5	16.6	16.5	15.6	14	12.2	10.6	20
F4.8	59.61	18.4	18	17.8	17.3	13	12.4	10.9	20
P4.8	59.2	16.7	16.6	15.6	14.1	13	11.1	9.3	21
F4.7	59.82	18	17.2	17	16.9	13.4	13.2	10.8	21
P4.9	59.55	17.3	16.4	16	15.2	14.1	12.6	11	21

### 4.3.1 Deflection data analysis

The maximum deflection for P locations in the winter and summer FWD surveys is presented in Figure 4.14. The data was plotted with the distance of the P location regarding the transaction edge between the short CRCP and the interlocked pavement. For sections 3 and 4, the maximum deflection lines are quite similar, except in the vicinity of two cracks that emerged after the first survey in 2013 (cracks F3.11 and F4.8). Deflections suffered increases around these locations. For sections 1 and 2, the development of more cracks resulted in higher deflections in the second survey. It is assumed that the development of cracks in the slab surface alters the slab stiffness.

Understandably, the deflections at points near the free edge are greater for sections 1, 3 and 4. The lack of anchorage allows the vertical displacement of these locations; the endpoints of section 2 are farther from the edge than those of the other sections; this explains the smaller deflections. The abnormal high values showed by section 1 are the result of the joint related distress previously mentioned. Another factor that favors maximum deflections increase are locations where traffic accesses the section (free edge to sections 1 and 4). The lack of anchorage intensifies the power of traffic fatigue at these points. This further attest the recommendations of Salles *et al.* (2015) that for new projects of the short CRCP, the transition joints should be anchored. The odd high deflections in the middle of section 4 can be due to non-visible cracks in the proximity of the FWD testing (F4.4 and F4.5) as shown in Figure 4.15.

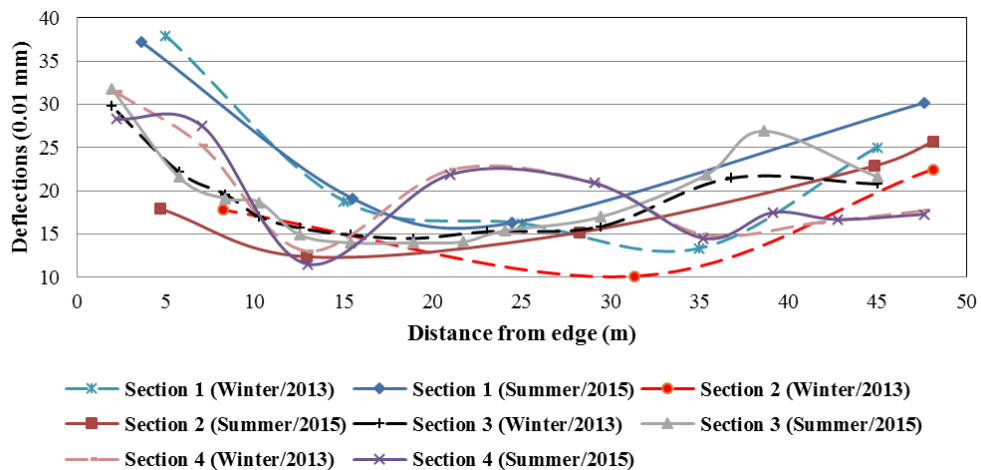


Figure 4. 14 – Maximum deflections trough the section length

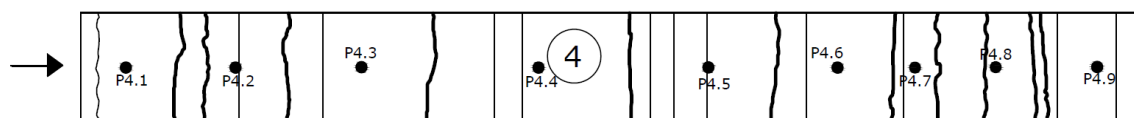


Figure 4. 15 – FWD testing map with non-visible cracks (Section 4)

The complete basin layout is presented in Figure 4.16 for panel (P) locations and in Figure 4.17 for crack (F) locations. Again, the higher deflection values are always located near the joint in a direct relation to the slab lack of anchorage allowing slab free movement, therefore increasing the deformations. Also, locations presenting high deflections as those at the start of sections 1 and 4 and end of section 3 were areas with thickness deficiencies as observed in the ultrasonic testing results (Tables 3.2 and 3.3) which may have aggravated the lack of anchorage effect. However, plotting the ultrasonic results for slab thickness versus the maximum deflection (Figure 4.18) did not present any reasonable trend. Counterintuitively, locations with thicker concrete exhibited high deflections as that of section 3 and a location with thickness lower than 180 mm showed low deflections (Section 2). It must be noted that ultrasonic measurements were not taken at the exact position of the FWD testing which makes the thickness assigned for each maximum deflection to be an approximation as thickness varied greatly even in short lengths. The lowest maximum deflection values are those located near the slab's center, as expected, due to greater stability of the region when compared to the pavement edge. It must be noted that due to the great rainfall from the days prior to the FWD testing, as seen in Figure 4.12b, the subgrade may have added moisture which can momentarily saturate the subgrade hampering its resistance. This effect would be intuitively more pronounced near the transversal joint due to the interlocked pavement greater permeability than the concrete slabs.

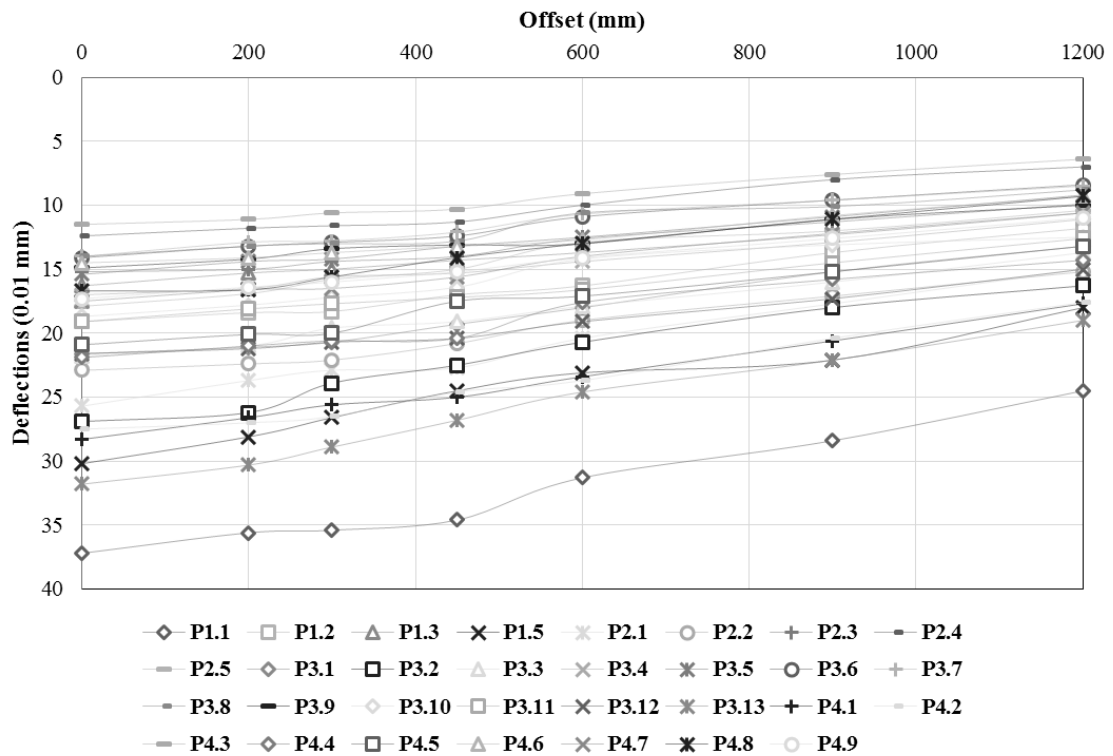


Figure 4. 16 – Deflection basins for panel (P) locations

In an experimental JPCP placed near the experimental CRCP sections, it was observed that joints without dowel bars experienced much higher displacements than those presented by joints with dowel bars (COLIM *et al.*, 2011). Although the joints (cracks) in CRCP do not have dowel bars, the small crack width in addition to the tightening strength provided by the longitudinal steel hold the slabs together increasing stiffness and reducing the deflections even in a physical discontinuity. Also, the comparison between deflections at the crack and in between cracks reinforces these assumptions. As for the shape, basins show a typical rigid pavements outline with a smooth decrease of deflections through the sensors.

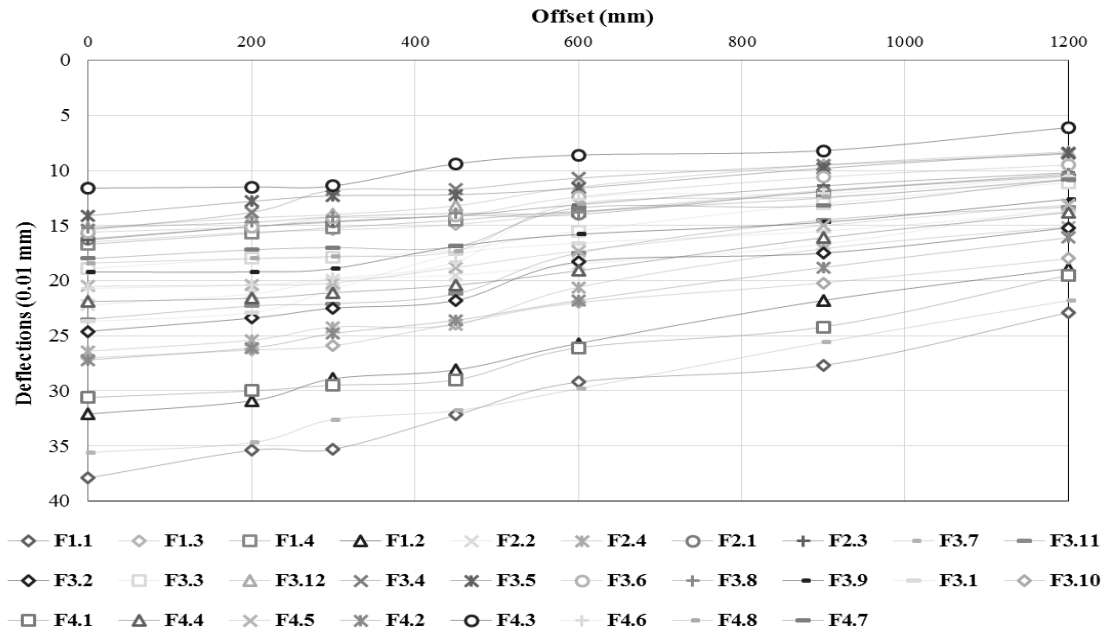


Figure 4. 17 – Deflection basins for crack (F) locations

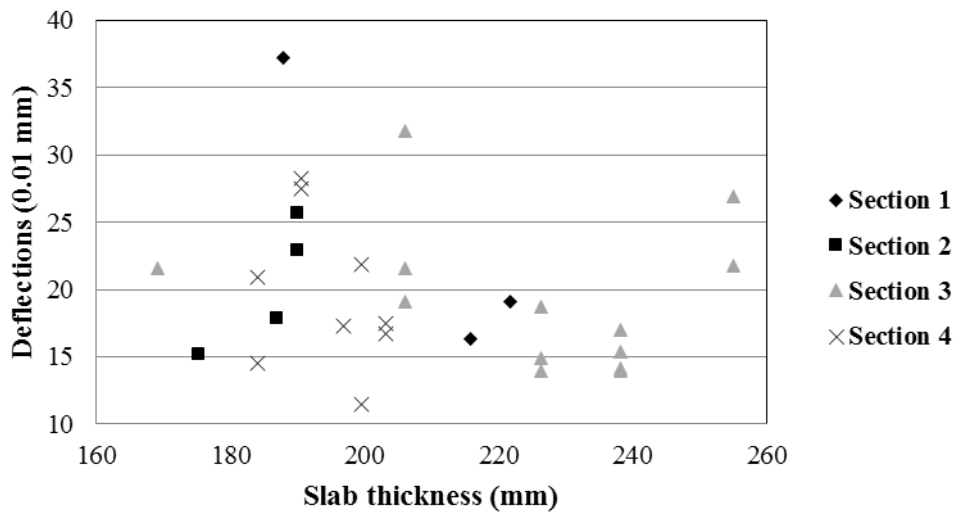


Figure 4. 18 – FWD testing maximum deflection versus ultrasonic testing slab thickness

#### 4.3.3 Load transfer efficiency (LTE) analysis

Figure 4.19 shows the individual LTE values for all cracks for both surveys. In the survey conducted in June 2013 all cracks showed LTE greater than 90%. This superior performance when compared to JPCP LTE can be explained by the amount of longitudinal reinforcement. In a hypothetical JPCP structure with a 250 mm thickness and 3.6 m wide slab where joints are reinforced with 32 mm diameter dowel bars spaced 300 mm, the steel percentage amounts

to 0.01%. When comparing to a typical CRCP structure with longitudinal reinforcement at 0.7%, the CRCP presents 70 times more steel in the transverse section than the JPCP. However, as discussed previously in Chapter 2, most authors consider that the reinforcement does not play a role in the CRCP LTE because the steel is above the slab half-height, i.e., in the compression flange, not acting in the slab bending moments. Nevertheless, the reinforcement wherever it is placed, acts on the shear forces that the slab is subjected to. Additionally, for the experimental short CRCP case, the reinforcement was misplaced slightly below the slab half-height therefore acting on the bending stresses.

In the second survey variations were noticed: some cracks had a higher LTE than in the first survey, due to the greater crack walls contact as a result of higher temperature on the day of the survey, as expected. Conversely, some cracks had a slightly inferior performance, in what could be function of time and traffic action wearing out the concrete. However, a crack presented LTE less than 85%, not consistent with the appropriate structure performance. The F3.4 crack (76.62%) was first seen in January 2012 and may have suffered extra deterioration over time.

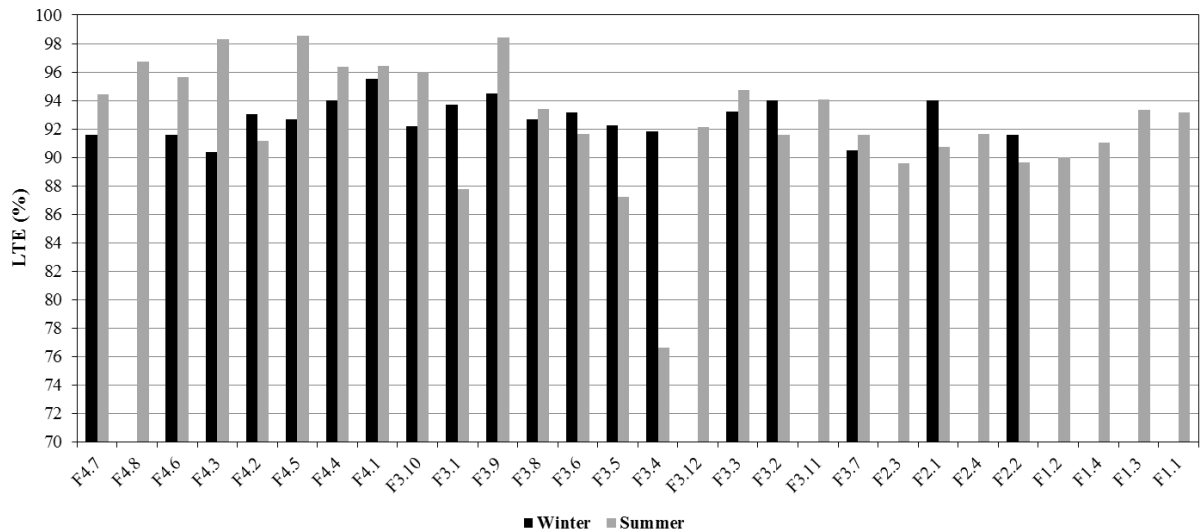
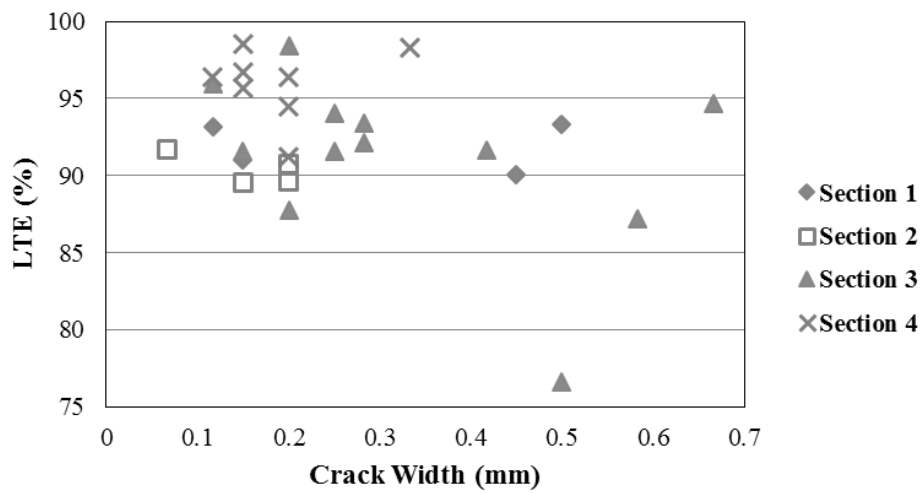
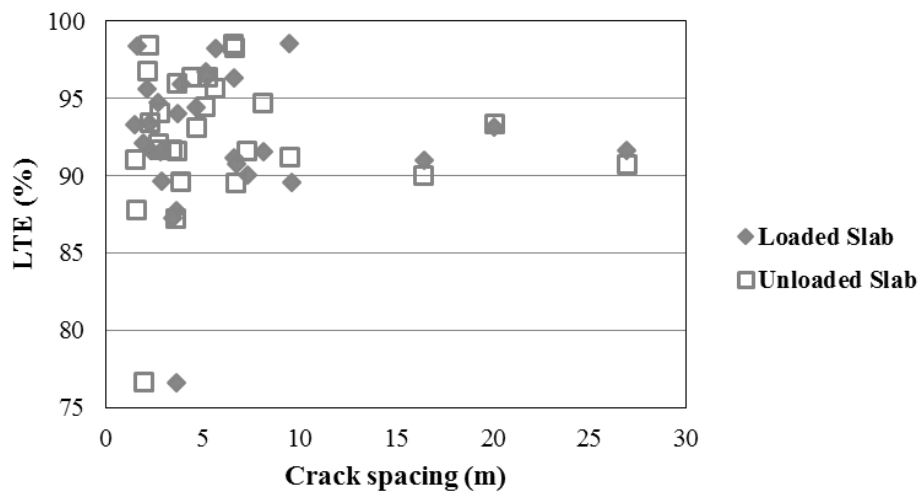


Figure 4. 19 – LTE in two different seasons

No relation was found between LTE and crack width (Figure 4.20a) and LTE and crack spacing (Figure 4.20b). Crack spacing was considered for both the loaded and the unloaded slab in the FWD test. Although some studies stress that large crack spacing can decrease LTE as the new AASTHO recommendations (maximum crack spacing at 1.8 m), crack spacing over 15 m, like those presented by sections 1 and 2 did no harm to the crack ability to transfer load.



(a)



(b)

Figure 4. 20 – Load transfer efficiency *versus* (a) crack width and (b) crack spacing

The same crack showed a great width that could explain the low LTE. However, counterintuitively, wider cracks, like F3.3 presented high levels of LTE (93.24%). Moreover, the crack width was measured only at the slab surface and may not indicate the real interlock between crack walls because crack width varies with depth.

Additionally, no satisfactory correlation was found between HTI and LTE, since LTE is mostly high and presents small variation and most cracks present a high HTI. However for crack F3.4, the HTI was 110 confirming the crack's deterioration.

#### *4.3.2.1 Panel LTE*

In Salles *et al.* (2015), the determination of LTE for the deflection data obtained in the panel's center (P points) disclosed an LTE similar to that found for cracks in the winter FWD survey. This result lead to the assumption that cracks were so tight that the slab was behaving as a continuous structure. The same analysis was performed for the summer FWD surveys, the panel "fictitious" LTE was calculated using Equation 1 with the deflections from sensors 1 and 3. Results can be found in Table 4.6. Again there is a great similarity of LTE. Only for panel P1.4 the result is incoherent in what can be regarded as a malfunction of the FWD device or a small object on the slab surface generating unreliable pressures. Excluding this result, the average LTE for panels and cracks was, respectively, 91.57 and 91.18. Therefore, the continuous behavior of the short CRCP was proven once more.

Table 4. 6 – LTE for cracks (F) and panels (P) on FWD summer survey

Section 1		Section 2		Section 3		Section 4	
P1.1	88.21	P2.1	89.11	P3.1	95.83	P4.1	90.46
F1.1	88.09	F2.2	89.57	F3.7	88.77	F4.1	96.41
P1.2	92.27	P2.2	96.51	P3.2	85.66	P4.2	96.36
F1.3	91.07	F2.4	91.67	F3.11	94.04	F4.4	96.35
P1.3	92.02	P2.3	89.57	P3.3	89.74	P4.3	90.71
F1.4	89.70	F2.1	88.69	F3.2	90.52	F4.5	98.54
P1.4	38.66	P2.4	93.62	P3.4	91.79	P4.4	93.18
F1.2	85.05	F2.3	87.65	F3.3	94.24	F4.2	90.44
P1.5	87.46	P2.5	88.16	P3.5	92.21	P4.5	95.69
				F3.12	90.26	F4.3	96.55
				P3.6	91.49	P4.6	92.47
				F3.4	76.62	F4.6	91.63
				P3.7	91.43	P4.7	93.10
				F3.5	87.20	F4.8	93.28
				P3.8	86.79	P4.8	93.41
				F3.6	91.70	F4.7	93.37
				P3.9	89.87	P4.9	92.49
				F3.8	89.38		
				P3.10	92.13		
				F3.9	98.44		
				P3.11	90.27		
				F3.1	87.76		
				P3.12	95.83		
				F3.5	95.98		
				P3.13	90.84		

#### 4.4 Short CRCP visual distresses

The short CRCP, as of February 2017, presents three locations where distresses can be observed. They are illustrated in the January 2017 crack map in Figure 4.21. Unlike the transverse cracks that are part of the CRCP structure, the cracks illustrated in red in Figure 4.21 must be considered performance failures. The failure in section 1 was firstly observed as a corner cracking in 2012 evolving dramatically ever since (Figure 4.22). It was assumed that a rutting distress on the interlocked pavement at the transaction joint with the short CRCP created a vertical step between both pavements making the impact of heavy vehicle assessing the short CRCP stronger. The meandering cracking observed in sections 3 and 4 were firstly detected in January 2017 and November 2016, respectively, and all cracks are strongly tight and hard to observe with the naked eye. Nevertheless, the division of the panel between

cracks F4.1 and F4.10 as well as the cracks in the next panel show potential for punchout or partial-punchout development due to the base non-erodible character.

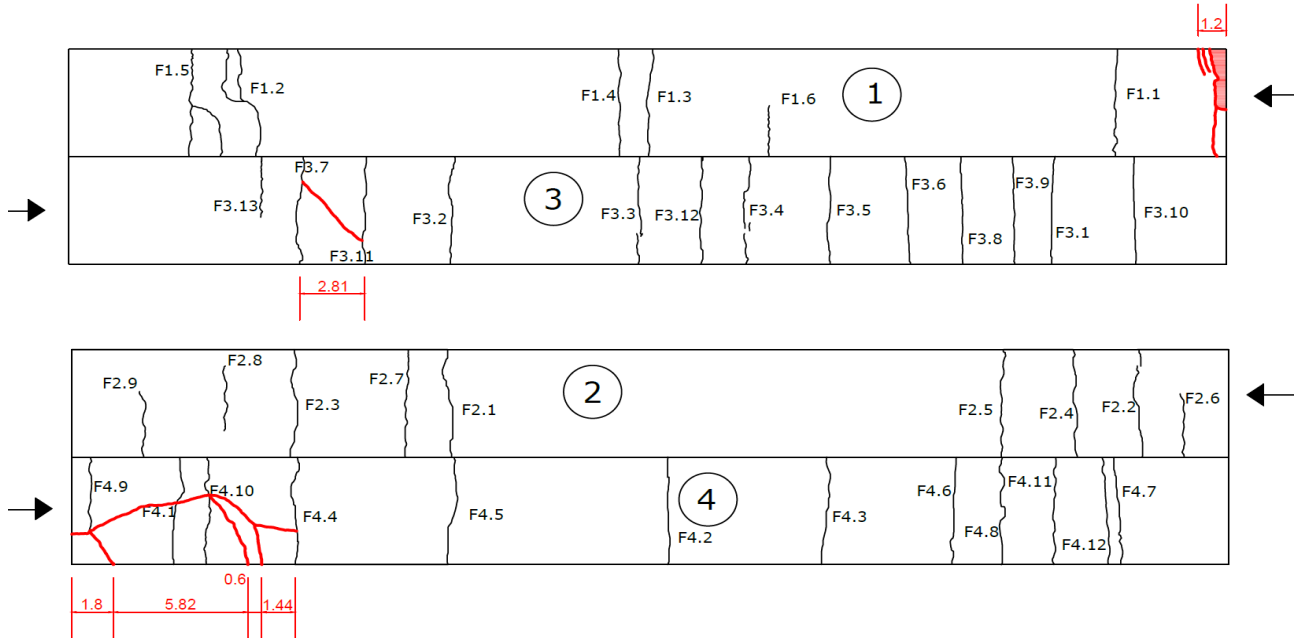


Figure 4. 21 – Cracking distresses visible at the short CRCP surface

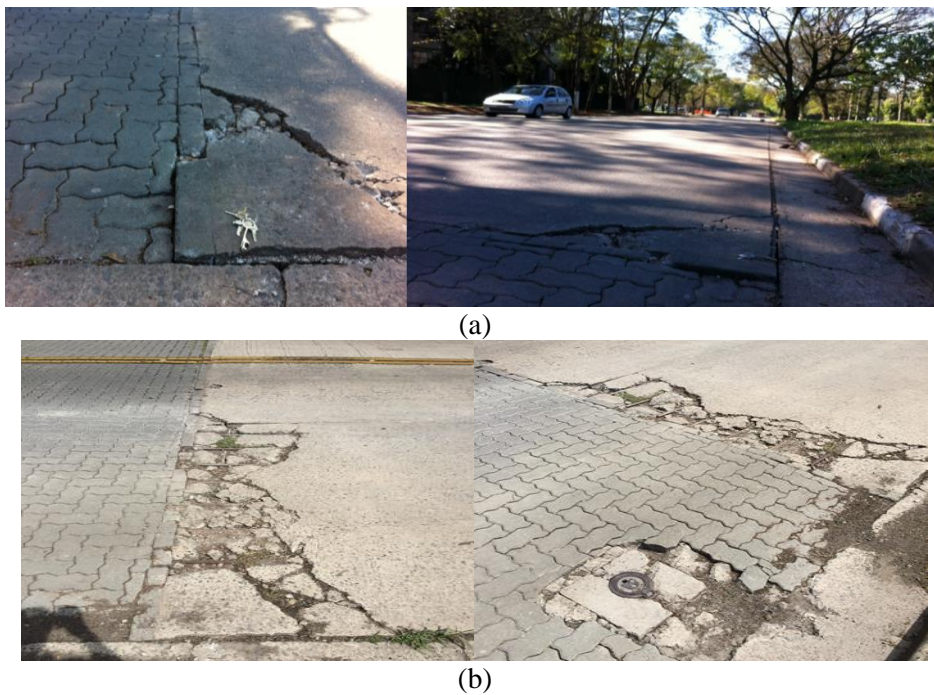


Figure 4. 22 – Cracking distress in section 1 in (a) 2013 and (b) 2017

Save for the meandering crack presented in Section 3, the other distresses present two features in common, namely, the proximity to the free edge where vehicles access the section and thickness deficiencies as indicated by the ultrasonic testing. Unfortunately there is no thickness information for that particular segment of section 3. The ultrasonic thickness survey stations closer to the panel between cracks F3.7 and F3.11 are stations 1 and 2 distanced at approximately five meters from the panel. Station 1 showed thickness deficiencies of 71 mm at the slab center regarding the design thickness of 240 mm while station 2 presented thickness in excess of 15 mm. The ultrasonic survey performed to disclose non-visible cracks at the slab center presents a high variability of thickness for this particular panel going from 163 to 267 mm. Regarding concerns with traffic safety, the distress in section 1 is due to rehabilitation in May 2017.

## 5 FIELD STRESSES SIMULATIONS

ISLAB2005 is a finite element software used to predict stresses in concrete pavements due to vehicle and environmental loads. The software was widely applied during the MEPDG development. The finite element method involves calculating a numerical solution based on the discretizing of the pavement slab into small rectangular elements (mesh). ISLAB2005 allows for a wide range of input variables, including geometry, areas, layers, subgrade, joints, temperature, load and voids. The user can choose the mesh size for both the X and Y directions on the slab. A finer mesh corresponds to a more detailed surface and more analysis locations in the output file (KHAZANOVICH *et al.*, 2000). The software was applied in this thesis to simulate stress data.

Strain data was obtained during a dynamic load test (DLT) with a loaded truck in an instrumented (strain gauges) area of Section 3 (Figure 5.1). Stresses were calculated based on the backcalculated concrete elasticity modulus presented in Table 4.3. Twenty dynamic load tests, 15 with constant low speed (10km/h), 3 with higher speed (above 30 km/h) and 2 with braking during the operation, were performed. A more detailed account on the dynamic load test procedure can be found in Salles (2014) and the preliminary results are presented in Salles *et al.* (2015). In brief, this segment of Section 3 was selected due to the small crack spacing between three consecutive cracks. For the instrumentation, the concrete gutter was removed and the concrete slab surface and sidewall were completely cleaned. The strain gauges (SG) were glued to the concrete applying an instantaneous adhesive which is proper for SG instrumentation. Tables 5.1 and 5.2 present the resulting stress data.

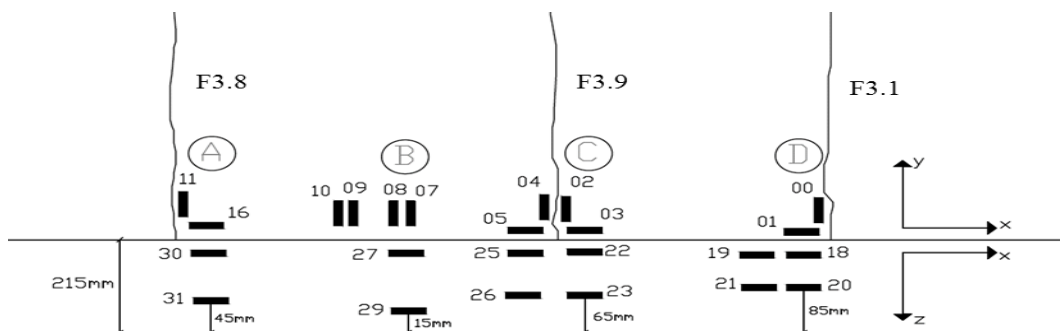


Figure 5. 1 – Strain gauge location in Section 3

Table 5. 1 – Dynamic load test stresses (MPa)

	SWA distance from the edge (cm)	Avg. Speed (km/h)	SG01		SG03		SG07		SG08		SG09		SG10		SG11		SG16	
			SWA	DWA	SWA	DWA	SWA	DWA	SWA	DWA	SWA	DWA	SWA	DWA	SWA	DWA	SWA	DWA
DLT01	93	6.81	-0.196	-0.607	-0.098	-0.389	NC	0.290	NC	0.223	NC	0.223	NC	0.218	NC	NC	-0.334	-1.257
DLT02	59	6.72	-0.266	-0.854	-0.122	-0.533	0.147	0.326	NC	0.260	0.074	0.296	NC	0.258	NC	NC	-0.482	-1.554
DLT03	54	7.27	-0.193	-0.799	-0.073	-0.537	0.147	0.363	NC	0.333	NC	0.298	NC	NC	NC	0.187	-0.407	-1.806
DLT04	56	7.59	-0.267	-0.848	NC	-0.633	NC	0.254	NC	0.334	NC	0.256	NC	1.865	NC	NC	-0.481	-1.955
DLT05	62	7.28	-0.244	-0.921	-0.148	-0.635	NC	0.290	NC	0.368	NC	0.218	NC	NC	NC	NC	-0.330	-1.804
DLT06	57	6.44	-0.291	-1.042	NC	-0.731	NC	0.254	NC	NC	NC	0.296	NC	NC	NC	NC	-0.405	-1.695
DLT07	59	8.48	-0.266	-0.920	-0.144	-0.610	0.147	0.327	NC	NC	NC	0.260	NC	0.258	NC	NC	-0.295	-1.991
DLT08	58	8.51	-0.242	-0.991	NC	-0.729	NC	0.290	NC	NC	NC	0.184	NC	0.258	NC	0.184	-0.479	-1.809
DLT09	65	8.48	-0.242	-0.871	-0.170	-0.633	NC	0.290	NC	0.368	NC	0.336	NC	0.258	NC	0.256	-0.403	-1.621
DLT10	48	9.08	-0.267	-1.043	-0.097	-0.683	NC	0.326	NC	0.368	NC	0.185	NC	NC	NC	NC	-0.368	-1.770
DLT11	62	9.01	-0.244	-0.899	-0.146	-0.582	NC	0.326	NC	0.407	NC	0.223	NC	0.147	NC	NC	-0.370	-1.844
DLT12	47	8.86	-0.316	-1.066	-0.244	-0.723	NC	0.326	NC	NC	NC	0.293	NC	NC	NC	NC	-0.480	-1.846
DLT13	48	9.08	-0.291	-1.139	-0.171	-0.538	NC	0.349	NC	NC	NC	0.221	NC	NC	NC	NC	-0.481	-1.957
DLT14	58	10.10	-0.217	-0.993	-0.148	-0.636	NC	0.290	NC	0.370	NC	0.298	NC	0.223	NC	NC	-0.407	-1.920
DLT15	57	8.45	-0.267	-0.993	-0.195	-0.659	NC	0.326	NC	0.296	NC	0.293	NC	NC	NC	NC	-0.440	-1.809
DLT16	44	32.40	-0.171	-0.850	-0.122	-0.585	NC	0.218	NC	0.368	NC	0.333	NC	0.293	NC	0.257	-0.185	-1.737
DLT17	39	42.00	-0.267	-1.019	-0.122	-0.560	NC	0.268	NC	0.368	NC	0.295	NC	NC	NC	0.184	-0.405	-1.771
DLT18	37	43.68	-0.195	-1.043	-0.196	-0.753	0.183	0.365	NC	0.405	NC	0.256	NC	NC	NC	0.184	-0.479	-1.984
DLT19	55	12.30	NC	-0.726	NC	-0.232	NC	NC	NC	NC	NC	NC	NC	NC	NC	NC	-0.479	-1.367
DLT20	54	12.60	-0.436	NC	-0.146	-0.146	NC	NC	NC	NC	NC	NC	NC	NC	NC	NC	-0.445	-1.292

NC = non-conclusive

Table 5. 2 – Dynamic load test stresses (MPa): part II

	SWA distance from the edge (cm)	Avg. Speed (km/h)	SG18		SG22		SG25		SG26		SG29		SG30		SG31	
			SWA	DWA	SWA	DWA	SWA	DWA	SWA	DWA	SWA	DWA	SWA	DWA	SWA	DWA
DLT01	93	6.81	NC	-0.291	NC	-0.216	NC	-0.290	NC	0.188	NC	0.286	NC	-0.437	0.147	0.473
DLT02	59	6.72	-0.121	-0.436	NC	-0.312	NC	NC	NC	0.253	NC	0.433	NC	-0.653	0.109	0.656
DLT03	54	7.27	NC	-0.389	NC	-0.309	NC	-0.328	NC	0.274	0.218	0.508	NC	-0.644	0.145	0.874
DLT04	56	7.59	NC	-0.437	NC	-0.557	NC	-0.546	NC	0.214	NC	0.544	-0.152	-0.764	0.256	0.907
DLT05	62	7.28	NC	-0.460	NC	-0.541	NC	-0.544	NC	NC	NC	0.580	NC	-0.691	NC	0.945
DLT06	57	6.44	NC	-0.532	-0.143	-0.398	NC	-0.615	NC	0.255	NC	0.691	NC	-0.525	NC	0.764
DLT07	59	8.48	-0.144	-0.435	NC	-0.360	NC	NC	NC	0.327	NC	0.580	NC	-0.691	0.218	0.508
DLT08	58	8.51	-0.169	-0.483	NC	-0.406	NC	-0.542	NC	0.217	NC	0.545	NC	-0.731	0.218	2.001
DLT09	65	8.48	NC	-0.386	NC	-0.473	NC	-0.399	NC	0.290	NC	0.508	-0.181	-0.655	0.509	1.493
DLT10	48	9.08	-0.145	-0.606	NC	-0.384	NC	-0.717	NC	0.325	NC	0.546	NC	-0.765	0.545	0.508
DLT11	62	9.01	-0.097	-0.411	-0.144	-0.539	NC	-0.500	NC	0.289	0.181	0.508	-0.183	-0.731	NC	NC
DLT12	47	8.86	-0.120	-0.460	-0.120	-0.288	NC	NC	NC	0.286	0.181	0.616	-0.257	-0.874	NC	1.090
DLT13	48	9.08	-0.122	-0.533	NC	-0.408	NC	-0.506	NC	0.290	0.181	0.613	NC	-0.799	NC	0.763
DLT14	58	10.10	-0.146	-0.460	-0.168	-0.335	NC	-0.504	0.111	0.290	0.147	0.544	-0.254	-0.762	0.216	0.470
DLT15	57	8.45	-0.098	-0.461	NC	NC	NC	-0.468	NC	0.214	0.214	0.544	NC	-0.691	NC	NC
DLT16	44	32.40	-0.097	-0.374	NC	-0.455	NC	-0.398	NC	0.288	NC	0.506	-0.182	-0.690	NC	NC
DLT17	39	42.00	-0.146	-0.487	NC	NC	-0.214	-0.540	0.147	0.396	0.181	0.546	-0.143	-0.728	NC	NC
DLT18	37	43.68	-0.097	-0.411	NC	NC	NC	-0.508	NC	0.250	0.183	0.617	-0.183	-0.762	NC	NC
DLT19	55	12.30	NC	-0.362	NC	NC	NC	NC	NC	0.218	NC	0.254	-0.219	-0.513	0.254	NC
DLT20	54	12.60	-0.145	NC	-0.119	NC	NC	NC	NC	0.218	NC	NC	-0.107	-0.437	0.363	0.689

NC = non-conclusive

## 5.1 Field stress simulation procedure

Four preliminary approaches to simulate the dynamic load test (DLT) were performed. Since group A SGs (11, 16, 30 and 31) presented greater amount of conclusive results, these SGs were selected to conduct the trials. As SGs 30 and 31 were not positioned at the real “top” and “bottom” of the slab due the presence of a concrete foot at the slab bottom, a stress diagram for these SGs was extrapolated (Figure 5.2). By extending the stress diagram it was possible to estimate the real top and bottom stresses for this location. For drawing purposes the stresses are multiplied by 10 in Figure 5.2.

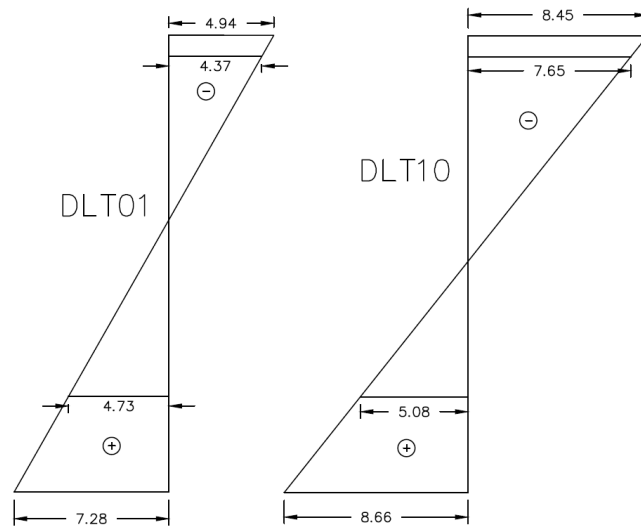


Figure 5. 2 – Stress diagram for SGs 30 and 31 in DLTs 01 and 10 (DWA)

Only DLTs with constant speed were simulated in this phase. The following considerations were made:

- 1) Concrete characteristics were assumed from basic knowledge of traditional concrete. Poisson's ratio was established at 0.15, density at  $2,400 \text{ kg/m}^3$  and coefficient of thermal expansion (CTE) at  $8 \times 10^{-6} / ^\circ\text{C}$ ;
- 2) Slab thickness was based on MIRA measurements done at the instrumented segment. The resulting thickness was 215 mm;

- 3) Modulus of elasticity (E) and subgrade reaction modulus (k) are presented in Table 4.3. For SGs groups A and B, E was 42,000 MPa and k was 105 MPa/m while for groups C and D, the values for E and k were 28,000 MPa and 100 MPa/m respectively. The subgrade was simulated as a frictionless Winkler model.
- 4) The asphalt base was simulated as a 60 mm thick base with a resilient modulus of 7000 MPa. The resilient modulus was estimated slightly higher than traditional hot mix asphalt modulus due to the less inflicting action of temperature as the base is an isolated layer without direct contact with the surface;
- 5) The interface between the concrete slab and the asphalt base was considered unbounded;
- 6) The cracks LTE, according to Table 4.3, was 92. Cracks were simulated as non-dowelled joint according to theoretical CRCP ISLAB simulations performed by Khazanovich *et al.* (2001).
- 7) Regarding the thermal differential, the temperature during the DLT was 20.9°C. Equations from Balbo and Severi (2002), a thermal gradient study performed on JPCP slabs near the short CRCP, were applied to calculate a thermal gradient of 0.45°C (0.81°F);
- 8) The truck loads according to Salles (2014) were 38,344 N for the single wheel axle (SWA) and 123,367 N for the dual wheel axle (DWA).

Initially, the slab was simulated (Figure 5.3) assuming the crack map presented in Figure 4.5. Although the DLT was done in 2013, (i. e., three years before the MIRA evaluation) the incipient cracks were considered to be there from the curing period, the second simulation was based on the crack map from the time when the DLTs were performed without any incipient crack. The map can be found in Figure 4.11. The third attempted to simulate the short CRCP was made changing only the consideration number 5. Instead of an unbounded interface between slab and base, a Totski model was adopted. This was done mostly considering that a very stiff base layer (asphalt base) makes the unbounded configuration of ISLAB to extend the joints (cracks) through the base because the two-layer system is analyzed as a structural equivalent single-layer system. On the other hand, the Totski model assumes the multi-layered pavement system as a series of springs and plates. The plate elements model the bending, whereas the springs accommodate the direct compression. Also, the ISLAB software allows for an exception input where all cracks in the second layer (base)

are considered as rigid. This results in a separation of the two layers where the crack is only at the slab, making the base layer continuous. Finally, regarding the LTE and deflection information provided in the last chapter that shows that the cracked slab is behaving as a continuously slab, section 3 was simulated as a 50 m slab without joints. Table 5.3 presents the average shift factor between field and simulated (field/ISLAB) stresses of these three simulations.



Figure 5. 3 – ISLAB simulation of section 3

Table 5. 3 – Shift factor for DLT simulations: model trials

Model	SWA					
	SG 16		SG 30		SG 31	
	Avg. SF	Std.	Avg. SF	Std.	Avg. SF	Std.
Unbounded (All Cracks)	2.66	139.07	-16.61	27.35	-46.60	66.01
Unbounded (Visible Cracks)	18.56	16.39	-53.48	58.45	-72.43	100.10
Totski (Visible Cracks)	18.32	16.68	-52.24	57.07	-70.76	97.74
Continuous	1.04	0.16	0.66	0.12	1.05	0.52

Model	DWA					
	SG 16		SG 30		SG 31	
	Avg. SF	Std.	Avg. SF	Std.	Avg. SF	Std.
Unbounded (All Cracks)	52.22	141.19	-9.55	35.85	-18.23	59.73
Unbounded (Visible Cracks)	79.99	160.81	-12.27	24.29	-21.85	42.76
Totski (Visible Cracks)	78.81	158.43	-11.99	23.72	-21.35	41.76
Continuous	1.79	0.19	0.86	0.10	1.44	0.62

For the basic cracked models, the correlation with field stresses were not coherent, presenting theoretical stresses far smaller than the ones measured with the DLT. Also the slab stress configuration was different making the ISLAB response incompatible with the field data, thus the huge and sometimes negative SF and the great standard deviation presented. Figure 5.4 shows the stresses for the DWA in SG 16 and 30. As can be seen, stresses from the cracked models were separated for better observation on the right graphs due to the small stress level. Additionally, the cracking models showed confusing results for SG positioned at the slab surface (SG 16) and especially at the slab top (SG 30).

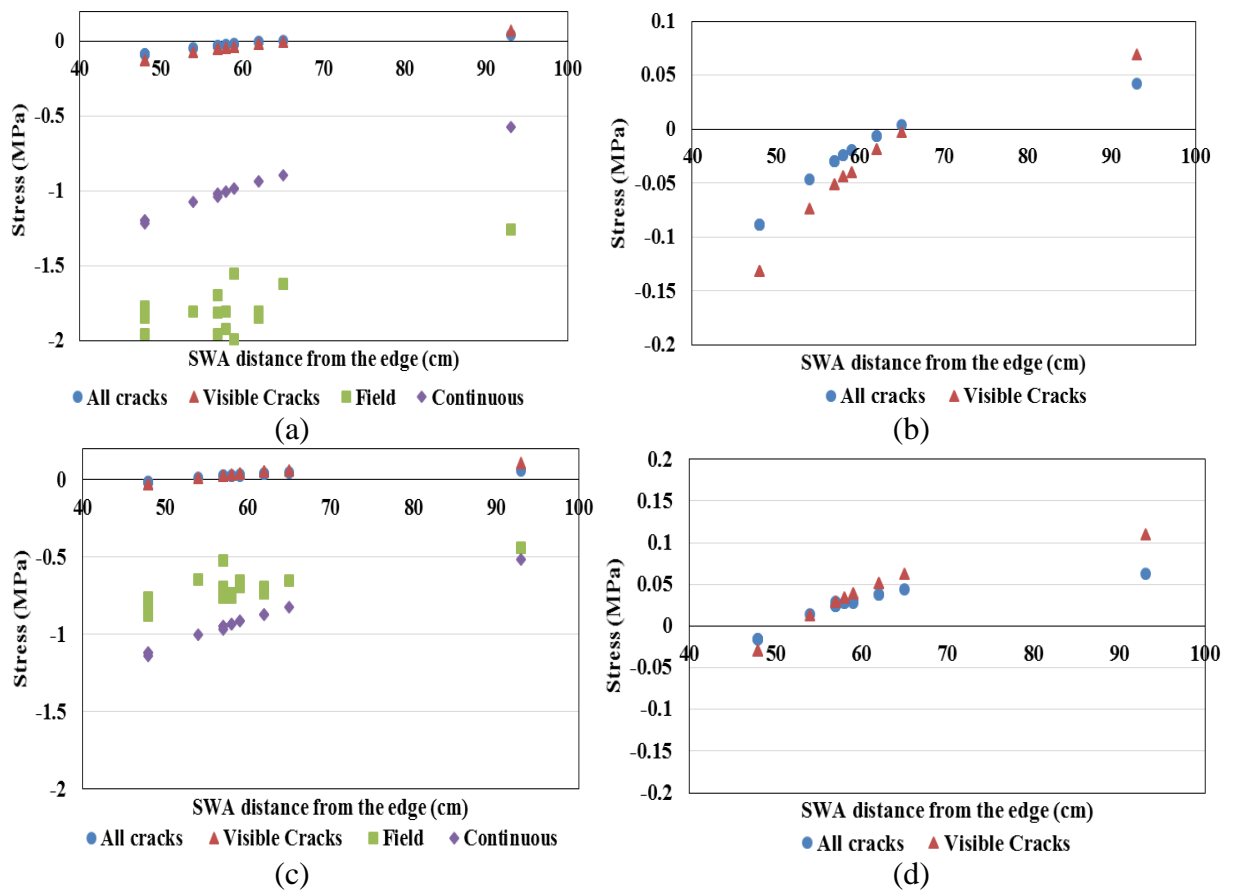


Figure 5. 4 - DWA stresses on (a) and (b) SG16; and (c) and (d) SG30 with vehicle distance from the edge

It was expected that, based on the field stresses, those areas would presented compression stresses, however the panels short length changed the slab stress diagram. The negative SF from SGs 30 and 31 in comparison to the positive SF from SG16 can be explained by the latter's greater proximity to the load. An insignificant change was observed when adopting

the Totski model (done only for the visible cracks to save computation time). Additionally, the simulation of a 20 cm concrete curb did not influence the slab configuration.

Ultimately, the simulation of a 50 m continuous slab resulted in a much more adequate approach to the field stresses because, as evidenced by the cracks LTE, the slab behaves as a continuous structure. Large slabs are expected to present higher stresses due to the increase in the bending and deflections. As can be seen in Figure 5.5, in the first two models, due to the SGs proximity to cracks (simulated as joints), the slab top suffered compression only right below the axles, meaning the edges slightly curled up under small tensile stresses. Whereas, for the continuous model, the compression extends along the load transversal line in accordance with what was found in the field. Critical stresses will be discussed in the next chapter. As some simulations point to a perfect match of field and theoretical stresses, it was decided that the continuous slab model would be applied to simulate the remaining DLTs. This finding goes in contrast with traditional CRCP modeling and design that focus on crack spacing and usually simulates cracks as high LTE joints.

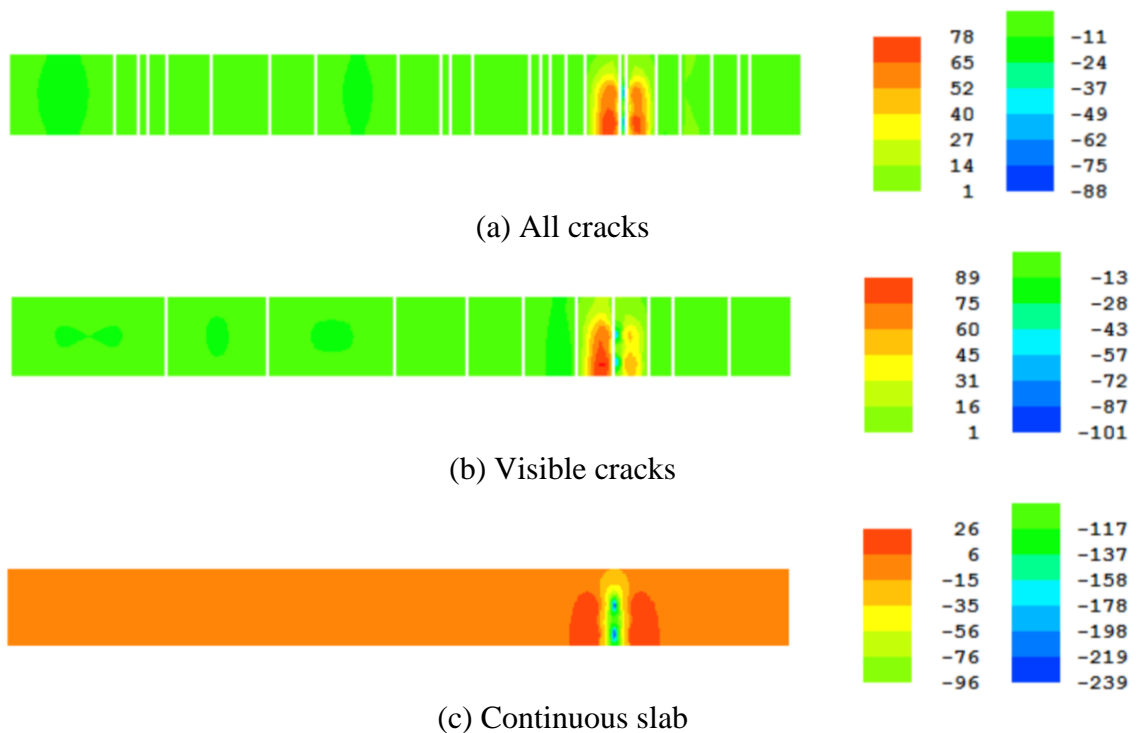


Figure 5. 5 - Longitudinal top stresses (DWA) on three simulation models for DLT 05

## 5.2 Shift factor between field and theoretical stresses

The full simulation results are presented in Tables 5.4 to 5.6. SG pair 25-26 received the same analysis diagram as described for SG pair 30-31. A stress diagram was traced and extended to determinate the actual top and bottom stresses on the slab. As SG 27, 23 and 20 failed to produce conclusive results, it was not possible to determine the stress diagram for its pairs, SG 29, 22, and 18, respectively. In order to still use those valuable results, a stress extension factor (SEF) was considered. It was observed a stress increase of 20% and 15% in SG 30 for the SWA and DWA stresses, respectively. Those values were used to estimate the stress increase in SG 18 as both SGs are equally distanced from the slab's top (10 mm). As SG 22 was 20 mm from the slab's top, an SEF of 1.3 was applied.

Regarding the bottom SGs, SG 26 presented a SEF of 2.38 while SG 31 showed 1.54. SGs 26 and 31 are 65 and 45 mm, respectively, from the slab bottom. A diagram using the stress line inclination for both those SGs was traced to estimate the SEF of a SG distanced 15 mm from the bottom. Figure 5.6 illustrates the procedure. The average between the SEFs from the lines of SGs 26 and 31 resulted in an SEF of 1.25.

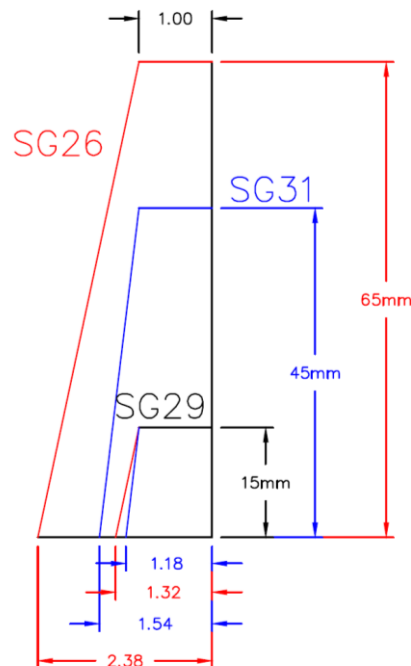


Figure 5. 6 – Stress increase factor for SG 29

Moreover, as ISLAB simulates a slab with a neutral axis positioned at the slab's half height, the simulation of SG pairs results in stress of same magnitude but opposite signs for the top and bottom. In the field case, this is not true because, besides concrete being a highly heterogeneous material with different degrees of compaction through the slab depth, it also has the presence, in the short CRCP case, of a longitudinal reinforcement located around the slab half height. This combination of factors may dislocate the neutral axis creating regions with greater stiffness and a non-symmetric stress diagram. However, for the case of the working SG pairs (25-26 and 30-31), the proximity to the crack helps to explain why the bottom stresses are 17% higher for pair 25-26 and 83% for pair 30-31. When the load approaches the physical discontinuity (crack) it creates compression making the crack width smaller, therefore increasing the structure tenacity at that point. Conversely, tensile forces cause the crack to open at bottom, weakening the material. This interaction (Figure 5.7) was also observed by Roesler and Kohler (2006) where loading near the crack made the crack tighter at the slab top and wider at the bottom.

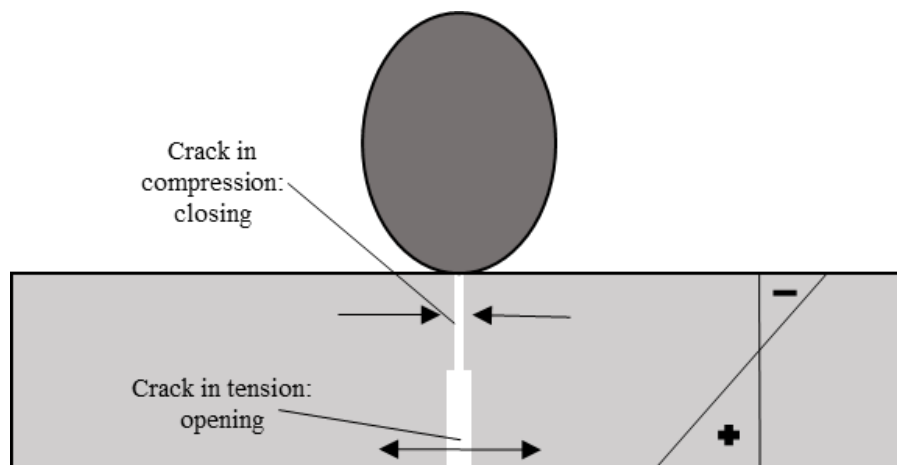


Figure 5. 7 – Wheel load effect on stress diagram at crack

Table 5. 4 – Shift factor between field and theoretical stresses: Part I

	SG 01						SG 03						SG 18					
	SWA			DWA			SWA			DWA			SWA			DWA		
	FIELD	ISLAB	SF															
DLT01	-0.196	-0.186	1.05	-0.607	-0.441	1.38	-0.098	-0.176	0.56	-0.389	-0.407	0.96	NC	-0.172	NC	-0.335	-0.400	0.84
DLT02	-0.266	-0.317	0.84	-0.854	-0.820	1.04	-0.122	-0.296	0.41	-0.533	-0.752	0.71	-0.146	-0.296	0.49	-0.502	-0.755	0.66
DLT03	-0.193	-0.348	0.55	-0.799	-0.903	0.89	-0.073	-0.317	0.23	-0.537	-0.814	0.66	NC	-0.324	NC	-0.448	-0.834	0.54
DLT04	-0.267	-0.331	0.81	-0.848	-0.852	1.00	NA	-0.303	NC	-0.633	-0.772	0.82	NC	-0.310	NC	-0.502	-0.786	0.64
DLT05	-0.244	-0.303	0.80	-0.921	-0.772	1.19	-0.148	-0.279	0.53	-0.635	-0.703	0.90	NC	-0.283	NC	-0.529	-0.710	0.74
DLT06	-0.291	-0.331	0.88	-1.042	-0.852	1.22	NA	-0.303	NC	-0.731	-0.772	0.95	NC	-0.310	NC	-0.612	-0.786	0.78
DLT07	-0.266	-0.317	0.84	-0.920	-0.820	1.12	-0.144	-0.296	0.49	-0.610	-0.752	0.81	NC	-0.296	NC	-0.501	-0.755	0.66
DLT08	-0.242	-0.324	0.75	-0.991	-0.834	1.19	NA	-0.300	NC	-0.729	-0.758	0.96	-0.204	-0.303	0.67	-0.555	-0.772	0.72
DLT09	-0.242	-0.290	0.84	-0.871	-0.731	1.19	-0.170	-0.269	0.63	-0.633	-0.669	0.95	NC	-0.269	NC	-0.444	-0.672	0.66
DLT10	-0.267	-0.386	0.69	-1.043	-1.020	1.02	-0.097	-0.352	0.27	-0.683	-0.910	0.75	-0.174	-0.362	0.48	-0.697	-0.938	0.74
DLT11	-0.244	-0.303	0.80	-0.899	-0.772	1.16	-0.146	-0.279	0.52	-0.582	-0.703	0.83	-0.117	-0.283	0.41	-0.473	-0.710	0.67
DLT12	-0.316	-0.386	0.82	-1.066	-1.020	1.04	-0.244	-0.352	0.70	-0.723	-0.910	0.79	-0.145	-0.362	0.40	-0.529	-0.938	0.56
DLT13	-0.291	-0.386	0.75	-1.139	-1.020	1.12	-0.171	-0.352	0.49	-0.538	-0.910	0.59	-0.147	-0.362	0.41	-0.613	-0.938	0.65
DLT14	-0.217	-0.324	0.67	-0.993	-0.834	1.19	-0.148	-0.300	0.49	-0.636	-0.758	0.84	-0.175	-0.303	0.58	-0.529	-0.772	0.68
DLT15	-0.267	-0.331	0.81	-0.993	-0.852	1.17	-0.195	-0.303	0.64	-0.659	-0.772	0.85	-0.118	-0.310	0.38	-0.530	-0.786	0.67
DLT 16	-0.171	-0.421	0.41	-0.850	-1.110	0.77	-0.122	-0.379	0.32	-0.585	-0.979	0.60	-0.117	-0.390	0.30	-0.430	-1.020	0.42
DLT17	-0.267	-0.462	0.58	-1.019	-1.241	0.82	-0.122	-0.410	0.30	-0.560	-1.076	0.52	-0.175	-0.427	0.41	-0.560	-1.131	0.50
DLT18	-0.195	-0.483	0.40	-1.043	-1.300	0.80	-0.196	-0.424	0.46	-0.753	-1.117	0.67	-0.117	-0.448	0.26	-0.473	-1.186	0.40
DLT19	NA	-0.348	NC	-0.726	-0.903	0.80	NA	-0.317	NC	-0.232	-0.814	0.28	NC	-0.324	NC	-0.416	-0.834	0.50
DLT20	-0.436	-0.348	1.25	NA	-0.903	NC	-0.146	-0.317	0.46	-0.146	-0.814	0.18	-0.174	-0.324	0.54	NC	-0.834	NC

Table 5. 5 – Shift factor between field and theoretical stresses: Part II

	SG 16						SG 22			SG 25			SG 26		
	SWA			DWA			DWA			DWA			DWA		
	FIELD	ISLAB	SF	FIELD	ISLAB	SF									
DLT01	-0.334	-0.247	1.35	-1.257	-0.570	2.20	-0.280	-0.386	0.73	-0.324	-0.510	0.64	0.409	0.510	0.80
DLT02	-0.482	-0.391	1.23	-1.554	-0.987	1.58	-0.406	-0.724	0.56	NC	-0.903	NC	0.429	0.903	0.48
DLT03	-0.407	-0.421	0.97	-1.806	-1.075	1.68	-0.401	-0.796	0.50	-0.371	-0.993	0.37	0.553	0.993	0.56
DLT04	-0.481	-0.409	1.18	-1.955	-1.038	1.88	-0.723	-0.752	0.96	-0.600	-0.938	0.64	0.566	0.938	0.60
DLT05	-0.330	-0.374	0.88	-1.804	-0.938	1.92	-0.703	-0.683	1.03	-0.604	-0.862	0.70	NC	0.862	NC
DLT06	-0.405	-0.403	1.01	-1.695	-1.021	1.66	-0.517	-0.752	0.69	-0.677	-0.938	0.72	0.658	0.938	0.70
DLT07	-0.295	-0.391	0.75	-1.991	-0.987	2.02	-0.468	-0.724	0.65	NC	-0.903	NC	0.777	0.903	0.86
DLT08	-0.479	-0.397	1.21	-1.809	-1.004	1.80	-0.528	-0.738	0.72	-0.596	-0.924	0.65	0.569	0.924	0.62
DLT09	-0.403	-0.358	1.13	-1.621	-0.892	1.82	-0.616	-0.648	0.95	-0.448	-0.820	0.55	0.609	0.820	0.74
DLT10	-0.368	-0.463	0.79	-1.770	-1.195	1.48	-0.499	-0.893	0.56	-0.791	-1.103	0.72	0.808	1.103	0.73
DLT11	-0.370	-0.374	0.99	-1.844	-0.938	1.97	-0.701	-0.683	1.03	-0.556	-0.862	0.65	0.655	0.862	0.76
DLT12	-0.480	-0.470	1.02	-1.846	-1.217	1.52	-0.375	-0.893	0.42	NC	-1.103	NC	0.681	1.103	0.62
DLT13	-0.481	-0.463	1.04	-1.957	-1.195	1.64	-0.530	-0.893	0.59	-0.563	-1.103	0.51	0.659	1.103	0.60
DLT14	-0.407	-0.397	1.03	-1.920	-1.004	1.91	-0.435	-0.738	0.59	-0.561	-0.924	0.61	0.658	0.924	0.71
DLT15	-0.440	-0.403	1.09	-1.809	-1.021	1.77	NC	-0.752	NC	-0.512	-0.938	0.55	0.530	0.938	0.57
DLT 16	-0.185	-0.494	0.37	-1.737	-1.285	1.35	-0.591	-0.965	0.61	-0.447	-1.189	0.38	0.606	1.189	0.51
DLT17	-0.405	-0.537	0.75	-1.771	-1.409	1.26	NA	-1.062	NC	-0.607	-1.310	0.46	0.830	1.310	0.63
DLT18	-0.479	-0.556	0.86	-1.984	-1.462	1.36	NA	-1.103	NC	-0.562	-1.362	0.41	0.601	1.362	0.44
DLT19	-0.479	-0.415	1.15	-1.367	-1.057	1.29	NA	-0.796	NC	NC	-0.993	NC	0.519	0.993	0.52
DLT20	-0.445	-0.421	1.06	-1.292	-1.075	1.20	NA	-0.796	NC	NC	-0.993	NC	0.519	0.993	0.52

Table 5. 6 – Shift factor between field and theoretical stresses: Part III

	SG 29			SG30						SG 31					
	DWA			SWA			DWA			SWA			DWA		
	FIELD	ISLAB	SF	FIELD	ISLAB	SF	FIELD	ISLAB	SF	FIELD	ISLAB	SF	FIELD	ISLAB	SF
DLT01	0.357	0.503	0.71	NC	NC	NC	-0.494	-0.518	0.95	0.215	0.230	0.93	0.728	0.518	1.41
DLT02	0.541	0.889	0.61	NC	NC	NC	-0.735	-0.915	0.80	0.160	0.368	0.43	1.024	0.915	1.12
DLT03	0.635	0.965	0.66	NC	NC	NC	-0.739	-1.000	0.74	0.212	0.397	0.54	1.300	1.000	1.30
DLT04	0.680	0.917	0.74	-0.176	-0.385	0.46	-0.868	-0.965	0.90	0.364	0.385	0.95	1.376	0.965	1.43
DLT05	0.725	0.841	0.86	NC	NC	NC	-0.793	-0.869	0.91	NC	NC	NC	1.405	0.869	1.62
DLT06	0.863	0.917	0.94	NC	NC	NC	-0.606	-0.948	0.64	NC	NC	NC	1.126	0.948	1.19
DLT07	0.725	0.889	0.81	NC	NC	NC	-0.766	-0.915	0.84	0.319	0.368	0.87	0.845	0.915	0.92
DLT08	0.683	0.903	0.75	NC	NC	NC	-0.902	-0.932	0.97	0.319	0.373	0.85	2.769	0.932	2.97
DLT09	0.635	0.800	0.79	-0.242	-0.336	0.72	-0.789	-0.825	0.96	0.709	0.336	2.11	2.097	0.825	2.54
DLT10	0.681	1.076	0.63	NC	NC	NC	-0.845	-1.115	0.76	0.796	0.437	1.82	0.866	1.115	0.78
DLT11	0.634	0.841	0.75	-0.221	-0.351	0.63	-0.840	-0.869	0.97	NC	NC	NC	NC	NC	NC
DLT12	0.770	1.076	0.71	-0.309	-0.444	0.70	-0.997	-1.136	0.88	NC	NC	NC	1.642	1.136	1.45
DLT13	0.767	1.076	0.71	NA	-0.437	NC	-0.897	-1.115	0.80	NC	NC	NC	1.202	1.115	1.08
DLT14	0.680	0.903	0.75	-0.306	-0.373	0.82	-0.893	-0.932	0.96	0.348	0.373	0.93	0.813	0.932	0.87
DLT15	0.680	0.917	0.74	NA	-0.379	NC	-0.794	-0.948	0.84	NC	0.379	NC	NA	0.948	NC
DLT 16	0.632	1.158	0.54	-0.219	-0.466	NC	-0.793	-1.200	0.66	NA	0.466	NC	NA	1.200	NC
DLT17	0.683	1.269	0.54	-0.172	-0.508	0.34	-0.837	-1.320	0.63	NC	0.508	NC	NA	1.320	NC
DLT18	0.771	1.317	0.58	-0.220	-0.526	0.42	-0.876	-1.371	0.64	NC	0.526	NC	NA	1.371	NC
DLT19	0.317	0.965	0.33	-0.249	-0.391	0.64	-0.589	-0.983	0.60	0.385	0.391	0.99	NA	0.983	NC
DLT20	NC	0.965	NC	-0.136	-0.397	0.34	-0.507	-1.000	0.51	0.495	0.397	1.25	1.005	1.000	1.00

Table 5.7 presents the final Shift factor (SF) between field and theoretical stresses for constant speed DLTs. Surface and bottom SGs presented a SF close to one as it is expected in a perfect simulation, nevertheless, the standard deviation was around half of the average indicating a need to exercise caution while applying these results. For the top SGs, the SF indicated, in average numbers, field stresses that were 30% smaller than simulated results. This is in accordance with another field/theoretical stress simulation in concrete pavements that found this correlation around 40% (CERVO *et al*, 2005). This also agrees with the fact that for the short CRCP, the wheel load over the crack affects the crack width decreasing the stresses as previously explained. Moreover, the graphs of these correlations are shown in Figure 5.8. While the bottom SGs exhibit a small correlation coefficient, the surface and top SGs show a more consistent (for such a practical experiment) linearity between theoretical and field stresses.

Table 5. 7 – Shift factor (SF) for field/ISLAB stresses

	Average SF	Std. Dev.
Surface	1.03	0.42
Top	0.69	0.17
Bottom	0.95	0.50

Regarding the high speed DLTs, it was expected that the simulated stresses would be higher than the field stresses because ISLAB can only simulate static loads. It is well established that static loads cause higher stress levels than dynamic loads in constant speed because the moving load has a momentary lifting effect on the total load as concluded by Kim *et al.* (2002), Zhang *et al.* (2007) and Xiao *et al* (2011). In the short CRCP case, this assumption was observed for all SG except for SG16 under the DWA. However, even for this SG, the SF for the high speed DTLs was much lower than for the constant low speed DLT (in average numbers from 1.79 to 1.32). In general, the ISLAB stresses were double the field stresses (SF of 0.5).

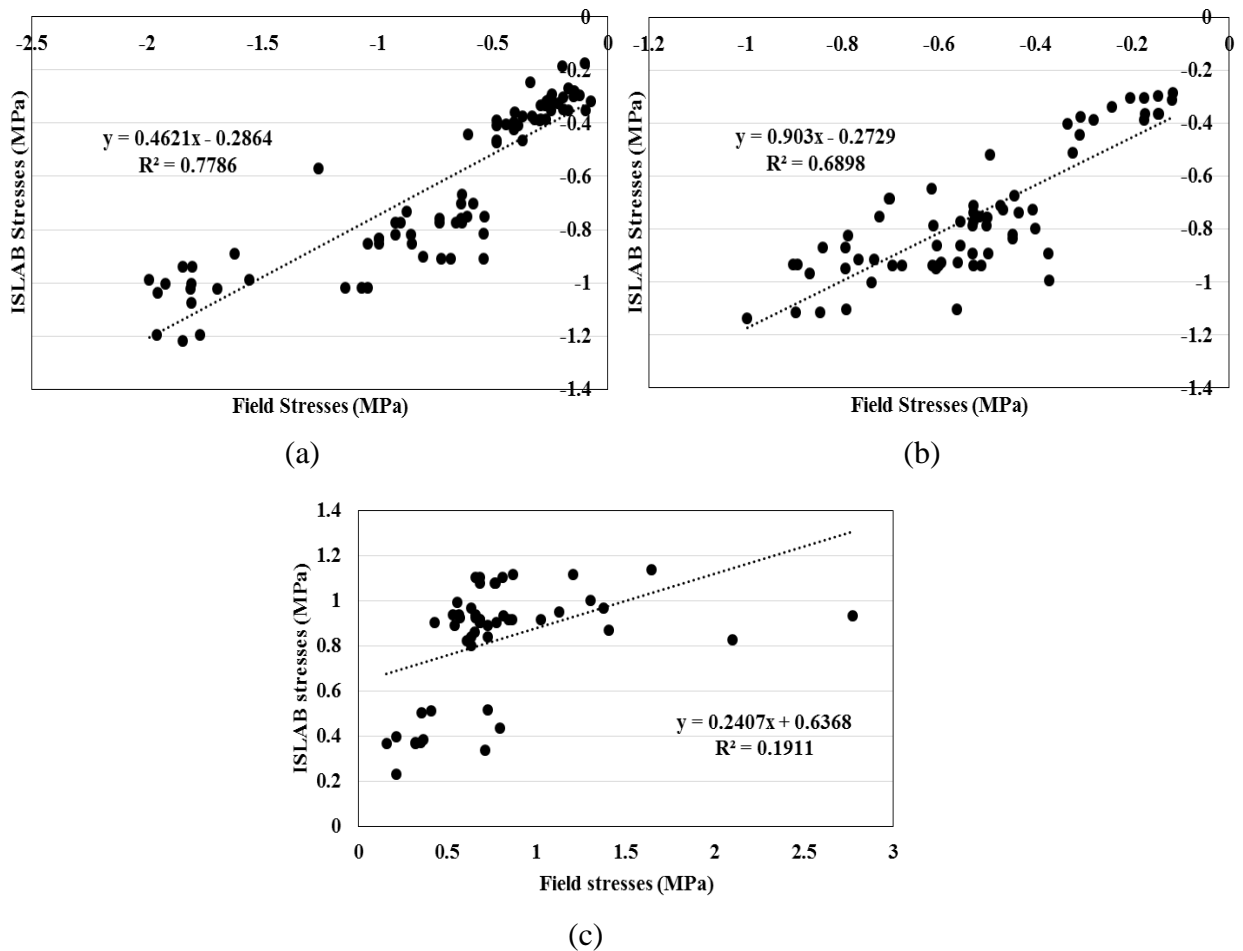


Figure 5. 8 – Correlation between field and ISLAB stresses for (a) surface, (b) top and (c) bottom SGs

When examining the braking DLTs, there must be a separation between the SWA and the DWA. As disclosed by Salles *et al.* (2015) in the short CRCP and also observed by Pereira *et al.* (2006) in an ultra-thin whitetopping, during braking, due to vehicle center of mass displacement, the SWA and the DWA become momentarily more and less loaded, respectively. As the braking operation was performed with the DWA coming to a full stop over the SG group B (Figure 5.9), the SWA braking effect would be expected for SGs 01 and 18 while the DWA effect would be captured by SGs 16, 29, 30 and 31. The expected SWA effect was observed for SG01, with field stress being 25% higher than simulated stresses. However SG 18 showed opposite results with a SF of 0.54. For the DWA, SGs 29 and 30 presented the anticipated result with a SF of 0.44 while, in the opposite direction, SG 16 exhibited field stresses 25% higher than simulated ones. Apparently SG16 captured much

higher strains than expected. In spite of this, the results of high speed and braking DLT simulations show mostly coherent results.

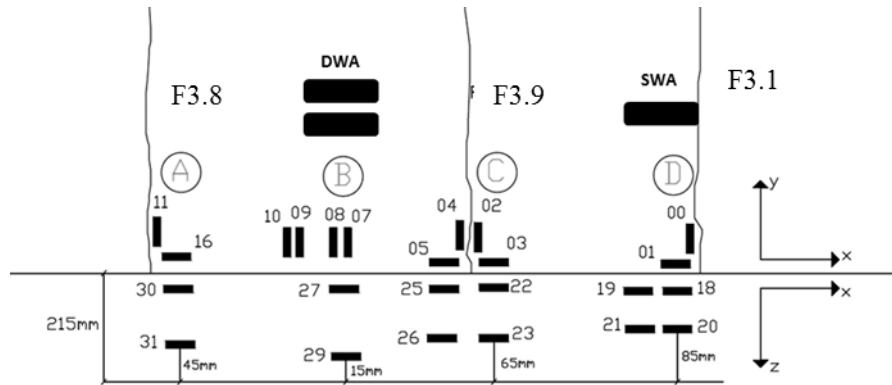


Figure 5. 9 – Braking position in the instrumented segment

### 5.2.1 Field stress simulation regarding thickness variation

In a further attempt to correct the ISLAB load simulation regarding the field dynamic test, the whole process of stress simulation was repeated concerning the thickness variation resulted from the ultrasonic testing as described in Chapter 3. As the previous simulation only considered the thickness measured (215 mm) at the instrumented segment of Section 3, there was the concern that the thickness variation effect in the stresses was not being properly addressed. Therefore, a new set of simulations was done dividing Section 3 into areas (Figure 5.10) with different thickness according to the ultrasonic testing results of stations 1 to 5 in the right (R), center (C) and left (L) positions. For the simulation, all the considerations made for the continuous slab simulation attempt were repeated save the temperature differential. Unfortunately, ISLAB does not compute thermal effects when areas with different parameters are created.

1.5 m	L1 (182.00 mm)	L2 (253.40 mm)	L3 (244.20 mm)	L4 (243.00 mm)	L5 (254.80 mm)
2.05 m	C1 (169.20 mm)	C2 (255.00 mm)	C3 (238.10 mm)	C4 (226.40 mm)	C5 (206.00 mm)
1.5 m	R1 (201.20 mm)	R2 (229.40 mm)	R3 (205.93 mm)	R4 (212.98 mm)	R5 (207.48 mm)
	10 m				

Figure 5. 10 – Section 3 areas with different thickness according to the ultrasonic survey

Results for the shift factors for both constant thickness and varying thickness conditions are presented in Table 5.8. For top SGs, the results show a slight improvement in the SF, however that is not true for the remaining SG. Moreover, there was a small increase in data variability (standard deviation) which can be interpreted as a less successful simulation. However, this small difference between results can also be consequence of field data variability which is expected for practical experiments.

Table 5. 8 – Shift factor (SF) for field/ISLAB stresses considering constant thickness and thickness variation

	Avg. SF		Std. Dev.	
	Constant Thickness	Thickness Variation	Constant Thickness	Thickness Variation
Surface	1.03	1.13	0.42	0.48
Top	0.69	0.73	0.17	0.19
Bottom	0.95	1.07	0.5	0.60

It was observed that stresses simulated with thickness variation were marginally smaller (average of 2%) than stresses simulated with constant thickness of 215 mm. As can be seen in Figure 5.10, the instrumented segment was placed in the R4 area, which has a 212.98 mm slab. It was expected that due to the thickness deficiency (approximately 2 mm), the stresses would be higher in the thickness variation simulation. Yet, as previously exposed, ISLAB does not consider thermal gradient effects when the slab is divided in areas. Therefore, the

effect of thermal gradient – even small ones (0.45 C in this case) – are significant for slab stresses.

To further verify this experiment, a 215 mm slab (case A) and a 212.98 mm slab (case B) without thermal differentials were simulated and compared to the thickness variation simulation (case C) and to the 215 mm slab with thermal gradient (simulation case for the previous section – case D). SG 01 position and DWA load were used in this comparison test. Figure 5.11 presents the results along with the field data.

Case B presents stresses slightly smaller than Case A, attributable to the 2 mm thinner slab of the latter. Case C presents higher stresses than cases A and B due to the thickness variation. The worse scenario is Case D, with the same constant thickness as Case A (215 mm) but considering a thermal differential. Interestingly, most field stresses are greater than Case D indicating the thickness variation plus thermal gradient has a combined effect on the slab stresses. However, as mentioned before, ISLAB cannot simulate thickness variation and thermal gradients. While the numerical difference between stresses for the four cases is not highly significant in terms of pavement design and performance, it is important to observe the sensitivity of the simulation software.

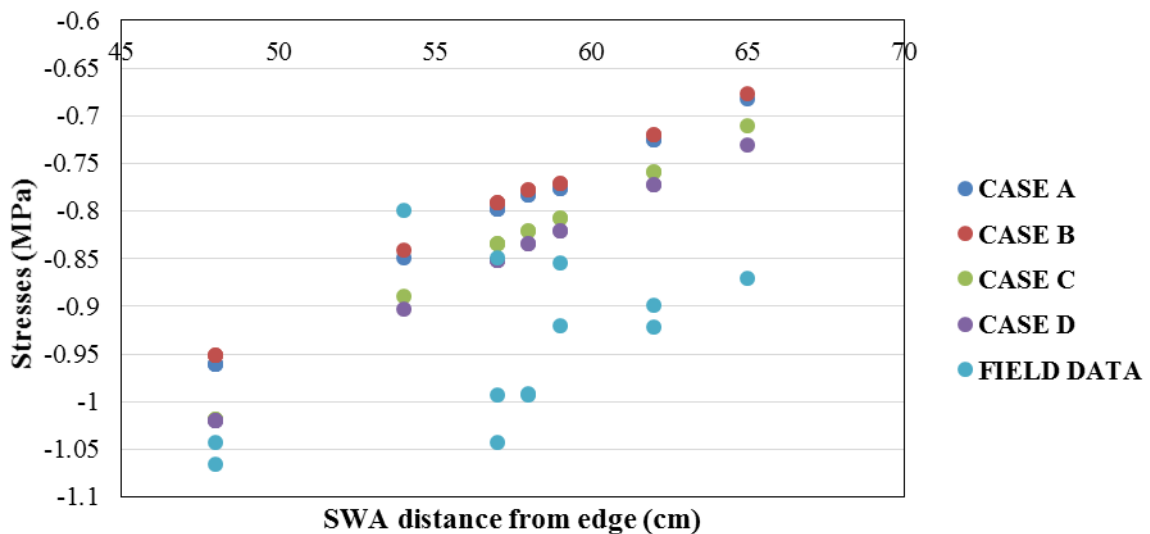


Figure 5. 11 – Simulation of constant thickness 212.98 mm slab (Case A); 215 mm slab (Case B); slab with thickness variation (Case C); and 215 mm slab with thermal gradient (case D)

## 6. DESIGN RECOMMENDATIONS FOR THE SHORT CRCP

The final chapter of this thesis develops and presents the primary goal of the research project: design recommendations for the short CRCP structure. For that, primarily, critical tensile stress positions for temperature and vehicle loadings are analyzed. Once the critical position is known, stress simulations are performed concerning variations in load (vehicle plus environmental), slab thickness and concrete modulus of rupture. Finally design recommendations regarding fatigue models are given in an abacus format.

### 6.1 Critical stress loading position

Despite the common rigid pavement knowledge based on Westergaard theory that edge loading generate higher stress levels, as seen in Huang and Wang (1973) and Tia *et al.* (1989), it was decided regarding the short CRCP configurations (continuous slab) to test a number of load positions (Figure 6.1) concerning vehicle and environmental loads.

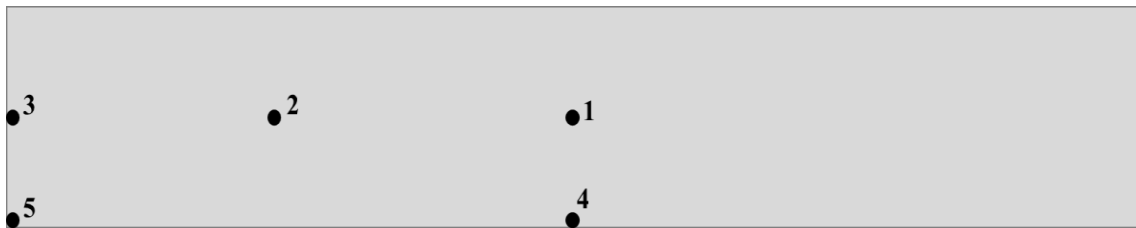


Figure 6. 1 – Critical loading locations: 1 (center); 2 (mid-center); 3 (edge); 4 (center-edge); and 5 (corner)

Firstly, only environmental loads (thermal gradients) were applied to the slab. The short CRCP was simulated as a 250 mm slab with an E of 30,000 MPa over a 60 mm asphalt base being the whole system under a 100 MPa/m modulus of subgrade reaction (k). Figure 6.2 presents the stress (psi) for the 10°F (5.55°C) thermal gradient in the slab bottom location in x (transversal) and y (longitudinal) directions. As can be seen, stresses in the longitudinal direction are slightly higher than on the transversal direction. Most of the slab area shows tensile stresses as expected. Also, the location with the highest stress is located a few meters (3.33 m) off the slab edge. When applying a 20°F (10.11°C) thermal gradient although the resulting stresses are higher, the stress configuration observed in Figure 6.2 remains the same

with the critical stresses located now at 4.55 m off the slab edge. Tables 6.1 and 6.2 presents the stresses for the complete simulations.

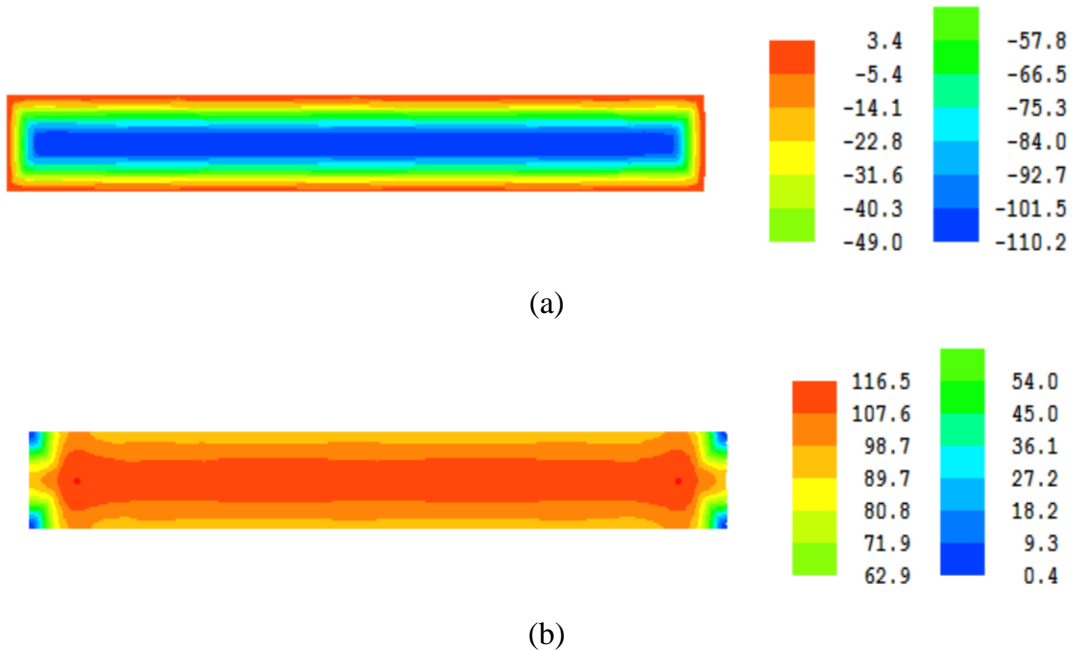


Figure 6. 2 – Principal stresses in a slab under a 10°F (5.55°C) thermal differential for (a) Top and (b) bottom positions

Center and mid-center stresses (locations 1 and 2 in Figure 6.1) are practically identical being both the highest stress locations in the regular location spots. Edge and center edge locations present points of almost null stresses in the opposite direction due to the slab end. This also explains the small values presented by the corner location. The magnitude of the stresses will be further discussed in the next section. Principal stresses are almost identical to the highest stress in any direction.

Table 6. 1 – Stresses due to thermal gradient of 10°F (5.55°C) in different slab locations

Location	$\Delta T$								
	10								
	Top				Bottom				Principal
	Y		X		Y		X		
M				MPa					
1 Center	25.00	2.53	-0.771	-0.755	0.771	0.755	0.771	0.771	
2 Mid-center	12.50	2.53	-0.771	-0.755	0.771	0.755	0.771	0.771	
3 Edge	50.00	2.53	0.001	-0.659	-0.001	0.659	0.659	0.659	
4 Center edge	25.00	0.00	-0.636	0.005	0.684	-0.005	0.663	0.663	
5 Corner	50.00	0.00	0.011	0.010	-0.011	-0.010	0.002	0.002	
6 Critical (10)	3.33	2.53	-0.804	NS	<b>0.804</b>	NS	<b>0.804</b>	<b>0.804</b>	

NS = not simulated

Table 6. 2 – Stresses due to thermal gradient of 20°F (10.11°C) in different slab locations

Location	$\Delta T$								
	20								
	Top				Bottom				Principal
	Y		X		Y		X		
M				MPa					
1 Center	25.00	2.53	-1.539	-1.482	1.539	1.482	1.539	1.539	
2 Mid-center	12.50	2.53	-1.538	-1.482	1.538	1.482	1.538	1.538	
3 Edge	50.00	2.53	0.001	-1.251	-0.001	1.251	1.251	1.251	
4 Center edge	25.00	0.00	-1.327	0.010	1.327	-0.010	1.327	1.327	
5 Corner	50.00	0.00	0.020	0.019	-0.020	-0.019	0.017	0.017	
6 Critical (20)	4.55	2.53	-1.605	NS	<b>1.605</b>	NS	<b>1.605</b>	<b>1.605</b>	

NS = not simulated

In order to simulate vehicle loads, the standard single axle (dual wheel) with a load of 80 kN and tire pressure of 0.55 MPa was applied. Thermal gradient was set at 10°F (5.55°C). The pavement configuration remained the same as that of the environmental testing. Concerning the results of the prior simulation, the single axle load was also positioned at the location 6 (Table 6.1). Table 6.3 displays the results. As anticipated, the location with the highest stresses was the center edge. Vehicle loading applied at the environmental load only critical location did not create greater stresses than in the other classic locations. Therefore the ensuing simulations were conducted with the stress analysis focused on the center edge location.

Table 6. 3 – Stresses due to thermal gradients and vehicle loading in different slab locations

Location		Top			Bottom		
		Y	X	Principal	Y	X	Principal
MPa							
1	Center	-1.503	-1.145	-1.145	1.503	1.145	1.510
2	Mid-center	-1.489	-1.131	-1.131	1.489	1.131	1.489
3	Edge	-0.807	-1.462	-0.765	0.807	1.462	1.503
4	Center edge	-2.055	-1.103	-1.103	<b>2.055</b>	1.103	<b>2.055</b>
5	Corner	-0.814	-1.324	0.862	0.814	1.324	1.393
6	Critical (10)	-1.393	-1.110	-1.124	1.393	1.110	1.441

## 6.2 Short CRCP simulation procedure

Based on the data provided by Chapter 5, the short CRCP structure was simulated as the experimental short CRCP, precisely, a continuous 50 m long and 5.05 m wide slab. Values for fixed and variable input parameters are given in Table 6.4. It was decided to vary vehicle load (standard dual wheeled single axle), thermal gradient, concrete slab thickness and modulus of rupture. The first two parameter variation was selected in view of the different vehicle loads and thermal gradients that the slab may be exposed to while the modulus of rupture was in accordance to the fatigue model applied in this study. Concrete slab thickness is the major design feature in design procedures and its variation was selected according to typical CRCP thickness found in the literature review.

Concerning the fixed parameters, the idea was to designers and constructors to use a standard concrete mixed as the one applied for the experimental short CRCP. The asphalt base, as mentioned in Chapter 5, is aiming at parameters of an asphalt layer without direct contact with the environment, i.e., less influenced by air temperature variation; thus the high resilient modulus. The subgrade reaction modulus was selected regarding the stiff asphalt base layer. As seen in previous studies, asphalt bases provide an enhanced performance for CRCPs due mainly to its non-erodible character.

Table 6. 4 – Input parameters for short CRCP simulation

Variable	Vehicle Load (Q)	kN	60, 80, 100, 120, 140
	Thermal Gradient ( $\Delta T$ )	$^{\circ}\text{C}$	0, 5, 10, 15, 20, 25
	Concrete Slab Thickness	mm	200, 250, 300, 350, 400
	Concrete Modulus of Rupture (MR)	MPa	3.5, 4.0, 4.5, 5.0, 5.5, 6.0
Fixed	Concrete Slab		
	Concrete Density	$\text{kg/m}^3$	2,400
	Coefficient of Thermal Expansion	$^{\circ}\text{C}^{-1}$	$8 \times 10^{-6}$
	Modulus of Elasticity	MPa	30,000
	Possion's Ratio		0.15
	Asphalt Base		
	Base Thickness	mm	60
	Asphalt Density	$\text{kg/m}^3$	2,200
	Resilient Modulus	MPa	7,000
	Possion's Ratio		0.35
	Subgrade		
	Modulus of Subgrade Reaction	MPa/m	100

#### 6.1.1 Tire/pavement contact area and finite element mesh

The tire/pavement contact area for the standard dual wheeled single axle was based on the study of Huang (1993) where the area was described as a false ellipse which is then simulated by ISLAB as a rectangle. Figure 6.3 shows an illustration of the false ellipsis and the correspondent ISLAB rectangle. Therefore, for the standard single axle with an 80 kN load and 0.55 MPa pressure, the tire/pavement contact area was approximately a 263 x 158 mm rectangle. Whenever the load was modified so was the tire pressure to provide an identical tire/pavement contact area. Similar simulations performed by Khazanovich *et al.* (2001) did not found any influence of the tire/pavement contact area in the top tensile stresses.

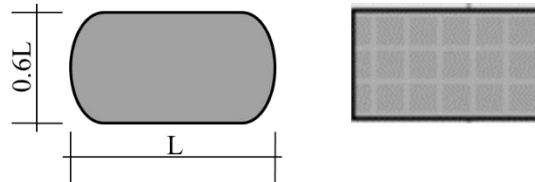


Figure 6. 3 – Illustration of the conceptual tire/pavement contact area and its ISLAB model

With reference to the tire/pavement contact area and the slab geometry, the finite element mesh was refined. Firstly, for computational time save, ISLAB standard medium mesh refinement was applied and then it was customized into a finer mesh around the axle load location. The mesh was refined until there was no significant change in the stress response. The final mesh was selected at 30 x 30 mm. Khazanovich *et al.* (2001) in ISLAB simulations for CRCP applied a 50 x 50 mm mesh. It was noticed that the finer the mesh, the smaller the stresses. Figure 6.4 shows a comparison between the medium mesh refinement and the customized mesh refinement that was applied to this study simulation. The principal stress difference between both meshes was 0.05 MPa which is quite small.

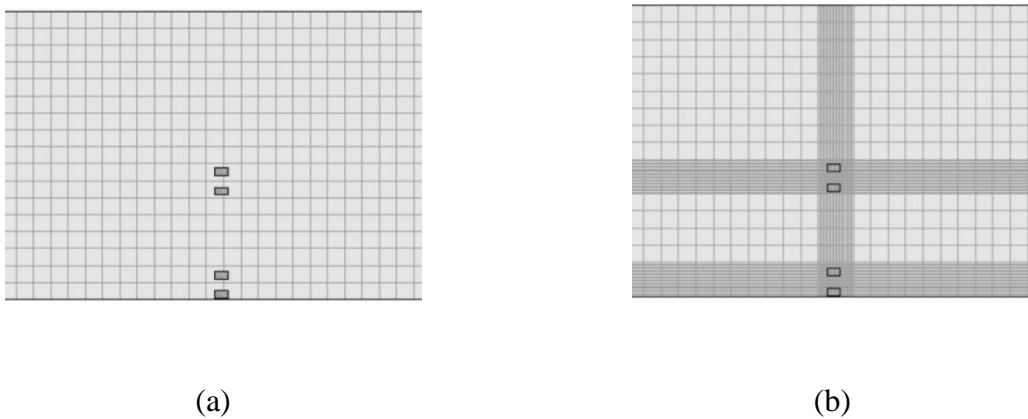


Figure 6. 4 – Mesh refinement in (a) custom medium mesh and (b) customized mesh

### 6.3 Short CRCP simulation analysis

The numerical simulations were held regarding the inputs displayed in Table 6.4. For each thickness, the combination of all axle loads and all thermal gradients were tested. Principal stresses results for the critical location are presented in Table 6.5.

As expected, the bigger the thermal differential, the greater the stresses. In Figure 6.5 (axle load of 80 kN), the stress due to only vehicle loading ( $\Delta T=0$ ) in a 200 mm thick slab are comparable to stresses in a slab with double thickness (400 mm) subjected to vehicle loading plus a 10°C thermal gradient, highlighting the environmental load great effect in concrete slabs. Also expected is the graph linear behavior caused by the linear thermal gradient applied

in the simulations. Moreover, for thicker slabs the difference in stresses is less evident than for thinner slabs for an equal thermal gradient. For example, the stress gap between thickness 200 and 250 mm is greater than for thickness 350 e 400 mm, indicating that although highly influential on performance due to other parameters, the benefit of building slabs thicker than 400 mm to mitigate uniform thermal effects is not as effective as increasing thickness in thinner slabs. Similar information can be obtained from Figure 6.6, where the stress decline is much more evident for thinner slabs.

Table 6. 5 – Principal stresses due to axle loading and thermal differential for a 200 mm slab

Thickness (mm)	Axle Load (kN)	$\Delta T$ (°C)					
		0	5	10	15	20	25
200	60	1.434	2.027	2.620	3.213	3.827	4.564
	80	1.910	2.503	3.096	3.689	4.295	4.950
	100	2.386	2.979	3.578	4.171	4.771	5.419
	120	2.861	3.454	4.054	4.647	5.247	5.881
	140	3.282	3.937	4.530	5.123	5.723	6.350
250	60	1.034	1.627	2.220	2.827	3.461	4.089
	80	1.379	1.972	2.572	3.172	3.813	4.447
	100	1.724	2.317	2.910	3.509	4.151	4.799
	120	2.068	2.661	3.254	3.854	4.495	5.150
	140	2.413	3.006	3.599	4.199	4.833	5.495
300	60	0.793	1.386	1.979	2.599	3.220	3.833
	80	1.055	1.648	2.241	2.861	3.489	4.116
	100	1.317	1.910	2.503	3.123	3.758	4.392
	120	1.579	2.172	2.765	3.385	4.027	4.661
	140	1.841	2.434	3.034	3.647	4.289	4.937
350	60	0.627	1.220	1.820	2.434	3.047	3.668
	80	0.841	1.434	2.027	2.648	3.268	3.889
	100	1.048	1.641	2.234	2.861	3.482	4.109
	120	1.255	1.848	2.448	3.068	3.696	4.323
	140	1.462	2.062	2.654	3.282	3.909	4.544
400	60	0.514	1.110	1.703	2.317	2.923	3.537
	80	0.686	1.282	1.875	2.489	3.110	3.716
	100	0.855	1.455	2.048	2.668	3.282	3.896
	120	1.027	1.620	2.220	2.841	3.461	4.082
	140	1.200	1.793	2.392	3.013	3.640	4.261

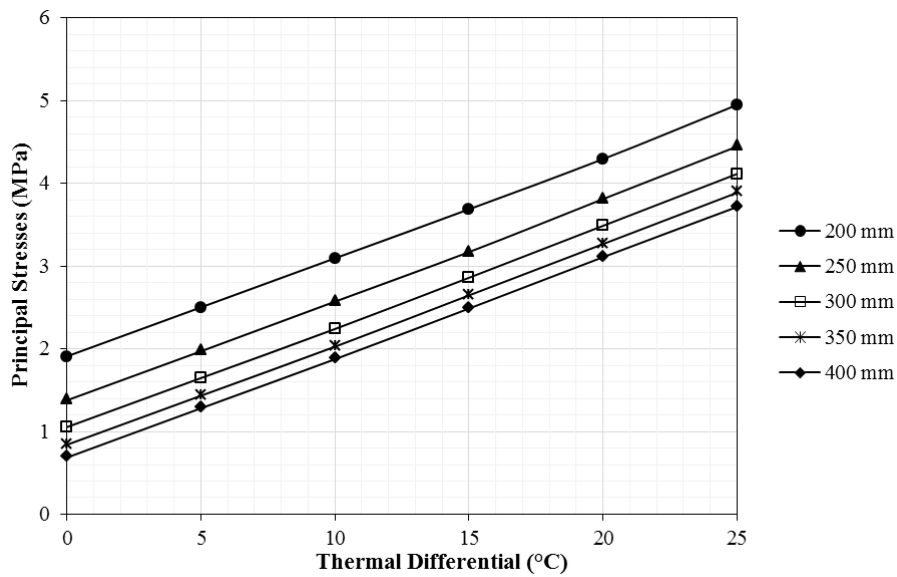


Figure 6. 5 – Short CRCP stresses due to thermal gradient variation for several slab thickness

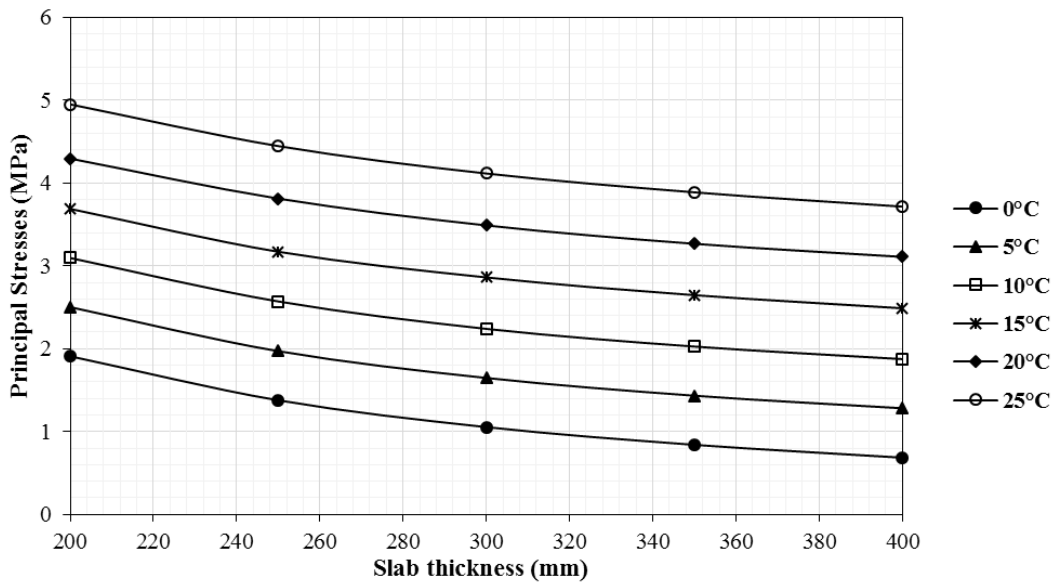


Figure 6. 6 – Short CRCP stresses due to slab thickness and thermal gradient variation

Considering the axle load variation (Figure 6.7) for a 250 mm slab, the increase in stress is linearly proportional to the increase in axle loading while the thermal gradient variation increases stresses in a constant way as also seen in Figure 6.6. In a similar study, Rodolfo (2001) found slightly higher stresses than those presented in Table 6.5. It must be noted, that

the referred study made simulations in an older version of ISLAB with a cementitious base (elasticity modulus of 10,000 MPa) and a  $k$  of 30 MPa/m. Additionally, the Rodolfo (2001) simulations were performed on a 5.5 m long and 3.45 m width single slab which does not simulate the entire JPCP structure. As seen in the shift factor determination in Chapter 5, while simulating a 215 mm slab under a maximum axle load of 123 kN and an almost zero-thermal differential, the stresses in a high LTE jointed structure, also different from classical JPCP because of the small crack (joint) spacing, were much smaller – and different from field stresses – than in a continuous structure. Nevertheless, the graphs presented in Figures 6.5 to 6.7 show great similarities with graphs in Rodolfo (2001) particularly regarding the parameters behavior.

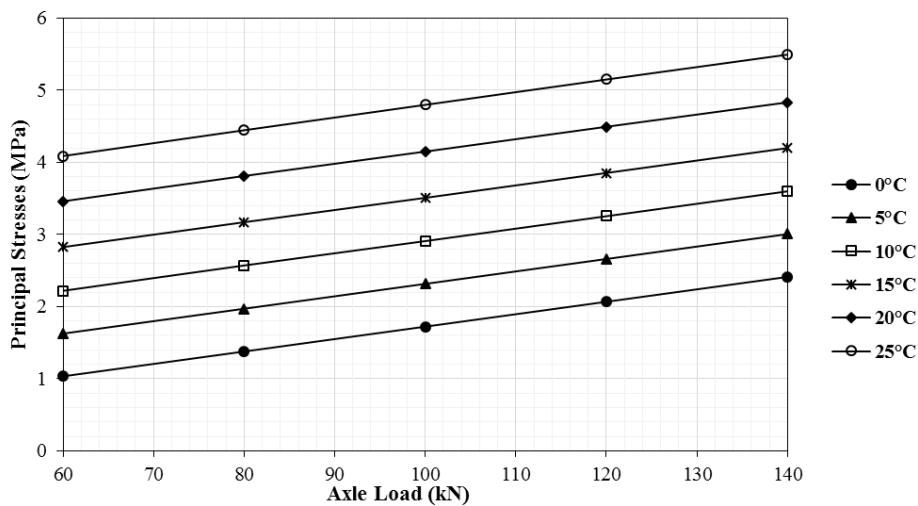


Figure 6. 7 – Short CRCP stresses due to axle load and thermal differential variation

In the same study, there was an observation that the increase in slab length from 4 to 5.5 m lead to an intensification in stresses by approximatively 20%, while an increase from 5.5 to 7 m resulted in a smaller stress growth (around 6%). To attest this conclusion regarding the short CRCP geometry, slab lengths of 1 (small crack spacing), 3 (large crack spacing), 5.5 (classic JPCP slab) and 50 m (short CRCP length) were simulated to observe the stress variation. The slab thickness for this simulations was 250 mm subjected to an axle load of 80kN and thermal differential of 0 and 5 and 15°C. Figure 6.8 presents the results. There is a stress increase of 20% when the slab length goes from 3 to 5.5 m, but only at the zero-thermal

gradient simulation. With the increase in thermal gradient, this stress difference goes higher and loses the proportionality observed by Rodolfo (2001). From 5 to 50 m there is a small and proportional stress difference where stresses in the shorter slab are slightly higher than in the larger slab, indicating that at some point the increase in stress with additional length observed by Rodolfo (2001) becomes insignificant and then reverses. When comparing 1 and 3 m slabs, with greater thermal gradients the stresses become more similar. Both situations can be explained by the slab geometry. Rodolfo (2001) only simulated classic JPCP slabs where the slab longitudinal direction (length) is greater than its transversal direction (width). Therefore, the principal stresses are in the longitudinal y direction. Regarding CRCPs the small crack width creates slabs with an inverse geometry, i.e., width greater than length which changes the direction of the principal stresses to the transverse x direction losing any observed proportionality. From the small sample simulated in this study, with zero-thermal differential, 1 and 3 m length slabs have their principal stresses in the longitudinal direction while with increase in thermal gradients there is a change in the stress configuration of short slabs according to the slab length as seen in Table 6.6.

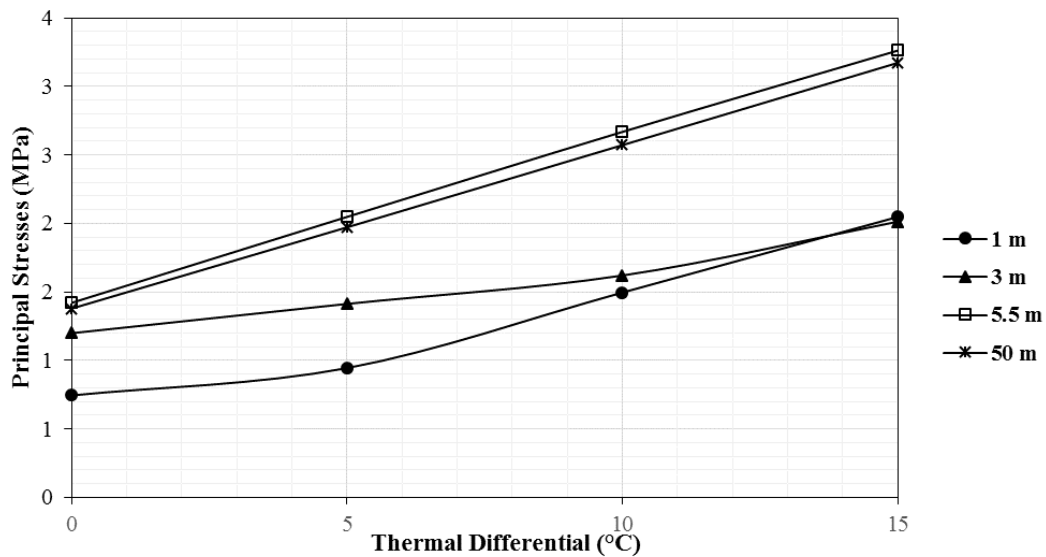


Figure 6. 8 – Stress in slabs with different lengths subjected to thermal gradient variation

Table 6. 6 – Slab bottom stresses direction versus slab length for different thermal gradients

Slab		$\Delta T$ (°C)					
		0			5		
Length (m)	Width (m)	X	Y	Principal	X	Y	Principal
1.00	5.05	0.386	<b>0.745</b>	0.745	<b>0.945</b>	0.731	0.945
3.00	5.05	0.386	<b>1.407</b>	1.407	0.979	<b>1.627</b>	1.627
Slab		10			15		
Length (m)	Width (m)	X	Y	Principal	X	Y	Principal
1.00	5.05	<b>1.496</b>	0.717	1.496	<b>2.048</b>	0.710	2.048
3.00	5.05	1.579	<b>1.834</b>	1.834	<b>2.041</b>	2.006	2.041

This results add further light to the way CRCP are designed regarding maximum stresses. For short slabs (small crack spacing), depending on the thermal gradient, the principal stresses are located in the transversal direction. This also explains the difficulty of simulating the dynamic load testing discussed in Chapter 5 with a cracked (jointed) slab. Additionally, only in the case of a 1 m length slab with a zero-thermal differential, the greater principal stress was localized at the slab top instead of the bottom which goes in contradiction with traditional CRCP design and punchout prediction that indicate slab top stresses greater than bottom stresses. Yet, it should be noted that MPDGE was designed and calibrated in the US, a temperate climate country which experiences negative thermal gradients being those the major causes of top-down cracking in JPCP as seen in Darter *et al.* (1995) and Hansen *et al.* (2002). If a  $-5^{\circ}\text{C}$  thermal gradient is applied to the short slabs, the top principal stress becomes the greater stress. Nevertheless, as shown by Balbo and Severi (2002), countries under tropical climate hardly experience any negative thermal gradients. Intuitively, one can argue that CRCPs in tropical environment are less susceptible to punchout development.

Moreover, if traditional CRCP presents a continuous behavior as that shown by the experimental short CRCP, CRCP design, regarding stresses, is more similar to JPCP design than the methods currently applied for CRCP design concerning positive thermal differentials. While further investigation, out of the scope of the thesis proposed here, is needed to investigate this possibility, the information on Figure 6.8 attests its potential.

## 6.4 Fatigue model selection and analysis

As to relate the simulated stresses along with a typical variation of concrete modulus of rupture (MR – Table 6.4) in order to compute an allowable number of load repetitions, a concrete fatigue model was selected. Several models were considered based on the classical relation between the maximum tensile stress due to vehicle and environmental loading and the concrete flexural strength (modulus of rupture), i.e., the stress-strength ratio (SSR).

During the fatigue model selection and analysis several aspects of development of such models must be considered. There should be caution regarding laboratorial investigation as those are not exactly representative of field performance due to several factors, such as: (i) difficulty in relating laboratory concrete slab and – specially – beam modulus of rupture to field concrete slabs modulus of rupture; (ii) field concrete more heterogeneous characteristics when compared to laboratory controlled concrete; (iii) vehicle load wandering in the field; (iv) field curling and warping; (v) loading frequency which in laboratory tests is higher leading to short loading times that are not similar to nor as harmful as real axle loads. These and other aspects make laboratory fatigue models to be conservative over predicting the concrete fatigue life (CERVO and BALBO., 2012).

Conversely, semi-empiric models established around field experiences and theoretical stress modeling while being more accurate to predict field behavior, yield limitations to material and traffic aspects of the field data applied.

The unofficial concrete pavement design method in Brazil is the PCA (1984) design model (ABCP, 1996). The method describes two fatigue models based on the SSR value as follows in Equations 60 and 61:

$$\text{for } SSR > 0.55, \quad \log N = 11.78 - 12.11(SSR) \quad (60)$$

$$\text{for } 0.45 < SSR < 0.55, \quad N = \left( \frac{4.2577}{SSR - 0.4325} \right)^{3.268} \quad (61)$$

Where N = number of allowable load repetitions.

However, as mentioned before, the method does not take in consideration the curling effect of thermal gradients which have a great influence on pavement performance.

One of the most famous models was developed by Darter (1977) based on flexural tests in over 140 beams. This model was applied for design of CRCP by the Department of Transportation of Illinois according to Beyer and Roesler (2009) being called the “zero maintenance” fatigue model. The fatigue model is expressed by Equation 62 (50% fatigue probability):

$$\log(N) = 17.61 - 17.61(SSR) \quad (62)$$

The same author later developed a new model analyzing laboratory results and field data from almost 30 years of observations on concrete pavements in airports (DARTER, 1990). The  $k$ -values were measured in situ while the concrete modulus of rupture was collected from laboratorial tests. The best fit model is presented in Equation 63:

$$\log(N) = 2.13 \left( \frac{1}{SSR} \right)^{1.2} \quad (63)$$

Koyanagawa *et al.* (1994) developed a model based on different concrete flexural strength due to several aggregate sizes. The model for a 5.2 concrete modulus of rupture is described by Equation 64 (50% fatigue probability), as follows:

$$\log(N) = 18.49 - 16.95(SSR) \quad (64)$$

In 1988, Majidzadeh (1998) developed the ARE<sup>7</sup> model based on the experimental sections of the AASHO road test. The model considered a standard axle of 80 kN and final pavement serviceability of 2.5. The model is represented by Equation 65, as follows:

$$N = 23.440 \left( \frac{1}{SSR} \right)^{3.21} \quad (65)$$

The National Cooperative Highway Research Program (NCHRP) model (Equation 66), developed by Tayabji and Jiang (1998), was based on correlation to the number of loading cycles and estimated stresses with a failure criterion of 50% cracked slabs.

$$\log(N) = 2.8127 \left( \frac{1}{SSR} \right)^{1.2214} \quad (66)$$

The MPDGE number for CRCP allowable loads repetitions can be determined by Equation 67 that as previously discussed employs top stress which are calculated based on, among other parameters, crack spacing, width and LTE. It is noticeable the similarities from this model to the Darter (1990) and Tayabji and Jiang (1998) models.

$$\log(N) = 2 \left( \frac{1}{SSR} \right)^{1.2} - 1 \quad (67)$$

Regarding Brazilian studies, Cervo (2004) developed two fatigue models (laboratory) described by Equations 68 and 69 for, respectively, typical unsaturated (dry) and saturated concretes applied in paving.

$$\log(N) = 25.858 - 25.142(SSR) \quad (68)$$

$$\log(N) = 13.408 - 12.102(SSR) \quad (69)$$

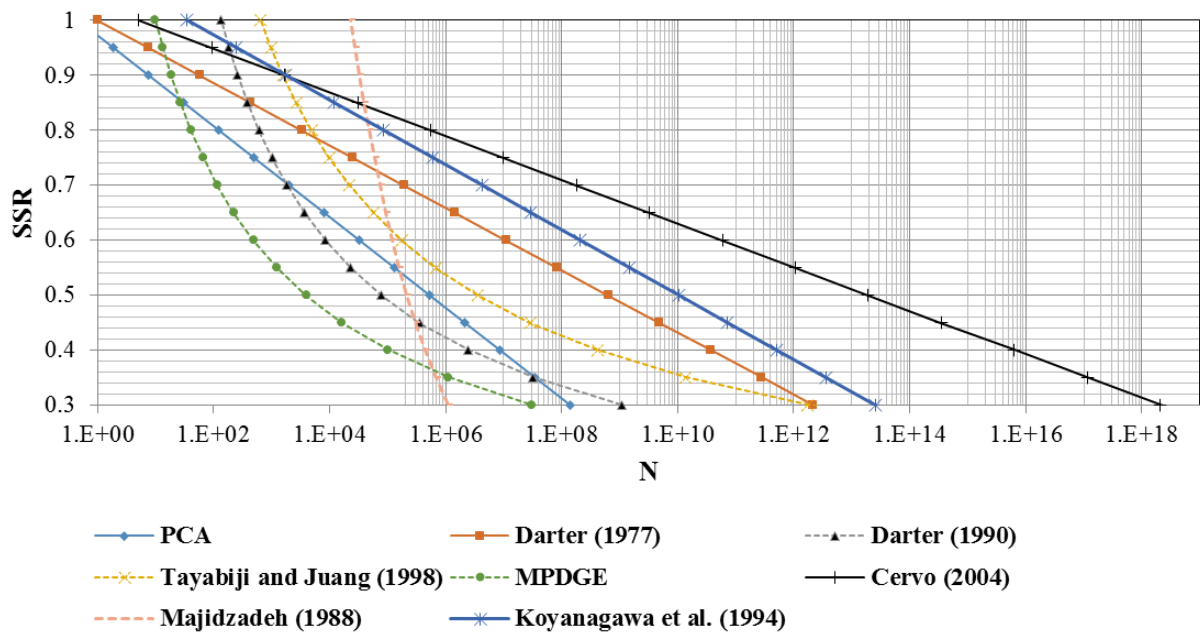
Cervo and Balbo (2012) also developed a shift factor between field and laboratory fatigue models described in mathematical form in Equation 70. The study involved a semi-empiric fatigue model for ultra-thin concrete slabs with high strength concrete (Balbo, 2003) and a laboratory fatigue model using the same concrete. The shift factor helps to mitigate the mentioned differences between field and laboratory fatigue life and clearly indicates that in situ concrete fails faster than laboratory tested concrete.

$$SF = \frac{N_{field}}{N_{lab}} = (SSR)^{4.2} \quad (70)$$

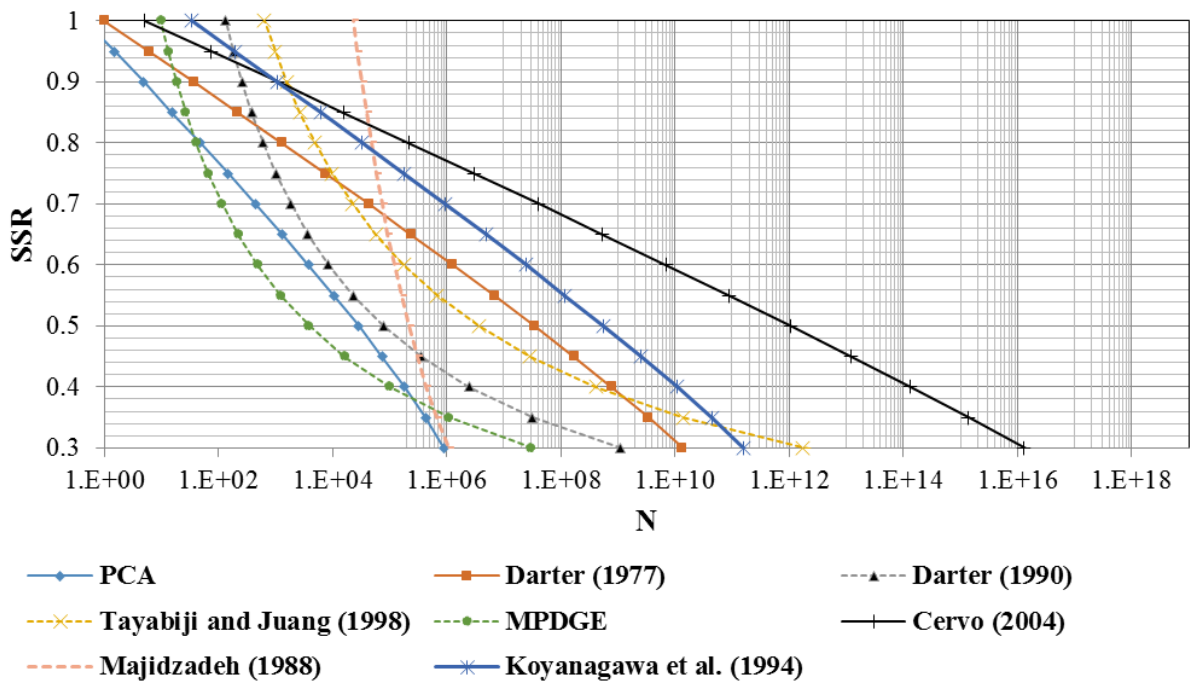
Figure 6.9a shows the stated models resulting fatigue life for a range of SSRs while Figure 6.9b presents, for the same SSR set, the fatigue life when applying the shift factor developed by Cervo and Balbo (2012). The shift factor was applied to the laboratory only models, namely: PCA (1984), Darter (1977), Koyanagawa *et al.* (1994) and Cervo (2004).

There is a clear difference between laboratory (continuous line) and field (dashed line) based fatigue models. In Figure 6.9a, save for the PCA (1984) model, the field based models are more conservative providing shorter fatigue life for SSR ranging from 0.3 to 0.7. As mentioned before, this result is due to the many differences between laboratory and field fatigue behavior, especially regarding the load frequency. The comparison also shows how conservative the PCA (1984), a laboratory based model, is. Moreover, it is interesting to see how the current MPDGE model compares to the other field based models. Apparently it was developed around the Darter (1990) and Tayabiji and Juang (1998) models as it presents a similar shaped line with added caution. After applying the Cervo and Balbo (2012) lab/field shift factor, the laboratory models become closer to the field models. However, there is still a huge gap between all the models analyzed which proves the difficulty in coming up with a general model for concrete pavements. Each of models researched present particularities like material, vehicle and environmental loading, fatigue criteria, slab geometry and so forth.

Regarding the short CRCP particularities, it was decided that the Cervo (2004) model would best represent the short CRCP fatigue life due to it being a Brazilian model based on conventional Brazilian concrete. Also, as the short CRCP presented a stress configuration unlike the traditional CRCP design suggests, i.e. not related to crack spacing, the MPDGE method was considered not applicable to the short CRCP.



(a)



(b)

Figure 6. 9 – (a) Analyzed fatigue models and (b) fatigue models with field/lab shift factor applied to laboratory only models

## 6.5 Short CRCP design chart

The proposed design model was developed relating a combination of thermal gradients, vehicle loads, slab thicknesses and concrete modulus of rupture as seen in Table 6.4. ISLAB simulations, discussed in a previous section, were performed in order to correlate such variables. As the original idea was to provide a chart format design, the effect of the thermal gradients combined with different vehicle loads had to be normalized to an equivalent load. For that, the stress originated by a particular combination of axle load and thermal differential was matched by a greater axle load with zero-thermal gradient through successive simulation trials. For example, in a 250 mm slab, an 80 kN axle load combined with a 10°C thermal differential creates a principal stress of 2.572 MPa. This exact stress level can be also reached applying a 149.46 kN axle load with zero-thermal differential. Thus, the equivalent zero-thermal gradient load would be representative in stress terms of the vehicle and environmental loads combined. Figure 6.10 presents the equivalent load variation for the 80 kN vehicle load. The graph is consistent with the linear behavior showed by the thermal differential analysis discussed previously. As the thermal gradient increases the difference between the equivalent loads for each thickness also grows, as expected. The relation between equivalent load and principal stresses is shown in Figure 6.11. The stress variation between thicker slabs (greater than 300 mm) is less accentuated than for thinner slabs. Therefore, caution must be placed when designing slabs with thickness smaller than 250 mm.

Figure 6.12 presents the Cervo (2004) fatigue model for a range of concrete modulus of rupture. Intuitively, for greater stresses, i.e., greater SSRs, there is a greater variance in number of load repetitions than for smaller stresses due to the difference in concrete tensile strength which for small SSRs is not as influential. This graph is the final step of the proposed design method where the stresses originated by the equivalent load are assigned a concrete modulus of rupture, which provides a SSR, indicating an allowable number of load repetitions (N) for the vehicle load combined with the thermal gradient defined in Figure 6.10.

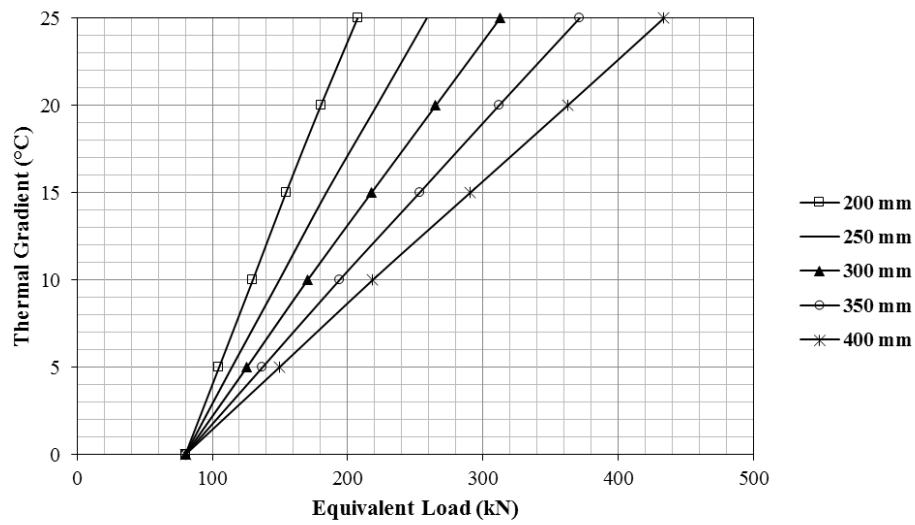


Figure 6. 10 – Equivalent zero-thermal gradient load for 80 kN vehicle load in different slab thicknesses

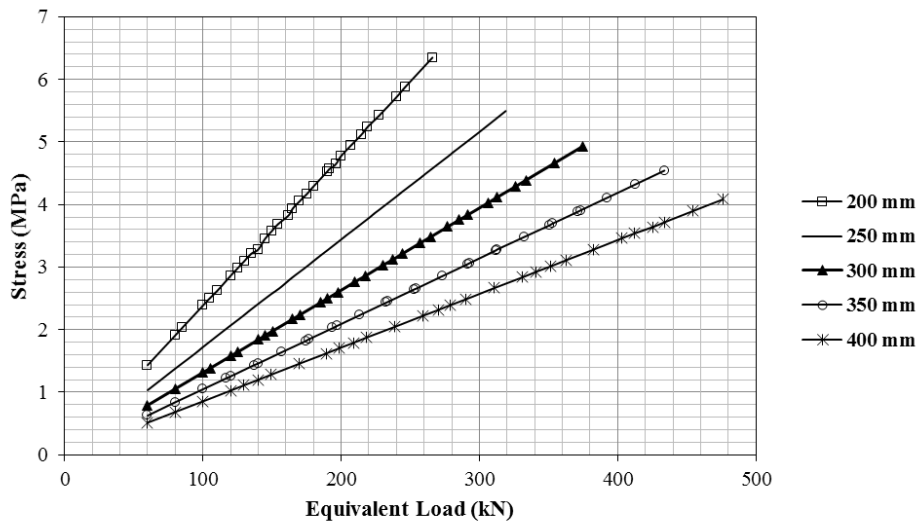


Figure 6. 11 – Equivalent zero-thermal gradient load versus principal stresses for different slab thicknesses

The design chart for the 80 kN load is shown in Figure 6.13. The design chart for the remaining axle loads simulated in this thesis are presented in the Appendix B.

For a new short CRCP project, in the first graph, the designer should select a thermal gradient and a slab thickness which would result in an equivalent load that when rebounded to the second graph would give a principal stress outcome. This principal stress combined with one

of the concrete modulus of rupture fatigue models in the third and final graph would finally indicate a number of allowable load repetitions. The chart can also be used in a reverse order.

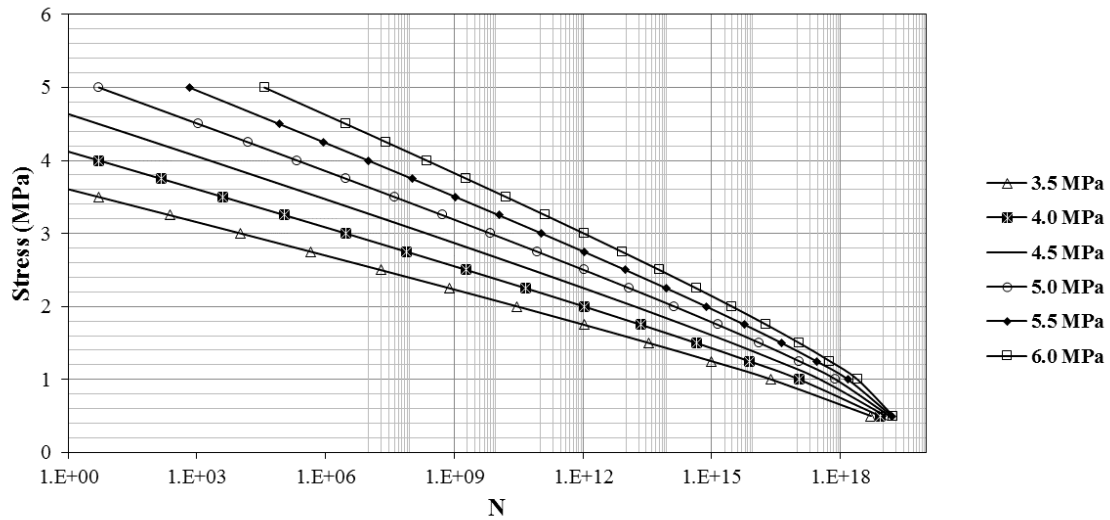


Figure 6.12 – Selected fatigue model for a range of concrete modulus of rupture

Attempts were made to create a single design chart that would englobe all simulated axle loads. However, due to the combination of different thickness with variations in axle load and thermal gradients as seen in Figures 6.5 to 6.7 discussed in a previous section of this chapter, a single graph with no error was not feasible. In order to mitigate this problem, the equivalent loads for all slab thicknesses were compared regarding the equivalent load for the 250 mm slab (Figure 6.14a). Results show meandering lines with larger variations for the 350 and 400 mm slabs due to their greater thickness difference for the “standard” slab (250 mm) and can be explained by the diverse response of a different slab thickness under the same combination of vehicle load and thermal gradient. Although, the linear tendency line coefficient of determination ( $R^2$ ) presents high values, small variations in the equivalent load can produce substantial variations in stresses that will yield way more significant variations in allowable number of load repetitions following the design charts which can provide besides dubious results, dangerously under designed slabs. Concerning the reliability of the proposed design chart, it was decided that only the critical points of the meandering lines – the ones that result in higher equivalent loads – would be considered. Figure 6.14b shows the adapted lines.

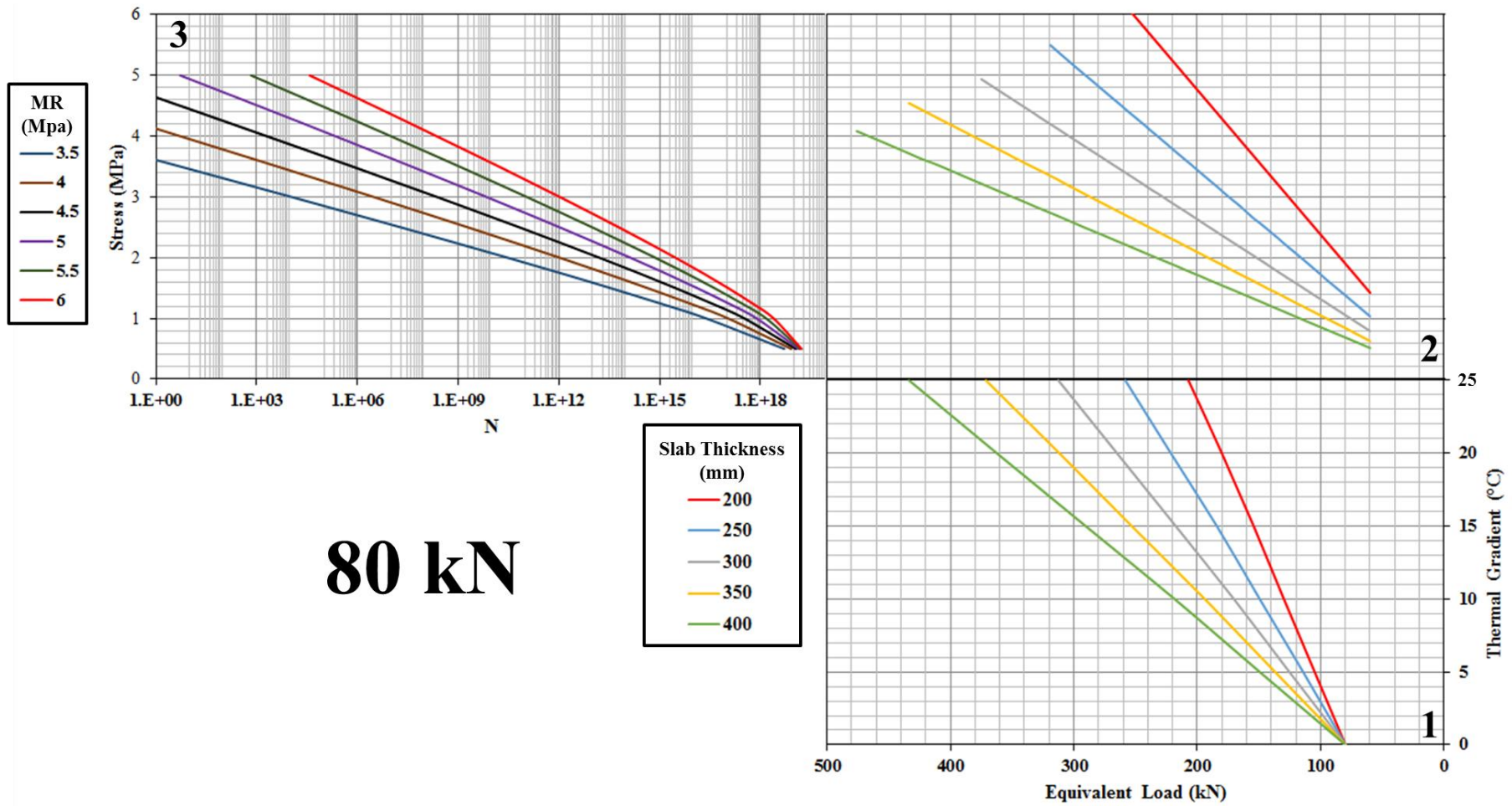
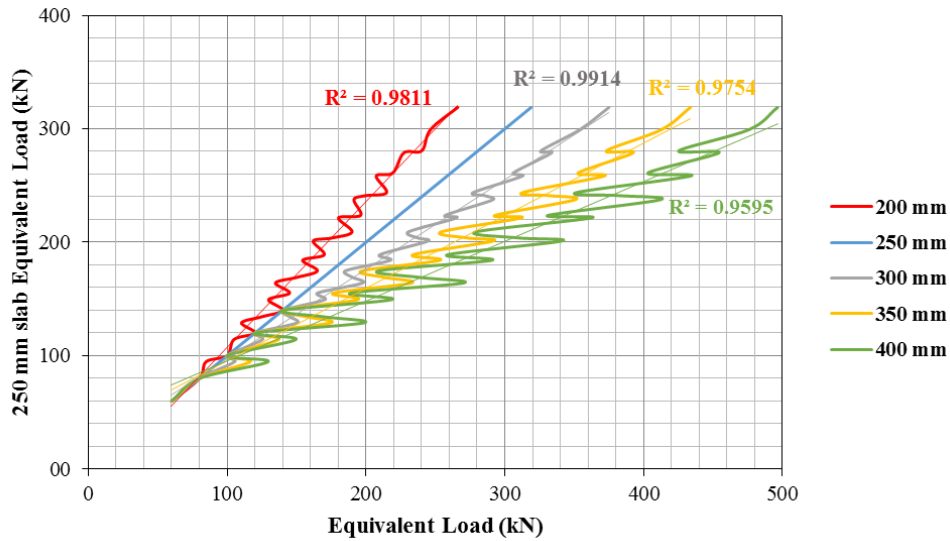
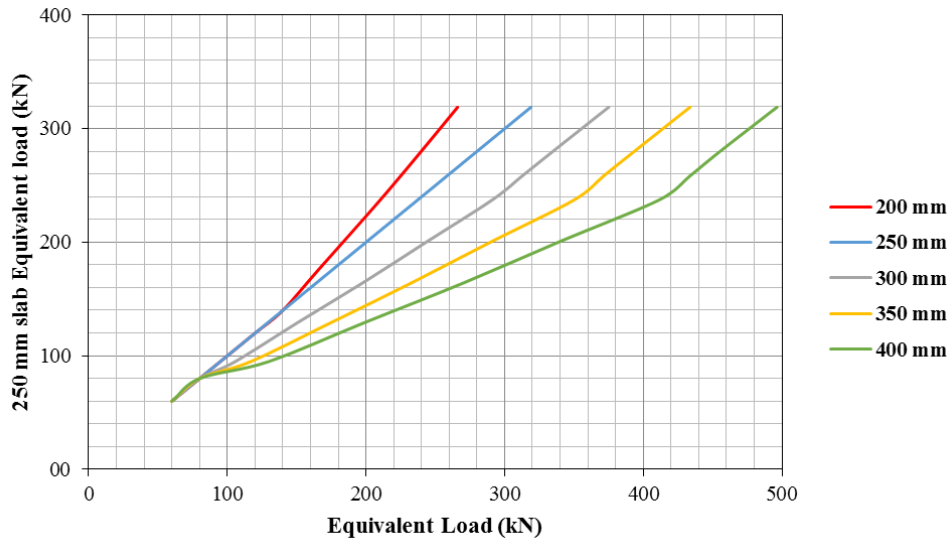


Figure 6. 13 – Short CRCP design chart for a 80 kN axle load



(a)



(b)

Figure 6. 14 – Equivalent 250 mm slab load *versus* (a) equivalent load for all thickness and (b) adapted critical value only lines

The complete design chart is presented in Figure 6.15. The designer firstly enters with the axle load relating it to a thermal gradient in the first graph following to the second graph where the desired thickness must be chosen so that the 250 mm slab equivalent load is related to the other slabs equivalent load. When rebounded to the third graph the design follows the same procedure previously explained for the axle loads design charts. Figure 6.16 shows an example which follows these inputs: a 100 kN axle load combined with a 10°C thermal gradient is applied in a 300 mm slab with the concrete modulus of rupture set at 4.5 MPa. The resulting number of allowable load repetitions (N) is  $9 \times 10^9$ .

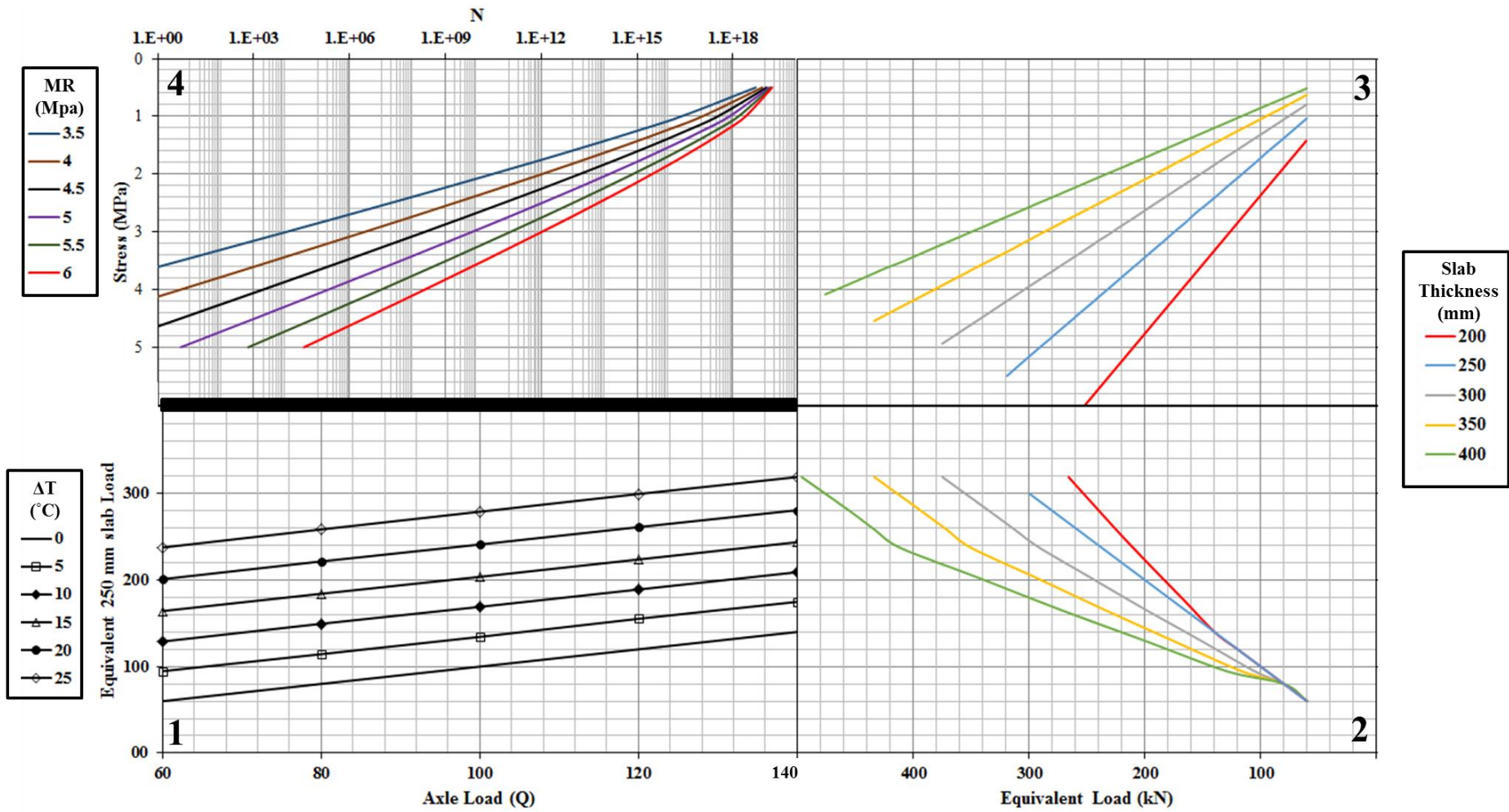


Figure 6. 15 – Complete design chart for the short CRCP



For a more precise approach of the N number, the Cervo (2004) fatigue model can be applied through Equation 68 using the chart resulting stress.

### 6.5.1 Fatigue life consumption

To conclude the proposed short CRCP model, the Palmgren-Miner linear damage hypothesis can be applied (MINER, 1945). This hypothesis is especially interesting for pavement fatigue analysis because it considers the cumulative effect of different stress levels on the overall material fatigue life. Considering that pavements are subjected to several combinations of axle and thermal loads, the Palmgren-Miner hypothesis is a practical tool to compute the fatigue effect of diverse load combinations through Equation 71.

$$\sum_{i=1}^k \frac{n_i}{N_i} = 1 \quad (71)$$

Where,

k = number of load cases;

i = stress;

$n_i$  = number of load repetitions for i stress;

$N_i$  = Number of allowable load repetitions for i stress.

For example, considering a hypothetical bus corridor, the São Paulo city hall standard instruction for heavy traffic bus corridors pavement design (PMSP, 2004a) indicates an expected traffic of  $5 \times 10^7$  standard 80 kN axle load repetitions for a 12-year project. Admitting a maximum thermal gradient of  $10^\circ\text{C}$  and a 4.5 MPa concrete modulus of rupture, Table 6.7 presents the design results (short CRCP design chart) when applying the Palmgren-Miner hypothesis for slab thickness of 200, 250 and 400 mm. A 200 mm slab would have endured slightly more than half of its fatigue life, while for thicker slabs this combination of axle load and thermal gradient would not significantly impact the slab fatigue life for this project. However, the short CRCP is proposed as a long-term durable solution which means higher than usual project lives. An 18 year increase in the design life, respecting the same traffic projection ( $N = 1.25 \times 10^8$ ), would result in the 200 mm slab not being suitable for this project anymore because the Palmgren-Miner damage would be higher than 1, i.e., more than 100% of the slab fatigue life would be consumed. As the 250 mm slab continues to not present significant damage, the short CRCP design method indicates that a slab with thickness

in between 200 and 250 mm would be the best option for a 30-year project with this loading configuration. A 215 mm slab would result in 54% fatigue life consumption.

Table 6. 7 – Design trials for a heavy traffic bus corridor applying the short CRCP design

Axle Load (kN)	$\Delta T$ (°C)	Thickness (mm)	Principal Stress (MPa)	N	Fatigue Damage (Palmgren-Miner) 12 year project	Fatigue Damage (Palmgren-Miner) 30 year project
80	10	250	2.57	2.93E+10	0.00	0.00
80	10	400	1.88	6.10E+13	0.00	0.00
80	10	200	3.10	7.55E+07	0.66	1.65

For another hypothetical bus corridor, considering the same amount of traffic (30-year project) but now with 60 kN front axle and 100 kN rear axle – most common weights for typical city buses according to Boile *et al.* (2003) – and a hotter climate where greater thermal gradients (15°C for this case) can be reached. Table 6.8 shows the results for all the simulated slab thicknesses. As can be seen, the front axle load is only significant for the 200 mm slab while the analysis of the rear load fatigue effect suggests only slabs thicker than 300 mm would be appropriate for the project. For a 350 mm slab the 100 kN load repetition would consume 11% of its fatigue life.

Therefore, the short CRCP design can be as complex as the designer desires, involving several axle load and thermal gradient configurations and even considering percentages of each axle load for a different thermal gradient as it is expected that buses traveling at night would experience milder thermal gradients than buses travelling during daytime. It only matters that the sum of the Palmgren-Miner hypothesis fatigue damage for all load configurations does not extrapolate the value 1 (100%). A proposed calculus sheet for the Palmgren-Miner fatigue damage can be found in Appendix C.

Table 6. 8 – Design trials for a heavy traffic bus corridor applying the short CRCP design chart with different axle loads

Axle Load (kN)	$\Delta T$ (°C)	Thickness (mm)	Principal Stress (MPa)	N	Fatigue Damage (Palmgren-Miner) 30 year project
60	15	200	3.21	2.03E+07	6.16
100	15	200	4.17	2.64E+02	474334.24
					$\Sigma = 474340.40$
60	15	250	2.82	1.78E+09	0.07
100	15	250	3.51	6.22E+05	200.85
					$\Sigma = 200.92$
60	15	300	2.59	2.40E+10	0.01
100	15	300	3.12	5.73E+07	2.18
					$\Sigma = 2.19$
60	15	350	2.43	1.44E+11	0.00
100	15	350	2.86	1.13E+09	0.11
					$\Sigma = 0.11$
60	15	400	2.31	5.44E+11	0.00
100	15	400	2.66	1.09E+10	0.01
					$\Sigma = 0.01$

#### 6.5.2 Analysis of the experimental short CRCP regarding the proposed design method

As seen at the end of Chapter 4 (Figure 4.21), the experimental short CRCP presented three distresses, namely: corner cracking at the Section 1's start, longitudinal cracking at Section 4's start and between cracks F3.7 and F3.11 in Section 3. For further analysis the distress will be referred as distress 1, 4 and 3, respectively. Distress 1 was firstly noticeable on October 2012, two years after construction while distresses 4 and 3 were evidenced on November 2016 and January 2017, respectively. Ultrasonic and coring data indicate that for distresses 1 and 4 there was thickness deficiency in those areas being both slabs on average slightly under 200 mm thick. For distress 3 there was no ultrasonic data in that region, although measurement points located near the area indicate a change in thickness from 163 to 267 mm. Therefore for analytical simplicity the thickness for all the distress areas was considered to be 200 mm.

In order to investigate the fatigue life consumption at the time of each one of the distresses were first visible at the slab surface, the traffic was analyzed. Traffic data obtained through personal communication from the USP campus chief Engineer shows an average daily traffic (ADT) distribution of 378 buses and 145 medium sized trucks on the avenue where the

experimental short CRCP is located. No weight characterization for the mentioned vehicles was provided. Thus, the buses were considered with 60 kN front axles and 100 kN rear axles while the trucks differ only in the rear axle (80kN). Therefore the number of axle load repetitions for each period is given in Table 6.9. If a 10°C thermal gradient is admitted for all the axle loadings, the fatigue consumption results can be observed in Table 6.10.

Table 6. 9 – Number of axle repetitions for the time when each distress became visible at the slab surface

Axle Load (kN)	ADT	Distresses		
		1	4	3
		Time Period (years)		
		2.08	6.17	6.33
60	523	3.98E+05	1.18E+06	1.21E+06
80	145	1.10E+05	3.26E+05	3.35E+05
100	378	2.87E+05	8.51E+05	8.74E+05

Table 6. 10 – Fatigue consumption analysis for the experimental short CRCP

Axle Load (kN)	$\Delta T$ (°C)	Thickness (mm)	Principal Stress (MPa)	N	Distresses		
					1	4	3
					Fatigue Damage	Fatigue Damage	Fatigue Damage
60	10	200	2.62	1.71E+10	0.00	0.00	0.00
80	10	200	3.09	8.09E+07	0.00	0.00	0.00
100	10	200	3.57	3.09E+05	0.93	2.75	2.83

Results point out that there is no damaging effect of the 60 kN and 80 kN axle loads, however for the 100 kN after just two years and one month from construction, the fatigue consumption would be at 93%. Extrapolating the period analysis to over six years results in almost 300% of fatigue life consumptions. Yet, it must be noted that the axle load and thermal gradient combination for this forensic study was quite simplistic. The São Paulo City Hall standard for concrete pavement design, based on the study from Balbo and Severi (2002), indicates periods of time when the thermal gradient would be maximum or zero according to the seasons (Table 6.11). Table 6.12 presents the traffic distribution on the USP campus according to the chief

engineer with the corresponded thermal gradient as suggested by Table 6.11. Thermal gradients outside of the peak time were considered as half of the maximum thermal gradient for computing time saving – in the original design software these periods are considered with linear growth between zero and maximum thermal gradient.

Table 6. 11 – Thermal gradient seasonal daily variation (Adapted from: PMSP, 2004b)

Season	Start Time for positive $\Delta T$	End Time for positive $\Delta T$	Time for Maximum $\Delta T$	$\Delta T$ (°C) Maximum
Spring	8h	18h	13-15h	12.5
Summer	8h	19h	13-15h	11.5
Fall	9h	18h	13-15h	8
Winter	9h	17h	13-15h	10

Table 6. 12 – Traffic distribution and respective thermal gradient for the experimental short CRCP

Time	ADT (%)	$\Delta T$ (°C)			
		Spring	Summer	Fall	Winter
5-8h	20	0	0	0	0
8-9h	7	6.25	5.75	0	0
9-13h	14	6.25	5.75	4	5
13-15h	4	12.5	11.5	8	10
15-17h	13	6.25	5.75	4	5
17-18h	8	6.25	5.75	4	0
18-19h	8	0	5.75	0	0
19h-24h	26	0	0	0	0

The fatigue life consumption analysis for each season can be found in Tables 6.13 to 6.16. As can be seen the single axle load/thermal gradient combination responsible for the pavement failure was the 100 kN load during the time period of maximum thermal gradient (13 to 15 hours) particularly during spring when most of the distresses were firstly visible at the slab surface. The sum for all seasons results in 43% fatigue life consumption for distress 1 and 126 and 130% for distress 4 and 3, respectively. These results are much more reasonable than the ones presented by Table 6.10 especially regarding distress 1. For a normal load this failure would only happen around the time that distress 4 and 3 occurred. Nonetheless, as discussed before, the traffic load effect on that area was intensified by a rutting distress in the

interlocked pavement close to the joint causing a vertical impact for heavy vehicles when accessing Section 1 which would create axle loads greater than 100 kN. The results clearly exemplify the need for accurate traffic, axle load and thermal gradient data for designing and evaluating pavement structures. Additionally, this fatigue analysis forecasts more fatigue failures in some areas of Section 2 and in mostly all Section 4 due to their thickness deficiencies as discussed in Chapter 3.

Table 6. 13 – Detailed fatigue consumption analysis for the experimental short CRCP during spring

						Distress			Distress		
						1	4	3			
						Time Period			1	4	3
Time	Axle Load (kN)	ADT	$\Delta T$ (°C)	Principal Stress (MPa)	N (design chart)	2.08	6.17	6.33	Fatigue Damage	Fatigue Damage	Fatigue Damage
5-8h	60	104.60	0	1.43	5.76E+15	1.99E+04	5.89E+04	6.05E+04	0.00	0.00	0.00
	80	29.00		1.91	4.20E+13	5.51E+03	1.63E+04	1.68E+04	0.00	0.00	0.00
	100	75.60		2.39	2.34E+11	1.44E+04	4.25E+04	4.37E+04	0.00	0.00	0.00
8-9h	60	36.61	6.25	2.18	2.39E+12	6.96E+03	2.06E+04	2.12E+04	0.00	0.00	0.00
	80	10.15		2.65	1.20E+10	1.93E+03	5.71E+03	5.87E+03	0.00	0.00	0.00
	100	26.46		3.13	5.18E+07	5.03E+03	1.49E+04	1.53E+04	0.00	0.00	0.00
9-13h	60	73.22	6.25	2.18	2.39E+12	1.39E+04	4.12E+04	4.23E+04	0.00	0.00	0.00
	80	20.30		2.65	1.20E+10	3.86E+03	1.14E+04	1.17E+04	0.00	0.00	0.00
	100	52.92		3.13	5.18E+07	1.01E+04	2.98E+04	3.06E+04	0.00	0.00	0.00
13-15h	60	20.92	12.5	2.92	5.92E+08	3.98E+03	1.18E+04	1.21E+04	0.00	0.00	0.00
	80	5.80		3.39	2.45E+06	1.10E+03	3.26E+03	3.35E+03	0.00	0.00	0.00
	100	15.12		3.87	8.66E+03	2.87E+03	8.51E+03	8.74E+03	0.33	0.98	1.01
15-17h	60	67.99	6.25	2.18	2.39E+12	1.29E+04	3.83E+04	3.93E+04	0.00	0.00	0.00
	80	18.85		2.65	1.20E+10	3.58E+03	1.06E+04	1.09E+04	0.00	0.00	0.00
	100	49.14		3.13	5.18E+07	9.34E+03	2.77E+04	2.84E+04	0.00	0.00	0.00
17-18h	60	41.84	6.25	2.18	2.39E+12	7.95E+03	2.35E+04	2.42E+04	0.00	0.00	0.00
	80	11.60		2.65	1.20E+10	2.21E+03	6.53E+03	6.70E+03	0.00	0.00	0.00
	100	30.24		3.13	5.18E+07	5.75E+03	1.70E+04	1.75E+04	0.00	0.00	0.00
18-19h	60	41.84	0	1.43	5.76E+15	7.95E+03	2.35E+04	2.42E+04	0.00	0.00	0.00
	80	11.60		1.91	4.20E+13	2.21E+03	6.53E+03	6.70E+03	0.00	0.00	0.00
	100	30.24		2.39	2.34E+11	5.75E+03	1.70E+04	1.75E+04	0.00	0.00	0.00
19-24h	60	135.98	0	1.43	5.76E+15	2.59E+04	7.65E+04	7.86E+04	0.00	0.00	0.00
	80	37.70		1.91	4.20E+13	7.17E+03	2.12E+04	2.18E+04	0.00	0.00	0.00
	100	98.28		2.39	2.34E+11	1.87E+04	5.53E+04	5.68E+04	0.00	0.00	0.00
$\Sigma$									0.33	0.99	1.01

Table 6. 14 – Detailed fatigue consumption analysis for the experimental short CRCP during summer

Time	Axle Load (kN)	ADT	$\Delta T$ (°C)	Principal Stress (MPa)	N (design chart)	Distress			Distress		
						1	4	3	Time Period		
						2.08	6.17	6.33	1	4	3
Fatigue Damage	Fatigue Damage	Fatigue Damage									
5-8h	60	104.6	0	1.43	5.76E+15	1.99E+04	5.89E+04	6.05E+04	0.00	0.00	0.00
	80	29		1.91	4.20E+13	5.51E+03	1.63E+04	1.68E+04	0.00	0.00	0.00
	100	75.6		2.39	2.34E+11	1.44E+04	4.25E+04	4.37E+04	0.00	0.00	0.00
8-9h	60	36.61	5.75	2.12	4.57E+12	6.96E+03	2.06E+04	2.12E+04	0.00	0.00	0.00
	80	10.15		2.59	2.35E+10	1.93E+03	5.71E+03	5.87E+03	0.00	0.00	0.00
	100	26.46		3.07	1.03E+08	5.03E+03	1.49E+04	1.53E+04	0.00	0.00	0.00
9-13h	60	73.22	5.75	2.12	4.57E+12	1.39E+04	4.12E+04	4.23E+04	0.00	0.00	0.00
	80	20.3		2.59	2.35E+10	3.86E+03	1.14E+04	1.17E+04	0.00	0.00	0.00
	100	52.92		3.07	1.03E+08	1.01E+04	2.98E+04	3.06E+04	0.00	0.00	0.00
13-15h	60	20.92	11.5	2.80	2.29E+09	3.98E+03	1.18E+04	1.21E+04	0.00	0.00	0.00
	80	5.8		3.27	9.69E+06	1.10E+03	3.26E+03	3.35E+03	0.00	0.00	0.00
	100	15.12		3.76	3.50E+04	2.87E+03	8.51E+03	8.74E+03	0.08	0.24	0.25
15-17h	60	67.99	5.75	2.12	4.57E+12	1.29E+04	3.83E+04	3.93E+04	0.00	0.00	0.00
	80	18.85		2.59	2.35E+10	3.58E+03	1.06E+04	1.09E+04	0.00	0.00	0.00
	100	49.14		3.07	1.03E+08	9.34E+03	2.77E+04	2.84E+04	0.00	0.00	0.00
17-18h	60	41.84	5.75	2.12	4.57E+12	7.95E+03	2.35E+04	2.42E+04	0.00	0.00	0.00
	80	11.6		2.59	2.35E+10	2.21E+03	6.53E+03	6.70E+03	0.00	0.00	0.00
	100	30.24		3.07	1.03E+08	5.75E+03	1.70E+04	1.75E+04	0.00	0.00	0.00
18-19h	60	41.84	5.75	2.12	4.57E+12	7.95E+03	2.35E+04	2.42E+04	0.00	0.00	0.00
	80	11.6		2.59	2.35E+10	2.21E+03	6.53E+03	6.70E+03	0.00	0.00	0.00
	100	30.24		3.07	1.03E+08	5.75E+03	1.70E+04	1.75E+04	0.00	0.00	0.00
19-24h	60	135.98	0	1.43	5.76E+15	2.59E+04	7.65E+04	7.86E+04	0.00	0.00	0.00
	80	37.7		1.91	4.20E+13	7.17E+03	2.12E+04	2.18E+04	0.00	0.00	0.00
	100	98.28		2.39	2.34E+11	1.87E+04	5.53E+04	5.68E+04	0.00	0.00	0.00
$\Sigma$									0.08	0.24	0.25

Table 6. 15 – Detailed fatigue consumption analysis for the experimental short CRCP during fall

						Distress			Distress		
						1	4	3			
						Time Period			1	4	3
Time	Axle Load (kN)	ADT	$\Delta T$ (°C)	Principal Stress (MPa)	N (design chart)	2.08	6.17	6.33	Fatigue Damage	Fatigue Damage	Fatigue Damage
5-8h	60	104.6	0	1.43	5.76E+15	1.99E+04	5.89E+04	6.05E+04	0.00	0.00	0.00
	80	29		1.91	4.20E+13	5.51E+03	1.63E+04	1.68E+04	0.00	0.00	0.00
	100	75.6		2.39	2.34E+11	1.44E+04	4.25E+04	4.37E+04	0.00	0.00	0.00
8-9h	60	36.61	0	1.43	5.76E+15	6.96E+03	2.06E+04	2.12E+04	0.00	0.00	0.00
	80	10.15		1.91	4.20E+13	1.93E+03	5.71E+03	5.87E+03	0.00	0.00	0.00
	100	26.46		2.39	2.34E+11	5.03E+03	1.49E+04	1.53E+04	0.00	0.00	0.00
9-13h	60	73.22	4	1.91	4.27E+13	1.39E+04	4.12E+04	4.23E+04	0.00	0.00	0.00
	80	20.3		2.38	2.39E+11	3.86E+03	1.14E+04	1.17E+04	0.00	0.00	0.00
	100	52.92		2.86	1.12E+09	1.01E+04	2.98E+04	3.06E+04	0.00	0.00	0.00
13-15h	60	20.92	8	2.38	2.43E+11	3.98E+03	1.18E+04	1.21E+04	0.00	0.00	0.00
	80	5.8		2.86	1.14E+09	1.10E+03	3.26E+03	3.35E+03	0.00	0.00	0.00
	100	15.12		3.34	4.59E+06	2.87E+03	8.51E+03	8.74E+03	0.00	0.00	0.00
15-17h	60	67.99	4	1.91	4.27E+13	1.29E+04	3.83E+04	3.93E+04	0.00	0.00	0.00
	80	18.85		2.38	2.39E+11	3.58E+03	1.06E+04	1.09E+04	0.00	0.00	0.00
	100	49.14		2.86	1.12E+09	9.34E+03	2.77E+04	2.84E+04	0.00	0.00	0.00
17-18h	60	41.84	4	1.91	4.27E+13	7.95E+03	2.35E+04	2.42E+04	0.00	0.00	0.00
	80	11.6		2.38	2.39E+11	2.21E+03	6.53E+03	6.70E+03	0.00	0.00	0.00
	100	30.24		2.86	1.12E+09	5.75E+03	1.70E+04	1.75E+04	0.00	0.00	0.00
18-19h	60	41.84	0	1.43	5.76E+15	7.95E+03	2.35E+04	2.42E+04	0.00	0.00	0.00
	80	11.6		1.91	4.20E+13	2.21E+03	6.53E+03	6.70E+03	0.00	0.00	0.00
	100	30.24		2.39	2.34E+11	5.75E+03	1.70E+04	1.75E+04	0.00	0.00	0.00
19-24h	60	135.98	0	1.43	5.76E+15	2.59E+04	7.65E+04	7.86E+04	0.00	0.00	0.00
	80	37.7		1.91	4.20E+13	7.17E+03	2.12E+04	2.18E+04	0.00	0.00	0.00
	100	98.28		2.39	2.34E+11	1.87E+04	5.53E+04	5.68E+04	0.00	0.00	0.00
$\Sigma$									0.00	0.00	0.00

Table 6. 16 – Detailed fatigue consumption analysis for the experimental short CRCP during winter

						Distress					
						1	4	3	Distress		
						Time Period			1	4	3
Time	Axle Load (kN)	ADT	$\Delta T$ (°C)	Principal Stress (MPa)	N (design chart)	2.08	6.17	6.33	Fatigue Damage	Fatigue Damage	Fatigue Damage
5-8h	60	104.6	0	1.43	5.76E+15	1.99E+04	5.89E+04	6.05E+04	0.00	0.00	0.00
	80	29		1.91	4.20E+13	5.51E+03	1.63E+04	1.68E+04	0.00	0.00	0.00
	100	75.6		2.39	2.34E+11	1.44E+04	4.25E+04	4.37E+04	0.00	0.00	0.00
8-9h	60	36.61	0	1.43	5.76E+15	6.96E+03	2.06E+04	2.12E+04	0.00	0.00	0.00
	80	10.15		1.91	4.20E+13	1.93E+03	5.71E+03	5.87E+03	0.00	0.00	0.00
	100	26.46		2.39	2.34E+11	5.03E+03	1.49E+04	1.53E+04	0.00	0.00	0.00
9-13h	60	73.22	5	2.03	1.20E+13	1.39E+04	4.12E+04	4.23E+04	0.00	0.00	0.00
	80	20.3		2.50	6.36E+10	3.86E+03	1.14E+04	1.17E+04	0.00	0.00	0.00
	100	52.92		2.98	2.89E+08	1.01E+04	2.98E+04	3.06E+04	0.00	0.00	0.00
13-15h	60	20.92	10	2.62	1.71E+10	3.98E+03	1.18E+04	1.21E+04	0.00	0.00	0.00
	80	5.8		3.10	7.55E+07	1.10E+03	3.26E+03	3.35E+03	0.00	0.00	0.00
	100	15.12		3.58	2.81E+05	2.87E+03	8.51E+03	8.74E+03	0.01	0.03	0.03
15-17h	60	67.99	5	2.03	1.20E+13	1.29E+04	3.83E+04	3.93E+04	0.00	0.00	0.00
	80	18.85		2.50	6.36E+10	3.58E+03	1.06E+04	1.09E+04	0.00	0.00	0.00
	100	49.14		2.98	2.89E+08	9.34E+03	2.77E+04	2.84E+04	0.00	0.00	0.00
17-18h	60	41.84	0	1.43	5.76E+15	7.95E+03	2.35E+04	2.42E+04	0.00	0.00	0.00
	80	11.6		1.91	4.20E+13	2.21E+03	6.53E+03	6.70E+03	0.00	0.00	0.00
	100	30.24		2.39	2.34E+11	5.75E+03	1.70E+04	1.75E+04	0.00	0.00	0.00
18-19h	60	41.84	0	1.43	5.76E+15	7.95E+03	2.35E+04	2.42E+04	0.00	0.00	0.00
	80	11.6		1.91	4.20E+13	2.21E+03	6.53E+03	6.70E+03	0.00	0.00	0.00
	100	30.24		2.39	2.34E+11	5.75E+03	1.70E+04	1.75E+04	0.00	0.00	0.00
19-24h	60	135.98	0	1.43	5.76E+15	2.59E+04	7.65E+04	7.86E+04	0.00	0.00	0.00
	80	37.7		1.91	4.20E+13	7.17E+03	2.12E+04	2.18E+04	0.00	0.00	0.00
	100	98.28		2.39	2.34E+11	1.87E+04	5.53E+04	5.68E+04	0.00	0.00	0.00
						$\Sigma$			0.01	0.03	0.03

## 6.6 Short CRCP design guidelines and final recommendations

Based on the information presented and discussed throughout the sixth chapter, the design guidelines and recommendations for short CRCP project are presented, as follows:

- 1) Short CRCP bus stops and terminals projects should be focused on long-term service life (over 20 years) and for locations subjected to heavy vehicle traffic;
- 2) Based on the first guideline and experience with the experimental short CRCP, slabs should be designed with minimum thickness, regarding of course vehicle and environmental loading, of 250 mm;
- 3) The short CRCP design chart (Figure 6.15) should be applied for conceptual design trials considering variations on slab thickness, vehicle loading, thermal gradient and concrete modulus of rupture. After defining such variables, the designer can use the information presented by the tables in Appendix A for a more precise determination of principal stresses and then apply Cervo (2004) fatigue model with the laboratory-field shift factor (Equations 68 and 70);
- 4) The allowable number of load repetitions provided by the design procedure should be related to the expected number of load repetitions (project N) regarding the Palmgreen-Miner fatigue life consumption hypothesis using the form table available in Appendix C;
- 5) Complete and accurate axle load and thermal gradient data must be applied when designing the short CRCP. If possible hourly variation of such parameters should be addressed. The São Paulo city hall standard for concrete pavement design (PMSP, 2004b) can provide thermal gradient hourly variation for the São Paulo climate. For other regions, the models developed by Balbo and Severi (2002) may be applied.
- 6) Hot-mix asphalt bases of minimum 60 mm thickness are mandatory for the design and construction of the short CRCP in order to maintain a high modulus of subgrade reaction and to provide a non-erodible foundation for the concrete slab;
- 7) The longitudinal steel percentage must be in between 0.7 and 0.8% to assure adequate crack width;
- 8) Steel depth must be at minimum 76 mm and maximum 100 mm from the slab surface to, respectively, protect the steel from corrosion agents and ensure tight cracks;
- 9) The concrete mix design must apply aggregates with low CTE potential;

10) Strict curing processes must be applied after construction to avoid great shrinkage. Curing compound, based on Rosler *et al.* (2016), is recommended at an application rate of 2.5 to 5 m<sup>2</sup>/liter during seven days.

11) Transition joints must be placed at the transverse edges of the 50 m short CRCP to avoid the joint-related distresses and early-failures observed in the experimental short CRCP. Rosler *et al.* (2016) at the recently published FHWA CRCP manual recommend four options for CRCP transition to JPCP, namely sleeper slab and wide flange (1), modified wide flange (2), doweled joint (3) and steel transitions (4). Option three was chosen for the short CRCP design recommendations due to its recognized construction simplicity although options one and two can also be applied. Option four is not suitable for the short CRCP because of the shorter slab length. Option three requires the application of typical JPCP dowel bars to connect the short CRCP slab to the subsequent JPCP slab, as seen in Figure 6.17. The joint must be sealed at all times which may require maintenance of the seal material.

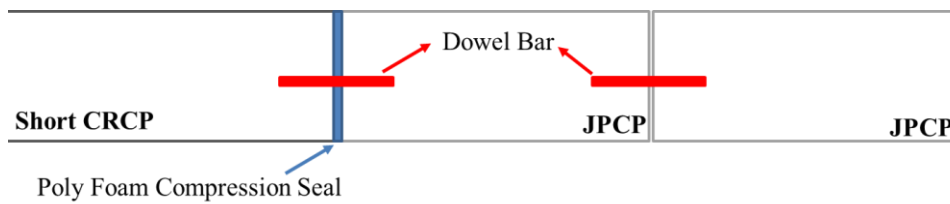


Figure 6. 17 – Proposed transition joint from short CRCP to JPCP (Adapted from Roesler *et al.*, 2016)

For asphalt pavement transitions, Roesler *et al.* (2016) proposes a classic solution for JPCP transition to asphalt pavements: an I steel beam connecting the CRCP to a sleeper slab which is connected to the asphalt pavement with a gradual thickness reduction as illustrated in Figure 6.18.

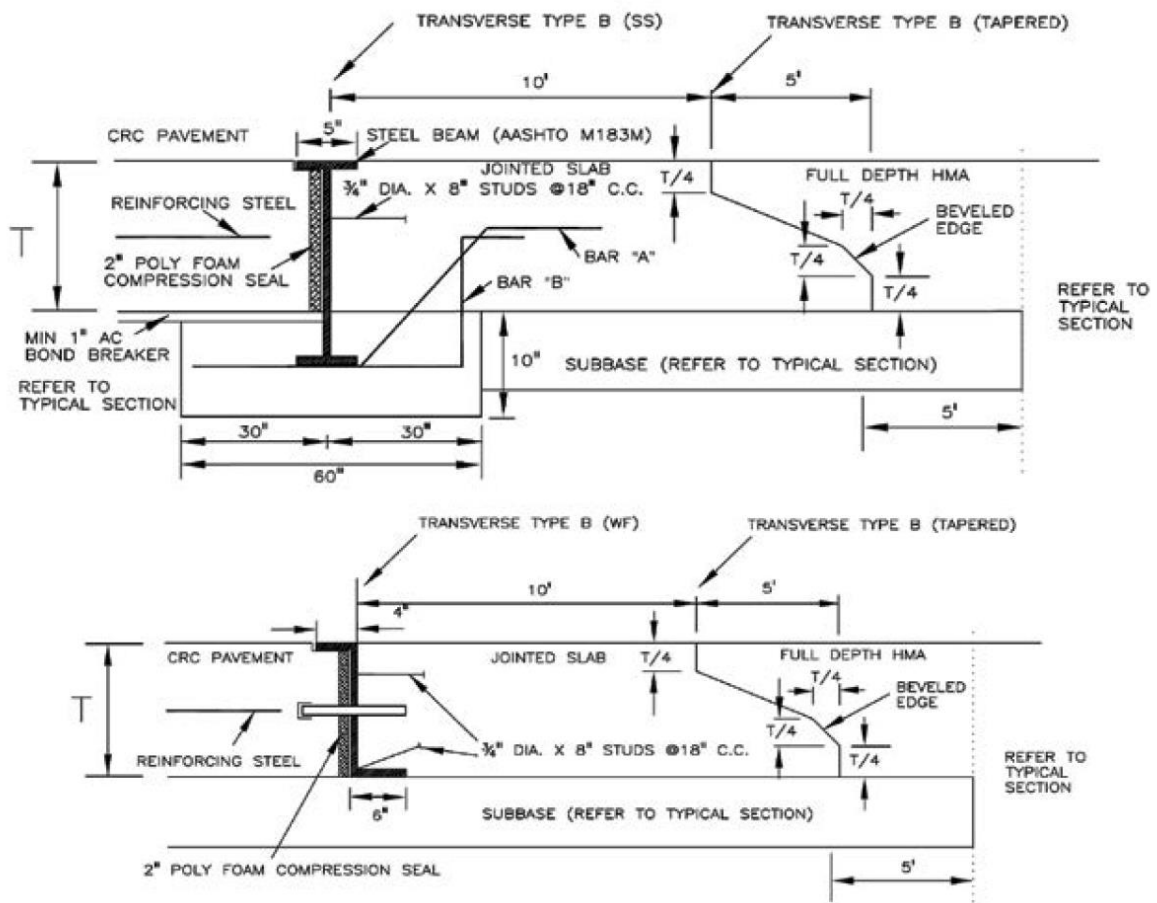


Figure 6. 18 – Proposed transition joint from short CRCP to asphalt pavement (ROESLER *et al.*, 2016)

## 7. CONCLUSIONS

Through the analysis conducted on the results obtained from the ultrasonic testing, the deflection testing, the theoretical stress simulation and the design recommendations discussed in chapters three, four, five and six, respectively, of this thesis, it is possible to summarize the following findings:

### **Ultrasonic testing (MIRA)**

- Average thickness was smaller than the designed one for all sections. Only five points presented thickness above 240 mm while several points showed slabs thinner than 200 mm. Coring attested the thickness measurements for five locations;
- Sections constructed side by side present similar average thickness and thickness profile;
- Hilbert transform indicator (HTI) shows a sound concrete condition for all sections;
- The longitudinal reinforcement was design to be slightly above the slab half-height, however, MIRA data disclosed steel bars slightly below the slab-half height. This can help explain the short CRCP cracking behavior as the reinforcement has less effect on cracking development when placed deeper in the slab;
- In face of new thickness and reinforcement characteristics, sections 3 and 4 present almost the same steel percentage in concordance with the sections similar cracking pattern;
- The MIRA simulation software successfully reproduced thickness and reinforcement readings. Nevertheless, for cracks, the simulation was not conclusive. The software developing team is currently working on improvements regarding distresses;
- The analysis of individual signal HTI shows potential to disclose depth characteristics of transverse cracks regarding full or partial development. In general, cracks with average HTI higher than 92 present a full-depth profile while cracks from 66 to 92 show partial development;
- In a continuous MIRA survey cracks can be identified by HTI peaks. Eleven non-visible cracks, found with this methodology, emerged in the slab surface in later crack surveys;
- Individual signal HTI for non-visible cracks showed similar signal loss to visible cracks. Just one crack presented a bottom-up profile. This is a strong indicative that

cracks originate from the reinforcement location and develop up and/or down with time;

### **Crack Pattern**

- The updated crack map with the inclusion of non-visible cracks disclosed a smaller number of cracks for the section with less steel percentage, as expected. Also, differences of 0.1 in steel percentage do not seem to effect the total number of cracks but on their development to the surface;
- The non-visible crack evidence provides important information on potential “Y” and cluster cracking before the problem becomes visible at the slab surface;
- Additionally, with the inclusion of non-visible cracks, the crack spacing becomes similar to traditional CRCP complying with the AASTHO crack spacing recommendations;
- Changes in steel depth are more influential to surface crack width than alterations on steel percentage and steel percentage/slab thickness ratio;
- Wider cracks on the surface are an indicative of fully developed cracks as they always show high HTI values;
- Transverse cracks have an effect on the slab stiffness configuration;
- As noted before, the lack of anchorage at the slabs end originates areas of great deflections near the transversal joint. Moreover, the free slab movement on these areas amplifies the damaging effect of vehicles accessing the slab;
- The short CRCP slab presents structural integrity even in a physical discontinuity (crack). Deflections in between cracks (panels) and at the crack present similar numbers while a fictitious panel LTE shows equivalent values to crack LTE.
- Thickness deficiencies in addition to the slabs lack of anchorage facilitate failures (corner and longitudinal cracking) at the start of two sections.

### **ISLAB Simulations**

- The hypothesis of the short CRCP behaving like a continuous slab was proved while simulating field stresses trough ISLAB. Theoretical stresses were much more similar to field ones when using a 50 m continuous concrete slab than when simulating cracks as joints with high LTE;

- Loading near the crack increases bottom stresses because of crack opening due to tensile forces. The opposite effect can be observe on top stresses where compressive forces are acting;
- A shift factor between field and theoretical stresses ranged in between averages 0.69 to 1.03 for the short CRCP dynamic load testing;
- Simulation of braking and high speed dynamic loads show coherent results for the dynamic load testing;
- Thickness variation and especially thermal gradients show significant influence on the short CRCP stresses.

### **Design Recommendations**

- The center edge location is the critical spot for the short CRCP design and analysis;
- Increasing thickness in thinner slabs (around 200 mm) is more beneficial, regarding thermal gradient related stresses, than in thicker slabs (around 400 mm);
- Axle loading, thermal gradient and thickness variation relations in the short CRCP show similarities to the similar variations in JPCP;
- The stress intensification expected when increasing slab length from 3 to 5 m and from 5 to 7 m was not observed when analyzing larger slabs (50 m length);
- Positive thermal gradients create slab bottom principal stress in contradiction with classic CRCP design which is focused on top stress;
- The proposed short CRCP for bus stops and terminals better serves long-term projects with an over 20 year design life;
- Slabs thinner than 250 mm are not recommend for classic bus traffic in a tropical environment;
- The proposed design chart is highly sensible for high thermal gradients;
- Accurate traffic and correspondent thermal gradient data are key factor for designing and evaluating short CRCPs;
- The proposed design chart was positively able to identify the causes of the experimental short CRCP failures.

The findings summarized above display the contributions of this research regarding the possibility of applying this novel structure for specific and vital infrastructure projects in Brazil. The proposed design chart is simple and user friendly and the decision of fixing some pavement parameters, as the asphalt base, help ensure a higher probability of the structure success. Additionally, for the international technical community point of view, this research highlights two main aspects of pavement technology, namely: the possibility of evaluating concrete cracking before the crack appears at the concrete surface knowing which part of the slab depth is cracked; and the need for a reevaluation of classic CRCP design concerning positive thermal gradients in view of the slab continuous behavior. Both these contributions need extra research testing the ultrasonic procedure in controlled slabs and calibrating the design method with field experience in hotter climates while also performing load tests and stress simulations in traditional CRCPs to verify the continuous behavior.

## REFERENCES

AL-QADI, I. L.; ELSEIFI, M. A. Mechanism and modeling of transverse cracking development in continuously reinforced concrete pavement. **International Journal of Pavement Engineering**, v. 7, n. 4, p. 341 – 349, 2006.

AMERICAN ASSOCIATION OF STATE HIGHWAY AND TRANSPORTATIONS OFFICIALS (AASHTO). **Guide for design of pavement structures**. AASHTO, Washington D.C., EUA, 1993.

AMERICAN ASSOCIATION OF STATE HIGHWAY AND TRANSPORTATIONS OFFICIALS (AASHTO). **1972 AASHTO Interim Guide for Design of Pavement Structures**, Washington, D.C., 1980.

AMERICAN ASSOCIATION OF STATE HIGHWAY AND TRANSPORTATIONS OFFICIALS (AASHTO). **AASHTO Guide for the Design of Pavement Structures**. Washington D.C., 1986.

AMERICAN ASSOCIATION OF STATE HIGHWAY AND TRANSPORTATIONS OFFICIALS (AASHTO). **Mechanistic-Empirical Pavement Design Guide: A manual of Practice**. AASHTO, Washington, DC., 2008.

AN, J.; NAM, J.; KWON, S.; JOH, S. Estimation of the Compressive Strength of Concrete Using Shear Wave Velocity. **New Technologies in Construction and Rehabilitation of Portland Cement Concrete Pavement and Bridge Deck Pavement**, pp.154-164, 2009.

ARA. Guide for Mechanistic-Empirical Design of New and Rehabilitated Pavement Structures. **Report NCHRP 1-37A**, Applied Research Associates, Inc., Albuquerque, NM, 2003.

ASSOCIAÇÃO BRASILEIRA DE CIMENTO PORTLAND (ABCP). **Dimensionamento de Pavimentos Rodoviários e Urbanos de Concreto pelo Método da PCA/84** (In Portuguese). ET-97. São Paulo, 1986.

BALBO, J. T. Performance in Fatigue Cracking of High Strength Concrete as Ultra-thin Whitetopping. **Proceedings of the 82<sup>nd</sup> Annual Transportation Research Board Meeting**. Transportation Research Board, Washington, D.C., 2003.

BALBO, J. T.; MASSOLA, A.; PEREIRA, D. Structural aspects of the experimental CRCP in São Paulo. **Proceedings of the 10<sup>th</sup> International Conference on Concrete Pavements**, Quebec City, Canada, 2012.

BALBO, J. T.; SEVERI, A. A. Thermal gradients in concrete pavements in tropical environment. Experimental appraisal. **Transportation Research Record: Journal of the Transportation Research Board**, v. 1809, p. 12 – 22, 2002.

BAMLER, R. A Comparison of Range-Doppler and Wavenumber Domain SAR Focusing 544 Algorithms. **Geoscience and Remote Sensing**, IEEE Transactions, vol. 30, pp. 706- 545, 1992.

BEYER, M.; ROESLER, J. Mechanical-Empirical Design Concepts for Continuously Reinforced Concrete Pavements in Illinois. **Report No FHWA-ICT-09-040**. Illinois Center for Transportation, Illinois, 2009.

BISHKO, A. V.; SAMOKRUTOV A. A.; SHEVALDYKIN, V. G. Ultrasonic Echo-Pulse Tomography of Concrete Using Shear Waves Low-Frequency Phased Antenna Arrays. **Proceedings of the 17th World Conference on Nondestructive Testing**, Shanghai, China, 2008.

BOILE, M.; NARAYANAN, P.; OZBAY, K. Impact of Buses on Highway Infrastructure. Case Study for New Jersey State. **Transportation Research Record: Journal of the Transportation Research Board**, v. 1841, p. 32 – 40, 2003.

CARBONARI, B. T.; CAVALARO, S. H.; CASTANHA, J. C. M; GUACELLI, P. A. G; SILVA, C. C. Utilization of the Ultrasonic Method to Evaluate the Properties of High Performance Concrete. **Ibracon Structures and Materials Journal**, v. 3, n.4, p. 494-511, 2010.

CERVO T. C.; SEVERI, A. A.; RODOLFO, M. P.; PEREIRA, D. S.; BALBO, J. T. Innovative Aspects of the Concrete Pavement Design Standard for São Paulo Highways. **Proceedings of the 8th International Conference on Concrete Pavements**, Colorado Springs, 2005.

CERVO, T. C. **Estudo da Resistencia à Fadiga de Concretos de Cimento Portland para Pavimentação**. Tese (Doutorado), (In Portuguese), Escola Politécnica da Universidade de São Paulo, São Paulo, 2004.

CERVO, T. C.; BALBO, J. T. Calibration of a Shift-Factor for the Fatigue Prediction of High Strength Concrete Pavement in the Field. **International Journal of Pavement Research and Technology**, v. 5, p. 153-160, 2012.

CHO, R., JOH, H., KWON, KANG, H. Nondestructive In-Place Strength Profiling of Concrete Pavements by Resonance Search Technique. **Proceedings of 86th Annual Meeting of the Transportation Research Board**, Washington, D.C., 2007.

CHOI, S.; HA, S; WON, M. C. Horizontal cracking of continuously reinforced concrete pavement under environmental loadings. **Construction and Building Materials**, v. 15, p. 4250 – 4262, 2011.

CLARK, M.R.; MCCANN, D. M.; FORDE, M. C. Application of infrared thermography to the non-destructive testing of concrete and masonry bridges. **NDT & E International**, v. 36, p. 265 – 275, 2003.

CLAYTON, D.; KHAZANOVICH, L.; SALLES, L. Linear Array Ultrasonic Test Results from Alkali-Silica Reaction (ASR) Specimens. **Report No ORNL/TM-2016/159**. Oak Ridge National Laboratory. Electrical and Electronics Systems Research Division, US Department of Energy, Washington, D.C., 2016.

COLIM, G. M.; BALBO J. T.; KHAZANOVICH, L. Effects of temperature changes on load transfer in plain concrete pavement joints. **Ibracon Structures and Materials Journal**, Vol. 4, N° 3, 2011.

CROVETTI, J. A. **Design and evaluation of jointed concrete pavement systems incorporating open-graded permeable bases**. Ph. D. Dissertation, University of Illinois, 1994.

DANIELS, D. J. **Surface-penetrating radar**. ERA Technology, Institution of Electrical Engineers Radar Series no. 6, London, 1996.

DARTER, M. Concrete Slab vs Beam Fatigue Models. **Proceedings of the 2<sup>nd</sup> International Workshop on the Theoretical Design of Concrete Pavements**, CROW-PIARC-CEMBUREAU, p. 472-481, Siguenza, 1990.

DARTER, M. Design of Zero-Maintenance Plain Jointed Concrete Pavement v: 1 Development of Design Procedures. **Report FHWA-RD-77-111**. Federal Highway Administration, Washington D.C., (1977).

DARTER, M.; HALL, K. T; KUO, C. M. Support under Portland Cement Concrete Pavements. **NCHRP Report 372**. National Research Council, Washington D.C., 1995.

DAVIDS, W.; TURKIYYAH, G.; MAHONEY, J. EverFE Rigid Pavement Three-Dimensional Finite Element Analysis Tool. **Transportation Research Record: Journal of the Transportation Research Board**, v. 1629, p. 41 – 49, 1998.

DEPARTAMENTO NACIONAL DE INFRA-ESTRUTURA DE TRANSPORTES (DNIT). **Manual de Pavimentos Rígidos**. Ministério dos Transportes, Rio de Janeiro, 2004.

DIOGENES, H. J. F; COSSOLINO, L. C.; PEREIRA, A. H. A.; DEBS, M. K. E; DELBS, A. L. H. Determination of modulus of elasticity of concrete from the acoustic response. **Ibracon Structures and Materials Journal**, v. 4, n. 5, p. 792-813, 2011.

DOSSEY, T; HUDSON, W. R. Distress as function of age in continuously reinforced concrete pavements: models developed for Texas pavement management information system. **Transportation Research Record: Journal of the Transportation Research Board**, v. 1455, p. 159 – 165, 1994.

EDWARDS, L. Evaluation of Technologies for Nondestructively Determining Concrete Pavement Thickness. **Proceedings of the 10<sup>th</sup> International Conference on Concrete Pavement**, ISCP, Québec City, Canada, 2012.

EL PAIS. **São Paulo, onde o carro é mais lento que o lento transporte público**. (in Portuguese). 2014 Available at: <[http://brasil.elpais.com/brasil/2014/09/19/politica/1411078450\\_215272.html](http://brasil.elpais.com/brasil/2014/09/19/politica/1411078450_215272.html)>. Accessed on June 13<sup>th</sup>, 2016.

ELFINO, M.; NAIR, H.; CRAWFORD, G.; GUDIMETTLA, J. Comparison of Predicted Distress Between Different Input Levels Using MPDEG for CRC Pavement. **Proceedings of the T & DI Congress 2011**. ASCE, Chicago, 2011.

ERES. **Guide for Mechanistic-Empirical Design of New and Rehabilitated Pavement Structures**. Final Report, Inc., ERES Division, Champaign, Illinois, 2004.

ESTADÃO. **Haddad entrega primeiro corredor de ônibus, mas só cumprirá 1/3 da meta**. (in Portuguese). 2016 Available at: <<http://sao-paulo.estadao.com.br/noticias/geral,haddad-entrega-primeiro-corredor-de-onibus--mas-so-cumprira-13-da-meta,10000005705>> Accessed on October 10<sup>th</sup>, 2016.

FOLHA DE SÃO PAULO. **Novo Rodoanel já precisa de reformas.** (in Portuguese). 2010 Available at: <<http://www1.folha.uol.com.br/fsp/cotidian/ff1304201020.htm>>. Accessed on June 13<sup>th</sup>, 2016.

FREESEMAN, J.; HOEGH, K.; KHAZANOVICH, L. Concrete Strength Required to Open to Traffic. **Report No. MN/RC 2016-01**, Minnesota Department of Transportation. St. Paul, 2016.

FREESEMAN, K. **Nondestructive Evaluation Advancements for Damage Detection in Concrete.** PhD dissertation. University of Minnesota, Minneapolis, 2016.

FREESEMAN, K., HOEGH, K., KHAZANOVICH, L. Concrete Strength Required to Open to Traffic. **Report No. MN/RC 2016-01**, Minnesota Department of Transportation. St. Paul, 2016.

FREESEMAN, K.; HOEGH, K.; KHAZANOVICH, L. K. Characterization of Concrete at Various Freeze-Thaw Damage Conditions Using SH-Waves. **Proceedings of the 42nd Review of Progress in Quantitative Nondestructive Evaluation (QNDE)**, Minneapolis, 2015.

GHARAIBEH, N. G.; DARTER, M. I.; HECKEL, L. B. Field performance of continuously reinforced concrete pavement in Illinois. **Transportation Research Record: Journal of the Transportation Research Board**, v. 1684, p. 44 – 50, 1999.

GRAFF, K. F. **Wave Motion in Elastic Solids**, Dover publications, 1991.

GROTE, K.; HUBBARD, S.; HARVEY, J.; RUBIN, Y. Evaluation of infiltration in layered pavements using surface GPR reflection techniques. **Journal of Applied Geophysics**, v. 57, p. 129 – 153, 2005.

HA, S.; YEONG, J.; WON, M.C. Evaluation of joint and crack load transfer final report. **Report No 0-5832-P1**, Texas Department of Transportation, 2012.

HALL, K. T. **Performance, evaluation and rehabilitation of asphalt-overlaid concrete pavements.** Ph.D. Dissertation. University of Illinois, 1991.

HANSEN, W.; SMILEY, D. L.; PENG, Y.; JENSEN, E. A. Validating Top-Down Premature Transverse Slab Cracking in Jointed Plain Concrete Pavement. **Transportation Research Record: Journal of the Transportation Research Board**, v. 1809, p. 52 – 59, 2002.

HAZA, A. O.; PETERSEN, C. G.; SAMOKRUTOV, A. **Three Dimensional Imaging of Concrete Structures Using Ultrasonic Shear Waves**. German Instruments SA, Denmark, 2011.

HEISEY, J., STOKOE, I.; MEYER, A. Moduli of pavement systems from spectral analysis of surface waves. **Transportation Research Record: Journal of the Transportation Research Board**, no. 852, 1982.

HOEGH, K. **Ultrasonic Linear Array Evaluation of Concrete Pavements**. Ph.D. Dissertation. University of Minnesota, Minneapolis, 2013.

HOEGH, K.; KHAZANOVICH, L. Correlation Analysis of 2D Tomographic Images for Flaw Detection in Pavements. **ASTM Journal of Testing and Evaluation**, v. 40, No, 2, p. 105 – 110, 2012.

HOEGH, K.; KHAZANOVICH, L. Extended synthetic aperture focusing technique for ultrasonic imaging of concrete. **NDT & E International**, v. 74, p. 33 – 42, 2015.

HOEGH, K.; KHAZANOVICH, L.; DAI, S.; YU, T. Evaluating asphalt concrete air void variation via GPR antenna array data. **Cases Studies in Nondestructive Testing and Evaluation**, v. 3, p. 27 – 33, 2015.

HOEGH, K.; KHAZANOVICH, L.; MASER, K. TRAN, N. Evaluation of Ultrasonic Technique for Detecting Delamination in Asphalt Pavements. **Transportation Research Record: Journal of the Transportation Research Board**, v. 2306, p. 105 – 110, 2012b.

HOEGH, K.; KHAZANOVICH, L.; WOREL, B. J.; YU, T. Detection of Subsurface Joint Deterioration Blind Test Comparison of Ultrasound Array Technology with Conventional Nondestructive Methods. **Transportation Research Record: Journal of the Transportation Research Board**, v. 2367, p. 3 – 12, 2013.

HOEGH, K.; KHAZANOVICH, L.; YU, T. Concrete Pavement Joint Diagnostics with Ultrasonic Tomography. **Transportation Research Record: Journal of the Transportation Research Board**, v. 2305, p. 54 – 61, 2012a.

HOEGH, K.; KHAZANOVICH, L.; YU, T. Ultrasonic Tomography for Evaluation of Concrete Pavements. **Transportation Research Record: Journal of the Transportation Research Board**, v. 2232, p. 85 – 94, 2011.

HOSSAIN, S.; ELFINO, M. K. Field Demonstration of Magnetic Tomography Technology for Determination of Dowel Bar Position in Concrete Pavement. **Report No FHWA/VTRC 06-R40**, Federal Highway Administration, 2006.

HUANG, Y. H. **Pavement Analysis and Design**. Prentice-Hall, Inc., New Jersey, 1993.

HUANG, Y. H.; WANG, S. T. Finite Analysis of Concrete Slabs and its Implications for Rigid Pavement Design. **Highway Research Record**, vol. 466, Highway Research Board, Washington D.C., p. 55-69, Washington D.C., 1973.

HUGENSCHMIDT, J. Concrete bridge inspection with a mobile GPR system. **Construction and Building Materials**, v. 16, p. 147 – 154, 2002.

HUGENSCHMIDT, J.; MASTRANGELO, R. Concrete bridge inspection with a mobile GPR system. **Cement & Concrete Composites**, v. 28, p. 384 – 392, 2006.

INFRAESTRUTURA URBANA. **São Paulo adota corredores de concreto**. (in Portuguese). 2011. Available at: <<http://infraestruturaurbana.pini.com.br/solucoes-tecnicas/7/sao-paulo-adota-corredores-de-concreto-235518-1.aspx>> Accessed on June 13<sup>th</sup>, 2016.

IOANNIDES, A. M.; HAMMONS, C. M.; DAVIS, C. M. Application of Artificial Neural Networks to Concrete Pavement Joint Evaluation. **Transportation Research Record: Journal of the Transportation Research Board**, v. 1540, p. 54 - 64, 1996.

IOANNIDES, A. M.; HAMMONS, M. I. Westergaard-Type Solution for the Edge Load Transfer Problem. **Transportation Research Record: Journal of the Transportation Research Board**, v. 1525, pp. 28–34, 1996.

IOANNIDES, A. M.; KOROVESIS, G. T. Aggregate interlock: A pure shear load transfer mechanism. **Transportation Research Record: Journal of the Transportation Research Board**, v. 1286, p. 14 - 24, 1990.

IOANNIDES, A. M.; KOROVESIS, G. T. Analysis and design of dowelled slab-on-grade pavement systems. **Journal of Transportation Engineering**, v. 118, No 6, p. 745 - 768, 1992.

JEONG, J. H.; ZOLLINGER, D. G. Characterization of stiffness parameters in design of continuously reinforced and jointed pavement. **Transportation Research Record: Journal of the Transportation Research Board**, v. 1778, p. 54 – 63, 2001.

JOHNSTON, D. P.; SURAHL, R. W. Effects of base type modeling long-term pavement performance of continuously reinforced concrete sections. **Transportation Research Record: Journal of the Transportation Research Board**, v. 1979, p. 93 – 101, 2006.

JUNG, Y. S.; ZOLLINGER, D. G.; EHSANUL, B. M. Improved Mechanistic–Empirical Continuously Reinforced Concrete Pavement Design Approach with Modified Punchout Model. **Transportation Research Record: Journal of the Transportation Research Board**, v. 2305, p. 32 – 42, 2012.

KHAZANOVICH, L.; GOTLIF, A. Evaluation of Joint and Crack Load Transfer Final Report. **Report No FHWA-RD-02-088**, Federal Highway Administration, 2003.

KHAZANOVICH, L.; SELEZNEVA, O. I.; YU, T. H.; DARTER, M. I. Development of Rapid Solutions for Prediction of Critical Continuously Reinforced Concrete Pavement Stresses. **Transportation Research Record: Journal of the Transportation Research Board**, v. 1778, p. 32 – 42, 2001.

KHAZANOVICH, L.; YU, H. T.; RAO S.; GALASOVA, K., SHATS, E.; JONES R. **ISLAB2000—Finite Element Analysis Program for Rigid and Composite Pavements. User's Guide**. ERES Consultants, Champaign, Ill., 2000.

KIM, S. M.; WON, M. C.; MCCULLOUGH, B. F. Dynamic stresses response of concrete pavements to moving tandem-axle loads. **Transportation Research Record, Washington, D. C., Transportation Research Board**, v 1809, 2002.

KIM, S. M.; WON, M.; MCCULLOUGH, B. F. Numerical modeling of continuously reinforced concrete pavement subjected to environmental loads. **Transportation Research Record: Journal of the Transportation Research Board**, v. 1629, p. 76 – 88, 1998.

KOHLER, E.; ROESLER, J. Active crack control for continuously reinforced concrete pavements. **Transportation Research Record: Journal of the Transportation Research Board**, v. 1900, p. 19 – 29, 2004.

KOHLER, E.; ROESLER, J. Nondestructive testing for crack width and variability on continuously reinforced concrete pavements. **Transportation Research Record: Journal of the Transportation Research Board**, v. 1974, p. 89 – 96, 2006.

KORONEV, B. G.; CHERNIGOVSKAYA, E. I. **Analysis of Plates on Elastic Foundation**. Gosstroizdat, Moscow, (in Russian), 1962.

KOYANAGAWA, M.; YONEYA, H.; KOKUBU, K. Evaluation of Reliability of Concrete Pavement in Consideration of Fatigue Properties. **Proceedings of the 2<sup>nd</sup> International Workshop on Evaluations of Concrete Pavements**, CROW-PIARC-CEMBUREAU, p. 207-216, Krumbach, 1990.

LEE, Y. H.; DARTER, M. I. Development of performance prediction models for Illinois continuously reinforced concrete pavements. **Transportation Research Record: Journal of the Transportation Research Board**, v. 1505, p. 75 – 84, 1995.

LIU, J.; ZHAO, D.; SHEN, J.; ZHANG, Y. Comparative Study on Crack and Factor of Continuously Reinforced Concrete Pavement in the Tunnel and Outside. **Proceedings of the 13th COTA International Conference of Transportation Professionals (CICTP 2013)**, Shenzhen, China, 2013.

LOU, Z.; TIAN, B.; LIU, Y. Experimental Study on Water Seepage Rate with Crack Width of Continuously Reinforced Concrete Pavement. **Advanced Materials Research**, v. 243-249, p. 4288 – 4292, 2011.

MA, J.; MCCULLOUGH, B. F. Analysis of load, temperature, and shrinkage effect on continuously reinforced concrete pavement. **Transportation Research Record: Journal of the Transportation Research Board**, v. 671, p. 29 – 39, 1978.

MAIERHOFER, C. Nondestructive Evaluation of Concrete Infrastructure with Ground Penetrating Radar. **Journal of Materials in Civil Engineering**, v. 15, p. 287 – 297, 2003.

MAITRA, S. R.; REDDY, K. S.; RAMACHANDRA, L. S. Load Transfer Characteristics of Aggregate Interlocking in Concrete Pavement. **Journal of Transportation Engineering**, v. 136, p. 190 - 195, 2010.

MAJIDZADEH, K. A Mechanistic Approach to Rigid Pavement Design. **Concrete Pavements**, p. 11-56, Elsevier Applied Science, 1988.

MCCULLOUGH, B. F.; DOSSEY, T. Controlling early-age cracking in continuously reinforced concrete pavement. Observations from 12 years of monitoring experimental test sections in Houston, Texas. **Transportation Research Record: Journal of the Transportation Research Board**, v. 1684, p. 35 – 43, 1999.

MINER, M. A. Cumulative Damage Fatigue. **Trans. ASME**, v.67, p. 159-164, 1945.

MOHAMED, A. R.; HANSEN, W. Effect of Nonlinear Temperature Gradient on Curling Stresses in Concrete Pavements. **Transportation Research Record: Journal of the Transportation Research Board**, v. 1568, pp. 65–71. 1997.

MOMENI, A. F. **Y-Cracking in continuously reinforced concrete pavements**. Master of Science Thesis. Kansas State University, Manhattan, 2013.

NAM, J. H.; KIM, S. M.; WON, M. C. Measurement and analysis of early-age concrete strains and stresses. Continuously reinforced concrete pavement under environmental loading. **Transportation Research Record: Journal of the Transportation Research Board**, v. 1947, p. 79 – 90, 2006.

NASIEF, H. G.; WHITED, G. C.; LOH, W. Y. Wisconsin Method for Probing Portland Cement Concrete Pavement for Thickness Statistical Comparison and Validation. **Transportation Research Record: Journal of the Transportation Research Board**, v. 2228, p. 99 – 107, 2011.

NCHRP. Guide for Mechanistic-Empirical Design of New and Rehabilitated Pavement Structures. **NCHRP 1-37A**. National Cooperative Highway Research Program, Transportation Research Board, Washington D.C., 2004.

O DIA. **Cheia de remendos, pista do BRT Transoeste será trocada no Recreio**. (in Portuguese). 2014. Available at: <<http://odia.ig.com.br/noticia/rio-de-janeiro/2014-10-17/cheia-de-remendos-pista-do-brt-transoeste-sera-trocada-no-recreio.html>> Accessed on June 13<sup>th</sup>, 2016.

OLHOEFT, G. R.; SMITH III, S. S. Automatic Processing and Modeling of GPR data for Pavement Thickness and Properties. **Proceedings of the 8th International Conference on Ground Penetrating Radar**, Gold Coast, Australia, 2000.

PARK, J. H.; CHOI, M. Y.; KIM W. T. Infrared Thermography and Modeling to the Concrete Deck with Internal Defects as a Non-destructive Testing. **Key Engineering Materials**, v. 270-273, p. 938 – 943, 2004.

PCA. **Thickness design for concrete pavements**. Portland Cement Association, HB-35, Chicago, 1966.

PEIFFER, A.; KOHLER, B.; PETZOLD, S. The acoustic finite integration technique for waves of cylindrical symmetry (CAFIT). **Journal of Acoustic Society of America**, v. 102, pp. 697 – 706, 1997.

PEREIRA, D. S.; BALBO, J. T.; KHAZANOVICH, L. Theoretical and field evaluation of interaction between ultra-thin whitetopping and existing asphalt pavement. **The International Journal of Pavement Engineering**, V. 7, p. 251-260, 2016.

PERLIN, L. P.; PINTO, R. C. A. Ultrasonic Tomography in Concrete. **Ibracon Structures and Materials Journal**, v. 6, n. 2, p. 246-269, 2013.

PIARC. **Continuously Reinforced Concrete Pavements**. Technical Committee on Concrete Roads, Permanent International Association of Roads Congresses, Paris, 1994.

PORTLAND CEMENT ASSOCIATION (PCA). **Thickness Design for Concrete Highway and Street Pavements**. Skokie, Illinois, 1984.

PRABHU, M.; BUCH, N.; VARMA, A. H.; THANDAVESWARA, D. Experimental Investigation of Effects of Dowel Misalignment on Joint Opening Behavior in Rigid Pavements. **Transportation Research Record: Journal of the Transportation Research Board**, v. 1947, p. 15 – 27, 2006.

PREFEITURA MUNICIPAL DE SÃO PAULO (PMSP). Dimensionamento de Pavimentos de Concreto. **IP-07/2004**. (In Portuguese). Prefeitura Municipal de São Paulo, São Paulo, 2004b.

PREFEITURA MUNICIPAL DE SÃO PAULO (PMSP). Dimensionamento de Pavimentos Flexíveis Tráfego Meio Pesado, Pesado, Muito Pesado e Faixa Exclusiva de Ônibus. **IP-05/2004**. (In Portuguese). Prefeitura Municipal de São Paulo, São Paulo, 2004a.

RADAPORT, G. Inspection of Prestressed Concrete Road Bridges by Ultrasound 3D Tomographer System. **Proceedings of the 24<sup>th</sup> World Road Congress**. PIARC, Paris, 2011.

RAO, C.; SELEZNEVA, O.; DARTER, M. I.; TITUS-GLOVER, L. T.; KHAZANOVICH, L. Calibration of Mechanistic–Empirical Performance Model for Continuously Reinforced Concrete Pavement Punch-outs. **Transportation Research Record: Journal of the Transportation Research Board**, v. 1896, pp. 15–22., 2004.

RAO, S.; HOEGH, K.; YU, T.; KHAZANOVICH, L. C Evaluation of Dowel Alignment Constructability in Portland Cement Concrete Pavements. **Transportation Research Record: Journal of the Transportation Research Board**, v. 2098, p. 86 – 93, 2009.

RASMUSSEN, R. O.; ROGERS, R.; FERRAGUT, T. R. **Continuously Reinforced Concrete Pavement Design and Construction Guidelines**. Federal Highway Administration, 2009.

REIS, E. E. Jr; MOZER, J. D.; BIANCHINI, A. C.; KESLER, C.E. Causes and Control of Cracking in Concrete Reinforced With High-Strength Steel Bars – A Review of Research. **Engineering Experiment Station Bulletin 479**, College of Engineering, University of Illinois. 1965.

REN, D.; HOUBEN, L. J. M.; RENS, L. Cracking Behavior of Continuously Reinforced Concrete Pavements in Belgium Characterization of Current Design Concept. **Transportation Research Record: Journal of the Transportation Research Board**, v. 2367, p. 97 – 106, 2013.

REN, D.; HOUBEN, L. J. M.; RENS, L. Monitoring Early-age Cracking of Continuously Reinforced Concrete Pavements on the E17 at Ghent (Belgium). **Sustainable Construction Materials**, p. 30 – 41, 2012.

RODOLFO, M. P. **Análise de Tensões em Pavimentos de Concreto com Base Cimentada e Sujeitos a Gradientes Térmicos**. Dissertação (mestrado), (In Portuguese), Escola Politécnica da Universidade de São Paulo, São Paulo, 2001.

ROESLER, J.; HILLER, J. E. Continuously Reinforced Concrete Pavement: Design Using the AASHTOWare Pavement ME Design Procedure. **Report No FHWA/TX-05/0-4517-2**, Federal Highway Administration, 2013.

ROESLER, J.; HILLER, J. E.; BRAND, A. S. **Continuously Reinforced Concrete Pavement Manual**. Guidelines for Design, Construction, Maintenance, and Rehabilitation. U. S. Department of Transportation. Federal Highway Administration, 2016.

RYU, S. W.; WON, H.; CHOI, S.; WON, M. C. Continuously reinforced bonded concrete overlay of distressed jointed plain concrete pavements. **Construction and Building Materials**, v. 40, p. 1110 – 1117, 2013.

SAARENKETO, T; SCULLION, T. Road evaluation with ground penetrating radar. **Journal of Applied Geophysics**, v. 43, p. 119 – 138, 2000.

SALLES, L S. **Análise de comportamento de pavimento de concreto continuamente armado de curta extensão**. Master of Science Dissertation (In Portuguese). Escola Politécnica da Universidade de São Paulo, São Paulo, 2014.

SALLES, L. S.; BALBO, J. T. Experimental continuously reinforced concrete pavement parameterization using nondestructive methods. **Ibracon Structures and Materials Journal**, v. 9, p. 263-274, 2016.

SALLES, L. S.; BALBO, J. T. Experimental short continuously reinforced concrete pavement: crack pattern and load transfer efficiency across cracks. **Proceedings of the 12th International Symposium on Concrete Roads**. EUPAVE, Prague, 2014.

SALLES, L. S.; BALBO, J. T. Tecnologia de Pavimentação em Concreto Continuamente Armado para Rodovias de Alta Durabilidade. **Proceedings of the 9<sup>th</sup> Congresso Brasileiro de Rodovias & Concessões** (In Portuguese). Brasília, 2015.

SALLES, L. S.; BALBO, J. T.; PEREIRA, D. S. Non-destructive Performance Evaluation of Experimental Short Continuously Reinforced Concrete Pavement. **International Journal of Pavement Research and Technology**, v. 8, p. 221-232, 2015.

SALLES, L. S.; CONWAY, R.; KHAZANOVICH, L.; BARNES, R.; PEREIRA, D. S.; BURNHAM, T. Portland Cement Concrete Pavement Thickness and Shear Wave Velocity Variation Versus Observed Pavement Distresses. **Proceedings of the 96th Annual Transportation Research Board Meeting**. Washington, D. C., 2017.

SAMOKUTOV, A.; SHEVALDYKIN, V. BOBROV, V.; KOZLOV, V. Development of acoustic methods and production of modern digital devices and technologies for ultrasonic non-destructive testing. **Journal ULTRAGARSAS**, v. 61, no. 4, p. 12 – 21, 2006.

SCULLION, T. Using Rolling Deflectometer and Ground Penetrating Radar Technologies for Full Coverage Testing of Jointed Concrete Pavements. **Report No FHWA-HIF-13-025**, Federal Highway Administration, 2006.

SELEZNEVA, O.; RAO, C.; DARTER, M. I.; ZOLLINGER, D.; KHAZANOVICH, L. Development of a mechanistic-empirical structural design procedure for continuously reinforced concrete pavements. **Transportation Research Record: Journal of the Transportation Research Board**, v. 1896, p. 46 – 56, 2004.

SHAHIN, M. Y. Use of the falling weight deflectometer for the non-destructive deflection testing of jointed concrete airfield pavements. **Proceedings of the 3<sup>rd</sup> International Conference on Concrete Pavement Design and Rehabilitation**, Purdue University, pp. 549-556, 1984.

SHEVALDYKIN, V.G., SAMOKRUTOV, A. A.; KOZLOV, V.N. Ultrasonic Low-Frequency Transducer with Dry Dot Contact and Their Applications for Evaluation of Concrete Structures. **Proceedings of the IEEE International Ultrasonics Symposium**, Munich, 2002.

SUH, Y. C.; MCCULLOUGH, B. F. Factors affecting crack width of continuously reinforced concrete pavement. **Transportation Research Record: Journal of the Transportation Research Board**, v. 1449, p. 134 – 140, 1994.

SUN, R.; COBOS, L.; WON, M. C. Behavior of the Longitudinal Construction Joint of Continuously Reinforced Concrete Pavement. **Geotechnical Special Publication**, N. 212, p. 200 – 207, 2011b.

SUN, R.; WON, H.; WON, M. C. The Application and Early-age Behaviors of Continuously Reinforced Bonded Concrete Overlay of Distressed Jointed Concrete Pavements. **Geotechnical Special Publication**, N. 212, p. 208 – 215, 2011a.

TAYABJI S. D.; JIANG, Y. J. Mechanistic Evaluation of Test Data from LTPP Jointed Plain Concrete Pavement Test Section. **Proceedings of the 4<sup>th</sup> International Workshop on the Design Theories and Their Verification of Concrete Slabs and Railroads**, CROW, Buçaco.

TAYABJI, S. D.; STEPHANOS, P. J.; GAGNON, J. S.; ZOLLINGER, D. G. Performance of Continuously Reinforced Concrete Pavement. Volume II: Field Investigations of CRC Pavements. **FHWA-RD-94-149**, FHWA, U.S. Department of Transportation, Washington, D.C, 1998b.

TAYABJI, S. D.; STEPHANOS, P. J.; ZOLLINGER, D. G. Nationwide field investigation of continuously reinforced concrete pavements. **Transportation Research Record: Journal of the Transportation Research Board**, v. 1482, p. 7 – 18, 1995.

TAYABJI, S. D.; ZOLLINGER, D. G.; KOROVESIS, G. T.; STEPHANOS, P. J.; GAGNON, J. S. Performance of Continuously Reinforced Concrete Pavement. Volume I: Summary of practice and annotated bibliography. **FHWA-RD-94-149**, FHWA, U.S. Department of Transportation, Washington, D.C, 1998a.

THOMLINSON, J. Temperature Variations and Consequent Stresses Produced by Daily and Seasonal Temperature Cycles in Concrete Slabs. **Concrete Constructional Engineering**, Vol. 36, No. 6, pp. 298–307, 1940.

TIA, M.; WU, C.-L.; RUTH, B. E.; BLOOMQUIST, D.; CHOUBANE, B. **Field Evaluation of Rigid Pavements for the Development of a Rigid Pavement Design System – PHASE IV**. Final Report. Department of Civil Engineering, University of Florida, Gainesville, 1989.

TOMPKINS, D. M.; KHAZANOVICH, L.; JOHNSON, D. M. Benefits of the Minnesota Road Research Project. **Transportation Research Record: Journal of the Transportation Research Board**, v. 2087, p. 12 – 19, 2008.

VANCURA, M.; KHAZANOVICH, L.; BARNES, R. Concrete Pavement Thickness Variation Assessment with Cores and Nondestructive Testing Measurements. **Transportation Research Record: Journal of the Transportation Research Board**, v. 2347, p. 61 – 68, 2013.

VANDENBOSSCHE, J. M.; NASSIRI, S.; RAMIREZ, L. C.; SHERWOOD, J. A. Evaluating the continuously reinforced concrete pavement performance models of the mechanistic-empirical pavement design guide **Road Materials and Pavement Design**, v. 6, N. 2, p. 235 – 248, 2012.

VERHOEVEN, K. Cracking and corrosion in continuously reinforced concrete pavements. **Proceedings of the 5<sup>th</sup> International Conference on Concrete Pavement Design and Rehabilitation**, Purdue University, West Lafayette, Indiana, 1992.

WON, M. C. Continuously reinforced concrete pavement: identification of distress mechanisms and improvement of mechanistic-empirical design procedures. **Transportation Research Record: Journal of the Transportation Research Board**, v. 2226, p. 51 – 59, 2011.

XIAO, T.; SUN, J. S.; WANG, X. H.; CHEN, Z. X. Dynamic response analysis of cement concrete pavement under different vehicle speeds. **Geotechnical Special Publication**, N° 212, Washington, D.C., ASCE, 2011.

ZERO HORA. **Problemas no piso afetam todos os corredores do BRT em Porto Alegre.** (in Portuguese). 2014 Available at: <<http://zh.clicrbs.com.br/rs/porto-alegre/transito/noticia/2014/12/problemas-no-piso-afetam-todos-os-corredores-do-brt-em-porto-alegre>> Accessed on June 13<sup>th</sup>, 2016.

ZHANG, W.; WANG, G.; MA, S.; LI, X. Field experimental study on measurement and analysis strain on the rigid pavement slab subjected to moving vehicle loads. **Proceedings of the International Conference on Transportation Engineering (ICTE)**, China, ASCE, 2007.

ZHANG, X. Effects of Base Characteristics on Curling Stresses of Continuously Reinforced Concrete Pavements. **Proceedings of the 12th COTA International Conference of Transportation Professionals (CICTP 2012)**, Beijing, China, 2012.

ZHANG, X.; ZHU, X.; SHEN, J. Statistical Analysis of Early-Age Crack Data: Preliminary Results from Continuously Reinforced Concrete Pavements in China. **Proceedings of the 12th COTA International Conference of Transportation Professionals (CICTP 2012)**, Beijing, China, 2012.

ZHANG, Y.; LIU, H. Finite element analysis of thermal stresses for continuous reinforced concrete pavement. **Journal of Highway and Transportation Research Development**, v. 1449, p. 11 – 17, 2012.

ZHANG, Y; LIU, H. B.; ZHONG, C. L. Analytical Solution of Continuously Reinforced Concrete Pavement (CRCP) under the Action of Temperature Stress. **Proceedings of the 10th International Conference of Chinese Transportation Professionals**. Beijing, China, 2010.

ZHOU, W.; CHOI, P.; SARAF, S.; RYU, S. W; WON, M. C. Premature distresses at transverse construction joints (TCJs) in continuously reinforced concrete pavements. **Construction and Building Materials**, v. 55, p. 212 – 219, 2014.

ZOLLINGER, D .G. **Investigation of Punchout Distress of Continuously Reinforced Concrete Pavements**. Ph.D. Dissertation. University of Illinois, Urbana-Champaign, 1989.

ZOLLINGER, D. G.; BARENBERG, E. J. Mechanistic design considerations for punchout distress in continuously reinforced concrete pavement. **Transportation Research Record: Journal of the Transportation Research Board**, v. 1286, p. 25 – 37, 1990.

ZOLLINGER, D. G.; BUCH, N.; XIN, D.; SOARES, J. Performance of Continuously Reinforced Concrete Pavements, Volume 6: CRC Pavement Design, Construction, and Performance. Final Report. **FHWA-RD-97-151**. FHWA, U.S. Department of Transportation, 1999.

ZOLLINGER, D.; JUNG, Y. TechBrief: Continuously Reinforced Concrete Pavement: Improved Transition Designs, **Report FHWA-HIF-13-026**, Federal Highway Administration, 2013.

## APPENDIX A

Table A. 1 – Equivalent zero-thermal gradient loads for different thermal gradients in a 200 mm concrete slab

$\Delta T$ (°C)											
0		5		10		15		20		25	
Load (kN)	Stresses (MPa)	Load (kN)	Stresses (MPa)	Load (kN)	Stresses (MPa)	Load (kN)	Stresses (MPa)	Load (kN)	Stresses (MPa)	Load (kN)	Stresses (MPa)
60	1.434	84.89	2.027	110.32	2.620	134.78	3.213	161.92	3.827	191.27	4.564
80	1.910	104.91	2.503	129.89	3.096	154.35	3.689	180.15	4.295	207.29	4.950
100	2.386	124.92	2.979	149.91	3.578	175.26	4.171	199.73	4.771	227.30	5.419
120	2.861	144.94	3.454	169.92	4.054	196.17	4.647	219.30	5.247	246.43	5.881
140	3.282	164.96	3.937	189.94	4.530	214.85	5.123	240.20	5.723	266.00	6.350

Table A. 2 – Equivalent zero-thermal gradient loads for different thermal gradients in a 250 mm concrete slab

$\Delta T$ (°C)											
0		5		10		15		20		25	
Load (kN)	Stresses (MPa)	Load (kN)	Stresses (MPa)	Load (kN)	Stresses (MPa)	Load (kN)	Stresses (MPa)	Load (kN)	Stresses (MPa)	Load (kN)	Stresses (MPa)
60	1.034	94.75	1.627	129.00	2.220	164.14	2.827	201.06	3.461	237.53	4.089
80	1.379	114.32	1.972	149.46	2.572	184.16	3.172	221.52	3.813	258.44	4.447
100	1.724	134.34	2.317	169.03	2.910	203.73	3.509	241.09	4.151	278.90	4.799
120	2.068	155.24	2.661	189.05	3.254	223.75	3.854	261.11	4.495	299.37	5.150
140	2.413	174.82	3.006	209.07	3.599	243.76	4.199	280.68	4.833	318.94	5.495

Table A. 3 – Equivalent zero-thermal gradient loads for different thermal gradients in a 300 mm concrete slab

$\Delta T$ (°C)											
0		5		10		15		20		25	
Load (kN)	Stresses (MPa)	Load (kN)	Stresses (MPa)	Load (kN)	Stresses (MPa)	Load (kN)	Stresses (MPa)	Load (kN)	Stresses (MPa)	Load (kN)	Stresses (MPa)
60	0.793	105.42	1.386	150.35	1.979	197.50	2.599	244.65	3.220	291.36	3.833
80	1.055	125.44	1.648	170.37	2.241	217.52	2.861	265.11	3.489	312.71	4.116
100	1.317	145.01	1.910	190.38	2.503	237.53	3.123	285.58	3.758	333.62	4.392
120	1.579	165.03	2.172	209.96	2.765	257.11	3.385	306.04	4.027	354.08	4.661
140	1.841	185.05	2.434	230.42	3.034	277.12	3.647	326.05	4.289	374.98	4.937

Table A. 4 – Equivalent zero-thermal gradient loads for different thermal gradients in a 350 mm concrete slab

$\Delta T$ (°C)											
0		5		10		15		20		25	
Load (kN)	Stresses (MPa)	Load (kN)	Stresses (MPa)	Load (kN)	Stresses (MPa)	Load (kN)	Stresses (MPa)	Load (kN)	Stresses (MPa)	Load (kN)	Stresses (MPa)
60	0.627	116.54	1.220	174.37	1.820	232.64	2.434	291.36	3.047	350.52	3.668
80	0.841	137.01	1.434	193.94	2.027	253.10	2.648	311.82	3.268	371.43	3.889
100	1.048	157.02	1.641	213.51	2.234	273.57	2.861	332.28	3.482	392.33	4.109
120	1.255	176.59	1.848	233.98	2.448	293.14	3.068	352.74	3.696	412.79	4.323
140	1.462	197.06	2.062	253.99	2.654	312.71	3.282	373.21	3.909	433.70	4.544

Table A. 5 – Equivalent zero-thermal gradient loads for different thermal gradients in a 400 mm concrete slab

$\Delta T$ (°C)											
0		5		10		15		20		25	
Load (kN)	Stresses (MPa)	Load (kN)	Stresses (MPa)	Load (kN)	Stresses (MPa)	Load (kN)	Stresses (MPa)	Load (kN)	Stresses (MPa)	Load (kN)	Stresses (MPa)
60	0.514	129.44	1.110	198.39	1.703	270.23	2.317	340.73	2.923	411.91	3.537
80	0.686	149.46	1.282	218.41	1.875	290.47	2.489	362.53	3.110	433.70	3.716
100	0.855	169.48	1.455	238.87	2.048	310.93	2.668	382.55	3.282	454.16	3.896
120	1.027	189.05	1.620	258.89	2.220	331.39	2.841	403.01	3.461	475.96	4.082
140	1.200	209.07	1.793	278.90	2.392	351.41	3.013	425.25	3.640	496.42	4.261

## APPENDIX B

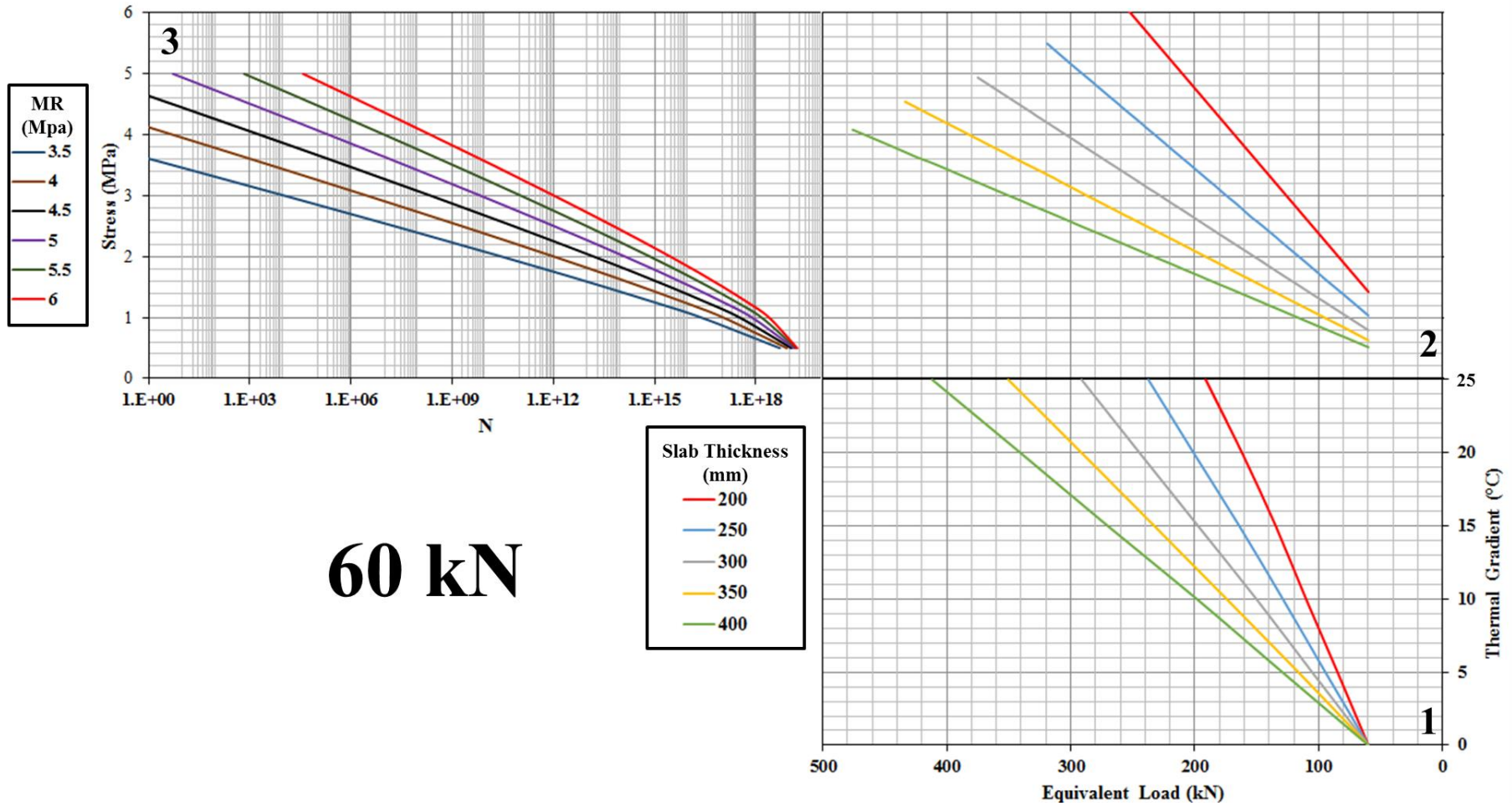


Figure B. 1 – Short CRCP design chart for a 60 kN axle load

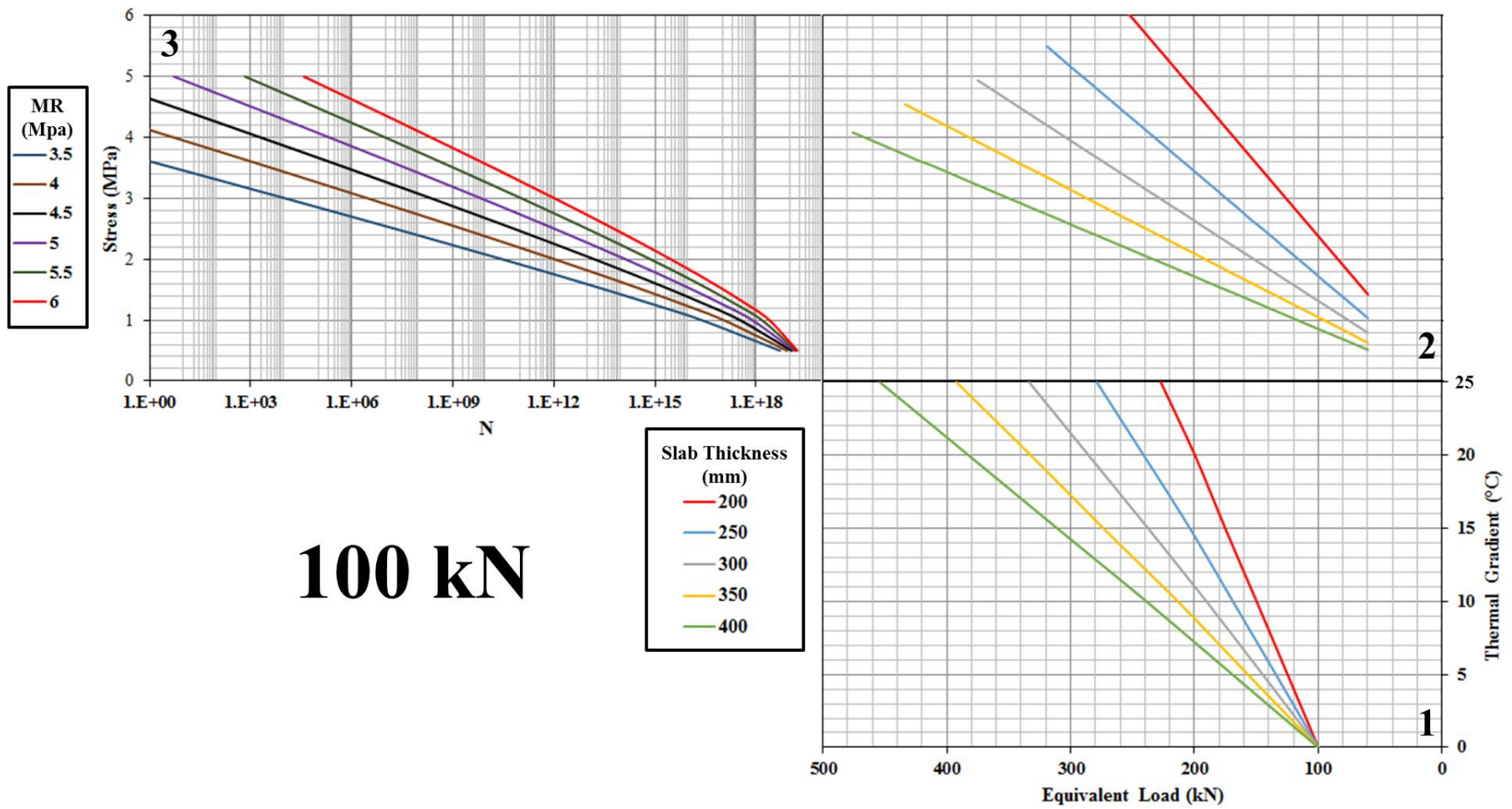


Figure B. 2 – Short CRCP design chart for a 100 kN axle load

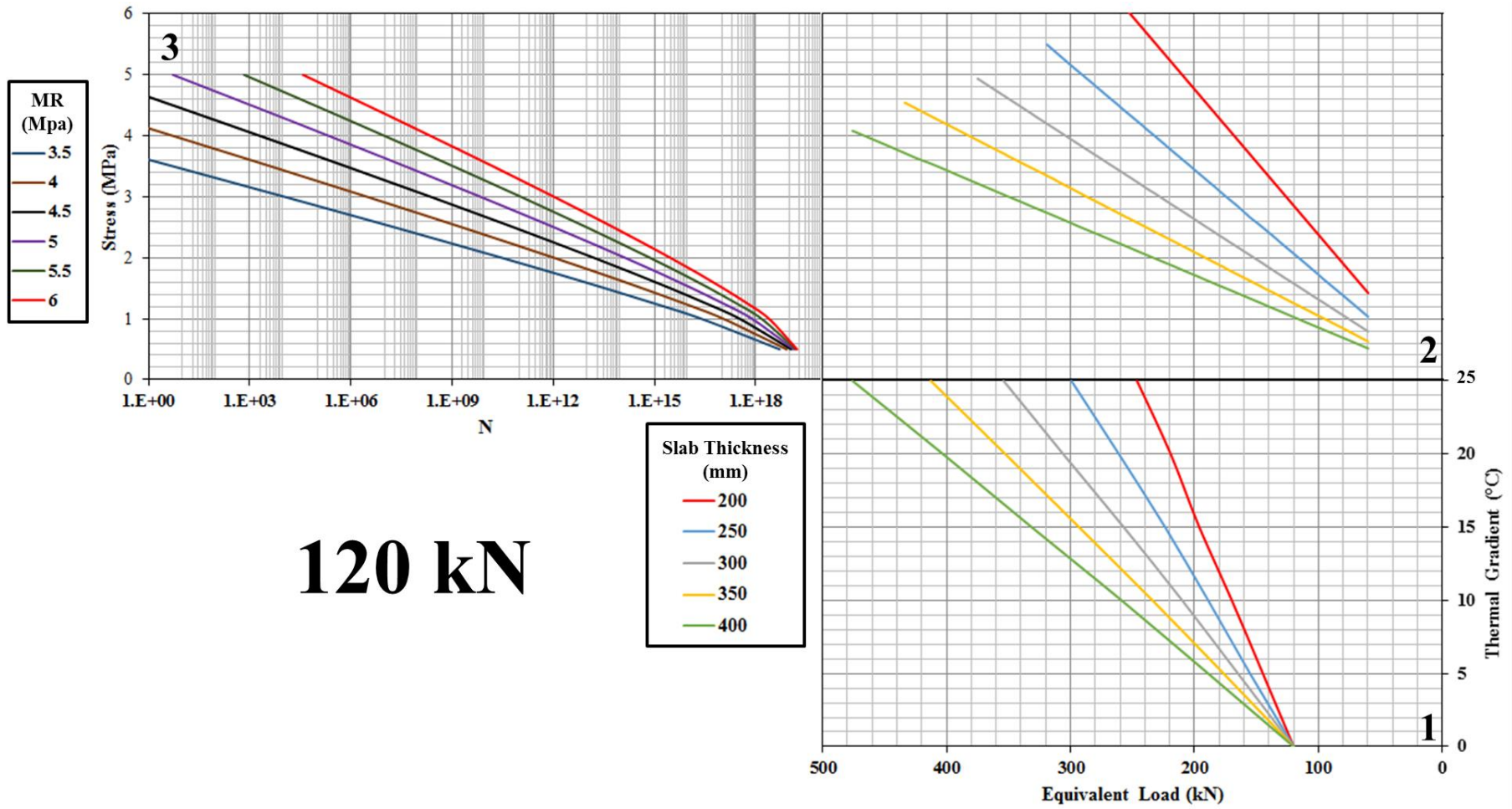


Figure B. 3 – Short CRCP design chart for a 120 kN axle load

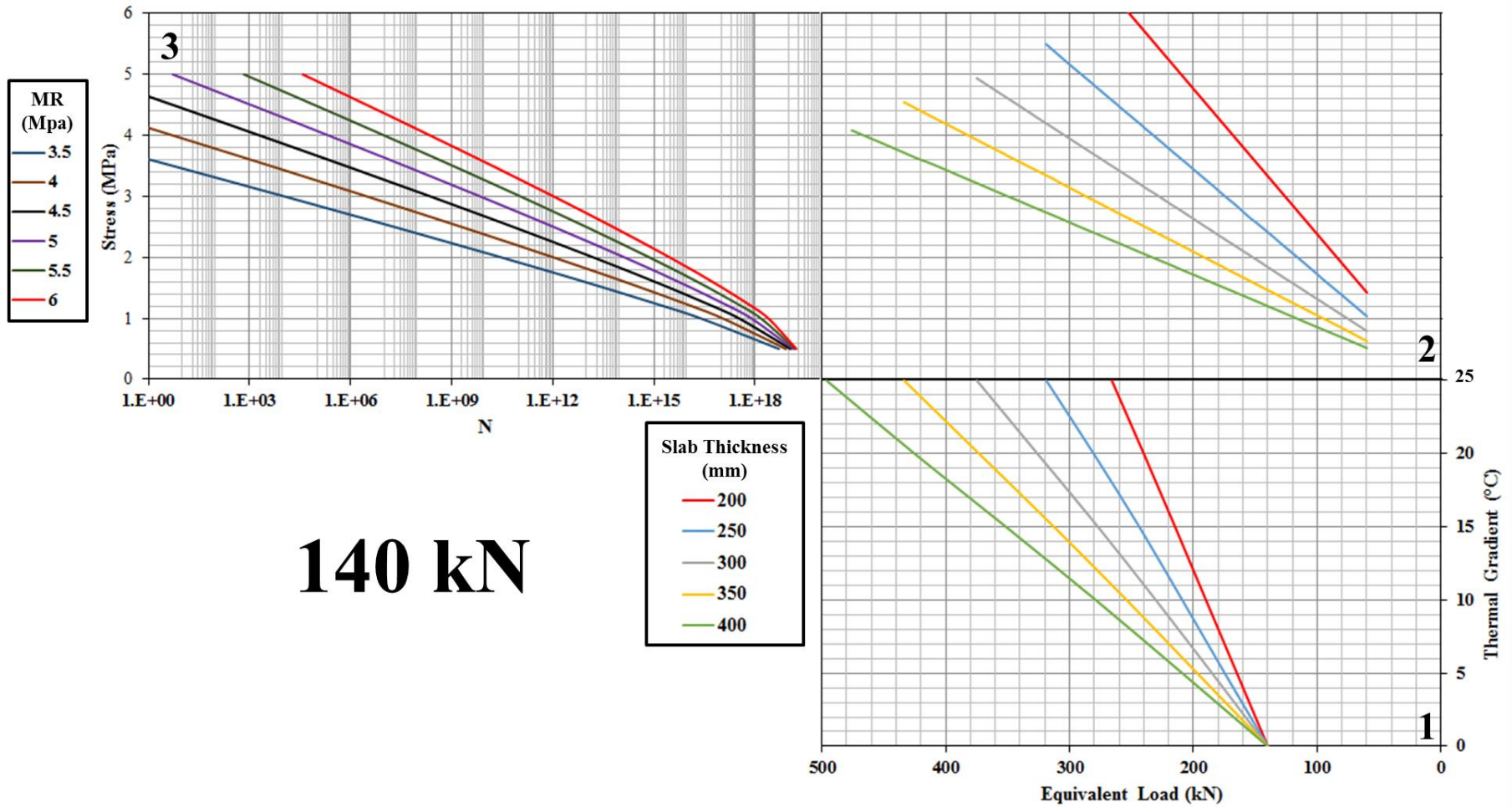


Figure B. 4 – Short CRCP design chart for a 140 kN axle load

## APPENDIX C

Table C. 1 – Proposed fatigue consumption analysis for short CRCPs

1	2	3	4	5	6	7	8
Load Tests	Axle Load (kN)	$\Delta T$ (°C)	Thickness (mm)	Principal Stress (MPa)	$N_{DC}$ (Design Chart)	$N_P$ Project	Fatigue Damage*
1							
2							
3							
4							
5							
6							
7							
8							
9							
10							
11							
12							
13							
14							
15							

\* In column 8, divide the value of column 7 for the value of column 6 ( $N_P/N_{DC}$ )

\*\* Sum all the values in column 8, if the result is lower than 1, the selected slab thickness is appropriate for the project.

\*\* $\Sigma$

## VITA

Lucio Salles de Salles was born on April 2<sup>nd</sup>, 1988 in Júlio de Castilhos (RS). Between 2006 and 2011 he studied civil engineering at the Federal University of Santa Maria (UFSM) and in 2014 received a M.S. in transportation engineering by the University of São Paulo (USP).

During his undergrad studies, he was an engineering intern at Bortoluzzi Construções and was granted a FIPE scholarship for undergrad research at UFSM. He concluded his final mandatory internship at Conterra Constuções in Porto Alegre (RS) and was hired as a civil engineer by the same company acting in infrastructure projects and construction.

In 2012, he joined the Graduate Program of the University of São Paulo working with research related to concrete pavements. After concluding his masters degree, he acted as a Professor at University Paulista (UNIP) from 2014 to 2015 and at University of Mogi das Cruzes (UMC) since 2015 teaching transportation engineering related courses.

From 2015 to 2016, he conducted part of his doctorate research at the University of Minnesota.

He has published six peer-reviewed papers and eleven conference papers attending eight international conferences and workshops on pavement research and technology. In 2015, his paper was selected as one of the five best papers on the 5<sup>th</sup> Innovation Saloon ABCR from the 9<sup>th</sup> Brazilian Conference of Highways and Concessions.